Modeling and Characterization of Ionic Polymer Transducers for Sensing and Actuation

by

Kevin Morris Farinholt

Dissertation submitted to the Faculty of the
Virginia Polytechnic Institute and State University
in partial fulfillment of the requirements for the degree of

Doctor of Philosophy

in

Mechanical Engineering

Donald J. Leo, Chair
Daniel J. Inman
Scott L. Hendricks
Kwang J. Kim
Timothy E. Long
Craig A. Woolsey

November 2005
Blacksburg, Virginia

Keywords: ionic polymer transducers, sensor, actuator, sensing response, impedance response

Modeling and Characterization of Ionic Polymer Transducers for Sensing and Actuation

Kevin Morris Farinholt, Ph.D.
Virginia Polytechnic Institute and State University, 2005
Advisor: Donald J. Leo

Abstract

Ionic polymer transducers comprise a class of active material that exhibit interesting chemoelectromechanical coupling capabilities. With the ability to convert energy between chemical, electrical and mechanical domains, these materials offer potential for use in numerous engineering applications. The research presented in this dissertation focuses primarily on the electromechanical coupling that exists within these ionic polymer materials. When plated with a conductive surface electrode, these ionomeric membranes function effectively as either sensors or actuators. Mechanically compliant, these transducers demonstrate large strain, but limited force, capabilites while operating at low excitation voltages.

The objective of this research is to improve understanding of the transduction properties inherent in the ionic polymer. Most of the existing work in this area has focused on the actuation response, therefore the focus of this research is on providing a better understanding of the sensing and impedance responses of the ionic polymer transducer. Using transport theory as the basis, a set of analytical models are developed to characterize the charge motion that develops within an ionomer when subject to either mechanical or electrical loading. These models characterize the internal potential and charge density responses of the membrane, as well as the expected surface current that would be measured as the result of external loading.

In addition to the analytical work, numerous experimental characterizations of the membrane are also presented. The ionic polymer's actuation, sensing and impedance responses are each considered as a function of the counterion and solvent type present within the ionic polymer. These studies demonstrate the importance of the ionomer's impedance response in understanding the electromechanical capabilites of an ionic polymer transducer. Most sample-to-sample variation can be attributed to the voltage to current conversion that occurs within the ionic polymer. By relating these experimental results to the analytical models, it is possible to characterize these changes in performance in terms of the effective diffusion and permittivity parameters of the transducer. A final series of experiments are also considered to determine the effectiveness of the model in predicting the impedance response as a function of temperature, solvent viscosity and preloading of the membrane.

Acknowledgments

First I would like to extend my sincerest thanks to my academic advisor Dr. Donald J. Leo for the years of encouragement, guidance, patience and friendship he has provided throughout my years as a graduate student at Virginia Tech. I would also like to thank Don for inspiring me to pursue my doctorate, and for the many other opportunities he has helped me to pursue throughout my graduate career. I would also like to thank Dr. Daniel J. Inman, Dr. Scott L. Hendricks, Dr. Timothy Long, Dr. Craig A. Woolsey and Dr. Barbar J. Akle for their advice and for serving as committee members.

I also want to acknowledge Dr. Kwang J. Kim of the University of Nevada, Reno who is serving as a member of my committee from outside of the university. I truly appreciate the many discussions and collaborations I have had with Dr. Kim throughout my doctoral research, and I am grateful that he is serving as an external reader on my dissertation. Many thanks also go to Dr. Haider Arafat of Virginia Tech who offered a considerable amount of time for conversations concerning the nonlinear aspects of my research. I would like to thank Dr. Thomas Wallmersperger of the Universität Stuttgart in Stuttgart, Germany as well. It has been a privilege to collaborate with Dr. Wallmersperger on numerous occasions, and his willingness to share ideas and discussions have been invaluable to my doctoral studies.

I would also like to thank all of my collegues here at the Center for Intelligent Material Systems and Structures for their insightfulness and willingness to help. Particular thanks goes to the polymer group, including former colleagues John Franklin, Kiran Mallavarapu, Dr. Kenneth Newbury and Dr. Lisa Weiland, as well as my current colleagues Dr. Barbar Akle, Dr. Mathew Bennett, Dr. Curt Kothera, Miles Buechler, Xingxi He and Vishnu Sundaresan.

I would like to acknowledge the National Defense Science and Engineering Graduate fellowship for the financial support that funded most of this research. Also I would like to acknowledge the Virginia Space Grant Consortium who provided supplemental funding during my tenure.

Lastly, I would like to thank my family and friends who have offered their continued encouragement throughout my time at Virginia Tech. I would like to thank my older brother Brian for convincing me to come to Virginia Tech for my education, and for my sisters, Malinda and Sheri, who each earned their undergraduate degrees

at Virginia Tech while I was pursuing my graduate studies at CIMSS. Most importantly, I would like to thank my parents, Joseph and Linda for their patience, support and love throughout my life. They served to instill a desire to learn in me that has lead me to this point in my life, and it is in the loving memory of my mother that I dedicate this work.

Kevin Morris Farinholt

Virginia Polytechnic Institute and State University
November 2005

This work is dedicated to my father
Joseph J. Farinholt,
and in loving memory of my mother,
Linda M. Farinholt

Contents

List of Tables

List of Figures

Nomenclature

Chapter 2

$\mathbf{E}, E$	electric field [V/m]	ϕ	electric potential [V]
$\mathbf{D}, D$	electric displacement [C/m^2]	ψ_s	stress-charge density
C^+ (C^-)	cation (anion) concentration [mol/m^3]		proportionality constant [J/C]
$\mathbf{J}, J$	current flux density [A/m^2]	ρ	charge density [C/m^3]
d	diffusion coefficient [m^2/s]	$\mathcal{K}_e$	dielectric permittivity [F/m]
ΔV	volumetric change [m^3/mol]	λ	characteristic time [s^{-1}]
$\mathbf{p}, p$	pressure [Pa]	β	length scale inverse [m^{-1}]
$\mathbf{v}, v$	fluid velocity [m/s]	σ	mechanical stress [Pa]
$P(x), Q(t)$	separable functions for charge density [-]		*Constants*
I	cross-section moment of inertia [m^4]	F	Faraday's constant - 96,487 [C/mol]
$w(L)$	tip deflection [m]	R	Gas Constant - 8.3143 [J/(mol K)]
M	applied moment [N-m]	T	temperature [K]
F_o	applied force [N]	l	beam length [m]
$q(t)$	surface charge [C/m^2]	h	L/2 [m]
$i(t)$	current [A]		*Independent Variables*
v_{out}	output of sensing circuit [V]	t	time [s]
Y	elastic modulus [Pa]	x	spatial coordinate

Chapter 3

$w(l,t)$	tip displacment [m]		
l	length of polymer [m]	t	time [s]
A, B, C	amplitude of exponential terms [-]	$\tau_{A,B,C}$	time constant of exponential terms [s]

Chapter 4

RC analysis

R	resistance [Ohms]	Z_R	resistive impedance [Ohms]
C	capacitance [C]	Z_C	capacitive impedance [Ohms]
R_m	membrane resistance [Ohms]	Z_m	membrane impedance [Ohms]
R_e	electrode resistance [Ohms]	Z_e	electrode impedance [Ohms]
C_e	electrode capacitance [C]	Z_t	total impedance [Ohms]
$v_c(t)$	capacitor voltage [V]	V	total voltage [V]
I	current [A]	ω	frequency [rad/s]
t	time [s]	s	Laplace variable
i, j	complex variable		

Impedance analysis - ˆ denotes dimensional term

$\hat{J}_{i(d)}$	diffusion driven flux of specie i [mol/m^2 s]	$\hat{\phi}$	internal potential [V]
$\hat{J}_{i(\hat{\phi})}$	potential driven flux of specie i [mol/m^2 s]	$\hat{v}$	solvent velocity [m/s]
$\hat{J}_{i(c)}$	free solvent driven flux of specie i [mol/m^2 s]	$\hat{p}$	external pressure [N/m^2]
$\hat{J}_{i(p)}$	pressure driven flux of specie i [mol/m^2 s]	$\hat{\rho}$	charge density [C/m^3]
$\hat{J}_i$	total flux of specie i [mol/m^2 s]	$\hat{E}$	electric field [V/m]
$\hat{C}_i$	concentration of specie i [mol/m^3]	F	Faraday's constant - 96,487 [C/mol]
$\hat{\varepsilon}_i$	chemical potential	R	gas constant - 8.3143 [J/(mol K)]
z_i	charge of specie i	T	temperature [K]
V_i	volume fraction of specie i	k'	hydraulic conductivity [m/s]
M_i	Molar mass of specie i [kg/mol]	C^+	concentration of cations [mol/m^3]
d_i	diffusion coefficient of specie i [m^2/s]	C^-	concentration of anions [mol/m^3]
$\hat{x}$	spatial variable [m]	L	total thickness of polymer [m]
$\hat{t}$	temporal variable [s]	κ	effective permittivity of transducer [F/m]
$\mathbf{E}$	electric field [V/m]	$\mathbf{D}$	electric displacement [V/F]
γ	characteristic length - $\frac{F^2 C^-}{\kappa R T}$ [1/m^2]	$\hat{\Phi}_1, \hat{\Phi}_2$	applied potentials [V]

Nondimensional analysis

$\phi(x,t)$	internal potential	$\rho(x,t)$	internal charge density
Φ_m	maximum applied voltage $\left\|\hat{\Phi}_2 - \hat{\Phi}_1\right\|$	λ	characteristic time - $d\gamma^2$
ϵ	dimensionless characteristic length $\frac{1}{L^2\gamma^2}$	β^2	natural length of transient solution
N_1	coefficient of flux equation - $\frac{d\kappa\gamma^2\Phi_m}{FL}$	N_2	coefficent of nonlinear term - $\frac{F\Phi_m}{RT}$
Φ_1, Φ_2	applied potentials $\frac{\hat{\Phi}_1}{\Phi_m}$, $\frac{\hat{\Phi}_2}{\Phi_m}$	$\Delta\Phi$	$\Phi_2 - \Phi_1$
$\varphi(x)$	spatial component of ϕ	$\eta(t)$	temporal component of ϕ
$a_1 - a_4$	coefficients of transient analysis	N	Normalization term
$\mathbf{A}, \mathbf{B}$	matrices of modal coefficients	a_{mn}, b_{mn}	coefficients of modal matrices
$\psi(x)$	in-phase spatial component of harmonic analysis	$\delta(x)$	out-of-phase spatial component of harmonic analysis
F	Amplitude of harmonic voltage $\frac{\Delta\Phi}{2}$	Ω	normalized driving frequency
a	constant in harmonic analysis $\frac{-1}{\epsilon}$	b	constant in harmonic analysis $\frac{-\Omega}{\epsilon}$
A	summation of a and b - $a + jb$	$\bar{A}$	complex conjugate of A - $a - jb$
$c_1 - c_8$	coefficients in harmonic analysis	Υ	common denominator in harmonic analysis
$Q_{it}(t)$	isothermal transient ionic charge (ITIQ)	$I_{it}(t)$	isothermal transient ionic current (ITIC)
$I_{ip}(t)$	in-phase component of ITIC	$I_{op}(t)$	out-of-phase component of ITIC
G, B	conductance, susceptance	Y, Z	admittance, impedance

Chapter 5

$\phi(x,t)$	internal potential	$\rho(x,t)$	internal charge density
ϕ^o	outer expansion of ϕ	ϕ^c	composite expansion of ϕ
ϕ^i	inner expansion of ϕ near $x = 0$	ϕ^I	inner expansion of ϕ near $x = 1$
$(\phi^o)^i$	inner expansion of outer expansion near 0	$(\phi^o)^I$	inner expansion of outer expansion near 1
$\left(\phi^i\right)^o$	outer expansion of inner expansion near 0	$\left(\phi^I\right)^o$	outer expansion of inner expansion near 1
ϵ	small scale parameter $\frac{1}{L^2\gamma^2}$	$\delta(\epsilon)$	general scaling term for expansions of ϕ
φ_0, φ_1	zeroth and first expansion terms of ϕ^o	$A_0 - B_1$	coefficients of ϕ^o
ξ	stretching coordinate near $x = 0$	ζ	stretching coordinate near $x = 1$
ν	order of the stretching parameter ϵ in ϕ^i, ϕ^I	ς	scaling of ϵ for nonlinear term
ψ_0, ψ_1	expansion terms for ϕ^i near $x = 0$	$a_0 - d_1$	coefficients of ϕ^i
$\tilde{\psi}_0, \tilde{\psi}_1$	expansion terms for ψ^i near $x = 1$	$\tilde{a}_0 - \tilde{d}_0$	coefficients of ϕ^I
N_2	nonlinear coefficient $\frac{F\Phi_m}{RT}$	Φ_1, Φ_2	applied potentials
Υ	change of coordinates $\Upsilon = \varphi'$	k, m	constants of integration
θ	characteristic angle from NL analysis	i	complex variable

Chapter 1

Introduction

Ionic polymer transducers comprise a class of active material that are well suited for a variety of applications due to their interesting chemoelectromechanical coupling capabilities. These ionomer-based transducers offer the capacity to convert energy between chemical, electrical and mechanical domains. This diversity in their energy conversion capabilities has led to their use in a range of seemingly unrelated applications. With proven effectiveness in electrolysis, humidification control, chlorine generation and fuel cell applications, these materials are becoming appreciated for their potential as sensor and actuator components as well. However, in order for these materials to reach this potential and become accepted in engineering applications, their properties and coupling mechanisms need to be understood and modeled. The modeling and experimental work presented in this dissertation serves to improve our understanding of these materials, offering a physical model that strives to describe both the sensing and actuation mechanisms of the ionic polymer transducers.

1.1 History

The ionic polymer transducer (IPT) is simply a transducer composed of an ionomer membrane that has been treated with conductive surface electrodes. These electrodes facilitate the application or measurement of an electric signal across the membrane thickness, enabling them to serve as actuator or sensor elements. While some ionic polymer work had been conducted as early as the 1930s, the name itself 'ionomer' didn't appear until 1965 when it was first used to define a class of olefin-based polymers containing a limited number of ionic groups [75]. These ionic groups were seen to have a large impact on the bulk properties of the materials, leading Rees and Vaughan [75] to label this distinctive class of materials as ionomers. However, as more polymers began to be developed the definition of an ionomer was forced to grow as well. Thus, in 1990 Eisenberg and Rinaudo proposed the commonly accepted definition of ionomers as "polymers in which the bulk properties are governed by ionic interactions in discrete

regions of the material (ionic aggregates)" [12]. Eisenberg also presents the conflicting history behind ionomers and their delineation from polyelectrolytes [11]. In this work Eisenberg explains that the definition set forth by himself and Rinaudo differentiates the ionomer from polyelectrolytes by basing the distinction on the material's physical properties rather than focusing strictly on composition.

Some of the earliest work in the chemomechanical and electromechanical behaviors of ionic materials was conducted by Katchalsky [35] and Kuhn [42, 43] in 1949. Their work focused on the mechanical response of polymeric gels through a sample of copolymerized methacrylic acid and divinyl benzene. Katchalsky found that the polyelectrolyte gel would experience mechanical deformations through pH changes in their environment, effectively making them chemomechanical transducers. Work by Hamlen *et al.* [30] in 1965 built upon these findings, using an electric stimulus to excite an ionic copolymer of polyvinyl alcohol and polyacrylic acid supplied by Katchalsky. A platinum electrode was introduced within the copolymer, which was then placed within a 1% sodium chloride solution. A second electrode was suspended in the solution, and a voltage was applied across the two electrodes. This potential resulted in a change in the pH content of the solution which in turn led to swelling and deswelling of the copolymer muscle. Thus the authors proved that they could drive the chemomechanical response through an electrical signal, thus producing an electrochemomechanical actuator. Similar work was also performed by Yannas *et al.* [96] in 1973. In their study the authors suspended an electroded collagen membrane within a series of electrolyte solutions. Applying electric fields up to 10 V/cm, the authors were successful in illustrating the electrochemomechanical response of these membranes in numerous types and concentrations of the electrolyte solution.

Over the decades following this work, there were numerous studies of the potential applications of these polyelectrolyte gels [77], however it wasn't until the early 1990s that they received a considerable amount of renewed interest. It was at this time that two research groups published findings that opened the door for much of the modern research on ionic polymer transducers. In 1992 Oguro *et al.* [69] published a study on a thin ion-conducting membrane that had been plated with conductive metal electrodes. Oguro found that a suitably prepared ionomer could exhibit large mechanical deformations in response to a small electric potential, elevating the thin films to actuating transducers. Within the same year another research group at Temple University published their results for a vibration sensor based upon the ion-exchange membrane Nafion^{TM} [76]. Sadeghipour *et al.* performed a series of tests using the Nafion transducer to sense accelerations of 2.5 to 9.5 g's and applied loads of .2 to 1.1 lbf. The results of these studies by Oguro *et al.* [69] and Sadeghipour *et al.* [76] have spawned a wave of analytical and experimental studies to understand the fundamental mechanisms and capabilities of the ionic polymer transducer.

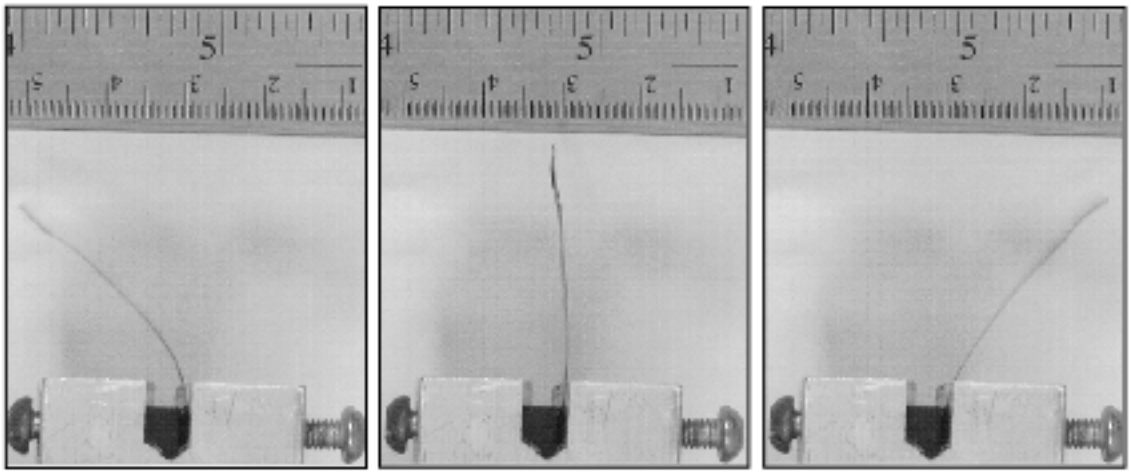

Figure 1.1: Response of an IPT transducer at resonance to a 3V signal.

1.2 Background

The physical response of an ionic polymer transducer (IPT) is that of a natural bender element. When clamped as a cantilevered sample and subject to an alternating potential, the IPT will respond with an oscillating transverse motion at the frequency of excitation (Figure 1.1). Operating under relatively low electric fields of 1kV/m to 10 kV/m, these materials exhibit large bending strains which can be tailored by changes in the polymer structure, fixed and mobile ionic groups, solvent properties and surface electrode treatments. Figure 1.2 is a cross sectional view of an ionic polymer sample along with an illustrative layout of the polymer components. Within the ionomer membrane there is a polymer backbone from which acidic pendant chains are attached. These pendant chains are neutralized through the introduction of a cation, typically in the form of H^+, Li^+, Na^+or other suitably charged ion. In the case of perfluorosulfonate ionomers such as Nafion, these ion pairs begin to associate with neighboring pairs to form small ionic clusters within the membrane. These small clusters arise do to the hydrophobicity of the backbone polymer, which causes the hydrophilic ion pairs to conglomerate into small cluster regions of 2 nm to 5 nm in diameter [25, 61, 59]. These small cluster regions can be thought of as weakly crosslinked or 'ionically' crosslinked sites within the polymer.

Over the past decade numerous models have been proposed to explain the internal mechanisms that govern the electromechanical response of the ionic polymer. While numerous mechanisms have been proposed in each of these models, one similarity arises through the concession that ions migrate toward the cathode surface of the polymer under an applied field. This concept can be visualized in the schematic of Figure 1.3. In this illustration there are three primary stages of the actuation response,

- The first state of the polymer is when the transducer is electrically neutral. No external field has been applied

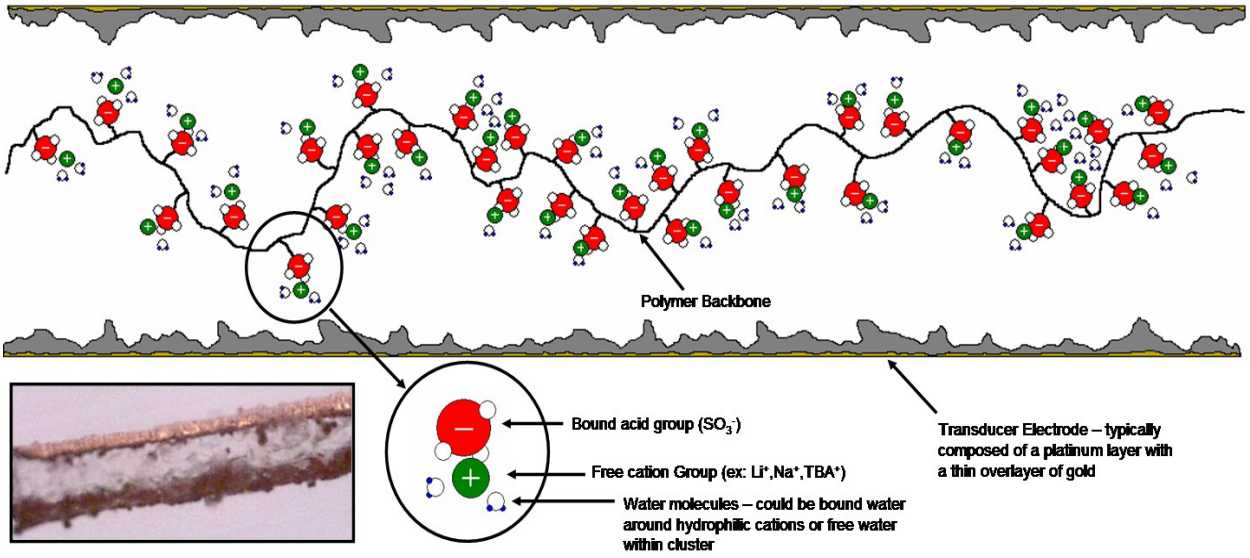

Figure 1.2: A simplified schematic of the IPT transducer element. The photograph in the lower left presents a visual image of the transducer cross section at 200x for comparison.

to the polymer and the cluster regions are at their lowest energy state.

- The second stage is the transient state of the material just following the application of an electric field. In this stage the ions begin to reorient due to the field and cations begin to dissociate from their cluster regions as they migrate toward the cathode surface. As the hydrophilic cations transport through the material thickness they carry a certain amount of bound water, actually driving some of the free water molecules toward the cathode. As these cations and water molecules move toward the surface internal forces develop, causing the material to swell and thus inducing a bending moment on the membrane [61, 10].

- The final stage in the initial response of the ionic polymer is that in which the cations and their associated water molecules accumulate at the cathode surface. At this point many of the proposed models diverge. Two main branches of the modeling community develop at this point, one attributing the material swelling to hydraulic forces [10, 4, 46] while the other argues that electrostatic repulsion causes internal stress at the cathode [61, 59].

At this point the overview of the actuation response stops short and does not attempt to describe what is going on inside the polymer during the back relaxation stage of polymer actuation. Observed primarily in the DC actuation of these materials, the Nafion-based transducer is well known for its back relaxation in the opposite direction under a constant electric potential. This is illustrated in more detail in Figure 1.4. The relaxation response has led to a considerable amount of conjecture as to its cause, however there haven't appeared any definitive models that can yet explain the phenomena. While there aren't any published models of this relaxation, there are two principle theories

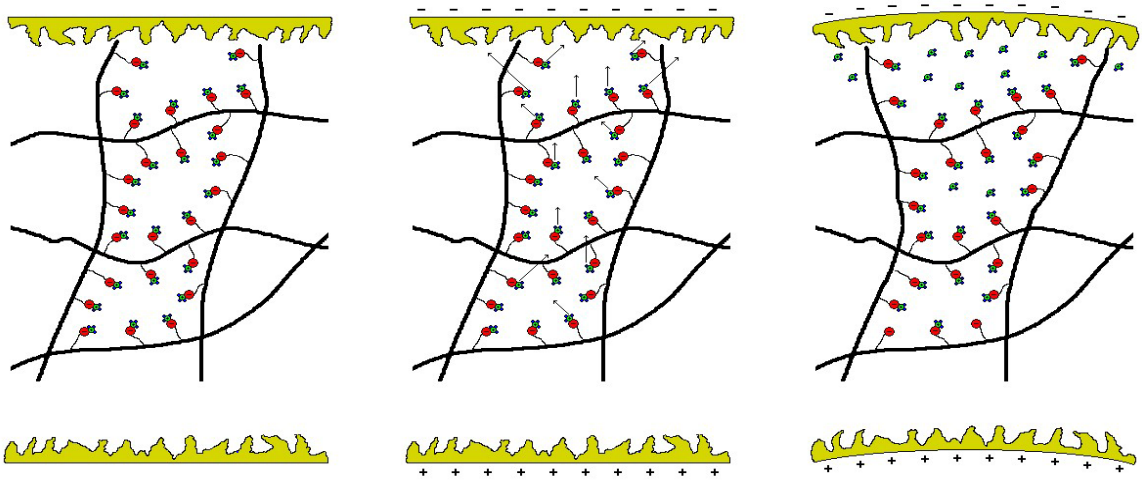

Figure 1.3: A simplified schematic illustrating the transport and actuation response of the ionic polymer transducer.

that attempt to model the behavior.

The first theory put forth to describe this back relaxation focuses on the idea of back diffusion of water within the membrane. As noted previously, under a constant field, ions are drawn to the cathode surface. This motion in turn causes the migrating ions to push free water along with them toward the negatively charged electrode. The overabundance of water, according to the hydraulic models, causes a pressure gradient that leads the initial deformation of the IPT [10, 4, 46]. Along this line of thinking, the relaxation of Nafion-based IPTs is therefore reasoned to be linked to the back diffusion of water within the membrane. Thus, as the cations begin to equilibrate at the cathode surface the free water molecules are drawn back into the bulk regions of the polymer due to hydrostatic forces, causing the hydraulic pressure at the cathode to decrease and the polymer to relax. While this theory would be very appropriate to describe small or almost full relaxations to the initial starting position, they fail to account for polymers in which the transducer actually relaxes beyond its original position, as seen in Figure 1.4.

The second explanation comes from the electrostatics approach of modeling IPTs. In this manner, Nemat-Nasser [60] has presented a theory on the reorganization of cations within the clusters, causing electrostatic forces that had originally swollen the cathode surface to actually reorient and constrict this surface of the polymer. This theory arises from Nemat-Nasser's observations of an experiment using an ethylene-glycol based transducer. By using a much more viscous solvent, the step response of the ionomer occurs over a much longer time scale. In this manner, Nemat-Nasser was able to observe the anode surface of the transducer dry out during the initial motion toward the cathode and remain dry throughout the experiment, even during the back relaxation stage. Additionally, he was able to see the glycol collect on the surface of the cathode and actually be dispelled during the relaxation stage, indicating that something other than hydraulic pressure must be involved in the fast initial response as well as the slow back relaxation. While this theory offers some interesting conjectures into the back relaxation of the

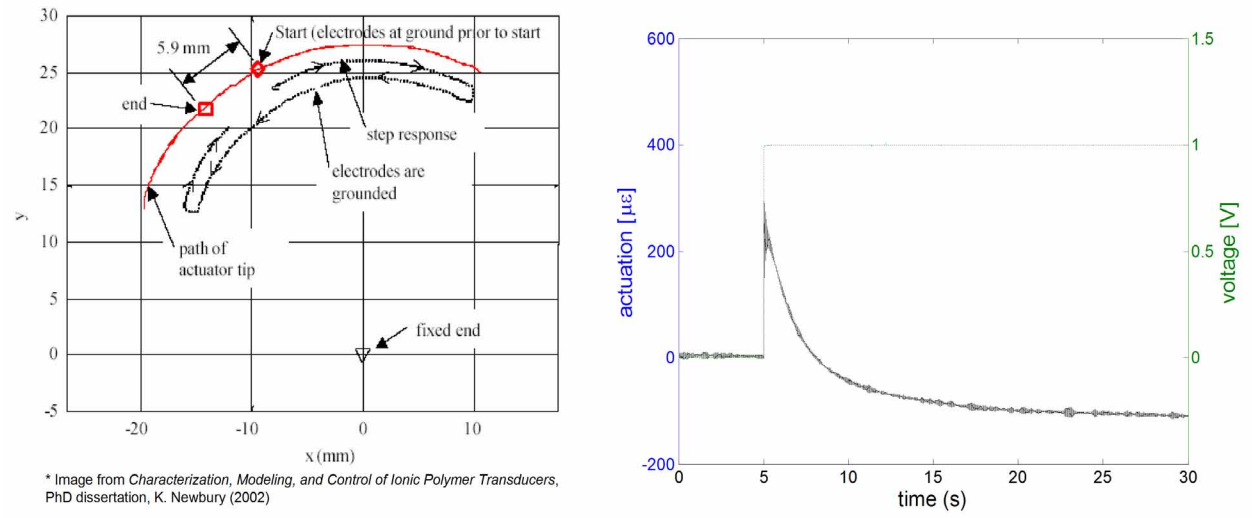

Figure 1.4: Relaxation of ionic polymer transducers under an applied electric potential.

polymer, the results have not appeared in any publications thus far.

While the actuation response of these ionomeric transducers has resulted in considerable interest, the sensing response has received far less consideration, especially with regard to quantitative analyses. Some models have begun to emerge over the last four years with the work by Nemat-Nasser and Li [61], Newbury and Leo [67, 68], and Farinholt and Leo [13, 15]. While models of the sensing mechanisms didn't begin to appear until the early 2000s, there had been several experimental studies designed to address the IPT's sensing capabilities. This work actually began with the reports of Sadeghipour *et al.* [76] and their Nafion-based accelerometer. Over the next decade others began considering the voltage response of ionic polymers with several studies conducted at the University of New Mexico. Mojarrad and Shahinpoor [56] presented a study on the voltage development for static deflections in the tip of a cantilevered sample of IPT. Their work showed a near-linear relationship between voltage and displacement for displacements from 1 mm to 16 mm. Other studies by Shahinpoor and Kim illustrate the transient sensing response of free vibration within the sample [82]. Recent work by Newbury and Leo [67, 68] has shown a linear low frequency relationship between strain and short circuit charge in cantilevered samples when subject to tip deflections. This work was then expanded of late to include axial and shear responses of ionic polymers through work by Farinholt *et al.* [16, 13, 14]. The most recent of these studies [14] also considers the impact of ions, solvent viscosity and solvent dielectric on the sensing response. These results constitute a significant portion of this document and will therefore be discussed in much more detail in the Chapter 3.

1.3 Literature Survey

To understand the issues surrounding ionic polymer transducers, a literature survey was conducted on three primary aspects of the IPT literature. The research that has been conducted thus far by the author focuses on Nafion-based IPT samples. Thus, the first aspect of this literature review focuses on Nafion itself. Looking at the history, characterization and sample preparation, this section overviews many of the most pertinent studies into the morphology, hydration, diffusion and transport properties of these membranes. Once a base understanding of the material is presented, the experimental studies of Nafion-based IPTs is examined, focusing on the current level of experimental procedures and how they relate to the analytical characterization of these transducers. The final section focuses on the modeling aspects of the IPTs, looking at both empirically-based and physics-based representations of the ionic polymer transducer.

1.3.1 Nafion Transducers - History and Characterization

As one of the most commercially abundant ionomers on the market today, the perfluorosulfonate ionomer Nafion was developed nearly 40 years ago by researchers at E.I. du Pont de Nemours. In the early 1960s Walther Grot was able to modify another of DuPont's well known products, Teflon^{TM}, to produce one of the first commercially available ionomers. In his work Grot was able to combine sulfonic acid groups to the fluorocarbon backbone, producing a material that possesses many of the physical attributes of the base Teflon material in addition to the ionic characteristics of the sulfonic sidechains. The chemical structure of the Nafion ionomer is presented in Figure 1.5 along with a visual depiction of the polymer and sidechain in it's hydrated state. When cast into a thin film, the ionomer forms two distinct regions within the membrane due to the hydrophobicity of the fluorocarbon backbone that constitutes the bulk of the ionomer. Thus, the hydrophilic pendant chains tend to conglomerate into small ionic clusters within the membrane, separating the ionomer into distinct hydrophobic and hydrophilic regions. Morphological studies by Gierke *et al.* [25, 26] use small angle x-ray techniques to characterize the ionic clusters within the Nafion membrane. Gierke *et al.* estimate the cluster orientation to be on the order of 3.5 nm to 4.75 nm in diameter for a 1200 equiv wt Nafion membrane, as a function of the neutralizing cation. Gierke also estimates that the ionic cluster size actually decreases with larger ions through an analysis of the alkali metals, looking over a range from H^+through Cs^+. From this work Hsu and Gierke [32] were able to develop a phenomenological model for the cluster diameters. This work was then used to support the cluster network model proposed by Gierke in 1977 [23, 24]. In this cluster network model Gierke had conjectured that the ionic clusters were actually connected by a network of small conductive channels. While it was initially developed to address chlor-alkali separation, this model has served as the foundation for numerous other models into the ion transport in fuel cells [86, 87, 88] as well as the electromechanical models [61, 15] that consider the materials for transducer elements.

Other morphological studies that are of interest to this work are those of Fujimura *et al.* [19, 20] and

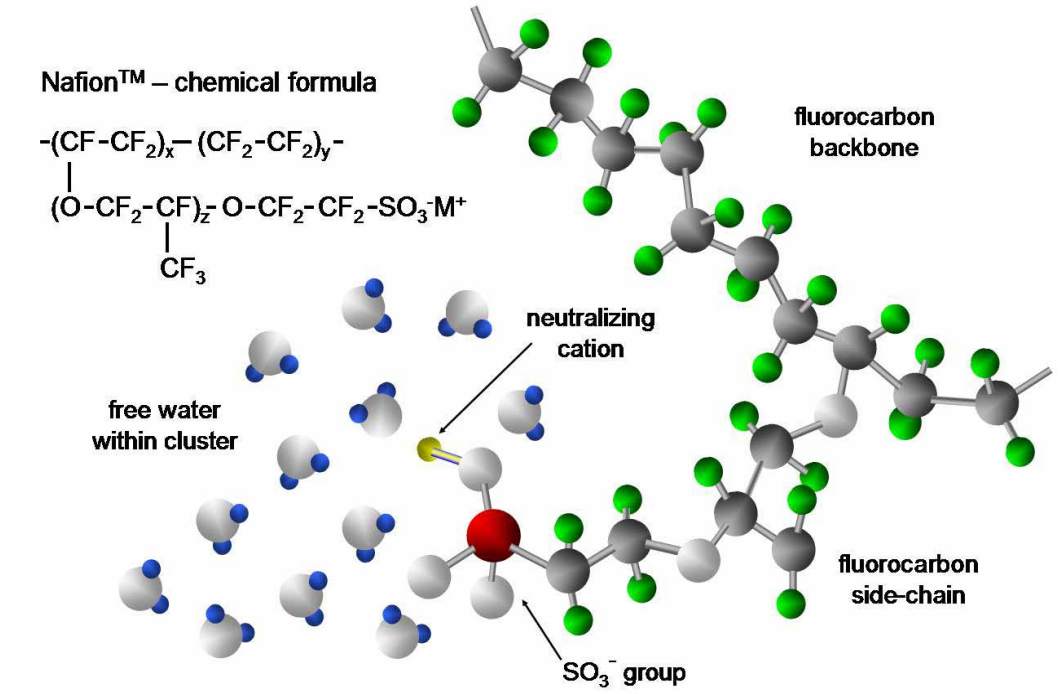

Figure 1.5: Chemical formula for Nafion with a visual depiction of the molecular structure.

Hashimoto *et al.* [31] of Japan. Much of the research conducted by this group focused on small- and wide-angle x-ray studies of Nafion as well as an augmented form of Nafion which contained carboxylate rather than sulfonate groups. Their analysis indicates a slightly larger estimate of the cluster diameter ($\approx$ 4.4 nm to 5.5 nm) than those reported by Gierke [25]. The interesting result to note however is their results for the carboxylic acid form of the perfluorinated membrane. Their analysis indicates that the carboxylate form of the ionomer absorbs far less water with a maximum uptake of only 6 wt% as compared to that of Nafion which was measured as 32 wt%. This in turn results in a much smaller cluster diameter with measured values ranging from 3.4 nm to 4.1 nm, over the five ionomer samples considered.

The third series of morphological studies of interest for the ionic polymer transducer is work by Barbi *et al.* [6] who investigated the structure of Nafion under mechanical load. The authors outfit their SAXS experiments with a straining stage that allowed Barbi *et al.* to induce strains up to 125% on samples of Nafion-117 membrane. Their work delves into deformation of individual clusters within the Nafion membrane as well as their reorientation under tensile loads. One of the most interesting results of their analysis (in terms of our application) can actually be seen in the visualization of Figure 1.6. From this figure it can clearly be seen that the authors expect large deformations in the cluster size and shape. And while the medium and high strain value used by Barbi *et al.* are much larger than those typically seen in most sensing applications, their results show promise for the fundamental modeling of

Figure 8: Sketch of a void–layer structure and its evolution during straining of Nafion 117® that is compatible with the nanostructure data extracted from the measured MAXS patterns. (a) native material. (b) medium elongation. The straining direction is indicated by a double arrow. (c) high elongation. The domain thickness, D_t, domain height, D_h, and the meridional long period of the CDF, L_m, that is resulting from struts crossing the void–layers.

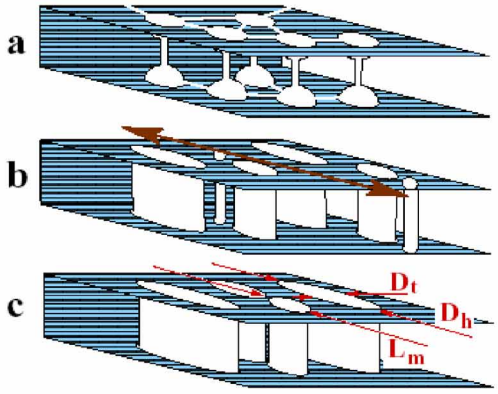

Figure 1.6: Visualization of the Medium-Angle X-ray analysis of Barbi *et al.* . Reprinted from *Polymer*, Vol 44, V. Barbi, S. Funari, R. Gehrke, N. Schamagl and N. Stribeck, 'Nanostructure of Nafion membrane material as a function of mechanical load studied by SAXS,' 4853-4861, Issue 17, Copyright 2003, with permission from Elsevier.

this mechanoelectrical response. Their results indicate that fundamental changes in the cluster morphology can be expected under an applied strain, lending credibility to the concept of ion motion or ion flux under an imposed deformation.

While these most recent studies offer promising implications for the transducer models, it is the morphological studies and model of Gierke *et al.* [23] that have formed the foundation for much of the transport theory that surrounds Nafion membranes. In addition to the morphological understanding of the Nafion membrane, the ion and solvent diffusion characteristics play a fundamental role in understanding ion transport, all features of the chlor-alkali, fuel cell and transducer applications of ion exchange membranes. Some of the leading work in understanding ion diffusion comes from the work of Yeager *et al.* in the late 1970s and the early 1980s [49, 84, 97, 98, 99]. Around the same time that Gierke proposed his cluster network model, Yeager was performing work on quantifying the self diffusion properties of numerous ions in the presence of aqueous and nonaqueous solvents. In 1977, Lopez, Kipling and Yeager [49] presented results on the self-diffusion of Na^+, $Cs^+$and I^- in water, methanol, acetonitrile and propylene carbonate, using radiotracer elements. The Nafion membrane was used to separate two volumes of solvent, one which was pure and the other which was doped with 0.050 M solution of the salt. Samples remained in the fixture until the radioactive tracer became detected in the acceptor side, at which time the samples were assumed to be at steady state and they were removed to test radioactivity, which was converted to the total number of moles of ion transferred. Results indicated that water and methanol offered similar diffusion constants for each of the cation species. However, those for iodide were seen to vary slightly. Lopez *et al.* also noted that the Nafion membrane would reach concentrations of 1 M $Na^+$and only 0.005 M I^- when placed in solutions of NaI, indicating the permselectivity of Nafion (a characteristic observed in each solvents studied). Yeager *et al.* went on to expand this analysis under controlled temperature and hydration levels [98, 99, 97], as well as to measure the ion selectivity

values for alkali and alkaline earth metals [84].

More recent studies of the self diffusion characteristics within Nafion have also been conducted by Goswami *et al.* [27]. Using a nonstationary radiotracer technique, they are able to measure the self-diffusion properties in a faster manner than the technique used by Yeager *et al.* . In this series of tests the Nafion membrane was placed in a 0.02 M salt solution containing radiotracer ions. During testing the solution was stirred rapidly to ensure equal concentrations throughout the bath. Samples were removed at specific time intervals, rinsed and tested to determine radioactivity before being replaced in the solution. The results of tests with $Na^+$and Cs^+provide good comparisons with those of Yeager and Steck [99] and Millet [51]

In addition to the direct diffusion studies of Yeager *et al.* and Goswami *et al.* , Millet [51] has presented work to correlate conductivity measurements with self-diffusion properties. In this work Millet assumes the validity of Einstein's relationship between absolute ion mobility and the self-diffusion coefficient. Correlating his predictions with the experimentally measured diffusion coefficient of Yeager and Steck [99], Millet obtains good correlation for $Na^+$and Cs^+in the unexpanded form of Nafion. Once the membrane has been expanded through heating in water, Millet's prediction for the Na^+membrane is overestimated while the Cs^+measurement is within 6% of Yeager's findings.

Millet's work [54, 52, 53] also extends to the diffusion of platinum ions within ion-exchange membranes, with predictive models based on layer and membrane diffusion controlled rates. This work was developed to provide predictive abilities in evaluating the Pt pollution within electrolyzer membranes. While this build up of Pt particles is undesirable in the electrolyzer applications, other researchers have focused on the diffusion of platinum to deposit conductive electrodes on the surface of ionic polymer transducers. Fedkiw *et al.* [17, 48] describe an impregnation-reduction technique for forming conductive electrodes on Nafion membranes. A similar technique is also used by Shahinpoor and Kim [79, 81, 82, 37] as they describe the diffusion of platinum particles within the Nafion substrate which is then reduced at the surface using a $NaBH_4$ or $LiBH_4$ reducing agent. This process produces a small dendritic platinum layer that typically extends 5 μm to 15 μm into the polymer membrane, which is then treated with an overlayer ($\approx 1\mu m$) of gold or silver to increase surface conductivity. Platinum is typically used as the initial layer since most other metals will oxidize within the IPT membrane. Bennett [7] developed a co-reduction technique in which he deposited a platinum-copper alloy within the Nafion membrane. His work found that the inclusion of non-noble metals could lower production costs, while the platinum content was seen to improve the transducer's life.

The impregnation-reduction technique used to plate these transducers yields an electrode structure that has a very high interfacial area between the platinum and ionomer. This high interfacial area provides an efficient means for applying an electric field to the IPT. When the polymers are in their hydrated state, the application of an electric field induces ion transport across the membrane. This transport of ions through membranes has been studied for many years, with general theory presented by Lakshminarayanaiah [44, 45]. Lakshminarayanaiah outlines three principle theories used in describing the transport phenomena. The first of these models relies on the Nerst-Planck

flux equation to provide an electrostatics model of ion transport. Relying on classical, or quasi-, thermodynamics this theory assumes that transport occurs isothermally. The second theory described by Lakshminarayanaiah is less restrictive than the Nernst-Planck model, relying on irreversible thermodynamics to consider nonisothermal systems. The third series of models rely on theories of rate processes to describe the transport phenomena. This approach allows for various levels of complexity in the modeling approach, offering both a general and unified view of the ion transport.

Of these models, the Nernst-Planck development serves as the most common approach in describing the transport of ions through ion-exchange membranes such as Nafion. The work of Bernardi and Verbrugge [8] and Verbrugge and Hill [86, 87, 88] consider the ion-exchange membrane as a solid-polymer-electrolyte for fuel cell applications. Their work models the flow of H^+protons across the polymer membrane through the Nernst-Planck relationship. This development uses the Nernst-Planck expression to describe the diffusion, migration and convection components of the ion transport, including solvent pressure and electric potential gradients to drive the ion motion. The result of the work by Verbrugge *et al.* is to develop a series of charge, potential and pressure profiles that vary through the polymer thickness and develop with time. While these profiles provide a representation of the internal charge and potential, the external current is not considered in the development of Verbrugge *et al.* [8, 86, 87, 88]. Greeuw and Hoenders [28] discusses the theoretical development of the isothermal transient ionic current (ITIC) for systems containing Na^+, $Li^+$and K^+in matrix structures of metal SiO_2-Si. This development is later used by Frenning *et al.* [22, 21] to include space charge, migration and diffusion effects of the ITIC. In their development, the measured surface current, or charge, is related to the product of the spatial coordinate and the charge density through the material thickness. Following their derivation, it is possible to predict the measured current within the Nafion-based IPTs as a function of either the theoretical charge density, or the electric displacement through the membrane. This result is discussed in more detail in the following chapter as we relate theoretical predictions with measured results.

1.3.2 Experimental History

While work had been conducted on the actuation properties of polyelectrolyte gels for nearly 55 years, experimental studies of the perfluorinated ionomer membranes didn't begin until the early 1990s with the work of Oguro *et al.* [69] and Sadeghipour *et al.* [76]. Their work provided a spark which has led to numerous experimental and analytical studies of these transducers. Shahinpoor *et al.* [78] presents a detailed overview of the development of polyelectrolyte and ionomer transducers up to, and beyond, the experimental work of Oguro and Sadeghipour. Shahinpoor himself has conducted a number of experimental studies on Nafion membranes, starting with his work in the mid 1990s. In 1997 Mojarad and Shahipoor [56] presented their work with ionic polymer sensors. Their findings indicated near linear scaling in the voltage to displacement relationship for step changes in tip deflection.

Interestingly, their results indicated a slightly different trend when the transducer was deflected in the opposite direction. Their theory behind this variation was the capacitive nature of the IPT. They reasoned that the polymer would incrementally build charge as it was deflected in one direction, which would cause a discharging effect when bent back in the opposite direction, causing a slightly skewed measurement. That same year, Shahinpoor *et al.* [83] also presented work in which they captured the actuation response as a function of frequency.

The work by Shahinpoor has continued over the past decade and has included numerous experimental results focusing on both the sensing and the actuation response of the ionic polymer transducers. His work with Ferrara *et al.* [18] and Keshavarzi *et al.* [36] illustrated the pressure response capabilities of the ionic polymer transducer. In the study with Ferrara *et al.* a small sample of plated Nafion 2 cm x 2 cm was subject to an increasing load from 0 to 500 kPA over 20 seconds, after which the load was removed over another 20 second interval. Interestingly, the sensing response of the IPT was not symmetric in the loading and unloading stages. Their work found that the unloading stage took nearly 3 times longer to settle as did the loading stage, a result that was also observed at higher loading conditions (0-900 kPA) as well. Shahinpoor has also conducted numerous studies into the actuation response as well. His work with Kim [80] considered the effects of counterion species on the actuation response of IPT. Using a low frequency excitation of 0.5 Hz and 1.2 V, they characterized the displacement to voltage response of transducers in H^+, Na^+, Li^+, K^+, Ca^{2+}, $Mg^{2+}$and Ba^{2+}forms. Based on their testing, Shahinpoor and Kim were able to rank the material sensitivities as a function of counterion, with Li^+yielding the greatest sensitivity and $H^+$the lowest.

Farinholt and Leo [14] found very similar results as they considered actuation, sensing and impedance responses of the ionic polymer in both frequency and time domains. Their analysis included several alkali metals Li^+, $Na^+$and Cs^+, a divalent cation Ca^{2+}as well as two organic cations $TEA^+$and TBA^+. Their results indicate that decreases in sensitivity could be acounted for by normalizing actuation and sensing responses by the transducer's impedance. By phrasing these responses in $\mu\epsilon/C$ and $V/\mu\epsilon$ the authors found that there was minimal variation between counterion species. Farinholt and Leo also investigated the effect that solvent viscosity and the dielectric nature of a solvent have on the transducer's response. These studies indicate that sensitivity decreases with increasing solvent viscosity and decreasing dielectric constant. Interestingly, the authors also found that the same normalization with respect to the polymer's impedance could be performed to greatly diminish variation due to the viscosity and dielectric properties of the solvent.

Newbury and Leo [65, 66, 67, 68] have also worked diligently in the characterization of ionic polymer transducers, considering the frequency response of these materials. Their studies indicate that charge to strain could be used to provide a sensing response that was linear at low frequencies (below 20 Hz). Newbury *et al.* also conducted a series of actuation experiments designed to provide the necessary coupling coefficients for his constitutive model of the IPT. From this characterization and modeling, Newbury was able to develop, actuate and control a 'polymer motor' that used actuator and sensor elements composed of ionic polymer transducers.

Additional control studies have also been conducted on these ionic polymer transducers, namely with the work by Mallavarapu and Leo [50] and Kothera [38, 39]. In each of these studies, the authors used feedback control to limit the relaxation effects of ionic polymers in order to obtain DC actuation. Mallavarapu and Leo implemented an integral controller on the IPT to obtain minimal overshoot and steady DC actuation over a short time window. Kothera extended this result and found that step response behavior could be maintained while the sample remained hydrated, limiting their operation to approximately 30 seconds.

One similarity amongst each of these studies is that they primarily consider the ionic polymer as a cantilevered bender. With the exception of the pressure responses studied by Sadeghipour [76], Ferrara *et al.* [18] and Keshavarzi *et al.* [36] the only orientation has been the bender element. In the past three years more attention has begun to focus on the other responses of the ionic polymer transducer. Parrott *et al.* [74] examined the axial response of a Nafion-based transducer under an applied electric potential. Measuring both in-plane strain and blocked force, he was able to identify the longitudinal response of the polymer in a clamped-clamped configuration. Farinholt *et al.* [16, 14] extended this work to consider the sensing response of axial samples as well as the polymer's response to a shear loading. In each of these studies we found that the polymer displayed distinctive sensing responses to several loading condition, implying that the IPT can serve as a sensor in numerous mounting configurations.

1.3.3 Modeling History

Since the development of the ionomer-based transducers, researchers have worked to improve our understanding of the IPT through both experimental and analytical approaches. Currently there are three levels to the modeling approach which range from the simplest to the most complex form. The first of these modeling techniques offers the least amount of insight into the fundamental mechanisms and is referred to as the black box model. This modeling technique provides a purely empirical model of the IPT and describes the actuator element through a series of curve fits based on experimental data. While this method is sufficient for direct control, it is size and sample dependent and offers very limited knowledge of the IPT mechanisms. The second level of modeling is considered the more enlightening grey box model. Still based somewhat on empirical data, this model combines fundamental physical laws with empirically derived parameters to define the IPT. These empirically determined parameters often correspond to processes or mechanisms that are not as well understood or too complex to be incorporated into the grey box models. The final level of models offer a more complex look at the IPT and are considered white box, or physical, models. This class of models relies on the underlying physical mechanisms of the IPT to develop a system of equations that fully describe the material response.

While each level provides distinctive advantages either in terms of simplicity or level of insight, they are each important in understanding the current state of IPT technology. The following section outlines many of the modeling approaches and some of the key contributors to the current understanding of these ionic polymer transducers.

Black Box Models

The black box model is one of the most direct methods for developing a predictive model of specific transducers. Based purely on the empirical response of a transducer, these models offer minimal insight into the governing mechanisms at work within the IPT. The first black box model of the IPT was developed in 1994 by Kanno *et al.* [33]. Their model, shown in equation 1.1

$$Y = Ae^{-\alpha t} + Be^{-\beta t} + Ce^{-\gamma t} + De^{-\delta t} + E, \tag{1.1}$$

offers nine fit parameters that can be used to fit the experimental results. Kanno *et al.* used a least squares method to determine the constant values, then repeated a series of tests at three separate voltages. They found that the constants could not describe each excitation level, thus making the model dependent on both sample geometry and excitation voltage.

Xiao and Bhattacharya [95] also proposed a black box model of the ionic polymer transducer, focusing on the curvature of the IPT sample as it develops with voltage and time. Interestingly, their development begins with more of an electrostatics development, however when placed in the reduced form used to model the macroscopic response of the IPT, they revert to a phenomenological model of the eigen-curvature. For a time dependent voltage, their model estimates the curvature through the first order expression

$$\frac{d\kappa}{dt} = \frac{1}{\tau}(\kappa_v V - \kappa), \tag{1.2}$$

where κ is the curvature of the sample, κ_v is the saturation curvature per volt, τ is the time constant, V is the applied voltage and t is the time variable. Using the principle of virtual work Xiao and Bhattacharya incorporate the concept of an applied load which is then simulated and characterized against experimental results. For 0 g and 25 g loads, their model conforms nicely to experimental data, however this is to be expected since this portion of the model is developed empirically.

Gray Box Models

While the black box models are simplistic in nature, they are often sample dependent and do not allow for scaling of the polymer geometry. As a more detailed approach, the gray box models rely on some of the physical principles, while also relying on empirical results to define some of the more complex processes. The first of these grey box models was proposed by Kanno *et al.* [34] in which he divides the model into two subsections: the electrical and the stress generation stages. Using an equivalent circuit model of the IPT, Kanno *et al.* develop a relationship that describes the electrical current that is developed from an applied voltage. This portion constitutes the electrical stage whose output, the current, then serves as the input to the stress generation or mechanical stage of the model. The

equilibrium expression developed in this model relates stress to current in the following manner,

$$\sigma = D(s)\varepsilon - \epsilon \left[\frac{\omega_n^2 s}{s^2 + 2\zeta\omega_n s + \omega_n^2} \right] I, \tag{1.3}$$

where σ is the stress vector, $D(s)$ the mechanical characteristic matrix of the polymer, ε the strain vector, ϵ the stress generation tensor, I the current output of the electrical stage, with ζ and ω serving as the dynamics parameters that relate I to the induced stress of the polymer. In this formulation the authors only consider the actuation response, producing a one directional model that can only yield the induced stress from an electrical current.

Work by deGennes *et al.* [10] relies on a model formulation that has the potential to describe both sensing and actuation responses, however their consideration of only steady-state results does not account for the transient field developed in sensing. Their model is based upon linear irreversible thermodynamics and relates the flux terms of electrical and water current to the driving forces of electric field and water pressure. In its developed form, their model has the form,

$$\begin{aligned} J &= \sigma E - L_{12}\nabla p \\ Q &= L_{21}E - K\nabla p. \end{aligned} \tag{1.4}$$

This model relates the charge density J and the water current Q to the electric field E and water pressure gradient ∇p. The remaining terms of this expression correspond to the membrane conductance σ, Darcy's permeability K, and the cross coupling coefficients L_{12} and L_{21} which are assumed to be equivalent. While offering a very concise representation of the system, deGennes *et al.* unfortunately stop short of comparing their predictions with the measured performance of IPTs.

Newbury and Leo [67, 68] offer a very similar development in their model, following the form of the piezoelectric constitutive model. Their model has the form

$$\begin{aligned} v &= \frac{Z_p}{1 + Z_p/R_{DC}} i + N \frac{Z_{m1}}{1 + Z_p/R_{DC}} \dot{u} \\ f &= N \frac{Z_{m1}}{1 + Z_p/R_{DC}} i + (Z_{m1} + Z_{m2})\dot{u}, \end{aligned} \tag{1.5}$$

and relates voltage v and force f to the electrical current i and polymer velocity $\dot{u}$ through a series of impedance terms. This development is based upon the equivalent circuit model shown in Figure 1.7. The impedance terms of this model correspond to the mechanical stiffness impedance of the polymer Z_{m1}, the inertial term Z_{m2}, the DC resistance R_{dc} and the transducer's capacity to store electrical charge Z_p. The principle advantages of this model over many of the previous derivations is that Newbury and Leo include the inertial impedance Z_{m2} which broadens the frequency range of their transducer model. The development still relies on curve fit algorithms to

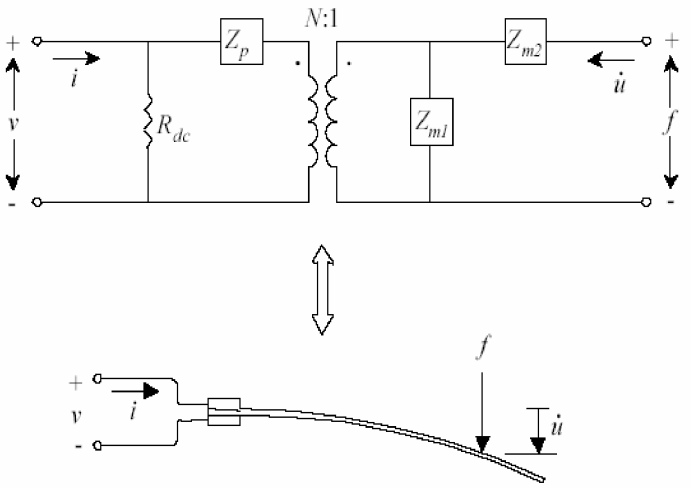

Figure 1.7: Equivalent circuit model for the ionic polymer transducer based upon the derivations of Newbury [65].

perform parameter identification, however their model allows for geometric scaling of the IPT. Newbury and Leo also conduct a series of experimental validations [68] that assess the model's predictive capabilities in both the time and frequency domains. Comparisons of predicted and measured results illustrate the usefulness of this modeling approach, especially since it offers a series of constitutive relationships paralleling the piezoelectric models.

The final grey box model considered in this survey is the work by Paquette *et al.* [73]. In this model the authors continue along the development of deGennes *et al.* [10], presenting an equivalent electrical circuit of the IPT that characterizes the upper and lower electrode surfaces as well as the bulk polymer membrane. This model assumes that the membrane is purely capacitive and that the upper and lower electrodes exhibit RC characteristics. The model enables Paquette *et al.* to model the current to voltage relationship in an equivalent circuit form. The concept is then integrated into the irreversible thermodynamics model of deGennes *et al.* to provide predictive capabilities for the blocked force response of the IPT.

Physical Models

One of the primary benefits of these grey box models is that they will serve as very useful tools in engineering design. However, these models still rely on empirical fits of experimental data, and therefore do not model the fundamental physics associated with the sensing and actuation properties of the ionic polymer transducers. Therefore a third class of models have now begun to emerge, trying to offer explanations for the underlying physics for the sensing and actuation responses of the ionomer-based transducers. Tadokoro *et al.* [85] developed a white box model of the ionic polymer that relies on water concentration to model the IPT response. Their model proposes that an applied voltage within the polymer induces a charge redistribution of cations toward the cathode surface. As these cations migrate

through the membrane they drag water molecules with them, which on the fast time scale causes swelling at the cathode and thus a bending moment on the IPT. As the voltage is held constant the osmotic pressure causes the water molecules to diffuse back into the anode region, causing a relaxation in the transducer. Electrostatic interactions produced by ionic motion are also modeled, however they have a minor influence as compared to the ion and water migration. Interestingly, this model is able to predict the counter motion of ionic polymer benders that is sometimes exhibited when excited by a constant electric field.

Asaka and Oguro [5] present a model that considers the presence of an electrokinetically induced pressure gradient as the dominant mechanism behind actuation in the ionic polymer transducer. They consider two underlying components in this model, internal swelling in the polymer due to changes in the hydration profile, and the internal stress induced by stretching the interfacial regions near the polymer-electrode boundary. Changes in the hydration profile are attributed to water flux within the polymer, which is subsequently related to cation migration and electro-osmotic effects within the polymer. The hydration profile and interfacial stresses couple together to produce the induced moment and are related to the resultant curvature of the IPT sample. Through comparison with experimental results, the authors determined that each of the terms in their curvature model were linearly related to the current density of the test sample.

A separate class of models has also been developed by Nemat-Nasser and Li [61] and Nemat-Nasser [59], using a field approach based on the micromechanics of ionic polymer materials. In this model actuation occurs due to the uptake of water at the interface between the polymer and the metal electrode [59]. In contrast to the work by deGennes *et al.* [10] and Tadokoro *et al.* [85], the model by Nemat-Nasser and Li [61] and Nemat-Nasser [59] does not explicitly include water motion and hydraulic pressure gradients as state variables. An ionic cluster model of the base material provides the basis for modeling electromechanical transduction between charge distribution and mechanical deformation. The voltage sensing properties are modeled as the product of an effective dipole moment induced by mechanical deformation of the polymer [61]. More recently this approach has been extended to model the relaxation exhibited by ionic polymers under the application of a constant electric field [59]. The relaxation model is based on the diffusion of cations out of the boundary layer that forms at the surface of the polymer due to applied electric field.

Xiao and Bhattacharya [95] also consider the actuation response of the ionic polymer transducer. They consider their development to be an elasto-electro-chemical formulation that is inspired by the work by Nemat-Nasser *et al.* [61, 62]. The polymer is treated as a soft insulating material that exhibits elastic properties. Ions are considered present within the membrane and are allowed to move throughout the medium. The model begins as a multidimensional model, but is restricted to a single dimension for analysis of the IPMC. Their work focuses a great deal on the boundary layer effect that is predicted to develop within the IPMC when driven by an applied voltage. Xiao presents several predictions of the internal potential and charge distribution for the steady-state system, plotting the spatial response as a fucntion of the characteristic length ε. For the physical system they estimate this

characteristic length to be on the order of Angstroms, considerably smaller than the predictions of Nemat-Nasser and Thomas [62]. From the analysis Xiao concludes that actuation is driven by this accumulation and depletion of cations within the ionic polymer, a result which supports the predictions of Nemat-Nasser [61, 59].

Weiland and Leo [92, 93, 94] also expand upon the analysis of Nemat-Nasser to consider the response of a single ion cluster within the ionomer membrane as it is subject to an external mechanical load or an applied electric field. The authors employ a computational micromechanics approach to study the effects that ion-ion interaction, pendant chain stiffness and cluster surface energy have on the charge redistribution within the cluster. The anion-cation pairs are considered pseudo dipoles in this development, and the system is considered under uniform and random distributions of anions. A Monte Carlo technique is used to establish the equilibrium, or lowest energy, state of ions within the cluster. The system is then subject to either mechanical or electrical loading, and the lowest energy state is recalculated. From this new equilibrium configuration the location of ions is quantified to determine an overall charge response (due to mechanical loading) or an internal stress (due to electrical loading). The authors also found that the equilibrium state rarely consisted of a complete pairing of anions and cations, indicating that there were some dissociated cations within the cluster in the equilibrium state. Subsequently, the authors conclude that these unpaired cations are what would effectively give rise to ion transport between neighboring cluster sites within the ionic polymer membrane, providing justification for the transport concepts used in the larger-scale models of Nemat-Nasser [61, 59], Asaka [5] and Xiao [95].

The research conducted in this dissertation builds upon these previous physical models, extending the macroscopic transport models to account for the sensing and impedance responses of the ionic polymer. Transport theory is assumed to be the dominant mechanism, as supported by the work by Xiao [95], Nemat-Nasser [59, 100] and Weiland [94, 93]. The next section outlines the major goals and contributions of this research, followed by a general overview of the disseration and how the results will be presented.

1.4 Research Goals and Contributions

The primary objective of this research is to improve the general understanding of ion motion within ionic polymers, and how this motion translates into the sensing and actuation response of these electroactive transducers. Throughout this research the objective is accomplished through modeling and experimental characterization of the ionic polymer transducers. A detailed discussion of each component of this analysis is presented in the following chapters, however the major contributions of this research can be summarized as follows,

- *Development of an analytical sensing model based upon transport theory.* The dominant trend for research in the area of ionic polymers has focused on the actuation response of the plated ionomer membranes. Very little emphasis has been placed upon the sensing reponse of these materials, motivating the investigation presented

in Chapter 2 of this dissertation. The approach used in this work is distinct from previous studies since it relies on the same transport theory used to describe both impedance and actuation responses. Existing models are either empirical in nature, or use separate fundamental mechanisms to describe the charge development induced by an imposed deformation. The model is seen to be able to match experimental results, and to predict the response when transducers are geometrically scaled. The principle benefit of this model is that it demonstrates that the same basic transport theory can be used to describe both actuation (as shown by Nemat-Nasser [61, 59]) and sensing .

- *Characterization of the actuation, sensing and impedance response as functions of counterion, solvent viscosity and solvent dielectric properties.* Based upon existing experimental studies of the IPT's actuation response [63, 64, 80, 100], this research extends the findings to the frequency domain while also considering the sensing and impedance responses as a function of the counterion and solvent properties. The results indicate that ion and solvent properties have significant effects on the electromechanical response of the IPT. Interestingly these variations can be linked directly to the ion and solvent effects on the transducer's electrical impedance. Thus, it is seen that the dominant mechanisms for sample-to-sample variation reside in the polymer's electrical response, rather than it's mechanical response. From this it is concluded that an understanding of the polymer's voltage to current relationship is essential to the development of a predictive model for the electromechanical response of the IPT.

- *Development of an impedance model.* Based upon the experimental results of Chapter 3, an impedance model of the ionic polymer transducer has been developed. This model begins with the same transport theory considered in sensing and actuation models, and is derived to yield a solution for the surface current that is expected to develop in response to a harmonic excitation voltage. From this model a frequency domain representation for the electrical impedance can be extracted as a function of the ambient temperature T, anion concentration C^-, polymer thickness L, diffusion coefficient d and the transducer's effective permittivity κ. While the first three of these parameters T, C^- and L can be measured directly or obtained from the manufacturer, the benefit of the model lies in it's ability to approximate d and κ directly from simple impedance models. Since these parameters are typically more difficult to measure, this ability is expected to ease the characterization of new membrane materials. Additionally this model could provide insight into the design of new ionomer membranes. With the ability to predict the impedance, and consequently the electromechancial response of the ionomer, it would not be difficult to predict which range of properties would be desirable in custom membrane materials. Thus, if this information where used in collaboration with Polymer Chemists, it may be possible to significantly enhance the performance capabilities of a new generation of ionomers.

- *Use of approximate methods to investigate other simplifications of the nonlinear transport equation.* One of the major assumptions of any of the analytical models for the ionic polymers is that the fundamental

transport equations can simply be linearized and studied accordingly. A simple comparison of coefficients is typically used to justify this linearization, however it is felt that some consideration should be given to other simplifications of the nonlinear continuity equation. Therefore, a case study has been undertaken to consider the effect that nonlinear boundary conditions have on the linearized transport equation, and to consider other approximate solutions to the nonlinear transport equation. Each variant of the system has been analyzed, and a spatial profile of the internal potential has been determined. These results were then compared to numerical simulations of the full nonlinear system provided by Wallmersperger of the Universität Stuttgart. Comparison of these results indicate that the linear system with linear boundary conditions actually provides the best approximation of the full nonlinear system. This result is attributed to the unique interaction that exists between the transport equation and the flux boundary conditions, providing additional support for analysis of the linearized transport problem.

1.5 Overview

This chapter has provided a general overview of the historical development of ionic polymer transducers and the current technological understanding of the IPT as a new class of active material. The remainder of this dissertation is organized in the following manner. Chapter 2 presents a sensing model of the ionic polymer, based on conventional transport theory. This model serves to predict the charge response for an ionic polymer membrane when subject to mechanical deformation. The modeling approach is compared to experimental results, illustrating good agreement with step excitations of the polymer tip as well as general geometric scaling of the test samples. Chapter 3 extends this experimental study to consider both time and frequency domain measurements. Sensing, actuation and impedance responses of the ionic polymer are all considered in this analysis. The effect of counterion specie, solvent viscosity and solvent dielectric properties are also studied. The actuation and sensing responses are then normalized with respect to the electrical impedance of the sample, indicating the importance of understanding the underlying voltage to charge flow characteristics of the ionic polymer. Chapter 4 focuses on this impedance relationship, developing an expression for the polymer's surface current as a function of the applied voltage at the transducer's outer electrodes. Relating these two quantities, the impedance response is then developed. A parametric study is presented which considers the effect that diffusion coefficient, temperature and the effective permittivity of the transducer have on the predicted impedance response. The analysis in Chapters 2 and 4 focus on the linearized set of transport equations. Chapter 5 considers other simplifications of the transport equation. A matched asymptotes method is used to develop approximate models of the steady-state equations. The nonlinear terms are considered at different scales in this analysis, with a comparison of the overall results presented at the close of the chapter. Chapter 6 presents a set of experimental studies that are used to validate the findings from Chapters 4 and 5. Chapter 7 serves to summarize the major results and conclusions of this research, and to present ideas for future work.

Chapter 2

Sensing model

The model development and experimental studies presented in this work have been derived for transducers fabricated from DuPont's ionomer membrane, plated on two opposing surfaces with thin conductive electrodes. The base material used in both modeling and experimental sections is Nafion-117 which has been plated using the co-reduction techniques of Bennett [7]. The model developed in this work focuses on the sensing response of the ionic polymer transducer. Newbury *et al.* [66] have shown that the current output of IPTs can be related to the rate of motion of the material. This correlation was observed through experimental measurements of short circuit current as related to the tip motion of the IPT element. This conclusion serves as the basis for our model development which looks into the physical mechanisms that give rise to charge and current generation as related to deformation imposed upon the ionic polymer transducer.

2.1 Electromechanical Model

The electromechanical model that has been developed for the Nafion based IPT relies on field and continuity relationships previously applied to ionic polymers in fuel cell research. The field equations used in this derivation relate electric field, displacement and potential,

$$\mathbf{E} = \frac{\mathbf{D}}{\kappa_e} \tag{2.1}$$

$$\mathbf{E} = -\nabla\phi \tag{2.2}$$

$$\nabla \cdot \mathbf{D} = \rho = F\left(C^{+} - C^{-}\right). \tag{2.3}$$

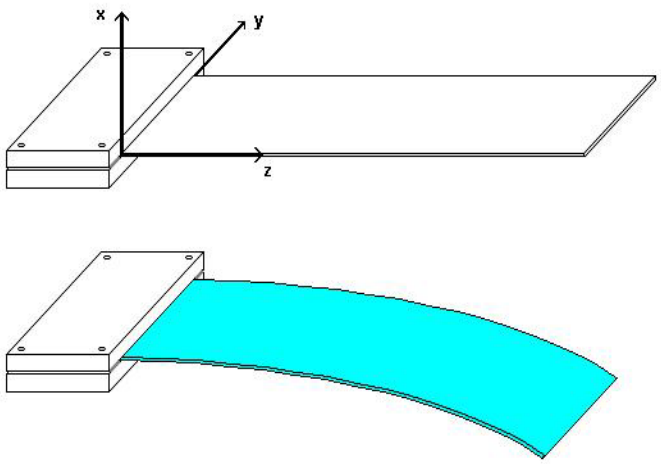

Figure 2.1: Illustrative geometry of the cantilevered sample considered in this model development.

While the continuity expression relates ion flux to cation concentration,

$$\nabla \cdot \mathbf{J} = -\frac{\partial C^+}{\partial t}. \tag{2.4}$$

Ion flux is considered to be composed of three primary terms: the diffusion, migration and convection terms,

$$J = -d\left(\nabla C^+ + \frac{C^+ F}{RT}\nabla\phi + \frac{C^+ \Delta V}{RT}\nabla \mathbf{p}\right) + C^+ \mathbf{v}. \tag{2.5}$$

The first assumption made in this model is that ion motion occurs in one dimension across the material thickness. This one-dimensional model allows us to assume that the variables only vary in the x direction, unless otherwise noted. This will also allow us to drop the boldface notation for convenience.

One of the first steps in this model development is to try and rephrase the continuity and flux equations in terms of a single variable. Beginning with cation concentration, we can solve equation 2.3 in terms of C^+,

$$C^+ = \frac{1}{F}\rho + C^-. \tag{2.6}$$

Due to the nature of the ionomer, anions are constrained to the polymer backbone and thus their concentration is considered to be spatially and temporally constant. Therefore, we can write the cation gradient specifically in terms of the electric field

$$\nabla C^+ \quad = \quad \frac{\kappa_e}{F}\nabla^2 E, \tag{2.7}$$

through the field relationships of equations 2.1-2.3.

We can also relate fluid velocity directly to the pressure gradient and electric potential gradient through a modified version of Darcy's Law [29],

$$v = k' \left[C^- FE - \nabla p \right], \tag{2.8}$$

where k' represents the hydraulic permeability. The second assumption in this work is that we can neglect the convection term, such that $v \to 0$. Under this assumption, the pressure gradient becomes a function of electric field,

$$\nabla p = C^- FE. \tag{2.9}$$

Substituting equations 2.6, 2.7 and 2.9 into the original flux equation, and assuming $v \to 0$, equation 2.5 becomes,

$$J = -d \left[\frac{\kappa_e}{F} \nabla^2 E + \left(\frac{\kappa_e}{F} \nabla E + C^- \right) \frac{F}{RT} \nabla \phi + \left(\frac{\kappa_e}{F} \nabla E + C^- \right) \frac{\Delta V}{RT} \left(-C^- F \nabla \phi \right) \right]. \tag{2.10}$$

Making the field substitution of $\nabla \phi = -E$, the flux becomes

$$J = -d \left(\frac{\kappa_e}{F} \nabla^2 E - \frac{\kappa_e}{RT} \left(1 - C^- \Delta V \right) \nabla E \cdot E - \frac{FC^-}{RT} \left(1 - C^- \Delta V \right) E \right). \tag{2.11}$$

The next step in this analysis is to calculate the gradient of the ion flux. By taking the gradient of the left and right sides of 2.11 we develop the following relation,

$$\begin{aligned} \nabla \cdot J &= -d \left(\frac{\kappa_e}{F} \nabla^3 E - \frac{\kappa_e \left(1 - C^- \Delta V \right)}{RT} \nabla^2 E \cdot E + \frac{\kappa_e \left(1 - C^- \Delta V \right)}{RT} (\nabla E)^2 - \frac{FC^- \left(1 - C^- \Delta V \right)}{RT} \nabla E \right). \\ &= -d \left(\frac{\kappa_e}{F} \nabla^3 E - \frac{\kappa_e \left(1 - C^- \Delta V \right)}{RT} \left[\nabla^2 E \cdot E + (\nabla E)^2 \right] - \frac{FC^- \left(1 - C^- \Delta V \right)}{RT} \nabla E \right). \end{aligned} \tag{2.12}$$

Substituting this equation into the original continuity equation, we can relate the time rate of change in cation concentration to electric field,

$$-\frac{\partial C^+}{\partial t} = -d \left(\frac{\kappa_e}{F} \nabla^3 E - \frac{\kappa_e \left(1 - C^- \Delta V \right)}{RT} \left[\nabla^2 E \cdot E + (\nabla E)^2 \right] - \frac{FC^- \left(1 - C^- \Delta V \right)}{RT} \nabla E \right). \tag{2.13}$$

Considering the time derivative of the cation concentration, $\frac{\partial C^+}{\partial t}$ becomes

$$\begin{aligned} \frac{\partial C^+}{\partial t} &= \frac{1}{F} \frac{\partial \rho}{\partial t} = \frac{\kappa_e}{F} \frac{\partial (\nabla E)}{\partial t} \\ &= \frac{\kappa_e}{F} \frac{\partial^2 E}{\partial x \partial t}. \end{aligned} \tag{2.14}$$

Substituting this relationship into the continuity equation, we develop a characteristic equation in terms of electric

field,

$$-\frac{\kappa_e}{F}\frac{\partial(\nabla E)}{\partial t} = -d\left(\frac{\kappa_e}{F}\nabla^3 E - \frac{\kappa_e\left(1-C^-\Delta V\right)}{RT}\left[\nabla^2 E\cdot E+(\nabla E)^2\right] - \frac{FC^-\left(1-C^-\Delta V\right)}{RT}\nabla E\right). \tag{2.15}$$

At this point we consider the nonlinear and linear terms of the continuity equation. Comparing the linear and nonlinear components of this expression, we can compare the constant coefficients of each term. In equation 2.19 the nonlinear coefficient has the form,

$$\frac{\kappa_e\left(1-C^-\Delta V\right)}{RT} \tag{2.16}$$

while the linear term is of the form

$$\frac{FC^-\left(1-C^-\Delta V\right)}{RT}. \tag{2.17}$$

Comparing these two expressions, their relative magnitudes can be determined through the fraction

$$\frac{FC^-}{\kappa_e}. \tag{2.18}$$

To better understand the magnitude of this term it is helpful to consider the physical, geometric and material properties of an typical Nafion-based transducer. These values can be found in Tables 2.1 and 2.2. If we consider the transducer in Li^+form, we find that the ratio between the linear and nonlinear terms is on the order of $5*10^{-10}$. Based on this argument, we consider the nonlinear term to be much less than the linear term, i.e.

$$\frac{\kappa_e\left(1-C^-\Delta V\right)}{RT}\left[\nabla^2 E\cdot E+(\nabla E)^2\right] \ll \frac{FC^-\left(1-C^-\Delta V\right)}{RT}\nabla E$$

and can therefore be neglected from our initial derivation. This reveals a characteristic equation of the form,

$$\frac{\kappa_e}{F}\frac{\partial(\nabla E)}{\partial t} - d\left(\frac{\kappa_e}{F}\nabla^3 E - \frac{FC^-\left(1-C^-\Delta V\right)}{RT}\nabla E\right) = 0. \tag{2.19}$$

Table 2.1: Physical constants and geometric parameters of the simulated sample .

Physical Constants			Geometric Parameters		
F (C/mol)	R (J/(mol K))	T (K)	width-b (m)	thickness-2h (m)	length-l (m)
96487	8.3143	300	$180\text{x}10^{-6}$	$8.47\text{x}10^{-3}$	$10\text{x}10^{-3}$

Table 2.2: Parameters used in modeling the Nafion-based transducer.

Cation	% Volume gain[a]	C^- (mol/m^3)	Diffusion Coefficient (m^2/s)	Measured Capacitance (mF)	κ_e (mF/m)
Li^+	61.7	1070	$1.389\text{x}10^{-10}$	11.3	2.04
Na^+	44.3	1200	[b]$1.030\text{x}10^{-10}$	10.4	1.88
K^+	18.7	1460	[b]$7.30\text{x}10^{-11}$	7.1	1.28
Cs^+	13.6	1530	[b]$1.94\text{x}10^{-11}$	7.3	1.32

a taken from [25]

b taken from [27]

It is now possible to perform a change of variable on this equation through the field equations 2.1 and 2.3. Rephrasing the continuity equation in terms of the charge density ρ, equation 2.19 is rewritten

$$\frac{\partial \rho}{\partial t} - d\nabla^2 \rho + \frac{F^2 d C^-}{\kappa_e RT}\left(1 - C^- \Delta V\right)\rho = 0. \tag{2.20}$$

Equation 2.20 is a partial differential equation (PDE) that models the spatial and temporal variation in charge density due to an initial charge distribution. It is similar in form to the equation modeling quasi-static charge redistribution due to an applied electric field as derived in Nemat-Nasser and Li [61]. The primary difference lies in the fact that the assumption of non-zero flux introduces an additional rate term and an additional term due to charge migration.

Rearranging in a general form, we consider the charge density to obey a separation principle. Assuming one-dimensional flow the charge density can be written as $\rho(x,t) = P(x)Q(t)$, so that the equation of motion becomes

$$P(x)\dot{Q}(t) - dP''(x)Q(t) + \tau P(x)Q(t) = 0, \tag{2.21}$$

where $1/\tau$ is a time constant (in seconds) expressed as

$$\tau = d\gamma^2 = d\frac{F^2 C^-}{\kappa_e RT}\left(1 - C^- \Delta V\right). \tag{2.22}$$

Separating the temporal and spatial components, the equation becomes,

$$-\frac{\dot{Q}(t)}{Q(t)} = \frac{-dP''(x) + \gamma^2 P(x)}{P(x)} = \lambda. \tag{2.23}$$

Now consider each equation that is produced from this expression

$$\dot{Q}(t) + \lambda Q(t) = 0 \tag{2.24}$$

$$P''(x) - \beta^2 P(x) = 0. \tag{2.25}$$

where $\frac{1}{\beta}$ is the characteristic length scale. β itself is defined as

$$\beta^2 = \frac{\gamma^2 - \lambda}{d}, \tag{2.26}$$

and has units of m^{-2}. The solution of the temporal equation is

$$Q(t) = c_1 e^{-\lambda t}. \tag{2.27}$$

The solution of the spatial equation is,

$$P(x) = a_1 e^{\beta x} + a_2 e^{-\beta x}. \tag{2.28}$$

In this study we consider the loading of a cantilevered transducer with imposed deflection at the tip. In this configuration the coordinate axis (i.e. $x = 0$) is defined to coincide with the neutral axis. At this point we make the assumption that stress and charge density are linearly related. This assumption is based upon the findings of Newbury and Leo [67, 68], and previous assumptions by Nemat-Nasser and Li [61]. If we impose this assumption we can impose the condition that charge density is zero at x = 0 to coincide with the neutral axis of the transducer. Applying this condition, the coefficients of the spatial solution are

$$P(0) = a_1 + a_2 = 0 \tag{2.29}$$

$$a_1 = -a_2. \tag{2.30}$$

Inserting this solution into the general solution of $P(x)$, we find

$$P(x) = 2a_1 \mathrm{sinh}\beta \mathrm{x}. \tag{2.31}$$

Imposing a boundary condition of $P(h) = \rho_0$ we find that

$$a_1 = \frac{\rho_0}{2\mathrm{sinh}\beta \mathrm{h}}. \tag{2.32}$$

Making this substitution for the a_1 coefficient, $P(x)$ becomes

$$P(x) = \frac{\rho_0}{\sinh\beta\mathrm{h}}\sinh\beta\mathrm{x}. \tag{2.33}$$

Combining the spatial and temporal components of the charge density we find the full form of $\rho(x,t)$

$$\rho(x,t) = \frac{\rho_0}{\sinh\beta\mathrm{h}}\left(\sinh\beta\mathrm{x}\right)e^{-\lambda t}, \tag{2.34}$$

where the coefficient of the temporal solution has been set equal to 1 to yield a charge density of ρ_0 at $t = 0$.

The expressions for electric field and electric potential are obtained by integrating equation 2.34 and applying the boundary conditions of zero potential at both faces. The equation for electric field is

$$E(x,t) = \frac{\rho_o}{\kappa_e\beta\sinh\beta\mathrm{h}}\left(\cosh\beta\mathrm{x}\right)e^{-\lambda t} + a_3. \tag{2.35}$$

Next we can integrate the field equation to obtain the electric potential

$$\phi(x,t) = -\frac{a_3\rho_o}{\kappa_e\beta^2\sinh\beta\mathrm{h}}\left(\sinh\beta\mathrm{x}\right)e^{-\lambda t} - a_3x + a_4. \tag{2.36}$$

We can now apply the boundary conditions to find the a_3 and a_4 coefficients:

$$\phi(h,t) = -\frac{\rho_o}{\kappa_e\beta^2\sinh\beta\mathrm{h}}\left(\sinh\beta\mathrm{h}\right)e^{-\lambda t} - a_3h + a_4 = 0 \tag{2.37}$$

$$\phi(-h,t) = \frac{\rho_o}{\kappa_e\beta^2\sinh\beta\mathrm{h}}\left(\sinh\beta\mathrm{h}\right)e^{-\lambda t} + a_3h + a_4 = 0. \tag{2.38}$$

Adding these two expressions, we find that a_4 must be zero. Applying this finding to either of the boundary conditions, we can then solve for the a_3 coefficient as

$$a_3 = -\frac{\rho_o}{\kappa_e\beta^2\sinh\beta\mathrm{h}}\left(\sinh\beta\mathrm{h}\right)e^{-\lambda t}. \tag{2.39}$$

Substituting this back into the field and potential equations, we find the analytical form of these functions to be

$$\rho(x,t) = \frac{\rho_o}{\sinh\beta\mathrm{h}}\left(\sinh\beta\mathrm{x}\right)e^{-\lambda t} \tag{2.40}$$

$$E(x,t) = \frac{\rho_o}{\kappa_e\beta\sinh\beta\mathrm{h}}\left(\cosh\beta\mathrm{x} - \frac{1}{\beta\mathrm{h}}\sinh\beta\mathrm{h}\right)e^{-\lambda t} \tag{2.41}$$

$$\phi(x,t) = \frac{\rho_o}{\kappa_e\beta^2\sinh\beta\mathrm{h}}\left(\sinh\beta\mathrm{x} - \frac{\mathrm{x}}{\mathrm{h}}\sinh\beta\mathrm{h}\right)e^{-\lambda t}. \tag{2.42}$$

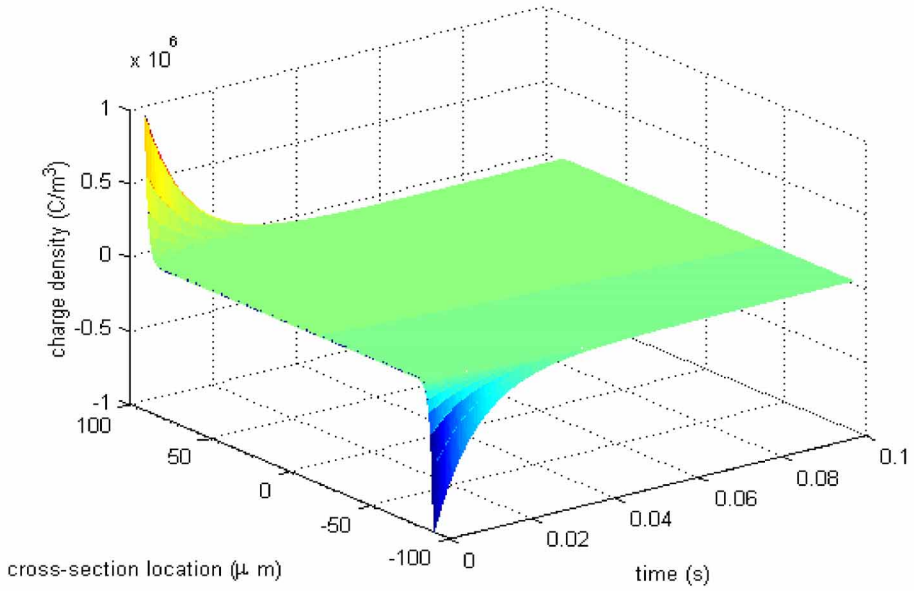

Figure 2.2: Charge density profile simulated for a tip deformation in a cantilevered sample of ionic polymer.

2.1.1 Analysis of Charge Density, Electric Field, and Electric Potential

The results summarized by equations 2.40, 2.41, and 2.42 are examined to understand the form of the charge sensing solution. To quantify the solution, we will utilize the values for a Nafion-based ionic polymer given in Tables 2.1 and 2.2.

The charge density, electric field, and electric potential are plotted using equations 2.40 through 2.42. The value of ρ_o was normalized to 1 for all of the plots. The results demonstrate that the charge density is approximately zero throughout most of the polymer but becomes positive towards the cathode (+h) and negative towards the anode (-h). The electric field is small throughout most of the polymer thickness but becomes larger near the polymer surface. As expected, the electric potential is approximately linear through the polymer except near the surface. The zero potential boundary conditions increase the gradient of the potential (which results in the increased electric field) and produce zero potential at both faces (x = +/- h). Zero potential is the most important difference between the charge sensing model and actuation models. For actuation models, the potential is nonzero at one of the faces and produces charge redistribution throughout the polymer thickness. Our model predicts that a potential, most likely smaller than the actuation potential, is produced due to the imposed mechanical deformation in the polymer.

The defining characteristic of the spatial response is the variation in the charge density, field, and potential near the surface of the polymer. The decay in the response from the surface value is a function of the value for β, as shown in equations 2.40 through 2.42. Larger values of β will produce faster decay and smaller transition regions

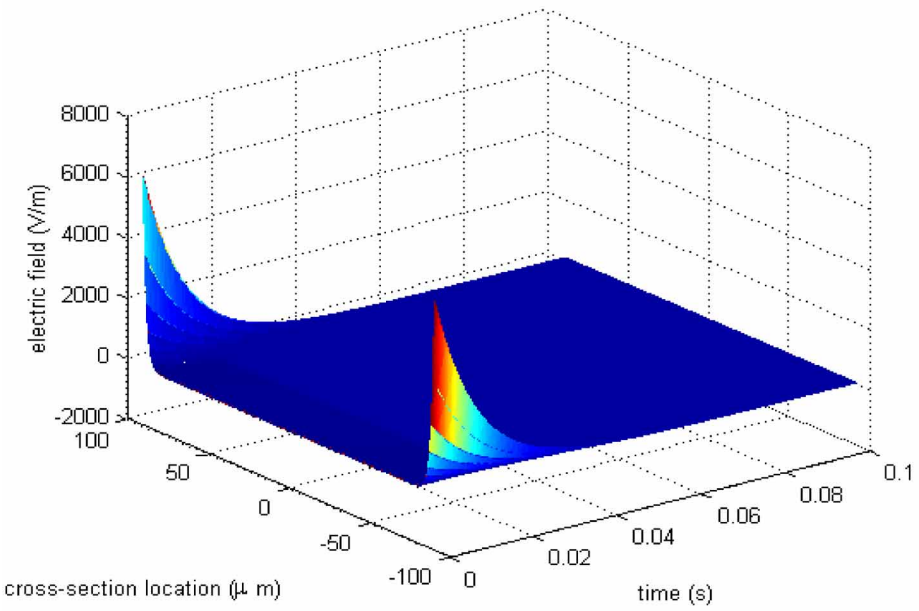

Figure 2.3: Electric field profile simulated for a tip deformation in a cantilevered sample of ionic polymer.

near the surface. This phenomenon is similar to the discussion in [59] regarding the boundary layer associated with applied electric field. Our model predicts that a similar boundary layer is formed when the material is deformed and the electrical boundary conditions require zero potential at both faces of the polymer.

Figures 2.2-2.4 are the initial condition responses of the charge density, electric field and electric potential once a step deformation has been imposed upon the transducer. All three quantities will decay with time as suggested by the time-dependent exponential in equations 2.40 through 2.42. The relationship between this time decay and the measured current and charge output is the subject of the next section of the chapter.

2.1.2 Relationship between Charge Density, Current, and Induced Stress

Our hypothesis in this dissertation is that charge density is proportional to the induced strain within the polymer. As discussed in the introduction, this hypothesis stems from the findings of Newbury and Leo [66], who have shown that ionic polymers exhibit a reciprocity between sensing and actuation. Previous work by Nemat-Nasser and Li [61] has modeled this idea through his proportionality term k_0. However, in this work we will use a different notation for this proportionality coefficient. In our experimental studies we have measured electric permittivities that are much larger than those reported in Nemat-Nasser and Li [61]. Our findings indicate that permittivities are on the order of 1.5x10^{-3} F/m, similar to those reported in the later works of Nemat-Nasser [59]. Therefore, we represent the relationship between mechanical stress and charge density through a generic term ψ_s, where ψ_s is not calculated in

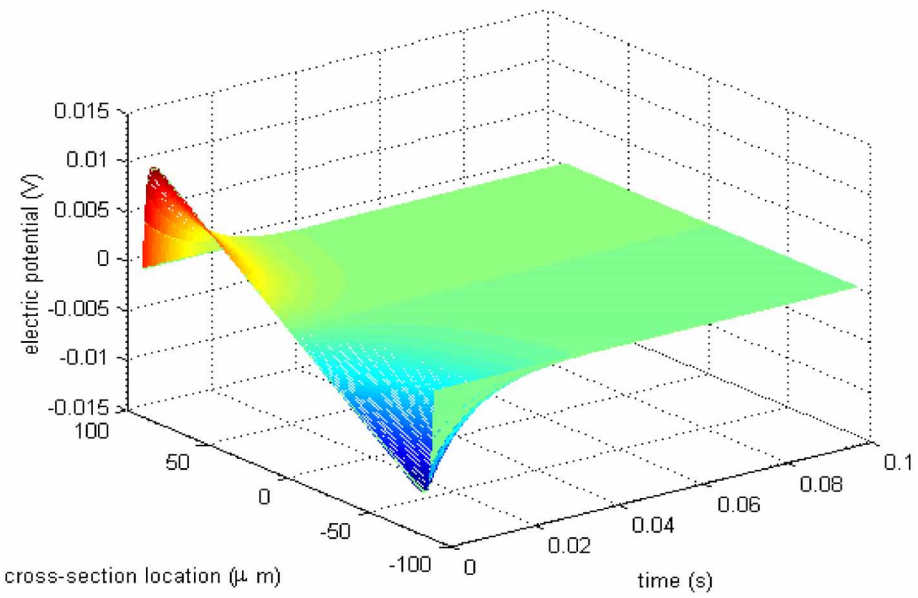

Figure 2.4: Electric potential profile simulated for a tip deformation in a cantilevered sample of ionic polymer.

the same manner as the k_0 coefficient of Nemat-Nasser [61]. In this manner the expression for stress to charge is given as

$$\sigma = \psi_s \rho, \tag{2.43}$$

In this work we will explore the possibility that this relationship also allows us to model the charge sensing response due to an imposed deformation.

To do so, we begin with the standard relationships for a beam with an end load. The moment at any position along the length is

$$M = F_0(l - z), \tag{2.44}$$

where F_0 is a function of the out-of-plane deflection at the tip $w(l)$. Solving for the value of F_0 we find

$$F_0 = \frac{3YIw(l)}{l^3}. \tag{2.45}$$

Next, we define the stress profile at the surface as

$$\sigma = -\frac{Mh}{I}. \tag{2.46}$$

Using the moment definition from above, we find the stress to be

$$\sigma = -\frac{3Yh(l-z)}{l^3}w(l). \tag{2.47}$$

Next, applying the ψ_s constant we have the initial charge density at any point along the length of the polymer

$$\rho_0 = \frac{3\frac{Y}{\psi_s}h(l-z)}{l^3}w(l). \tag{2.48}$$

Provided that the charge density of the IPT is symmetric across the material thickness, the surface charge is equivalent to the integral of the electric displacement over the surface of the polymer. However, if we assume that asymmetries may develop (especially in the case of actuation), the surface charge is derived from the isothermal transient ionic current (ITIC) [28, 22]. The ITIC is defined as the spatial integral,

$$I(t) = \frac{d}{dt}\left[\frac{1}{2h}\int_{-h}^{h} x\rho(x,t)dx\right], \tag{2.49}$$

and thus the charge at the surface has the form,

$$Q(t) = \frac{1}{2h}\int_{-h}^{h} x\rho(x,t)dx. \tag{2.50}$$

Solving for this surface charge per unit area, we find

$$\begin{aligned} Q(t) &= \frac{1}{2h}\int_{-h}^{h} x\frac{\rho_0}{\mathrm{sinh}\beta\mathrm{h}}\left(\mathrm{sinh}\beta\mathrm{x}\right)e^{-\lambda t}dx \\ &= \frac{\rho_0}{2h\mathrm{sinh}\beta\mathrm{h}}\left(\frac{2h}{\beta}\mathrm{coh}\beta\mathrm{h} - \frac{2}{\beta^2}\mathrm{sinh}\beta\mathrm{h}\right)e^{-\lambda t} \\ &= \frac{\rho_0}{\beta^2 h\mathrm{sinh}\beta\mathrm{h}}\left(\beta h\mathrm{coh}\beta\mathrm{h} - \mathrm{sinh}\beta\mathrm{h}\right)e^{-\lambda t} \end{aligned} \tag{2.51}$$

which can thus be simplified to give us the isothermal transient ionic charge,

$$Q(t) = \frac{\rho_0}{\beta^2 h}(\beta h\mathrm{coth}\beta\mathrm{h} - 1)\mathrm{e}^{-\lambda\mathrm{t}}. \tag{2.52}$$

Similarly, we can solve for the isothermal transient ionic current by taking the time derivative of the transient charge. This gives us an expression for ITIC,

$$I(t) = \frac{\lambda\rho_0}{\beta^2 h}(1 - \beta h\mathrm{coth}\beta\mathrm{h})\mathrm{e}^{-\lambda\mathrm{t}}. \tag{2.53}$$

The surface charge induced by mechanical deformation is equivalent to the integral of the electric displace-

ment over the surface of the polymer,

$$q(t) = \int_0^l \int_{-b/2}^{b/2} D(h,t) dy dz = w(l) \frac{Y}{\beta \psi_s} \frac{3}{2} \frac{bh}{l} \left(\frac{\cosh \beta \mathrm{h}}{\sinh \beta \mathrm{h}} - \frac{1}{\beta \mathrm{h}} \right) e^{-\lambda t}. \tag{2.54}$$

The expression for current is obtained by substituting equation 2.48 into the expression for electric field, equation 2.41, and then writing the expression for the time derivative of the electric displacement,

$$i(t) = \int_0^l \int_{-b/2}^{b/2} \frac{\partial D(h,t)}{\partial t} dy dz = -\lambda w(l) \frac{Y}{\beta \psi_s} \frac{3}{2} \frac{bh}{l} \left(\frac{\cosh \beta \mathrm{h}}{\sinh \beta \mathrm{h}} - \frac{1}{\beta \mathrm{h}} \right) e^{-\lambda t}. \tag{2.55}$$

If $\beta \mathrm{h} >> 1$, then

$$\frac{\cosh \beta \mathrm{h}}{\sinh \beta \mathrm{h}} - \frac{1}{\beta \mathrm{h}} \approx 1, \tag{2.56}$$

and the expressions for charge and current can be approximated as

$$q(t) \approx w(l) \frac{Y}{\beta \psi_s} \frac{3}{2} \frac{bh}{l} e^{-\lambda t} \qquad i(t) \approx -\lambda w(l) \frac{Y}{\beta \psi_s} \frac{3}{2} \frac{bh}{l} e^{-\lambda t}. \tag{2.57}$$

These results will be correlated with experimental results in the next section.

2.1.3 Correlation with Experimental Results

The basic tenets of the charge sensing model are correlated with experimental results for a set of cantilevered samples of ionic polymer material. The samples consist of a Nafion 117 substrate approximately 180 μm thick with metalized platinum-copper-gold electrodes plated on both sides. The thickness of the electrodes is approximately 1-3 μm thick across the surface of the membrane.

The test setup consists of a cantilevered sample of ionic polymer material excited by an electromagnetic shaker. The polymer was insulated from the shaker through a Teflon$^{\mathrm{TM}}$ stinger, and tip deflections were induced by exciting the shaker with a step voltage. The velocity at the tip of the polymer was measured using a laser vibrometer while short circuit current was measured using the conditioning circuit developed by Newbury [65]. The output voltage of the signal conditioning circuit is related to the current through Ohm's law

$$v_{out} = i(t) R. \tag{2.58}$$

The output resistance is chosen to be 100 kΩ for all tests, resulting in a sensitivity of 10 μA/V for the signal conditioning circuit.

The experiments included in this study were meant to focus on the effects of geometrically scaling the polymer transducer and the effects of different cation species on material sensitivity. Four separate alkali metals (Li,

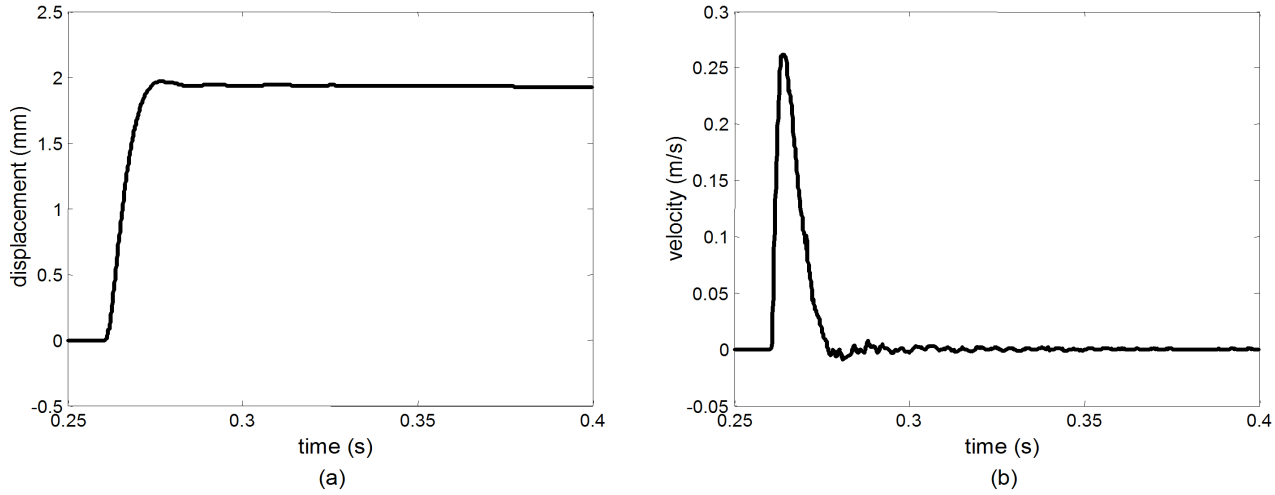

Figure 2.5: Step displacement (a) and velocity (b) of a sample with a nominal length of 10 mm and a width of 8.5 mm.

Na, K, and Cs) were considered in this study. Eight sets of tests were performed for each cation species, represented by two separate polymer widths and four separate free lengths. The first set of tests were conducted on a sample 8.5 mm wide with nominal thickness of 180 μm (h = 90 μm). The free length of the sample was varied from 10 mm to 25 mm in increments of 5 mm. Ten responses were measured at each sample length. This set of four tests were then repeated for a sample 3.5 mm wide. The result is a set of thirty-two data sets: four different free lengths at two different polymer widths, each repeated for four separate cation species. Each test was performed in air with the polymer being continually hydrated by brushing water on the material surface between measurements.

The imposed tip displacement was held constant for each of the sample length in this study. Figure 2.5 presents a representative result from these tests. Figures 2.5a and b illustrate that the change in displacement was on the order of 2 mm while velocities were approximately 0.2 to 0.3 m/s. These numbers were consistent with all of the other tests performed on the cantilevered samples.

The current measured in this test is shown in Figure 2.6a. We see that the basic tenet of the model is verified with this test. A step change in displacement induces a mechanical stress in the material, which, in turn produces a discharge of current in the material. Figure 2.6a indicates that this current discharge is approximately proportional to velocity once the displacement has reached an approximately constant value. If we define the sensitivity of the polymer as the ratio of peak current to peak velocity, we can overlay the current with the normalized velocity to determine the relationship between the two quantities. One issue that is present in this study is the presence of a 4 to 8 ms time delay between the peak current and the peak velocity. This delay is thought to be a function of either the polymer itself or the signal conditioning circuit. Figure 2.6b presents the measured time delay for the 8 mm wide sample. If this time delay were to merely be a function of the polymer, we would expect there to be a scatter

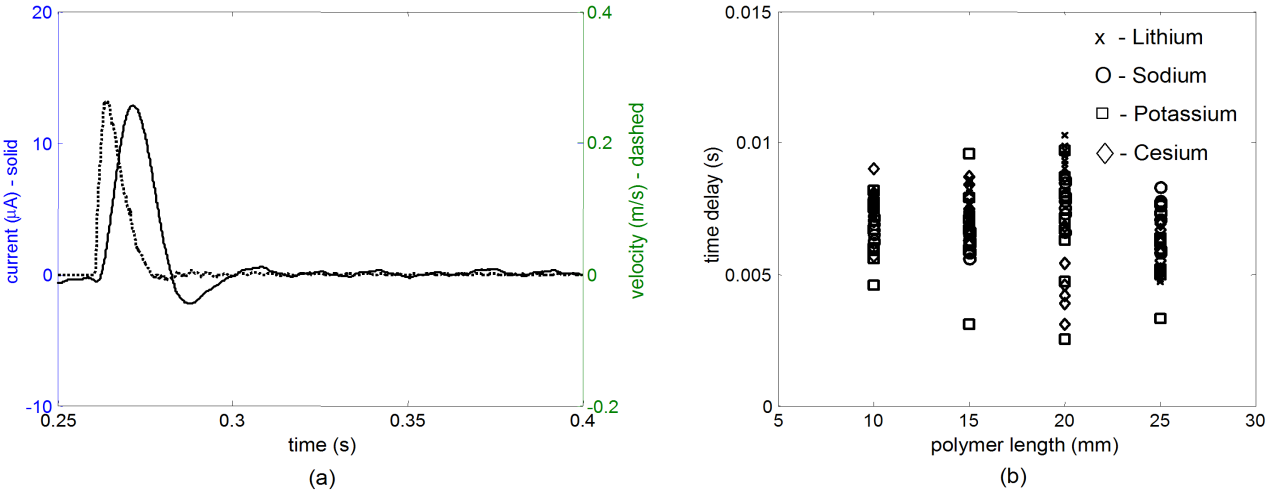

Figure 2.6: Measured current output plotted with polymer velocity (a) and time delay between peak velocity and peak current as a function of polymer free length for the 8.5 mm wide sample (b). The average time delay for this study was 7.5 ms for 8.5 mm widths and 4.0 ms for 3.5 mm widths.

in the time delay data for each of the different cation species. The data in Figure 2.6b represents all of the cation types considered in our study. Our findings indicate that the time delay is relatively constant for each of the cation species, leading us to believe that the delay is most likely associated with the current conditioning circuit. Other tests using passive RC components instead of the polymer indicate that there is a capacitance dependent time delay within the signal conditioning circuit itself. However, since we cannot assume that the time delay lies solely in the conditioning circuit, we choose to neglect its influence in the present study. Ignoring this issue of a time delay, we define the polymer sensitivity simply as the ratio of peak current to peak velocity. In this manner, the sensitivity for this particular test is approximately 49.0 μA/(m/s).

While Figures 2.5 and 2.6 verify the basic premise of the charge sensing model, further validation of the model was obtained by investigating the change in sensitivity as a function of polymer geometry and cation type. Equation 2.57 indicates that the current output due to a step change in polymer displacement will scale linearly with width and inversely with free length. As stated previously, the sensitivity is taken as the ratio of peak current output to peak velocity, and has been calculated for each of the ten measurements for a specified sample length, width and cation type. Figure 2.7 presents these sensitivities as a function of polymer length and cation species. Figure 2.7a includes data for the 3.5 mm sample width, while Figure 2.7b corresponds to data taken for the 8.5 mm sample width. By comparing the sensitivities of Figure 2.7 it is clear that the sensitivity increases with decreasing sample length and is larger for the wider sample.

The relationship between length and sensitivity can be determined more accurately by fitting a straight line to a logarithmic plot of sensitivity versus polymer length. A true inverse relationship would yield a slope of -1 on

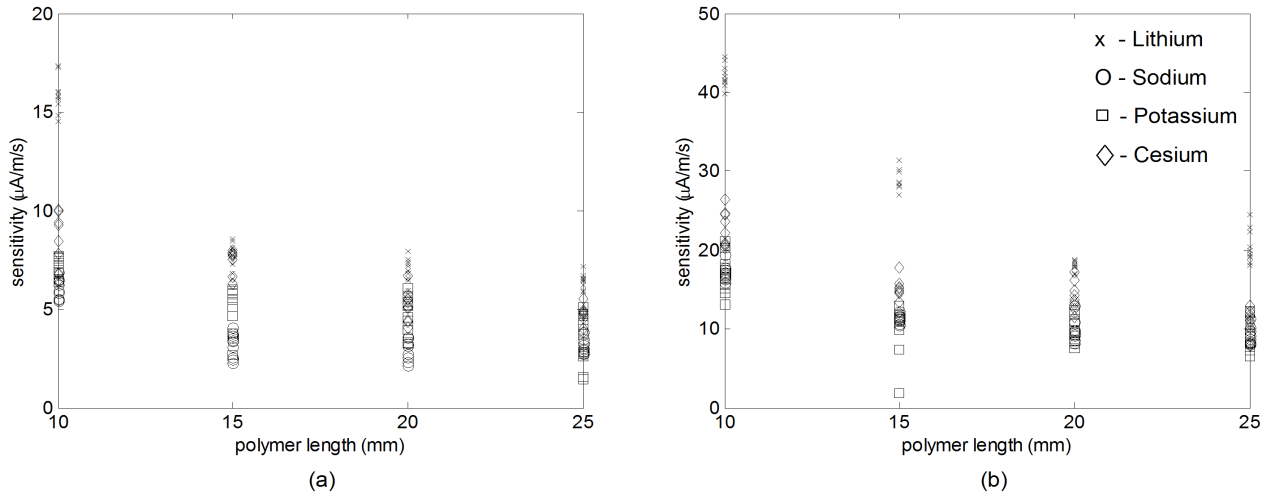

Figure 2.7: Sensitivity as a function of length for the 3.5 mm wide sample (a) and the 8.5 mm wide sample (b).

such a log-log plot. Figure 2.8 provides a least squares fit of the logarithmic data for each of the counter-ions. The slope corresponding to each of the cation types is presented to the right of the figure. From this study, we see that lithium follows the predicted trend very well with a slope of -0.995 μC/mm. However, there does exist a discrepancy among the other cation species. For each of the other cations a linear curve fit yields slopes between -0.70 and -0.75 μC/mm. If we include error bounds of one standard deviation for each of the free lengths, it is seen that a slope of -1 μC/mm fits well within the accuracy of the experimental data for each of the four cations. It should be noted that the scatter found in this data is consistent with other experimental studies of ionic polymers (see for example [59], [80]).

Another interesting component of Figure 2.8 is the sensitivity of each sample as a function of counter-ion. In the Li^+ form, the sensitivity of these materials is the highest, as would be expected from the literature on actuation properties ([80]). However, previous studies into the actuation performance of ionic polymers indicate that within the alkali metal group, voltage to strain sensitivities decrease with larger ions. If we exclude the lithium data for the moment, sensing seems to provide a trend were sensitivity actually increases with cation size. This behavior was slightly unexpected from our initial modeling efforts, however, it is thought that this variation may be explained in later studies through the scaling factor ψ_s.

The final aspect of quantifying the charge sensing model involves determining whether or not the model can accurately predict the amount of charge generated by an induced stress within the polymer. The approximation for charge in equation 2.57 is a function of the transducer geometry, the material modulus, the length parameter β and the coupling coefficient ψ_s. The physical constants and geometric parameters used in this simulation are presented in Table 2.1. The material modulus comes from experimental characterizations conducted by [7] and is taken as 75

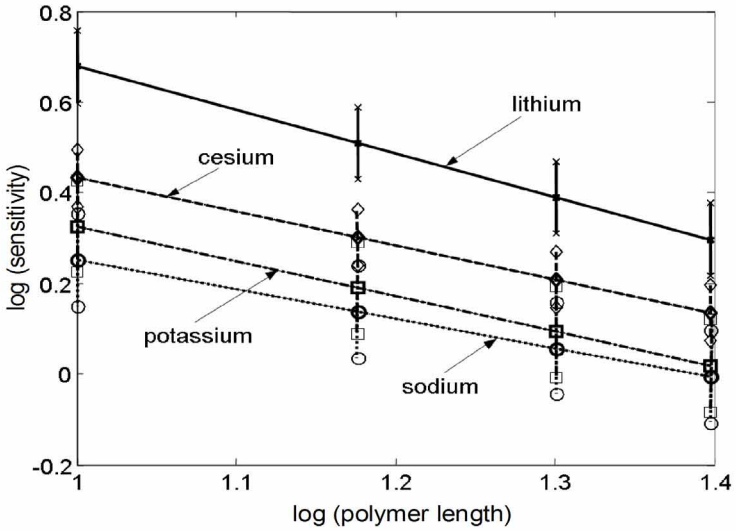

Cation Type	Slope
Li^+	-0.957
Na^+	-0.645
K^+	-0.775
Cs^+	-0.744

Figure 2.8: Normalized sensitivity plotted as a function of $\log_{10}$(polymer length).

MPa for the fully hydrated sample. We determine the length parameter β through equation 2.26. Coefficients for this expression are found in Tables 2.1 and 2.2 with decay times $1/\lambda$ of 6 ms. Applying these coefficients, we estimate boundary layers of 0.48 μm to 1.14 μm. This defines all except one of the model parameters. The one remaining parameter, ψ_s is left as a free variable within our present derivation. This value will be fit with the experimental data and then compared to previous estimates of the coupling coefficient.

To investigate the accuracy of this model, we compare the predicted charge response with that measured experimentally. In order to do so, we numerically integrate the measured current to determine the charge induced by a mechanical deformation. Figure 2.9a presents both the charge response and the imposed displacement for a polymer sample in Li^+ form. This charge response is then replotted in Figure 2.9b and compared to the model predictions from equation 2.57. The coupling coefficient used in this model prediction corresponds to a value of 265 J/C. Comparing this term with the k_0 terms presented in [61], we find that our values for ψ_s are only slightly larger than those predicted by Nemat-Nasser and Li. The general agreement between the measured data and the predicted response lead us to believe that the electrostatic equations can be used directly to address both the sensing and actuation ([61, 59]) response of ionic polymers.

2.2 Chapter summary

In this chapter a sensing model has been developed for the IPT. Using electrostatic relationships as the basis for the development, a set of expressions are developed to describe the internal potential and charge density that result from

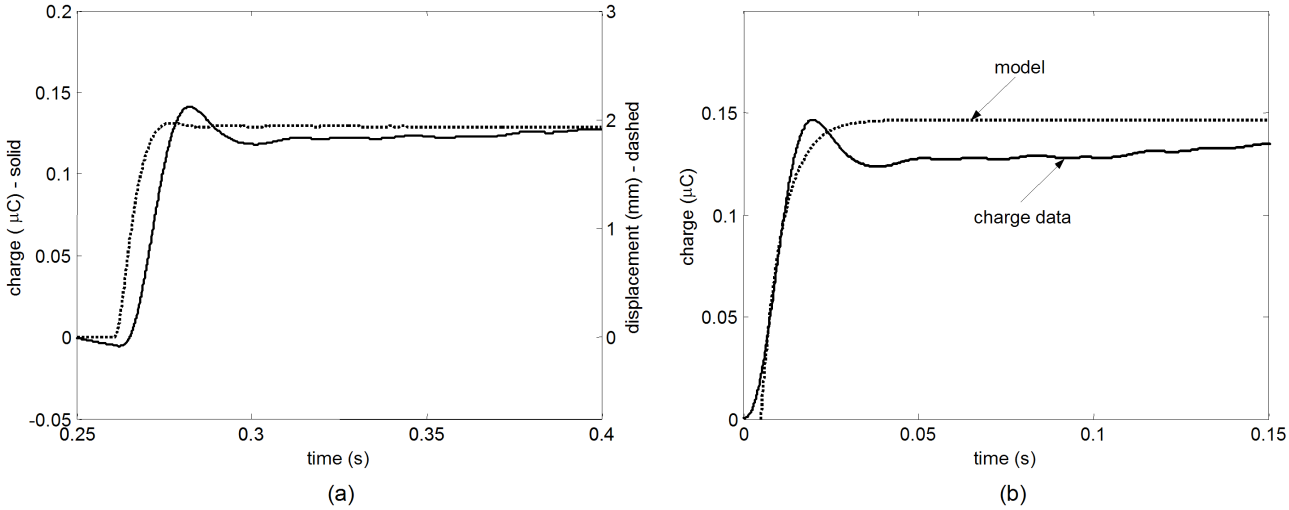

Figure 2.9: Charge induced by mechanical stress along with the tip deflection of the polymer transducer (a). Model prediction of electrical charge plotted along with experimental data (b).

an imposed deformation. This induced strain is assumed to be proportional to the charge density at the electrodes, serving as the boundary conditions for the modeling approach. A step change in deformation is assumed and the transient charge density is developed. From the charge density, expressions for the isothermal transient ionic current are used to predict the surface current induced within the polymer. An experimental study is conducted to consider how the sensing response scales with the geometry of the transducer. Results indicate that the polymer scales linearly with increased width and inversely with the polymer length. These results agree with model predictions. Finally the time response of the IPT is considered when subject to step change in strain. Comparison with experimental results show good correlation in predicting the induced surface current.

Chapter 3

Effects of counterion and solvent on sensing and actuation response

The sensing model of Chapter 2 offers interesting insight into many of the parameters that are expected to influence the response of the ionic polymer transducer. In the model validation experiments of the previous section the geometric parameters of the test sample were seen to have a significant effect on the IPT's sensing response. Similarly, the counterion specie was also seen to have a very evident impact on the ionic polymer's charge response to imposed deformations. This result, shown in Figure 2.8, provides motivation for the experimental studies considered in this chapter. In the model of Chapter 2, the effects of the counterion cannot be imposed as directly, or as intuitively as the geometric parameters. Therefore, we must consider other means by which the counterion can enter into the modeling process. From the general continuity expression, it is postulated that counterions influence the diffusion properties and the effective permittivity of the ionic polymer, in turn influencing the electromechanical response of the tranducer. Chapter 3 investigates this idea further by looking at the effects of counterions on the actuation, sensing and impedance responses of the ionic polymer transducer. Other variations are also considered, looking at what effect solvent properties, namely viscosity and dielectric permittivity, have on the diffusion coefficient and effective permittivity of the transducer.

3.1 Experimental Studies

In addition to the model validation experiments discussed in the previous section, several detailed studies have also been conducted to look further into the effects of counterion, solvent viscosity and solvent dielectric on the actuation and sensing responses of ionic polymer transducers. In each of these studies, the water-based Li^+ form

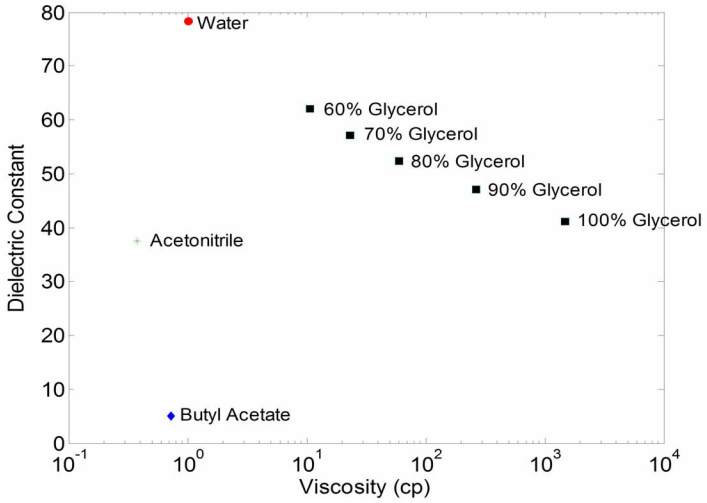

Figure 3.1: Solvent dielectric plotted as a function of solvent viscosity for each solvent considered in this experimental section.

of the Nafion^{TM} transducer has been used as a baseline. The first of these studies was designed to build upon the experiments used in our model validation, incorporating a wider range of cations within the IPT. For these experiments alkali and alkaline earth metals were used as well as two larger organic cations. In addition, these tests broadened the analysis approach to include both actuation and sensing responses in both time and frequency domains.

The second series of experiments presented in this chapter investigate the IPT response when solvated with glycerol-water mixtures. By using this method of mixtures, we were able to obtain a wide range of solvent viscosities, ranging from 1 cp (100% water) to 1500 cp (1000% glycerol) in six intervals. The solvent viscosity for each of these mixtures were measured experimentally (at 23^{o}C) and compared against published findings [55]. The six glycerol-water mixtures used in this study are represented with 0%, 60%, 70%, 80%, 90% and 100% glycerol content, with the measured values presented in Table 3.1.

The third series of experiments presented in this chapter are designed to look at the effects of solvent dielectric on the ionic polymer transducer. Three solvents were utilized in this portion of the study, again using water ($\epsilon = 78.4$) as the baseline. The two remaining solvents were selected due to the fact that they possess similar

Table 3.1: Solvent properties

Solvent	butyl acetate	acetonitrile	100% water	60% glycerol	70% glycerol	80% glycerol	90% glycerol	100% glycerol
Viscosity (cp)	0.73	0.38	1.01	10.68	23.04	59.9	265.98	1500.00
Dielectric (ϵ/ϵ_o)	5.1	37.5	78.4	62.03	57.06	52.27	46.98	41.14

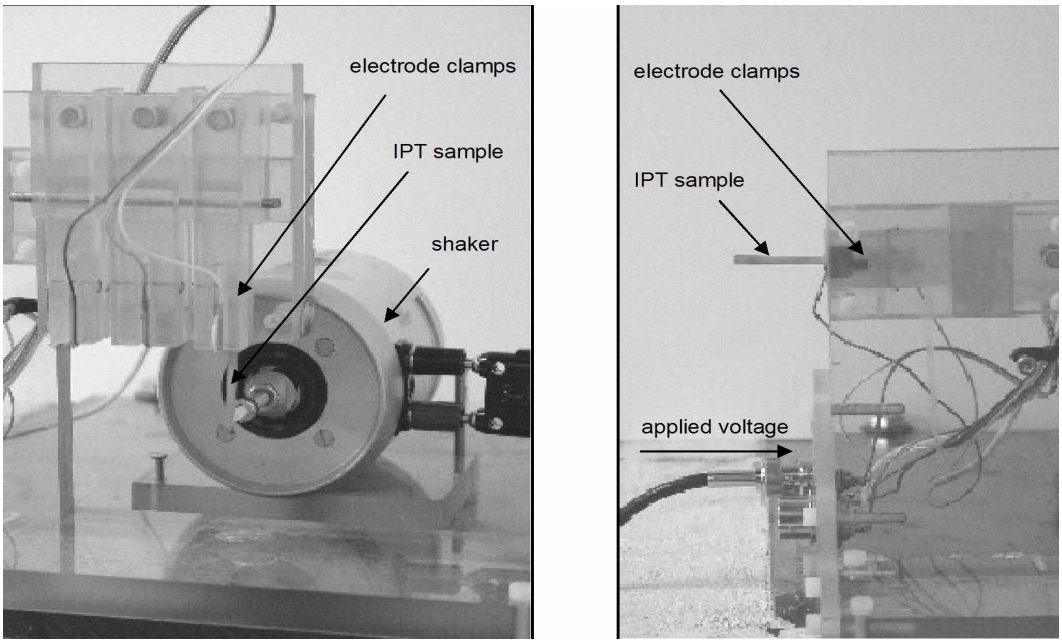

Figure 3.2: Fixtures used to measure sensing (left) and actuation (right) responses of the cantilevered ionic polymer transducer.

viscosities but widely varying dielectric constants. The solvents selected in this portion of the study were acetonitrile ($\epsilon = 37.5$) and butyl acetate ($\epsilon = 5.1$), whose dielectric and viscosity properties are presented in Table 3.1. Figure 3.1 presents the solvent dielectric as a function of viscosity for each of the solvents considered in the second and third portions of this experimental study.

In each series of experiments, actuation and sensing responses were measured in both the frequency and time domains. In each test series, all of the samples were cut from the same sheet of plated Nafion^{TM} membrane in order to minimize sample to sample variation. In the cation and dielectric studies, samples were cut in their dry state with dimensions of 3 mm x 44 mm x 0.2 mm. The viscosity based samples were taken from another sample sheet and were cut to 4 mm x 35 mm x 0.2 mm before being hydrated in their respective solvents. The principle test fixture used in each of these test series is shown in detail in Figure 3.2. This fixture was designed to allow testing of both sensing and actuation for IPT samples clamped in a cantilevered configuration.

Sensing tests were conducted with the IPT sample clamped in a vertical position, shown in Figure 3.2a. An LDS V203 electromagnetic shaker was used to impose tip deflections in the polymer transducer, using a nylon tipped stinger to approximate a point load on the cantilevered sample. Tip deflections of the transducer were measured using a Polytec OFV 3001/303 laser vibrometer while the polymer's electrical response was measured using a charge sensing circuit designed by Newbury [65]. Frequency response functions were measured using a Tektronix 2630 Fourier analyzer which was used to drive the LDS shaker (through an HP 6825A Bipolar Amplifier) with a series of random excitation signals.

Actuation tests were also conducted on each IPT sample, however they were mounted in the horizontal configuration of Figure 3.2b. In this series of tests, the samples were subject to random (700mV RMS) and square ($\pm$1V peak) wave excitation voltages. Output displacements were again measured using a Polytec OFV 3001/303 laser vibrometer. In addition to the displacement and voltage signals, the current drawn by the IPT was also measured in order to obtain both the electrical impedance (V/I) and actuation (D/V) responses of the transducer. FRFs were again measured using the Tektronix 2630 Fourier analyzer while time response data was measured using a dSPACE 1005 DSP system.

3.1.1 Counterion Effects

The counterion experiment presented in this section builds upon the findings of our model validation work, as well as previous studies that have investigated the effects of cations on the actuation response of IPTs [80]. As discussed in the model validation section of Chapter 2, counterions have been shown to play an important role in the performance of ionic polymer transducers. In this study, five counterions have been examined and are compared to the baseline performance of each transducer in Li^+ form. In this study two alkali metals are considered, Na^+ and Cs^+. A divalent cation has also been included in the form of Ca^{2+}, with two organic cations TEA^+ (tetrathylammonium) and TBA^+ (tetrabutylammonium) included as well. Three separate tests were conducted on each of the test samples in this study, examining sensing and actuation (both in the frequency and time domains) as well as the electrical impedance before and after cation exchanges. Each sample was first tested the Li^+ form to provide a baseline, then boiled in H_2SO_4 and placed in 0.5M solutions of M^+Cl^- (where M^+ corresponds to the target cation). Samples were then flushed with distilled water repeatedly to lower the concentration of free salt within the ionomer.

Following sample preparation, both actuation and sensing tests were performed. Figure 3.3 presents a comparison of the first sample placed Na+ form. In the actuation response, we obtain a frequency response that is characteristic for most cantilevered vibrations problems. At low frequencies the polymer has a flat freqeuncy response. Then as the frequency increases, the excitation approaches the natural mechanical resonance of the cantilevered sample, resulting in the resonant peak shown in the actuation response. Similarly, the sensing response exhibits a dynamic response which is attributed to the test configuration used in experiments. Buechler [9] associates the resonant peaks in the sensing response to the mounting and loading configurations applied to the test sample. In the Na^+ form there appears to be good correlation between the actuation responses of the Na^+ and Li^+ based transducers. Interestingly, the sensing response exhibits a very different behavior as the sensing response it is 5-10 times lower for the Na+ sample as the frequency increases toward resonance. In these measurements, the frequency relates the transducer motion ($\mu\epsilon$) to applied voltage (V) in actuation and measured charge (C) to imposed deformation ($\mu\epsilon$). The third measurement conducted in these experiments relates the applied voltage to current response. This measurement can be used to replot the actuation in terms of $\mu\epsilon/C/m^2$ and sensing in terms of $V/\mu\epsilon$.

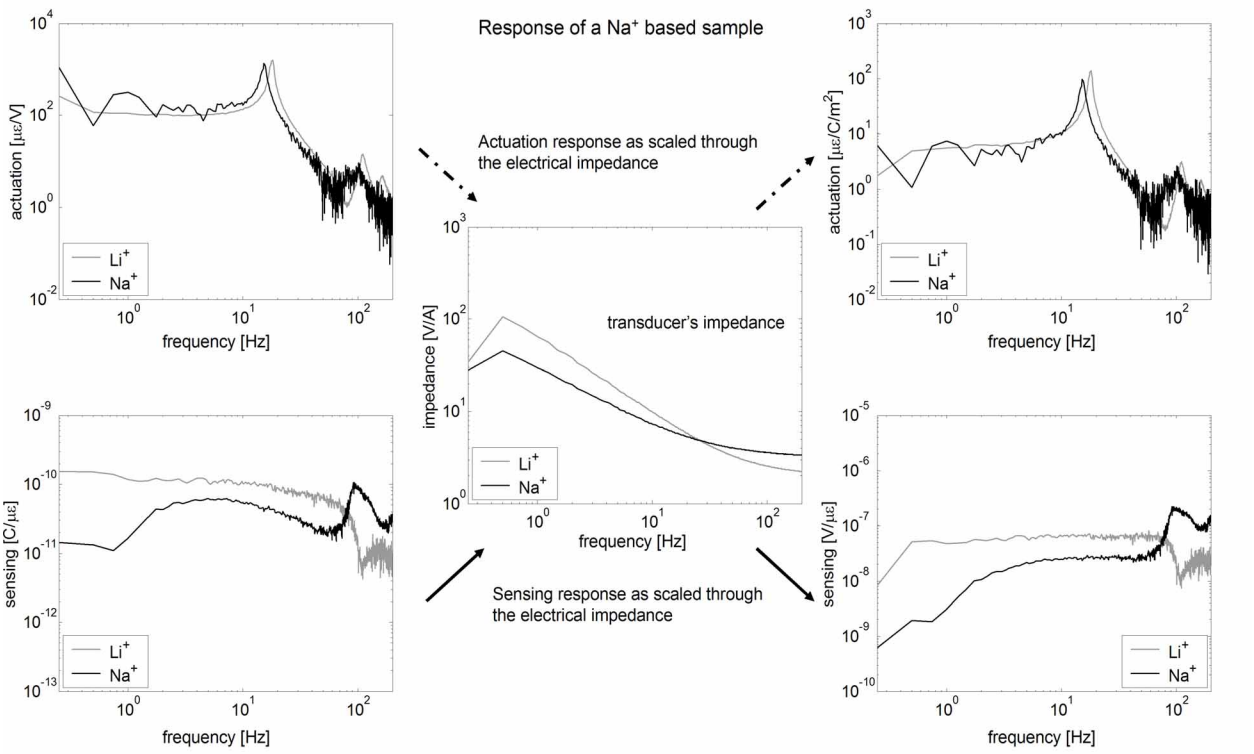

Figure 3.3: Sensing and actuation response for Na^+ based sample.

Since the electrical impedance for these two counterions is similar, we would not expect a drastic change due to this transformation. However, it is this relationship that will lead to a fundamental observation that can be made as the counterions pose greater impact on the electrical impedance of the ionic polymer.

The presence of Cs^+results in very similar behavior, as shown in Figure 3.4, except that the reduction in sensing is not quite as pronounced beyond 7 Hz. Comparing the relative sensitivity of Na^+, and $Cs^+$to their respective Li^+performance, it is seen that the $Li^+$and Cs^+samples provide the higher sensing capabilities than the Na^+based samples, consistent with the results previously shown by Farinholt and Leo [15]. Another interesting feature of the Cs^+sample is the time domain actuation response. Figure 3.5 presents the results of a $\frac{1}{4}$ Hz square wave used to excite the transducer, first in Li^+form and then in Cs^+form following the ion exchange. In the sensing response, each cation exhibits a very similar charge response to an imposed deformation of approximately $\pm 500\mu\epsilon$. The form and magnitude of these responses are very similar, with the Cs^+sample showing a slightly smaller sensitivity. In actuation the magnitudes are very similar, however the form is much different. In the Li^+form, the actuation response is very representative of an underdamped beam with high overshoot followed by a decaying oscillation as the response settles. In the Cs^+form there exists some oscillation, however the response continues to rise over the full 2s interval of applied voltage. Time responses of the Na^+samples indicate that they behave very similarly to

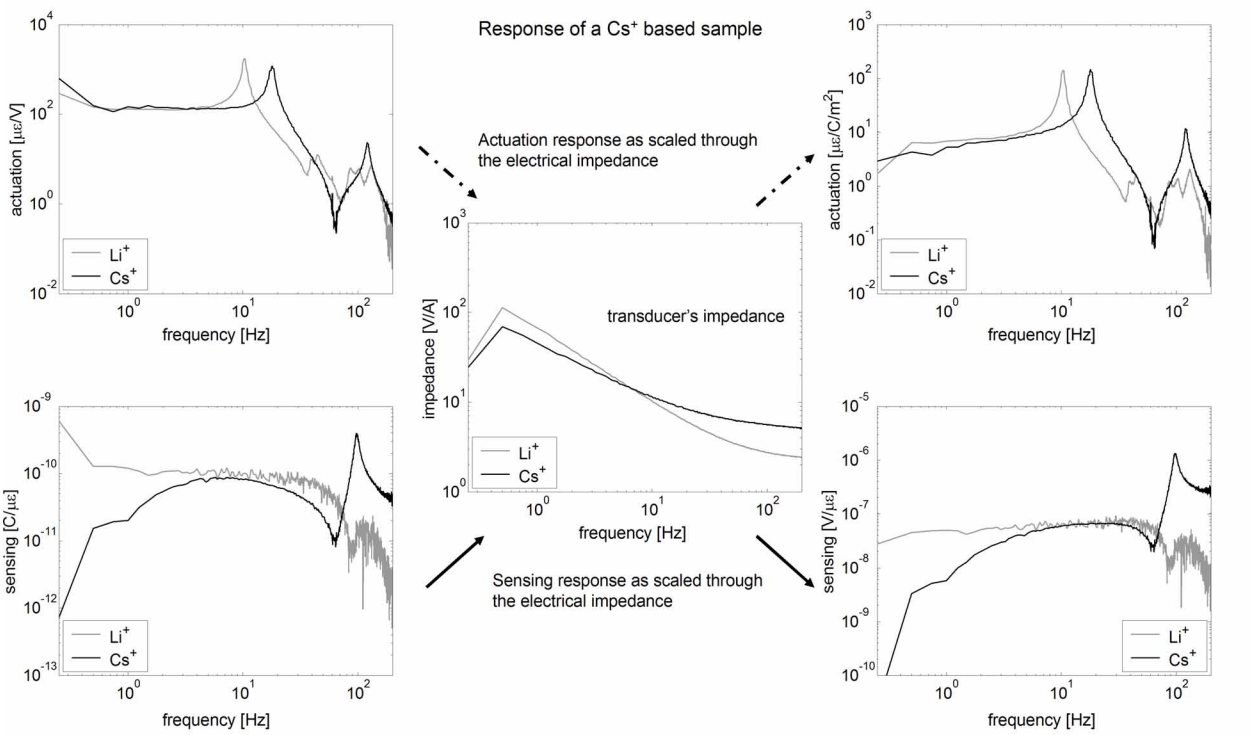

Figure 3.4: Sensing and actuation response for Cs^+ based sample.

Li^+, a result that is also consistent with other transducers that were tested in K^+form.

The next cation of interest in this portion of the study is the divalent cation Ca^{2+}. Previous studies by Shahinpoor and Kim [80] have investigated the actuation response for low frequency harmonic excitations. Using a 0.5 Hz, 1.2 V_{RMS} sine wave, they found that the presence of the Ca^{2+}cation reduced the transducer's performance by approximately 50% as compared to the Li^+baseline. In our work the frequency range of interest was typically much higher, looking over a frequency band of 0-200Hz. The results shown in Figure 3.6 indicate that at higher frequencies the actuation response is very similar to that of the Li^+based transducer. Interestingly the sensing

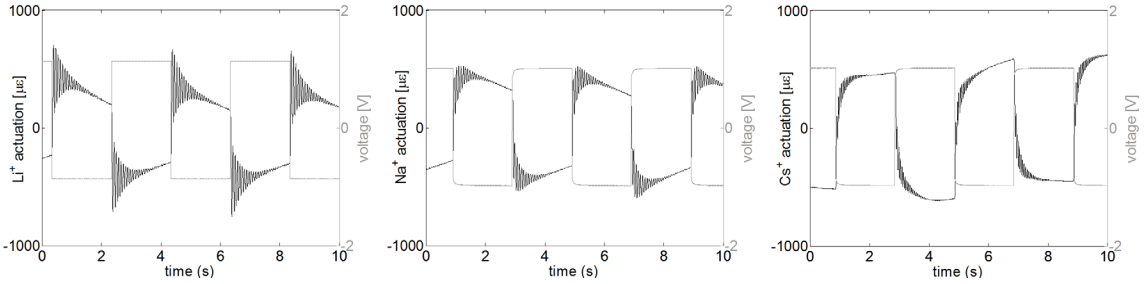

Figure 3.5: Actuation response of Li^+, $Na^+$and Cs^+based ionic polymer transducers when excited by a 1V square wave at 0.25 Hz.

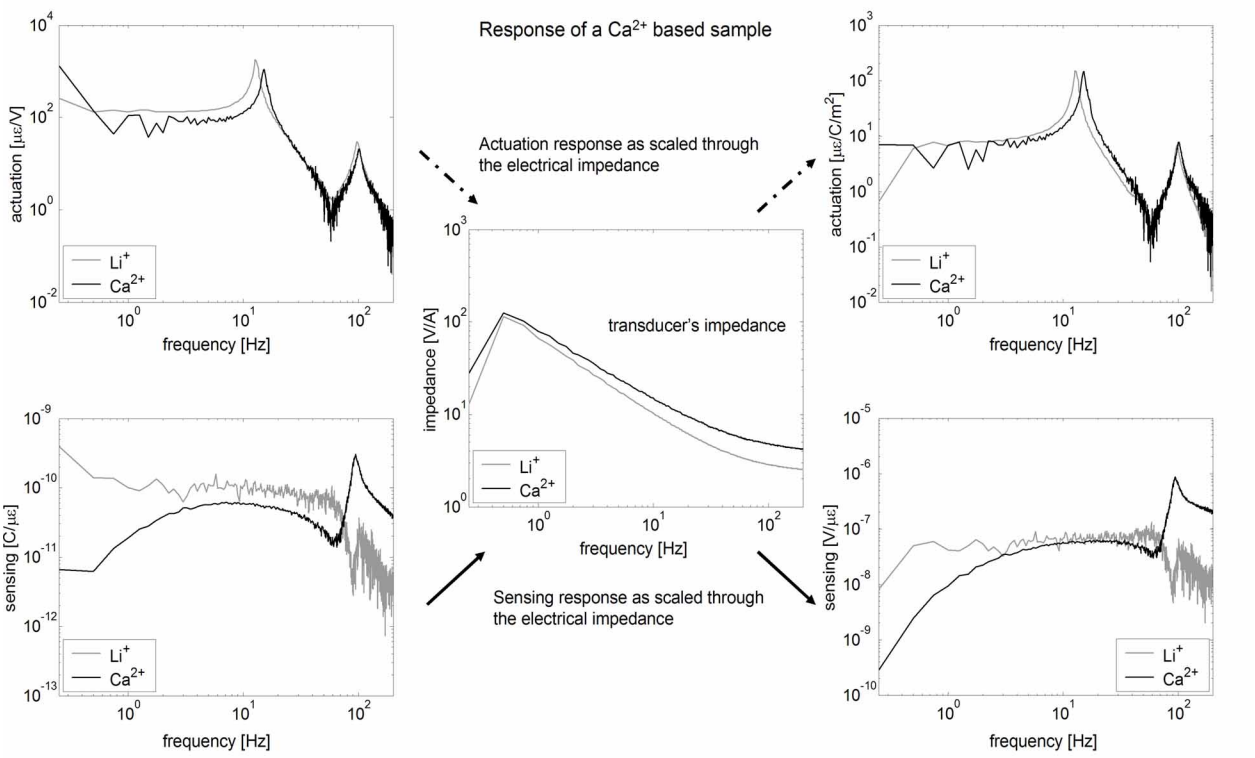

Figure 3.6: Sensing and actuation response for Ca^{2+}based sample.

response exhibits less of a similarity, especially at frequencies below 2 Hz. Beyond 50 Hz the signal is dominated by a mechanical resonance and thus it is harder to draw conclusions over this region. Additionally, the electrical impedance of the $Li^{+}$and Ca^{2+}samples are relatively similar with the Ca^{2+}form having slightly higher electrical impedance than Li^{+}. When compared to the previous monovalent cations tested Ca^{2+}exhibits an actuation response very similar to that of the Na^{+}sample (Figure 3.3) with more low frequency distortion in the actuation response as well as a much more distorted antiresonance between the first and second mode. Interestingly, the sensing response of the Ca^{2+}sample is much more in accordance with the Cs^{+}based transducer. Another interesting facet of each response is the variation in the electrical impedance, which is seen to be much more different in the case of the divalent counterion than in either of the other alkali cations. The alkali cations actually experience a reduction in the low frequency V/I relationship while the divalent cation exhibits a consistently larger impedance over the 0-200 Hz frequency band.

The third group of counterions considered in this study focus on the organic cations $TEA^{+}$and TBA^{+}. As the smaller of the two cations TEA^{+}will be the first to be discussed. Unlike the alkali and the alkaline earth metals, the presence of this organic cation causes a distinctive change in the form of the IPT's performance. This variance in the IPT's response is seen most clearly in the material's electrical impedance, shown in Figure 3.7. At

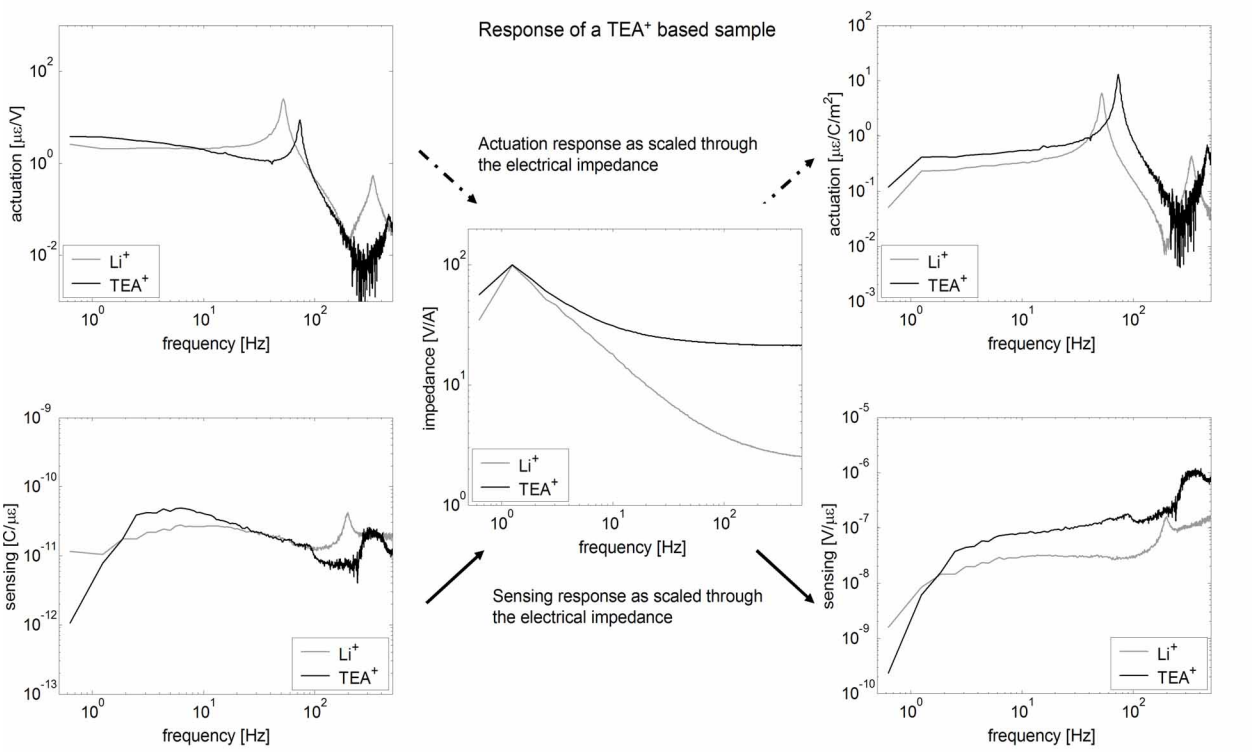

Figure 3.7: Sensing and actuation response for TEA^+ based sample.

frequencies below 2 Hz the material's impedance scales similar to the divalent cation. However, a large separation begins to develop at higher frequencies where the transducer is seen to become much more resistive in the presence of TEA^+. Thus, if we consider the measured actuation ($\mu\epsilon/V$) and sensing ($C/\mu\epsilon$) responses we can see that the electrical impedance plays a direct role in altering the transducer's performance. In TEA^+form the IPT response in no longer relatively constant over low frequencies, as the low frequency response exhibits an initial slope in the actuation response. At this point it is important to note that the electrical impedance can be used to transform the $\mu\epsilon/V$ relationship into one that relates strain to charge, shown in the upper right plot of Figure 3.7. When compared to the transformed Li^+baseline, it is apparent that the impedance transformation causes the TEA^+sample to coalesce with the baseline response once normalized to a $\mu\epsilon/C/m^2$ relationship. This observation hints at the importance of the voltage to current response in understanding the performance of the ionic polymer material. This result indicates the importance of the electrical conversion characteristics within the material, and how changes in the counterion play into the induced charge flow that results from an applied electric potential. And while this fact is seen in the TEA^+based study, it is much more apparent with the larger organic TBA^+counterion.

As the final counterion of this study, $TBA^+$is considerably larger than any of the cations previously examined in this series of experiments. The actuation and sensing responses of the IPT in TBA^+form are presented in Figure

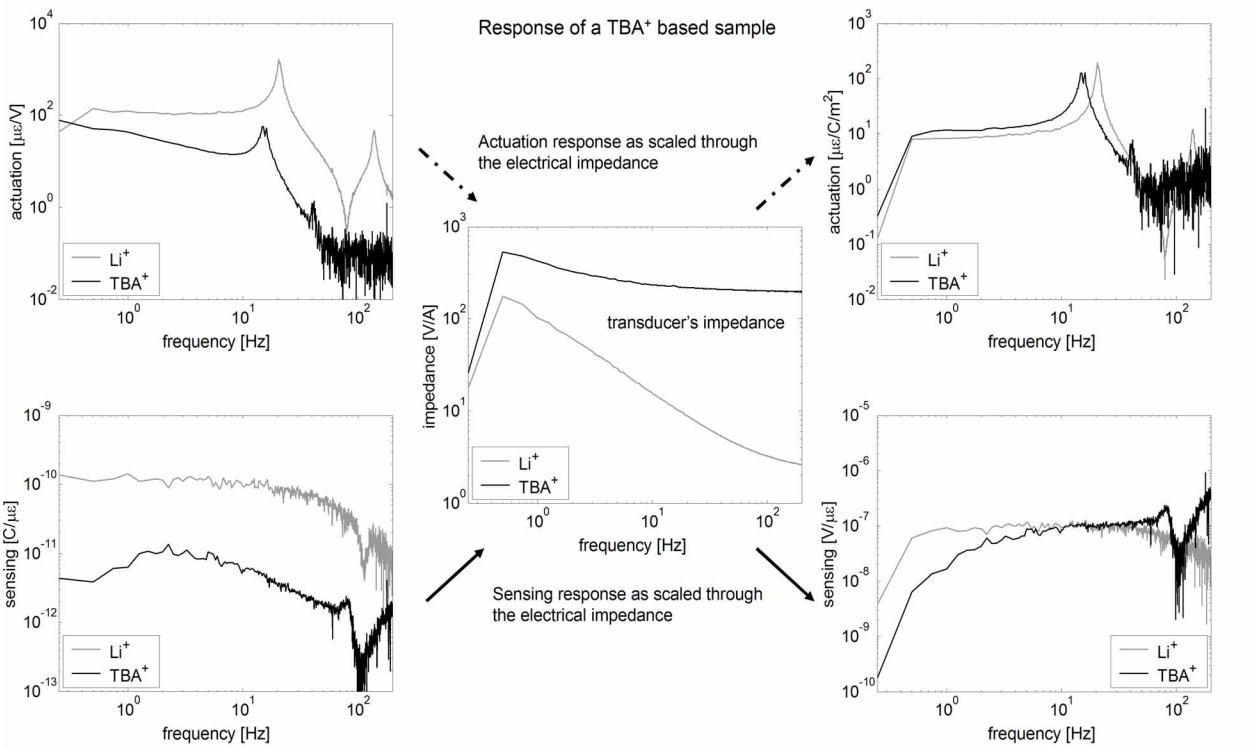

Figure 3.8: Sensing and actuation response for TBA^+ based sample.

3.8 along with the electrical impedance of the sample. The presence of this large organic cation results in a much higher, more resistive impedance response, a characteristic which translates directly into the $\mu\epsilon/V$ sensitivity. As in the case of the TEA^+sample, TBA^+provides a low frequency decay that is even more pronounced in this counterion form. Using the electrical impedance to transform this actuation response, we again see a coalescence in the $\mu\epsilon/C/m^2$ relationship. The sensing response also exhibits a marked difference when comparing the measured ($C/\mu\epsilon$) and the transformed ($V/\mu\epsilon$) response of the IPT. From the measured response of this sample, it appears that the TBA^+sample is much worse in sensing as compared to the Li^+form of the same transducer. However, once normalized with respect to the electrical impedance it becomes apparent that the electric potential to strain relationship is much more consistent between cation species, further emphasizing the importance of the transducer's voltage to charge conversion capabilities.

This result is also apparent in the time response of the ionic polymer transducer. As in the case of the $Na^+$and Cs^+time studies, the TBA^+sample was subject to a 1V, 1/4 Hz square wave while tip deflections were monitored using a laser vibrometer. Considering first the baseline response of the polymer in Li^+form, we see from Figure 3.9 that the baseline sample exhibits a very fast initial response. The Li^+sample also exhibits the characteristic transient oscillation of an underdamped cantilevered sample along with a slow back relaxation while

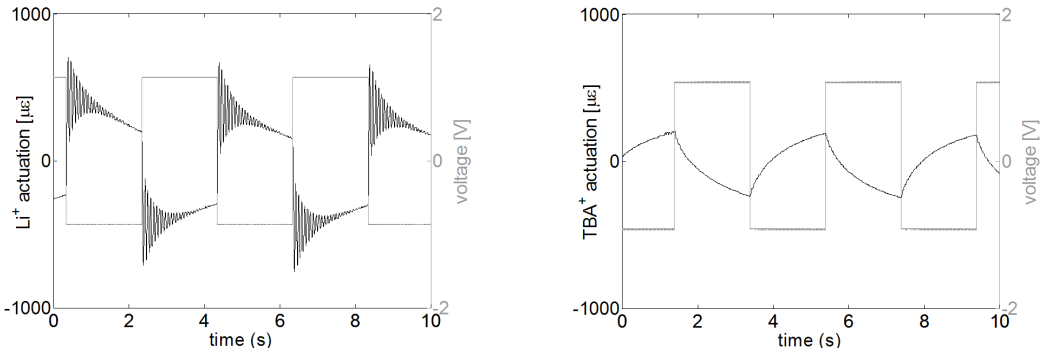

Figure 3.9: Time response for $Li^+$and TBA^+based samples.

the voltage is held constant. Comparatively, the TBA^+sample yields a much slower response, similar to the charging profile of a simple capacitor. This comparison relates back to one of the founding assumptions of our electrostatics model, that internal stress and charge density are linearly related within the IPT material. While this assumption was initially applied in the sensing response where tip displacements were limited to small deflections, the TBA^+sample indicates that the assumption should apply for our actuation response as well. Thus, as charge motion is regulated in such a manner that it does not excite the elastic response of the polymer, the mechanical response of the membrane should follow linearly, a prediction also supported in the $\mu\epsilon/C/m^2$ relationship of Figure 3.8.

3.1.2 Solvent Viscosity Effects

The second series of experiments that were conducted focus on the effects of solvent viscosity on the IPT response. Each transducer was cut from the same sheet of electroded Nafion^{TM} and were cut into 4 mm x 35 mm x 0.2 mm samples. Each of these samples were prepared by an MSE senior design team, and included five cation species (Li^+, Na^+, K^+, $Cs^+$and TEA^+) along with six concentrations of a glycerol-water solvent, yielding a total of 30 test specimen. One from each of these test populations were hydrated in distilled H_2O to serve as the baseline, while each of the remaining samples were place in 60%, 70%, 80%, 90% and 100% solutions of a glycerol-water mixture. The viscosity and dielectric properties for each of these mixtures were calculated and can be found in Table 3.1 and Figure 3.1. Each of the results presented in this section are for the Li^+based transducer as the trends were consistent from one cation species to the other.

The first series of experiments focused on the frequency response of the IPT to a random excitation signal. Since these transducers were shorter and wider than those used in the cation study, the frequency band was increased to 500 Hz in order to try and capture the first two resonance frequencies. Figure 3.10 presents the measured actuation, sensing and impedance responses for each of the glycerol mixtures. The most apparent shift in the material response can again be seen in the electrical impedance of the IPT. As the solvent viscosity increases the voltage to current

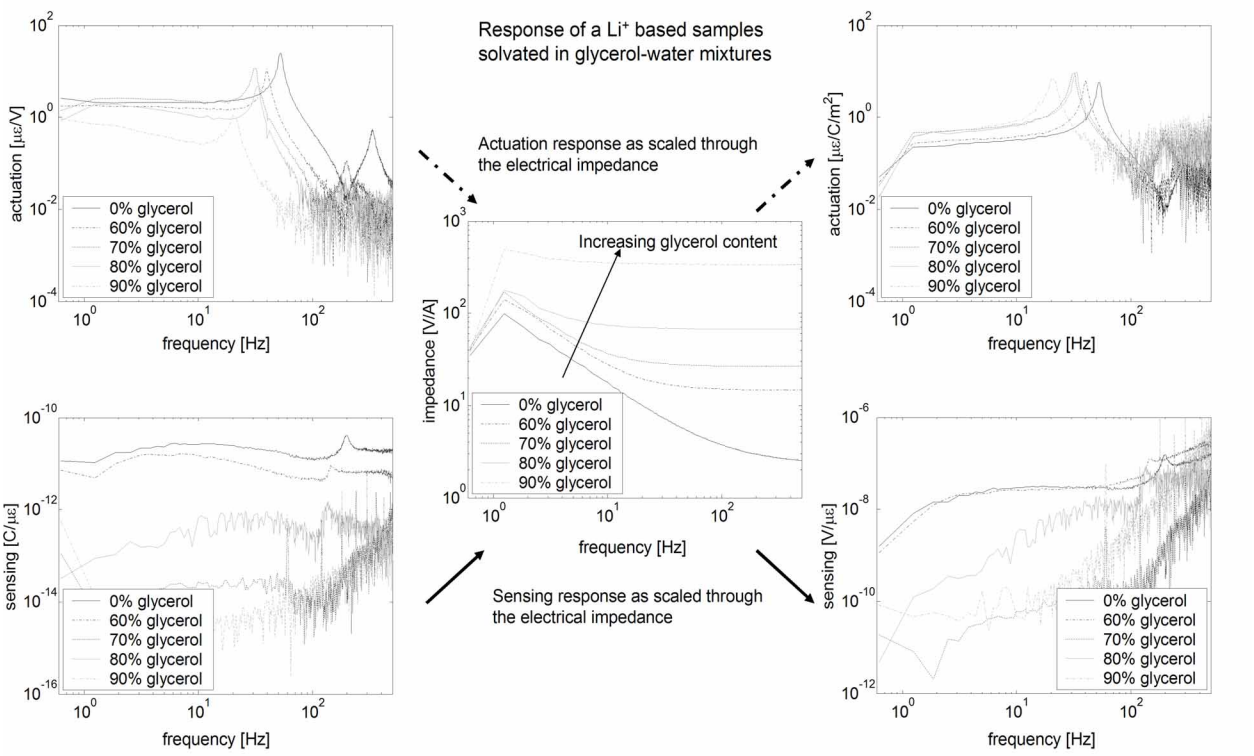

Figure 3.10: Frequency response for each of the glycerol-water samples.

relationship is seen to continually increase, becoming more resistive in nature with higher concentrations of glycerol. The shift in the electrical impedance in turn corresponds to the development of a decay in the low frequency performance of the actuation response. In addition to steadily decreasing performance, the presence of a higher concentration glycerol solvent also lowers the natural frequency of the transducer.

Sensing responses were also seen to be highly affected by the glycerol levels, more so as the result of experimental difficulties rather than the material response. The sensing results of Figure 3.10 illustrate this point with high distortion levels in the samples of higher glycerol concentration. At these higher concentrations ($> 70\%$) the surfaces of the transducer became coated in a glycerol film, which was seen to lead to a serious measurement issue due to the small charge densities and electric fields generated by an applied strain. These issues were not as problematic in the actuation response, as actuation fields are typically much higher than those measured in sensing. Therefore, we could only draw conclusions from two of the viscosity samples, those at 0% and 60% glycerol content. From these two samples it can be seen that viscosity plays a role in the $C/\mu\epsilon$ sensitivity. However, once normalized by the material's electrical impedance, the viscosity effects become much less apparent.

Performing a similar transformation on the measured $\mu\epsilon/V$ responses we see that the results collapse to form a fairly consistent set in terms of $\mu\epsilon/C/m^2$. Once the V/I variations are removed from the measured response, most

of the variance in the $\mu\epsilon/C/m^2$ response tends to reside in shifts in the natural frequency rather than in the form of response. Looking more closely at these results it must be noted that the shifts in the actuation and impedance responses of the glycerol study are almost identical to those seen in our previous study of the TBA^+based sample. This is a very interesting observation since two separate variables within the IPT have been varied, yet they both seem to produce the same result on the $\mu\epsilon/V$ response of the membrane. Looking closely at this result, we can consider what is actually occurring within the polymer when each of these changes are imposed on the IPT. In the case of the TBA^+based sample the cation itself is very large and hydrophobic, increasing the difficulty with which the ion can move through the membrane under an applied field. This resistance to conduction is seen directly in the measured impedance as the membrane becomes much more resistive in the presence of the TBA^+counterion. Similarly, in the glycerol based transducers, the Li^+ion encounters much more resistance as it migrates through the polymer (again seen in the V/I relationship). Therefore, if we think of this resistance in terms of the ion conduction within the material, we can see that the reduction in the $\mu\epsilon/V$ response is actually due to a reduction in the ionic conductivity of the membrane. This argument also holds for the transformed actuation response. The $\mu\epsilon/C/m^2$ response relates the polymer motion to the ion motion within the polymer, a relationship that has been shown again and again to be consistent from one sample configuration to the next. Thus, we can presume that changes in IPT performance result from changes in the ionic conductivity of the material, a conclusion that can have direct implications in the development of new ionomer membranes for actuation purposes.

The solvent viscosity is also seen to play an important role in the time response of the ionic polymer transducer. The step responses of Figure 3.11 show the material response to a 1V step input that is held constant for 55s. The results of this study agree with previous studies of [61, 59], illustrating that more viscous concentrations drastically slow the polymer response. In pure water form there is a fast initial rise that is followed by a slow back relaxation that actually causes polymer to deflect below its orignial starting position. This response becomes much more gradual as the solvent viscosity increases, a feature that is again predicted in the frequency domain analysis of Figure 3.10. From the forms presented in Figure 3.11 it is seen that many are noticably exponential in nature. A two term exponential expansion of the form,

$$w(l,t) = A\left(1 - e^{-t/\tau_A}\right) + B\left(1 - e^{-t/\tau_B}\right) \tag{3.1}$$

is assumed for the system. $w(l,t)$ represents the tip displacement response, A and B correspond to the magnitude of each fit and τ_A and τ_b correspond to the time constants of each term. Using this general form, some agreement is found in the lowest viscosity sample, giving a suitable fit for the water based transducer. At higher glycerol concentrations $\geq 60\%$, a three term exponential expansion is needed to capture the fastest time constant, while also

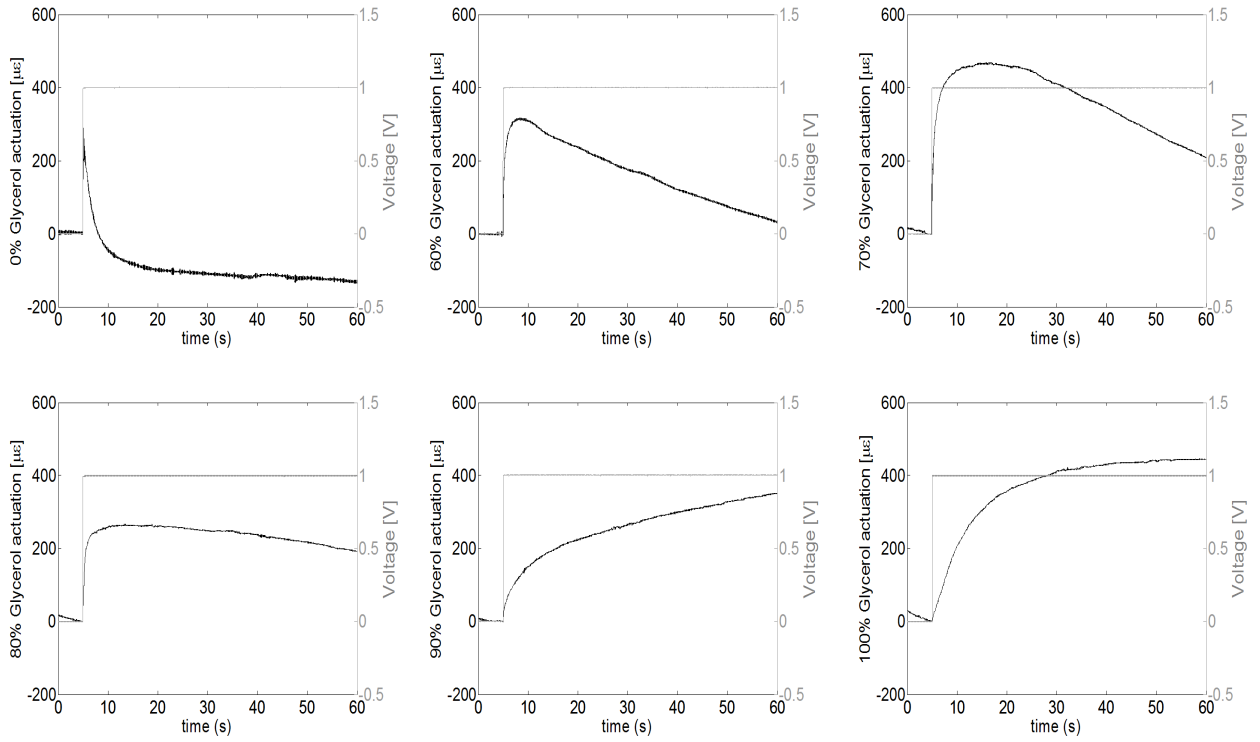

Figure 3.11: Time response for each of the glycerol-water samples.

providing sufficient agreement at longer time scales. This fitting method has the same form as before with,

$$w(l,t) = A\left(1 - e^{-t/\tau_A}\right) + B\left(1 - e^{-t/\tau_B}\right) + C\left(1 - e^{-t/\tau_C}\right) \tag{3.2}$$

Table 3.2 presents the fit parameters that were determined based upon the cost function $\mathrm{err} = |\mathrm{w(l,t)} - \mathrm{data}|$. The results for three distinct glycerol concentrations, 0%, 80% and 100% are presented in Figure 3.12. The plots shown in Figure 3.12 illustrate good correlation between the exponential fits and experimental data. From the parameters

Table 3.2: Parameters used in exponential fits of the viscosity dependent actuation response.

glycerol content	A	τ_A	B	τ_B	C	τ_C
0%	255.6	0.05	-370.6	3.0	-	-
60%	339.5	0.53	-757.5	81.2	107.5	51.8
70%	380.3	0.52	-970.6	49.9	482.2	12.9
80%	235.2	0.55	-197.2	47.6	104.7	10.0
90%	142.2	2.56	96.7	58.7	215.7	46.9
100%	426.8	6.01	-817.6	9.4	839.1	11.3

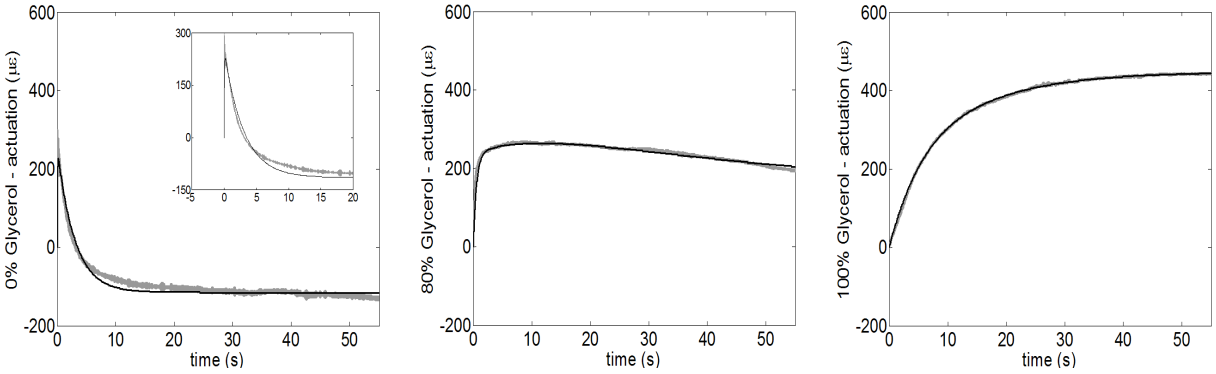

Figure 3.12: Exponential fits for three of the glycerol samples. Results correspond to concentrations of 0%, 80% and 100% glycerol.

outlined in Table 3.2 it is seen that the fastest time constant τ_A steadily increases with glycerol content. Since the tip displacement of the polymer is related to cation motion, the steady increase in τ_A indicates that the polymer's diffusion coefficient decreases with increased glycerol concentration. This characteristic is also supported by the impedance curves of Figure 3.10. As the glycerol content increases the resistive nature of the transducer increases as well, indicative of a drop in the diffusion coefficient. This effect will be discussed in more detail in the analytical development of the next chapter, and again in Chapter 6. The next study in this experimental work attempts to limit the viscous effects of the solvating liquid, in an attempt to understand the impacts of solvent dielectrics on the IPT response.

3.1.3 Effect of Varying Dielectric Properties

The final portion of this experimental section looks at how the dielectric nature of a solvent influences the material's electromechanical response. For this series of experiments five solvents were originally selected. These solvents were to include: butyl acetate, acetonitrile, propylene carbonate, water and formamide which would yield a range in dielectric constant from 5.1 to 111 (with water serving as the baseline at 78.4). The study began with a population of 10 samples, all containing Li^+as the counterion and each sample solvated in water. Tests were performed on each sample in the population to determine a baseline response for each transducer. The samples were then dried and two samples were placed in each of the target solvent. Upon solvation, the surface conductivity of each transducer was measured, and it was determined that the propylene carbonate and formamide samples had swollen to the extent that they cracked their electrodes, rendering them useless in this study. Therefore, the test population was to consist of the samples in butyl acetate, acetonitrile and those rehydrated in water. The viscosity and dielectric properties of each solvent are tabulated in Table 3.1 and plotted in Figure 3.1.

From the solvents that yielded functional transducers, we were able to obtain a 52.4% and a 93.5% reduction

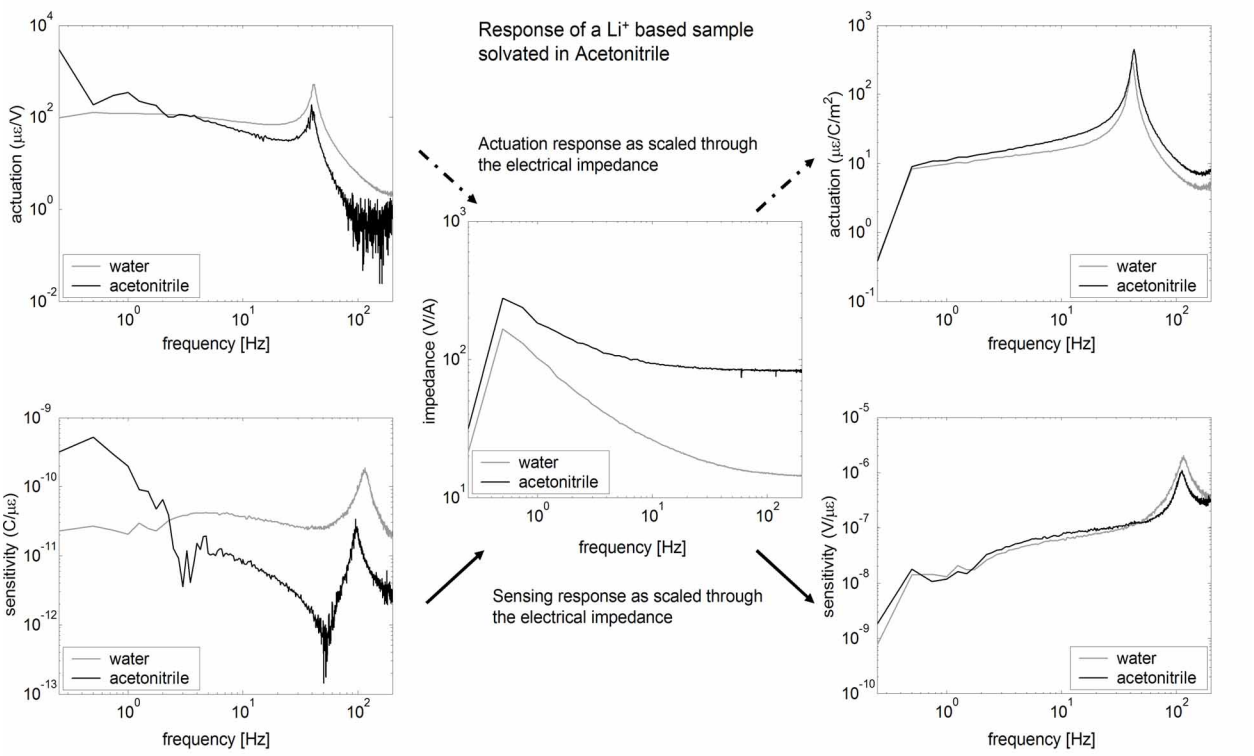

Figure 3.13: Frequency response for a sample solvated in water and acetonitrile.

in the solvent dielectric through the use of acetonitrile and butyl acetate, respectively. The first of these solvents that we will consider is acetonitrile. Figure 3.13 presents the actuation, sensing and impedance responses of a sample in both water and acetonitrile forms. As in each of the previous two studies, it is evident that the presence of acetonitrile influences each of the measured responses. This is most apparent in the sensing response which is markedly different than the baseline. However, this response collapses almost identically on top of the baseline response once each is normalized relative to their respective electrical impedances. This is also the case for the actuation response which exhibits a relatively noisy measured response that is much smoother once the electrical impedance is taken into account.

The effects of the impedance are also evident in the periodic excitation of the water and acetonitrile samples through a 1 volt, 1/4 Hz square wave. Figure 3.14 presents the actuation response of one sample to such a square wave excitation. The baseline response of the transducer is a fast initial response followed by the slow back relaxation that is characteristic of the hydrated Nafion^{TM} IPTs. Comparatively, the acetonitrile sample reacts with a much slower initial response, similar to that of the $TBA^{+}$and glycerol based samples of the previous study. The sample does not appear to relax within the period of this excitation.

The second solvent considered in this study was butyl acetate which has the lowest dielectric constant of

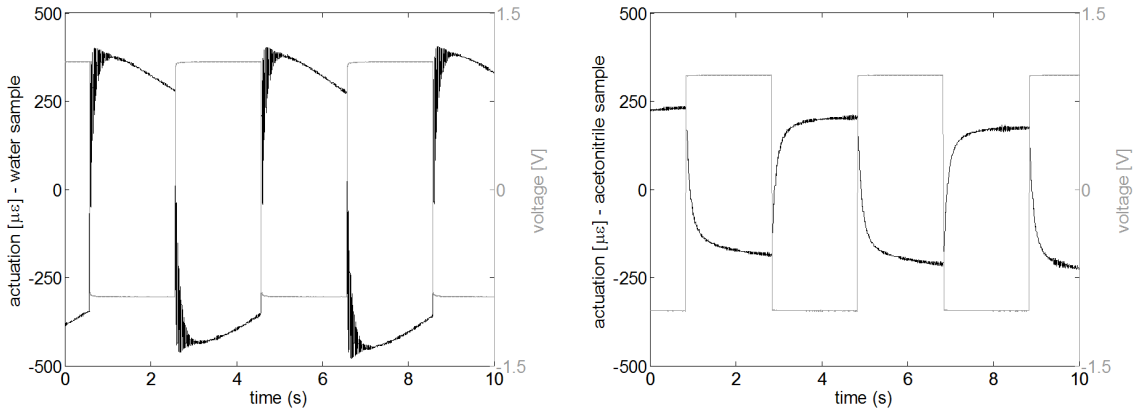

Figure 3.14: Time response for a sample solvated in water and acetonitrile.

any solvent considered for this test. The main obstacle in dealing with this solvent is the rapid rate with which it evaporates in open air. Therefore tests were performed quickly with fewer averages for each test run. The dielectric property of this material is approximately 15 times lower than that of water, with a dielectric constant of 5.1. Previous studies had investigated the swelling properties of this solvent on the Nafion$^{\mathrm{TM}}$ membrane, so we know beforehand that it would be possible to solvate the transducers with this solvent. Once the samples were prepared, the first series of tests were performed and an interesting result was observed in the material's frequency response. Figure 3.15 presents both sensing and actuation responses, and it can be seen from these results that a distinctive feature develops at low frequencies, with an antiresonance developing at 1 Hz. This feature was distinctive in each sample for both sensing and actuation. Additionally, the feature was not apparent in the V/I relationship. This fact indicates that the mechanism behind this low frequency occurrence lies in the $\mu\epsilon/C$ relationship, as shown in Figure 3.15. Currently we have been trying to reduplicate these experimental findings, however we have not been able to maintain good surface conductivity in the new samples we have tried to fabricate. This feature is something that offers a great deal of interest for our current research, however without more detailed measurements of the low frequency response it is difficult to draw any definitive conclusions.

When excited with a periodic excitation, the butyl acetate samples behave similarly to the acetonitrile samples, except that the initial response is even slower for the butyl acetate sample, as shown in Figure 3.16. Peak displacements for the butyl acetate sample are also much less than those measured for the baseline sample, which is expected given the frequency response of this transducer. Of each of the solvents successfully tested thus far in our analysis, butyl acetate offers the most promising response as it hints at a secondary mechanism that becomes more predominant in the presence of a solvent such as butyl acetate. More tests are planned on this solvent in the near future, which should hopefully provide more insight into the ionic polymer transducer.

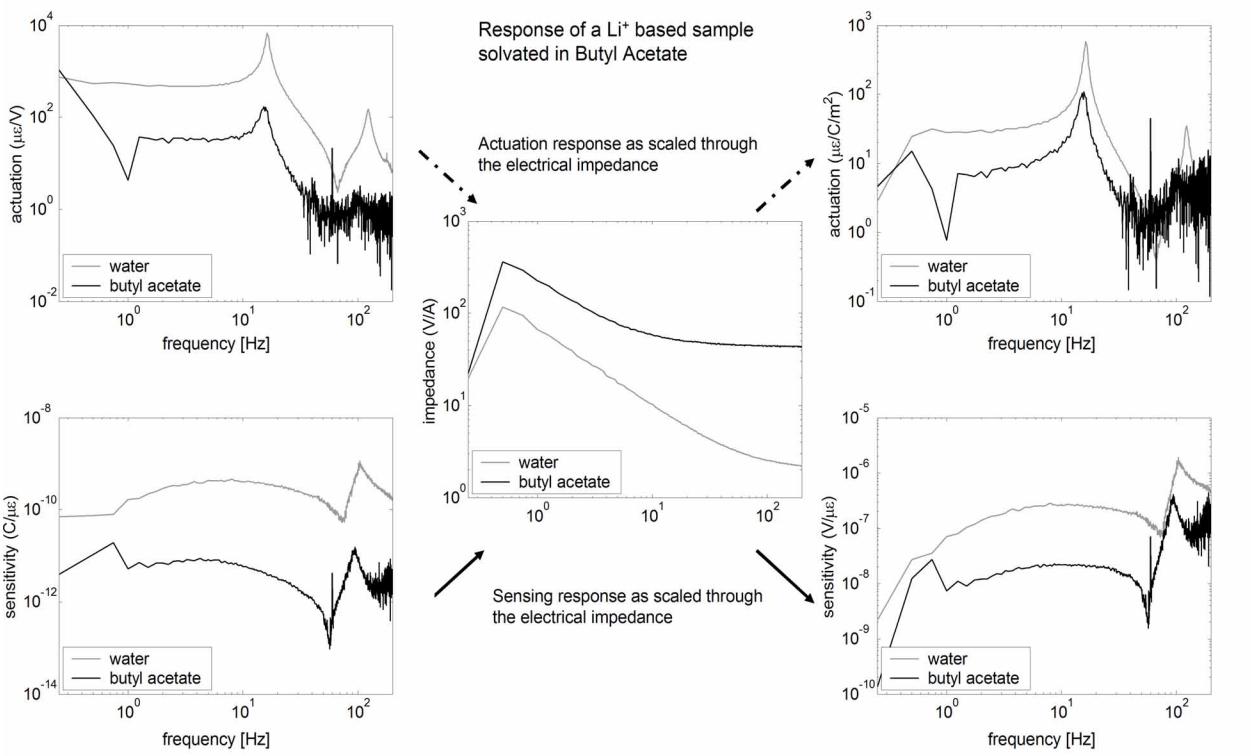

Figure 3.15: Frequency response for a sample solvated in water and butyl acetate.

3.2 Discussion - normalization by impedance

As discussed in the preceding sections, the polymer's internal impedance serves a critical role in determining the IPT's performance as an actuator or sensor. In this section comparisons are made between the measured and normalized responses of the cation, viscosity and dielectric studies. This comparison is meant to quantify the error in each study relative to their respective baseline samples. These comparisons are carried out for the measured frequency response functions. The comparison considers a comparison of the low frequency magnitude in the cation studies. Data was averaged over 1Hz to 9Hz for the target cation and their Li^+baseline responses. Δ Actuation

Table 3.3: Low frequency error in actuation and sensing responses for cation studies.

Cation	Δ Actuation ($\mu\epsilon/V$)		Δ Actuation ($\mu\epsilon/C/m^2$)		Δ Sensing 1E-11 ($C/\mu\epsilon$)		Δ Sensing 1E-9 ($V/\mu\epsilon$)	
Na^+	-30.71	(30.2%)	1.55	(23.4%)	5.00	(49.8%)	39.56	(61.1%)
Cs^+	-6.16	(4.9%)	-0.52	(7.2%)	1.99	(20.8%)	4.61	(7.2%)
Ca^{2+}	49.58	(36.9%)	0.64	(7.8%)	4.27	(43.2%)	11.05	(16.6%)
TBA^+	88.60	(81.9%)	-3.65	(38.1%)	9.26	(94.2%)	5.89	(5.9 %)

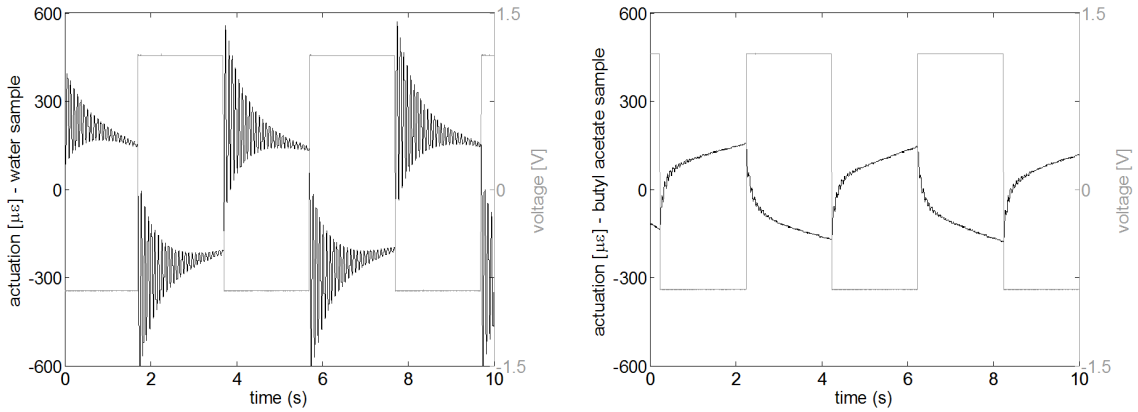

Figure 3.16: Time response for a sample solvated in water and butyl acetate.

and Δ Sensing are taken as the difference between these two averages, and the error is taken as this difference divided by Li^+average, i.e. $\left|\frac{Li^+ - Na^+}{Li^+}\right|$. These measurements are presented in Table 3.3. Comparing the error in the measured $(\mu\epsilon/V$ and $C/\mu\epsilon)$ and normalized $\left(\mu\epsilon/C/m^2\right.$ and $\left.V/\mu\epsilon\right)$ responses, it is seen that normalization generally reduces the error between the response of the target cation and its corresponding Li^+baseline response. There are two exceptions in this case: the sensing response of $Na^+$and the actuation response of Cs^+. In each of these cases the measured verses normalized error were relatively close. In the divalent and organic cations the low frequency error was reduced significantly through the normalization procedure, supporting our initial conclusions about the importance of the ionic polymer's electrical impedance.

The second comparison focuses on the low frequency slope in the actuation response for the glycerol samples, the organic cation samples and the test sample solvated in acetonitrile. The low frequency slope was fit from 1Hz to 10Hz for both the baseline and test sample. This was performed for both the measured and the normalized actuation response. Table 3.4 presents the information about these low frequency slopes. From these measurements

Table 3.4: Characterization of low frequency actuation response for viscosity, cation and solvent dielectric samples.

Condition	Measured Response $\left(\frac{\mu\epsilon/V}{\text{decade}}\right)$		Normalized Response $\left(\frac{\mu\epsilon/C/m^2}{\text{decade}}\right)$	
	baseline (H_2O, Li^+)	test sample	baseline (H_2O, Li^+)	test sample
60% glycerol	-0.02	-0.27	0.11	0.10
70% glycerol	-0.02	-0.47	0.11	0.23
80% glycerol	-0.02	-1.31	0.11	0.33
90% glycerol	-0.02	-0.54	0.11	0.45
TEA^+	0.70	-1.70	0.26	0.36
TBA^+	-16.40	-45.20	2.30	3.04
acetonitrile	-50.0	-216.00	11.10	6.30

it is clearly seen that the normalization causes the low frequency slope to converge toward the samples' respective baseline measurements. When taken in conjunction with the results from Table 3.3, these comparisons offer strong motivation for the analytical study of the impedance response that is presented next in Chapter 4.

3.3 Chapter summary

This chapter has focused on the ionic polymer's response as a function of counterion, solvent viscosity and solvent dielectric. Each study monitored the actuation, impedance and sensing response in both the time and frequency domain. In each case the Li^+ counterion was used as a baseline while water was used as the reference solvent. Frequency domain analysis showed that the transducer's sensitivity in both actuation and sensing were highly dependent upon changes in the ionomer's characteristic impedance. In the counterion study Li^+ produced the most sensitive transducer, while other counterions tended to increase the transducer's resistive nature, decreasing it's sensitivity in actuation and sensing studies. Higher solvent viscosities tended to soften the transducer, lowering it's mechanical impedance while also slowing the actuation response. Similar reductions were also seen in the sensing response. The dielectric property of the solvent was also found to be a key factor in determining the IPT's performance. Studies with acetonitrile and butyl-acetate showed significant reductions in the transducer's actuation and sensing response. In each study it was consistently seen that the polymer's response seemed to scale proportionately with respect to the polymer's electrical impedance. When normalized by the polymer's voltage to current relationship, experimental results began to coalesce on one another. This facet of the experimental study gives rise to the impedance modeling presented in next chapter.

Chapter 4

Modeling the impedance response

One of the principle results of our experimental study in Chapter 3 is that both sensing and actuation responses are governed by the motion of charge within the ionic polymer. Through each variation in counterion, solvent viscosity and solvent dielectric, we found that shifts in the actuation and sensing sensitivity could be directly correlated with changes in the polymer's electrical impedance. This result supports one of the basic tenets of our modeling approach: that both actuation and sensing responses rely on the same fundamental mechanism, and that this mechanism is tied directly to the motion of cations through the polymer membrane. Specifically, the chemical and physical composition of the ionomer membrane enables the polymer to behave as a transport membrane, and it is the effectiveness of this transport mechanism that governs how well the polymer operates as a transducer. In this manner transport theory is used to describe the cation motion that results when an ionic polymer is subject to an external electric potential. This chapter focuses on the development of an electrical impedance model, beginning with the development of general flux equations and developing these into steady-state models that describe the current and impedance response for step and harmonic excitations. Transport theory serves as the basis for this model, and the applied potential enters as a set of boundary conditions on the transport model. From the transport equations we continue our development as we derive expressions for the internal potential and charge density as fucntions of both step and harmonic excitations. Limits on these responses are also considered as we account for cation depletion near the anode. Nemat-Nasser [59] predicts the development of a saturation region near the anode as charge density approaches the level of the fixed anionic concentration, i.e. $\rho = -FC^{-}$. This model considers the saturation effect and quantifies the saturation voltage for a step input and a saturation curve for harmonic excitations that accounts for frequency and magnitude of the excitation signal.

In the harmonic case we extend the analysis to develop models for the surface charge and surface current as a function of the applied potential. Relating the induced current to the applied potential produces an impedance model of the IPT that is compared to equivalent RC models, as well as experimental data for an ionic polymer

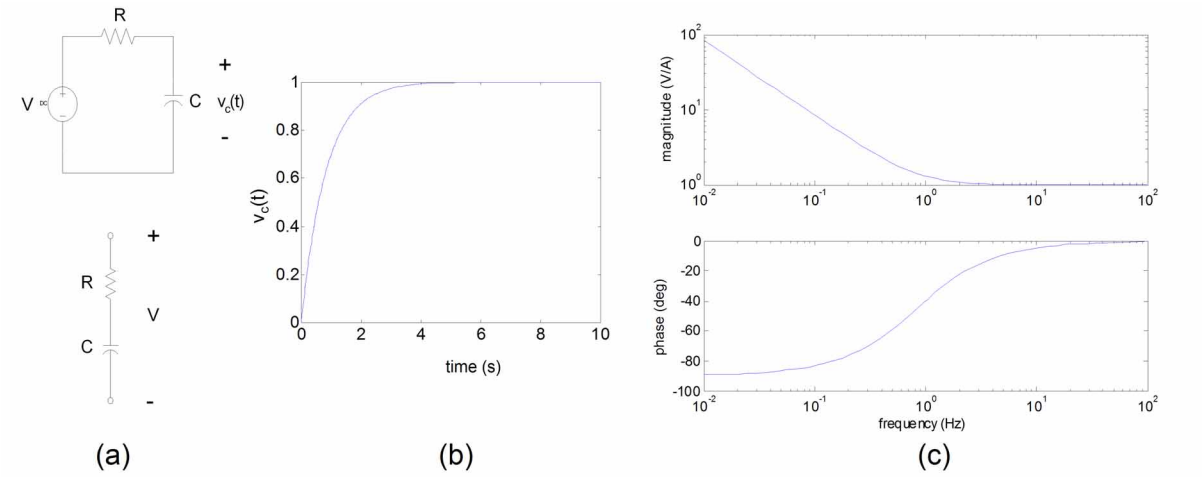

Figure 4.1: Simple circuit diagrams - (a) corresponds to a simple RC circuit while (b) corresponds to a simple electrical equivalent circuit for the ionic polymer transducer

transducer tested in the lab. The final section of this chapter considers the effect of parameter variations on the predicted impedance response. The effect of diffusion constant, electric permittivity and temperature are analyzed and discussed as they scale the transducer's impedance response as well as the effective time constant of the IPT.

4.1 Consider the simple RC model and analysis

Before we begin the impedance analysis of the ionic polymer, it would be beneficial to consider a set of RC models and examine how simple resistive and capacitive systems behave in the time and frequency domain. Such techniques have been used in numerous empirical models of the ionic polymer transducer. In 2003 Paquette *et al.* [73] developed an equivalent circuit model of the IPT using a parallel RC circuit to describe the upper and lower electrode regions and a purely resistive term to describe the bulk polymer. Newbury and Leo [66, 67] relied upon a transformer model to couple the sensing and actuation responses of the polymer. In 2004 Akle *et al.* [3, 2] presented a simple electrical impedance model of the IPT in an effort to quantify the capacitive nature of several ionomer based transducer.

In this part of the analysis we consider two RC models. The first of these models is shown in Figure 4.1a and respresents a set of RC components in series with one another. Performing a simple current summation on this circuit obtain the first order differential relationship,

$$C\frac{dv_c(t)}{dt} + \frac{v_c(t) - V}{R} = 0$$
$$RC\dot{v}_c(t) + v_c(t) = V$$

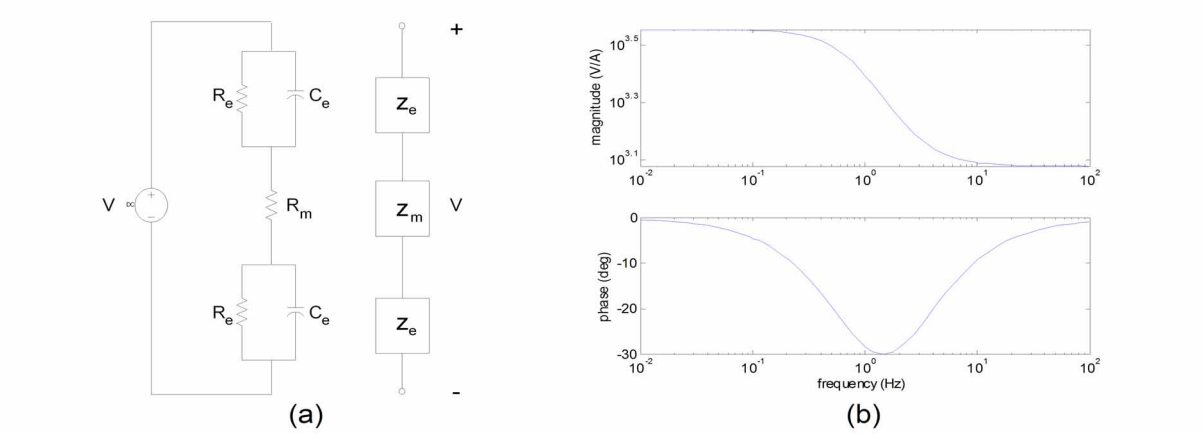

Figure 4.2: Simulate electrical impedance response of an RC circuit designed to emulate the IPT. Parameters were chosen as R_e = 1.2kΩ, C_e = 1 mF and R_m = 1.2kΩ.

Assuming that the voltage across the capacitor $v_c(t)$ is initially 0, the solution for $v_c(t)$ becomes,

$$v_c(t) = V - Ve^{-t/RC}$$

This solution describes the voltage response of the capacitor to a step change in the applied voltage V, and is shown in Figure 4.1b. As stated in the development this solution corresponds to the voltage developed within the capacitor. If we want to consider the voltage across the coupled RC components, we consider the arrangement shown in the lower plot of Figure 4.1a. Grouping these terms together, we formulate the voltage to current relationship that describes the overall impedance of the system,

$$V = (Z_R + Z_C)\, I = \left(R + \frac{1}{sC}\right) I$$
$$\frac{V}{I} = \frac{sRC + 1}{sC}$$

Figure 4.1c presents frequency response of the impedance profile. System values are taken as $R = 1.2\text{k}\Omega$ and $C = 1\text{mF}$. Analysis of the magnitude response indicates a low frequency decay that is attributed to the system pole at $s = 0$. From the phase response it is seen that the system responds accordingly, beginning with a phase response of -90^o and transitioning to 0^o following the corner frequency of the magnitude response.

In order to better simulate the actual IPT composition, we consider three predominant regions within the transducer: two regions that define the upper and lower electrode regions and one that constitutes the bulk polymer membrane. This model follows the same form as that posed by Paquette *et al.* [73] and is illustrated in Figure 4.2. The electrodes are modeled as simple parallel RC regions, while a purely resistive term comprising the bulk of the polymer. To proceed with our development we formulate an equivalent impedance model of these three regions.

$$Z_e = \frac{1}{\frac{1}{R_e} + j\omega C_e} = \frac{R_e}{1 + j\omega R_e C_e} \qquad\qquad Z_m = R_m$$

Combining each of these impedance components in series, we get a total relative impedance for the transducer,

$$\begin{aligned} Z_T &= 2Z_e + Z_m = \frac{2R_e}{1 + j\omega R_e C_e} + R_m = \frac{2R_e + R_m(1 + sR_eC_e)}{1 + sR_eC_e} \\ &= \frac{sR_mR_eC_e + 2R_e + R_m}{sR_eC_e + 1} \end{aligned}$$

This expression describes the frequency domain representation of the circuit models shown in Figure 4.2a. Looking at the actual frequency response, we notice that the system response begins with zero slope, then passes through a break frequency near 0.83 Hz and then begins to level off near 8.3 Hz. The phase response behaves accordingly with an expected notch in the phase that dips to -30^o at its lowest point. This type of response is indicative of transducers solvated in ionic liquid, where performance is predominantly in the lower frequency range below $\approx$ 10Hz.

The next several sections of this analysis delve into the impedance response of the IPT as derived from the electrostatic equations governing ion transport across membranes. Both step and harmonic excitations are considered and saturation effects are analyzed with respect to applied potential, as well as applied frequency in the case of a harmonic excitation. Modeling techniques focus on predicting the internal potential response relative to the imposed external potential. From this internal profile, charge density predictions are generated as well as models of the apparent surface current through analysis of the isothermal transient ionic current. This surface current is then used to develop frequency domain profiles of the IPT's electrical impedance, the results of which are then compared to experimental measurements.

4.2 Flux and Continuity Development

In the case of the impedance or actuation response of the polymer, the modeling approach begins by considering the physical equations that describe ion transport and ion motion through ion-exchange membranes. The first of these relationships is that of the ion flux used to describe the transport phenomena through membranes. Lakshminarayanaiah [44] defines four principle components that make up the overall flux through a ionically conductive membrane. The first of these flux terms is the result of diffusion, defined by the gradient of the chemical potential $\frac{\partial \hat{\varepsilon}_i}{\partial \hat{x}}$. This gives us the first flux term defined as,

$$\hat{J}_{i(d)} = \frac{d_i \hat{C}_i}{RT}\left(\frac{\partial \hat{\varepsilon}_i}{\partial \hat{x}}\right) \tag{4.1}$$

Lakshminarayanaiah goes on to rephrase this expression solely in terms of the ion concentration $\hat{C}_i$ by assuming that the solution is ideal and that the activity coefficient is constant. Thus, the diffusion induced flux can be written

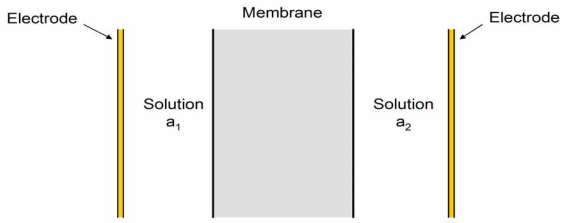

Figure 4.3: Membrane configuration used in the development of the transport equations

in the form,

$$\hat{J}_{i(d)} = -d_i \frac{\partial \hat{C}_i}{\partial \hat{x}}. \tag{4.2}$$

The second term considered in this analysis is the flux induced by an applied electric potential. When the membrane is under the influence of an external potential a corresponding flux develops in the form,

$$\hat{J}_{i(\hat{\phi})} = -d_i z_i \frac{F\hat{C}_i}{RT} \frac{\partial \hat{\phi}_i}{\partial \hat{x}} \tag{4.3}$$

In general transport theory two additional components are considered in the overall flux expression. If we look to the work of Lakshminarayanaiah we see that these components correspond to internal motion of free solvent within the membrane and an externally imposed pressure. The first of these terms corresponds to the flow of free solvent through the membrane, given by the expression

$$\hat{J}_{i(c)} = \hat{C}_i \hat{v}, \tag{4.4}$$

where the velocity term can be described by Darcy's Law

$$\hat{v} = k' \left(C^- FE - \frac{\partial \hat{p}}{\partial \hat{x}} \right). \tag{4.5}$$

Lakshminarayanaiah defines this flux term in the case of a membrane used to separate two distinct volumes of solution (illustrated in Figure 4.3). In this configuration ion motion can pull bound solvent molecules with it in the case of hydrophilic ions, while also pushing free solvent in front of it as the ion diffuses through the membrane. This flux term described in equation 4.4 corresponds to the motion of this free solvent. The fourth flux term considered in many transport models is the flux induced by an external force or pressure. This component is given by the

relationship

$$\hat{J}_{i(\hat{p})} = -d_i \frac{\hat{C}_i}{RT}\left[M_i\left(\frac{V_i}{M_i} - \frac{V_w}{M_w}\right)\right]\frac{\partial \hat{p}}{\partial \hat{x}} \tag{4.6}$$

where we had previously defined the term ΔV to be $M_i\left(\frac{V_i}{M_i} - \frac{V_w}{M_w}\right)$. Thus, once all of these terms are combined we obtain a total ion flux expression,

$$\hat{J}_i \quad = \quad \hat{J}_{i(c)} + \hat{J}_{i(d)} + \hat{J}_{i(\hat{\phi})} + \hat{J}_{i(\hat{p})} \tag{4.7}$$

or in more explicit terms,

$$\hat{J}_i \quad = \quad \hat{C}_i\hat{v} - d_i\left(\frac{\partial \hat{C}_i}{\partial \hat{x}} + z_i\frac{F\hat{C}_i}{RT}\frac{\partial \hat{\phi}_i}{\partial \hat{x}} + \frac{\hat{C}_i}{RT}\left[M_i\left(\frac{V_i}{M_i} - \frac{V_w}{M_w}\right)\right]\frac{\partial \hat{p}}{\partial \hat{x}}\right) \tag{4.8}$$

For the Nafion membrane there is only one mobile ion species, allowing us to simplify this expression to

$$\hat{J} \quad = \quad \hat{C}^+\hat{v} - d\left(\frac{\partial \hat{C}^+}{\partial \hat{x}} + \frac{F\hat{C}^+}{RT}\frac{\partial \hat{\phi}}{\partial \hat{x}} + \frac{\Delta V\hat{C}^+}{RT}\frac{\partial \hat{p}}{\partial \hat{x}}\right), \tag{4.9}$$

As an additional simplification, we assume that the motion of free water within the IPT is negligible. Thus we can simplify equation 4.9 to

$$\hat{J} \quad = \quad -d\left(\frac{\partial \hat{C}^+}{\partial \hat{x}} + \frac{F\hat{C}^+}{RT}\frac{\partial \hat{\phi}}{\partial \hat{x}} + \frac{\Delta V\hat{C}^+}{RT}\frac{\partial \hat{p}}{\partial \hat{x}}\right), \tag{4.10}$$

In terms of the actuation response we must also consider how relevant the external pressure term is to the transducer. Since we are dealing primarily with the cantilevered IPT samples, we can assume that no external pressure is imposed on the membrane, making the pressure induced flux negligible as well. Thus, the full form of the flux expression to be considered in this derivation will have the form,

$$\hat{J} = -d\frac{\partial \hat{C}^+}{\partial \hat{x}} - d\frac{F\hat{C}^+}{RT}\frac{\partial \hat{\phi}}{\partial \hat{x}} \tag{4.11}$$

From this expression it can be seen that the ion flux depends on the spatial variation of cations as well as the interaction between the cation distribution and the spatial variation of the internal potential. With regard to analysis, it is best to rephrase this flux expression in terms of the potential function $\hat{\phi}$. To accomplish this we begin by imposing the definition of charge density, $\hat{\rho} = F(\hat{C}^+ - C^-)$ to transform the flux relationship into terms of

charge density and potential,

$$\hat{J} = -\frac{d}{F}\frac{\partial \hat{\rho}}{\partial \hat{x}} - \frac{d}{RT}\hat{\rho}\frac{\partial \hat{\phi}}{\partial \hat{x}} - \frac{dFC^-}{RT}\frac{\partial \hat{\phi}}{\partial \hat{x}} \tag{4.12}$$

Looking closely at this expression for the ion flux, we see that it is composed of a term related to the spatial gradient of the charge density $\frac{\partial \hat{\rho}}{\partial \hat{x}}$, the gradient of the electric potential $\frac{\partial \hat{\phi}}{\partial \hat{x}}$, and the interaction between the charge density and the electric potential gradient $\hat{\rho} \cdot \frac{\partial \hat{\phi}}{\partial \hat{x}}$. This relationship can offer some interesting insight into the transducer model that we are considering. Since the IPT is plated with two gold electrodes at the upper and lower surfaces, we assume that the transducer represents a closed system. Specifically, this imposes a condition that ion flux must be zero at the electrodes, i.e. ions cannot enter or leave the system through the electrode layer. Thus, if we formulate this condition analytically, we see that the charge density and electric field will be related at the electrode interface through the expression

$$\frac{\partial \hat{\rho}}{\partial \hat{x}} + \frac{F^2C^-}{RT}\frac{\partial \hat{\phi}}{\partial \hat{x}}\bigg|_{x=0,L} = \frac{-F}{RT}\hat{\rho}\frac{\partial \hat{\phi}}{\partial \hat{x}}\bigg|_{x=0,L} \tag{4.13}$$

At this point we continue our development of the flux by continuing our development toward a flux expression solely in terms of the internal potential $\hat{\phi}$. To accomplish this we consider the field relationships that relate charge density, electric field, electric displacement and electric potential. These relationships have the form

$$\begin{aligned} \mathbf{E} &= \tfrac{\mathbf{D}}{\kappa} \qquad & \mathbf{E} &= -\nabla\hat{\phi} \\ \nabla\mathbf{D} &= \hat{\rho} \qquad & \hat{\rho} &= \kappa\nabla\mathbf{E} \end{aligned} \tag{4.14}$$

From these expressions we can define the charge density in terms of potential so that $\hat{\rho} = -\kappa\nabla^2\hat{\phi}$, allowing us to rephrase equation 4.12 as,

$$\begin{aligned} \hat{J} &= \frac{d\kappa}{F}\frac{\partial^3\hat{\phi}}{\partial\hat{x}^3} + \frac{d\kappa}{RT}\frac{\partial^2\hat{\phi}}{\partial\hat{x}^2}\cdot\frac{\partial\hat{\phi}}{\partial\hat{x}} - \frac{dFC^-}{RT}\frac{\partial\hat{\phi}}{\partial\hat{x}} \\ &= \frac{d\kappa}{F}\left(\frac{\partial^3\hat{\phi}}{\partial\hat{x}^3} + \frac{F}{RT}\left[\frac{\partial^2\hat{\phi}}{\partial\hat{x}^2}\cdot\frac{\partial\hat{\phi}}{\partial\hat{x}}\right] - \frac{F^2C^-}{\kappa RT}\frac{\partial\hat{\phi}}{\partial\hat{x}}\right) \end{aligned} \tag{4.15}$$

Thus, we have formulated an expression for ion flux that relies solely on internal potential and material and environmental properties. However for an expression that defines the transport properties of the IPT, we want to understand the rate of cation motion within the polymer membrane. Therefore we define our governing partial differential equation to be the continuity relationship which relates the rate of ion motion to the gradient of the ion

flux, expressed as

$$-\frac{\partial \hat{C}^{+}}{\partial \hat{t}} \quad = \quad \nabla \hat{J} \tag{4.16}$$

It can be seen in this expression that we need to determine the gradient of the flux through the polymer thickness. Therefore we differentiate equation 4.15 to obtain,

$$\frac{\partial \hat{J}}{\partial \hat{x}} \quad = \quad \frac{d\kappa}{F}\left(\frac{\partial^4 \hat{\phi}}{\partial \hat{x}^4} + \frac{F}{RT}\left[\frac{\partial^3 \hat{\phi}}{\partial \hat{x}^3}\cdot\frac{\partial \hat{\phi}}{\partial \hat{x}} + \frac{\partial^2 \hat{\phi}}{\partial \hat{x}^2}\cdot\frac{\partial^2 \hat{\phi}}{\partial \hat{x}^2}\right] - \frac{F^2 C^{-}}{\kappa RT}\frac{\partial^2 \hat{\phi}}{\partial \hat{x}^2}\right) \tag{4.17}$$

Since the anion concentration is constant with space and time, we can write the rate of cation motion as $\frac{\partial \hat{C}^{+}}{\partial \hat{t}} = \frac{1}{F}\frac{\partial \hat{\rho}}{\partial \hat{t}}$. From this we can impose the field relationship between charge density and electric potential to express the rate term as $\frac{\partial \hat{C}^{+}}{\partial \hat{t}} = \frac{-\kappa}{F}\frac{\partial}{\partial \hat{t}}\left[\frac{\partial^2 \hat{\phi}}{\partial \hat{x}^2}\right]$. This produces a continuity expression that has the form

$$\frac{\kappa}{F}\frac{\partial}{\partial \hat{t}}\left[\frac{\partial^2 \hat{\phi}}{\partial \hat{x}^2}\right] - \frac{d\kappa}{F}\left(\frac{\partial^4 \hat{\phi}}{\partial \hat{x}^4} + \frac{F}{RT}\left[\frac{\partial^3 \hat{\phi}}{\partial \hat{x}^3}\cdot\frac{\partial \hat{\phi}}{\partial \hat{x}} + \frac{\partial^2 \hat{\phi}}{\partial \hat{x}^2}\cdot\frac{\partial^2 \hat{\phi}}{\partial \hat{x}^2}\right] - \frac{F^2 C^{-}}{\kappa RT}\frac{\partial^2 \hat{\phi}}{\partial \hat{x}^2}\right) \quad = \quad 0 \tag{4.18}$$

Multiplying through by $\frac{\kappa}{F}$ and defining $\gamma^2 = \frac{F^2 C^{-}}{\kappa RT}$,

$$\frac{\partial}{\partial \hat{t}}\left[\frac{\partial^2 \hat{\phi}}{\partial \hat{x}^2}\right] - d\frac{\partial^4 \hat{\phi}}{\partial \hat{x}^4} - \frac{dF}{RT}\left[\frac{\partial^3 \hat{\phi}}{\partial \hat{x}^3}\cdot\frac{\partial \hat{\phi}}{\partial \hat{x}} + \frac{\partial^2 \hat{\phi}}{\partial \hat{x}^2}\cdot\frac{\partial^2 \hat{\phi}}{\partial \hat{x}^2}\right] + d\gamma^2\frac{\partial^2 \hat{\phi}}{\partial \hat{x}^2} = 0 \tag{4.19}$$

This describes the full nonlinear expression in terms of electric potential. In the actuation response this equation is subject to applied nonhomogeneous potential boundary conditions,

$$\hat{\phi}(\hat{x},\hat{t})\Big|_{\hat{x}=0} = \hat{\Phi}_1(\hat{t}) \qquad \hat{\phi}(\hat{x},\hat{t})\Big|_{\hat{x}=L} = \hat{\Phi}_2(\hat{t}), \tag{4.20}$$

the homogeneous flux boundary conditions

$$\begin{aligned}
\frac{d\kappa}{F}\left(\frac{\partial^3 \hat{\phi}}{\partial \hat{x}^3} + \frac{F}{RT}\left[\frac{\partial^2 \hat{\phi}}{\partial \hat{x}^2}\cdot\frac{\partial \hat{\phi}}{\partial \hat{x}}\right] - \frac{F^2 C^{-}}{\kappa RT}\frac{\partial \hat{\phi}}{\partial \hat{x}}\right)\Bigg|_{\hat{x}=0} &= 0, \quad \text{and} \\
\frac{d\kappa}{F}\left(\frac{\partial^3 \hat{\phi}}{\partial \hat{x}^3} + \frac{F}{RT}\left[\frac{\partial^2 \hat{\phi}}{\partial \hat{x}^2}\cdot\frac{\partial \hat{\phi}}{\partial \hat{x}}\right] - \frac{F^2 C^{-}}{\kappa RT}\frac{\partial \hat{\phi}}{\partial \hat{x}}\right)\Bigg|_{\hat{x}=L} &= 0,
\end{aligned} \tag{4.21}$$

as well as the initial condition

$$-\kappa\,\frac{\partial^2 \hat{\phi}(x,t)}{\partial \hat{x}^2}\Bigg|_{\hat{t}=0} = 0 \tag{4.22}$$

This produces the nonlinear form of the continuity expression. At this point we will consider non-dimensionalizing the system.

4.3 System in nondimensional form

In the system defined by equation 4.19 $\hat{\phi}$ represents the dependent variable while $\hat{t}$ and $\hat{x}$ are the independent variables. For the length scale we will define the polymer thickness L to be the characteristic length. Similarly, we define the time constant λ to be equal to the characteristic time of the PDE $\frac{dF^2C^-}{\kappa RT}$. The potential will be normalized by the maximum applied potential $\Phi_m = \left| \hat{\Phi}_2 - \hat{\Phi}_1 \right|$. Thus, we define the dimensionless variables according to

$$\phi = \frac{\hat{\phi}}{\Phi_m} \qquad x = \frac{\hat{x}}{L} \qquad t = \lambda \hat{t} \tag{4.23}$$

From this we define the derivatives of interest to be

$$\begin{aligned}
\frac{\partial \hat{\phi}}{\partial \hat{x}} &= \frac{\partial(\Phi_m \phi)}{\partial x}\frac{\partial x}{\partial \hat{x}} &&= \frac{\Phi_m}{L}\frac{\partial \phi}{\partial x} \\
\frac{\partial^2 \hat{\phi}}{\partial \hat{x}^2} &= \frac{\partial^2(\Phi_m \phi)}{\partial x^2}\left(\frac{\partial x}{\partial \hat{x}}\right)^2 &&= \frac{\Phi_m}{L^2}\frac{\partial^2 \phi}{\partial x^2} \\
&\vdots \\
\frac{\partial}{\partial \hat{t}}\left(\frac{\partial^2 \hat{\phi}}{\partial \hat{x}^2}\right) &= \frac{\partial}{\partial t}\left[\frac{\Phi_m}{L^2}\frac{\partial^2 \phi}{\partial x^2}\right]\frac{\partial t}{\partial \hat{t}} &&= \frac{\Phi_m \lambda}{L^2}\frac{\partial}{\partial t}\left(\frac{\partial^2 \phi}{\partial x^2}\right)
\end{aligned}$$

Based upon these derivatives, we can rephrase equation 4.19 as

$$\frac{\Phi_m \lambda}{L^2}\frac{\partial}{\partial t}\left(\frac{\partial^2 \phi}{\partial x^2}\right) - \frac{d\Phi_m}{L^4}\frac{\partial^4 \phi}{\partial x^4} - \frac{dF}{RT}\frac{\Phi_m^2}{L^4}\left[\frac{\partial^3 \phi}{\partial x^3}\frac{\partial \phi}{\partial x} + \left(\frac{\partial^2 \phi}{\partial x^2}\right)^2\right] + \frac{d\gamma^2 \Phi_m}{L^2}\frac{\partial^2 \phi}{\partial x^2} = 0 \tag{4.24}$$

At this point, we express the time constant λ as $\frac{dF^2C^-}{\kappa RT}$ or $d\gamma^2$, and divide through by the first coefficient. This yields the equation,

$$\frac{\partial}{\partial t}\left(\frac{\partial^2 \phi}{\partial x^2}\right) - \epsilon\frac{\partial^4 \phi}{\partial x^4} - \epsilon\frac{F\Phi_m}{RT}\left[\frac{\partial^3 \phi}{\partial x^3}\frac{\partial \phi}{\partial x} + \left(\frac{\partial^2 \phi}{\partial x^2}\right)^2\right] + \frac{\partial^2 \phi}{\partial x^2} = 0 \tag{4.25}$$

where ϵ is the dimensionless parameter defined as $\frac{1}{L^2\gamma^2}$. With this, we next consider formulating the boundary conditions for this problem. Beginning with the electrical potential conditions at the electrodes, we find that,

$$\phi|_{x=0} = \frac{\hat{\Phi}_1(t)}{\Phi_m} \quad \text{and} \quad \phi|_{x=1} = \frac{\hat{\Phi}_2(t)}{\Phi_m} \tag{4.26}$$

where Φ_m was defined as $\left|\hat{\Phi}_2 - \hat{\Phi}_1\right|$. Similarly we can consider the transformed flux boundary condition, formulating it as

$$\begin{aligned} \frac{d\kappa\gamma^2\Phi_m}{FL}\left(\epsilon\frac{\partial^3\phi}{\partial x^3} + \epsilon\frac{F\Phi_m}{RT}\left[\frac{\partial^2\phi}{\partial x^2}\cdot\frac{\partial\phi}{\partial x}\right] - \frac{\partial\phi}{\partial x}\right)\Bigg|_{x=0} &= 0, \quad \text{and} \\ \frac{d\kappa\gamma^2\Phi_m}{FL}\left(\epsilon\frac{\partial^3\phi}{\partial x^3} + \epsilon\frac{F\Phi_m}{RT}\left[\frac{\partial^2\phi}{\partial x^2}\cdot\frac{\partial\phi}{\partial x}\right] - \frac{\partial\phi}{\partial x}\right)\Bigg|_{x=1} &= 0 \end{aligned} \tag{4.27}$$

Likewise, the nondimensional initial condition will have the form

$$\frac{-\kappa\Phi_m}{L^2}\frac{\partial^2\phi}{\partial x^2}\Bigg|_{t=0} = 0 \tag{4.28}$$

Using a short hand notation we rewrite the problem in the form

$$\frac{\partial\phi^{''}}{\partial t} - \epsilon\phi^{iv} - \epsilon N_2\left[\phi^{'''}\phi^{'} + \left(\phi^{''}\right)^2\right] + \phi^{''} = 0 \tag{4.29}$$

which is subject to the boundary conditions

$$x = 0 \rightarrow \qquad \phi = \Phi_1, \quad \text{and} \quad N_1\left(\epsilon\phi^{'''} + \epsilon N_2\left[\phi^{''}\phi^{'}\right] - \phi^{'}\right) = 0, \tag{4.30}$$

$$x = 1 \rightarrow \qquad \phi = \Phi_2, \quad \text{and} \quad N_1\left(\epsilon\phi^{'''} + \epsilon N_2\left[\phi^{''}\phi^{'}\right] - \phi^{'}\right) = 0 \tag{4.31}$$

where the terms N_1, N_2, Φ_1 and Φ_2 are defined as

$$N_1 = \frac{d\kappa\gamma^2\Phi_m}{FL} \qquad N_2 = \frac{F\Phi_m}{RT} \qquad \Phi_1 = \frac{\hat{\Phi}_1(t)}{\Phi_m} \qquad \Phi_2 = \frac{\hat{\Phi}_2(t)}{\Phi_m} \tag{4.32}$$

4.3.1 Linear modeshapes and frequencies

Dropping the nonlinear and forcing terms from equations 4.29-4.36, and assuming a single mode expotential decay for the solution,

$$\phi(x,t) = \varphi(x)e^{-\alpha t} \tag{4.33}$$

we obtain the linear eigenvalue problem

$$\begin{aligned} \epsilon\varphi^{iv} + (\alpha - 1)\varphi^{''} &= 0 \\ \varphi^{iv} + \beta^2\varphi^{''} &= 0 \end{aligned} \tag{4.34}$$

where $\beta = \frac{(\alpha-1)}{\epsilon}$. Similarly the boundary conditions become,

$$x = 0 \rightarrow \qquad \varphi = 0, \quad \text{and} \quad N_1\left(\epsilon\varphi^{'''} - \varphi^{'}\right) = 0 \tag{4.35}$$

$$x = 1 \rightarrow \qquad \varphi = 0, \quad \text{and} \quad N_1\left(\epsilon\varphi^{'''} - \varphi^{'}\right) = 0 \tag{4.36}$$

The general solution to equation 4.34 has the form,

$$\varphi(x) = \frac{-a_1}{\beta^2}\sin(\beta x) - \frac{a_2}{\beta^2}\cos(\beta x) + a_3 x + a_4 \tag{4.37}$$

which has the cooresponding derivatives,

$$\begin{aligned} \varphi^{'}(x) &= \frac{-a_1}{\beta}\cos(\beta x) + \frac{a_2}{\beta}\sin(\beta x) + a_3, & \varphi^{''}(x) &= a_1\sin(\beta x) + a_2\cos(\beta x) \\ \varphi^{'''}(x) &= a_1\beta\cos(\beta x) - a_2\beta\sin(\beta x), & \varphi^{iv}(x) &= -a_1\beta^2\sin(\beta x) - a_2\beta^2\cos(\beta x) \end{aligned}$$

At this point we can consider the boundary values/ boundary conditions imposed on the system. Beginning with the potential boundary condition at $x = 0$, we find

$$\begin{aligned} \varphi(0) &= \frac{-a_1}{\beta^2}\sin(0) - \frac{a_2}{\beta^2}\cos(0) + a_3 0 + a_4 = 0 = -\frac{a_2}{\beta^2}\cos(0) + a_4 \\ &\Longrightarrow a_4 = \frac{a_2}{\beta^2} \end{aligned} \tag{4.38}$$

Substituting this into the second boundary condition at $x = 1$

$$\begin{aligned} \varphi(1) &= \frac{-a_1}{\beta^2}\sin(\beta) - \frac{a_2}{\beta^2}\cos(\beta) + a_3 + a_4 = \frac{-a_1}{\beta^2}\sin(\beta) - \frac{a_2}{\beta^2}\cos(\beta) + a_3 + \frac{a_2}{\beta^2} \\ &= \frac{-a_1}{\beta^2}\sin(\beta) + \frac{a_2}{\beta^2}\left(1 - \cos(\beta)\right) + a_3 \end{aligned} \tag{4.39}$$

Next we consider the flux boundary conditions, beginning at $x = 0$

$$\begin{aligned} J(0) &= a_1\epsilon\beta\cos(0) - a_2\epsilon\beta\sin(0) + \frac{a_1}{\beta}\cos(0) - \frac{a_2}{\beta}\sin(0) - a_3 = 0 \\ &= \frac{a_1}{\beta}\left(\epsilon\beta^2 + 1\right) - a_3 = 0 \\ &\Longrightarrow a_3 = \frac{a_1}{\beta}\left(\epsilon\beta^2 + 1\right) \end{aligned} \tag{4.40}$$

Substituting this and the result from equation 4.38 into the second flux boundary condition at $x = 1$ we find

$$\begin{aligned} J(1) &= a_1\epsilon\beta\cos(\beta) - a_2\epsilon\beta\sin(\beta) + \frac{a_1}{\beta}\cos(\beta) - \frac{a_2}{\beta}\sin(\beta) - a_3 = 0 \\ &= \frac{a_1}{\beta}\left(\epsilon\beta^2+1\right)\cos(\beta) - \frac{a_2}{\beta}\left(\epsilon\beta^2+1\right)\sin(\beta) - a_3 \\ &= \frac{a_1}{\beta}\left(\epsilon\beta^2+1\right)(\cos(\beta)-1) - \frac{a_2}{\beta}\left(\epsilon\beta^2+1\right)\sin(\beta) \\ &\implies a_2 = a_1\frac{\cos(\beta)-1}{\sin(\beta)} \end{aligned} \tag{4.41}$$

At this point it is helpful to use the half-angle identities to establish the identity

$$\tan(\beta/2) = \frac{1-\cos(\beta)}{\sin(\beta)} \tag{4.42}$$

Throughout the rest of this derivation we will interchange these expressions to take advantage when simplifying other expressions. With this we can rephrase coefficients $a_2 - a_4$ in terms of a_1,

$$a_2 = -a_1\tan(\beta/2), \qquad a_3 = \frac{a_1}{\beta}\left(\epsilon\beta^2+1\right), \qquad a_4 = \frac{-a_1}{\beta^2}\tan(\beta/2) \tag{4.43}$$

Substituting this into the second boundary potential boundary condition at $x = 1$ we have

$$\begin{aligned} \varphi(1) &= \frac{-a_1}{\beta^2}\sin(\beta) + \frac{a_2}{\beta^2}(1-\cos(\beta)) + a_3 = 0 \\ &= a_1\left(\frac{-\sin^2(\beta) + 2\cos(\beta) - \cos^2(\beta) - 1}{\beta^2\sin(\beta)} + \frac{\epsilon\beta^2+1}{\beta}\right) \\ &= \frac{-a_1}{\beta^2}\left(2\tan(\beta/2) - \beta\left(\epsilon\beta^2+1\right)\right) \end{aligned} \tag{4.44}$$

Since this must equal zero, either a_1 or the transcendental expression in β must be zero. Assuming that $a_1 \neq 0$ we can divide through by this term and develop the transcendental relationship for β

$$\tan\left(\frac{\beta}{2}\right) = \frac{\beta\left(\epsilon\beta^2+1\right)}{2} \tag{4.45}$$

Substituting this back into our expression for the $\varphi(x)$ we get

$$\begin{aligned} \varphi(x) &= \frac{-a_1}{\beta^2}\sin\beta x - a_1\frac{\cos\beta - 1}{\beta^2\sin\beta}\cos\beta x + a_1\frac{\epsilon\beta^2+1}{\beta}x + a_1\frac{\cos\beta-1}{\beta^2\sin\beta} \\ &= \frac{a_1}{\beta^2}\left[-\sin\beta x - \frac{\cos\beta-1}{\sin\beta}\cos\beta x + \beta\left(\epsilon\beta^2+1\right)x + \frac{\cos\beta-1}{\sin\beta}\right] \\ &= \frac{-a_1}{\beta^2}\left[\sin\beta x + \frac{\cos\beta-1}{\sin\beta}(\cos\beta x - 1) - \beta\left(\epsilon\beta^2+1\right)x\right] \end{aligned} \tag{4.46}$$

We can use the half-angle identities again, along with the transcendental relationship for β to further compress the $\varphi(x)$ expression to

$$\varphi(x) = \frac{-a_1}{\beta^2}\left[\sin(\beta x) - \tan\left(\frac{\beta}{2}\right)(2x + \cos(\beta x) - 1)\right] \tag{4.47}$$

Since the original PDE is contains the highest of 4^{th} order with the lowest of 2^{nd} order, we normalize this expression such that

$$N = \int_0^1 \varphi_n^{''}(x) \cdot \varphi_n^{''}(x)dx = 1 \tag{4.48}$$

thus the constant a_1 will have the form

$$a_n = \frac{1}{\sqrt{N}} = \sqrt{\frac{2\beta_n \cos^2\frac{\beta_n}{2}}{\beta_n - \sin\beta_n}} \tag{4.49}$$

This produces a set of modeshapes of the form

$$\varphi_n(x) = \frac{-1}{\beta_n^2}\sqrt{\frac{2\beta_n \cos^2\frac{\beta_n}{2}}{\beta_n - \sin\beta_n}}\left[\sin(\beta x) - \tan\left(\frac{\beta}{2}\right)(2x + \cos(\beta x) - 1)\right] \tag{4.50}$$

4.3.2 Extending the analysis to include the temporal component

With the spatial component solved for for $\varphi(x)$ the next step is to incorporate the temporal component and solve for the total solution. To accomplish this we recognize that the normalization procedure performed in equation 4.48 produces a set of orthogonal modeshapes when considering a modal analysis of the original PDE. Therefore we can denote the total solution as a set of matrix equations which correspond to the modal problem given as

$$\mathbf{A}\frac{\partial\eta(t)}{\partial t} - \mathbf{B}\eta(t) = 0 \tag{4.51}$$

where the coefficients of the $\mathbf{A}$ and $\mathbf{B}$ matrices are given as

$$\begin{aligned} a_{mn} &= \int_{-h}^{h} \hat{\varphi}_m^{''}(x)\hat{\varphi}_n^{''}(x)dx \\ b_{mn} &= d\int_{-h}^{h} \hat{\varphi}_m^{''}(x)\left(\hat{\varphi}_n^{iv}(x) - \gamma^2\hat{\varphi}_n^{''}(x)\right)dx \end{aligned}$$

Rearranging the matrix equations, we find that

$$\frac{\dot{\eta}(t)}{\eta(t)} = \mathbf{A}^{-1}\mathbf{B} \tag{4.52}$$

Since this is a first order PDE, the solution will be an exponential function $e^{-\lambda t}$. Thus the fraction $\frac{\dot{\eta}(t)}{\eta(t)}$ becomes $\frac{-\lambda e^{-\lambda t}}{e^{-\lambda t}} = -\lambda$. This indicates that the time constants will be

$$\lambda = -\mathbf{A}^{-1}\mathbf{B} \tag{4.53}$$

In the case of the x-scaling from $0 \leq x \leq L$ the matrix $\mathbf{A}^{-1}\mathbf{B}$ is diagonal. Thus the time constants associated with the individual modes are taken as the diagonal terms of the $\mathbf{A}^{-1}\mathbf{B}$ matrix. From this we get the solution

$$\begin{aligned}
\phi_h(x,t) &= \sum_{n=1}^{\infty} \varphi_n(x)\eta(t) \\
&= \sum_{n=1}^{\infty} \frac{-1}{\beta_n^2} \sqrt{\frac{2\beta_n \cos^2\left(\frac{\beta_n}{2}\right)}{\beta_n - \sin\beta_n}} \left[\sin(\beta_n x) - \tan\left(\frac{\beta_n}{2}\right)(2x + \cos(\beta_n x) - 1)\right] e^{-\lambda_n t}
\end{aligned} \tag{4.54}$$

Similarly, we will formulate the charge density relationship as the second spatial derivative of electric potential,

$$\begin{aligned}
\rho_h(x,t) &= \frac{-\kappa\Phi_m}{L^2} * \frac{\partial^2\phi(x,t)}{\partial x^2} \\
&= \frac{\kappa\Phi_m}{L^2} \sum_{n=1}^{\infty} \sqrt{\frac{2\beta_n \cos^2\left(\frac{\beta_n}{2}\right)}{\beta_n - \sin\beta_n}} \left[-\sin(\beta_n x) + \tan\left(\frac{\beta_n}{2}\right)\cos(\beta_n x)\right] e^{-\lambda_n t}
\end{aligned} \tag{4.55}$$

As in the previous derivations, this linear component diverges as additional modes are included in the summation. This feature is due to the nature of the multiplier coefficient

$$\sqrt{\frac{2\beta_n \cos^2\left(\frac{\beta_n}{2}\right)}{\beta_n - \sin\beta_n}} \tag{4.56}$$

Taking the limit of this coefficient indicates that it is periodic, varying in magnitude between 0 and $\sqrt{2}$. Therefore, modes associated with higher eigenvalues continually add to the charge density function. This amplification is predominantly seen in the boundary layer.

4.4 Steady-state response - step excitation

Due to the divergent nature of the charge density from the transient analysis, we shift our focus to consider the steady-state response of the IPT. The goal of this analysis is to examine the accumulation of charge density at steady state as a function of the applied potential, and to examine saturation limits we expect to develop at higher levels of applied voltage. In this manner we begin our analysis by again considering the linearized system, represented by

the equation,

$$\frac{\partial \phi^{''}}{\partial t} - \epsilon \phi^{iv} + \phi^{''} = 0 \tag{4.57}$$

In the steady-state analysis the time varying component disappears, leaving us with the fourth order PDE

$$-\epsilon \phi^{iv} + \phi^{''} = 0 \tag{4.58}$$

Since we are dealing with a linearized system, we assume that separation of variables still holds. Therefore, we define the potential function to be of the form $\phi(x,t) = \varphi(x)\eta(t)$. Applying this definition to the equation 4.58 and dividing through by the term $-\epsilon$, we get the expression

$$\left(\varphi^{iv}(x) - \frac{1}{\epsilon}\varphi^{''}(x)\right)\eta(t) = 0 \tag{4.59}$$

This analysis will consider the steady-state response to an applied step voltage. In the long term this will represent a constant temporal component. This constant is assigned a value of 1, allowing us to simply consider the linear differential equation,

$$\frac{\partial^2}{\partial x^2}\left(\phi^{''}(x) - \frac{1}{\epsilon}\phi(x)\right) \tag{4.60}$$

The general solution to this expression has the form

$$\phi_{ss}(x) = a_1 \epsilon \sinh\frac{x}{\sqrt{\epsilon}} + a_2 \epsilon \cosh\frac{x}{\sqrt{\epsilon}} + a_3 x + a_4. \tag{4.61}$$

4.4.1 Limits on the step excitation

To continue this linear analysis, we recognize that the solution presented in equation 4.61 is subject to the linear boundary conditions prescribing the applied potential and the ion flux at the membrane boundaries. Since we are considering the steady-state response of the polymer, the boundary conditions will have the form,

$$x = 0 \rightarrow \qquad \phi = \Phi_1, \quad \text{and} \quad \mathrm{N}_1\left(\epsilon\phi^{'''} - \phi^{'}\right) = 0 \tag{4.62}$$

$$x = 1 \rightarrow \qquad \phi = \Phi_2, \quad \text{and} \quad \mathrm{N}_1\left(\epsilon\phi^{'''} - \phi^{'}\right) = 0 \tag{4.63}$$

Applying the potential boundary conditions to the general steady-state solution from equation 4.61 we find that

$$a_1\epsilon\sinh(0) + a_2\epsilon\cosh(0) + a_3 0 + a_4 = \Phi_1 \tag{4.64}$$

$$a_1\epsilon\sinh\frac{1}{\sqrt{\epsilon}} + a_2\epsilon\cosh\frac{1}{\sqrt{\epsilon}} + a_3 + a_4 = \Phi_2 \tag{4.65}$$

These conditions can be further simplified to yield an expression for a_4, and a simplified form of the boundary condition at $x = 1$,

$$a_4 = \Phi_1 - a_2\epsilon \tag{4.66}$$

$$a_1\epsilon\sinh\frac{1}{\sqrt{\epsilon}} + a_2\epsilon\left(\cosh\frac{1}{\sqrt{\epsilon}} - 1\right) + a_3 = \Phi_2 - \Phi_1 \tag{4.67}$$

Similarly, we can use the flux boundry conditions to formulate the second set of boundary conditions

$$N_1\left[\frac{a_1\epsilon}{\sqrt{\epsilon}}\cosh 0 + \frac{a_2\epsilon}{\sqrt{\epsilon}}\sinh 0 - \left(a_1\sqrt{\epsilon}\cosh 0 + a_2\sqrt{\epsilon}\sinh 0 + a_3\right)\right] = 0 \tag{4.68}$$

$$N_1\left[\frac{a_1\epsilon}{\sqrt{\epsilon}}\cosh\frac{1}{\sqrt{\epsilon}} + \frac{a_2\epsilon}{\sqrt{\epsilon}}\sinh\frac{1}{\sqrt{\epsilon}} - \left(a_1\sqrt{\epsilon}\cosh\frac{1}{\sqrt{\epsilon}} + a_2\sqrt{\epsilon}\sinh\frac{1}{\sqrt{\epsilon}} + a_3\right)\right] = 0 \tag{4.69}$$

From the flux boundary condition at $x = 0$ we find that the constants a_1 and a_3 are related in the manner,

$$a_3 = 0 \tag{4.70}$$

Looking carefully at the flux boundary conditions in equations 4.68 - 4.69 we see that the flux condition at $x = 1$ does not offer any additional information, and infact redundant with respect to the condition at $x = 0$. Therefore we must consider another condition that will provide insight into this problem. As we stated before, the membrane is considered to be a closed system through the material thickness. As such, charged cannot enter or leave the bounds of $0 \leq x \leq 1$. Thus we can conclude that the integral of the charge density in this case must remain constant. And, since we began with an equal distribution of cations and anions this integral must be zero across the material thickness. From the nondimensionalization, the charge density can be expressed as $\rho_{ss}(x) = -\frac{d^2\phi_{ss}(x)}{dx^2}$. In this manner the charge density constraint takes the form,

$$\int_0^1 -\frac{\partial^2\phi(x)}{\partial x^2}dx = 0. \tag{4.71}$$

Evaluating this integral, we find

$$a_1\sqrt{\epsilon}\left(\cosh\frac{1}{\sqrt{\epsilon}} - 1\right) + a_2\sqrt{\epsilon}\sinh\frac{1}{\sqrt{\epsilon}} = 0 \tag{4.72}$$

which can be solved to yield a relationship between the unknown coeffcients a_1 and a_2,

$$a_2 = \frac{1 - \cosh \frac{1}{\sqrt{\epsilon}}}{\sinh \frac{1}{\sqrt{\epsilon}}} \; a_1 \tag{4.73}$$

Using the identities that $\sinh^2 y = \frac{1}{2}(\cosh 2y - 1)$ and that $\sinh 2y = 2 \sinh y \cosh y$, we can rephrase a_2 as $a_2 = -a_1 \tanh \frac{1}{2\sqrt{\epsilon}}$. Substituting this expression in to the second potential condition from equation 4.67 we get

$$\begin{aligned} a_1 \epsilon \sinh \frac{1}{\sqrt{\epsilon}} + a_1 \epsilon \tanh \frac{1}{2\sqrt{\epsilon}} \left(\cosh \frac{1}{\sqrt{\epsilon}} - 1 \right) &= \Phi_2 - \Phi_1 \\ 2a_1 \epsilon \left(\sinh \frac{1}{2\sqrt{\epsilon}} \cosh \frac{1}{2\sqrt{\epsilon}} - \tanh \frac{1}{2\sqrt{\epsilon}} \sinh^2 \frac{1}{2\sqrt{\epsilon}} \right) &= \Delta\Phi \\ 2a_1 \epsilon \tanh \frac{1}{2\sqrt{\epsilon}} \left(\cosh^2 \frac{1}{2\sqrt{\epsilon}} - \sinh^2 \frac{1}{2\sqrt{\epsilon}} \right) &= \Delta\Phi \end{aligned} \tag{4.74}$$

Using the fundamental hyperbolic identity $\cosh^2 \frac{1}{2\sqrt{\epsilon}} - \sinh^2 \frac{1}{2\sqrt{\epsilon}} = 1$, the potential boundary condition simplifies to the expression,

$$2a_1 \epsilon \tanh \frac{1}{2\sqrt{\epsilon}} = \Delta\Phi \tag{4.75}$$

From this expression we can solve for the a_1 coefficient, and consequently the remaining coefficients a_2 - a_4. This yields the set of coefficients,

$$a_1 = \frac{\Delta\Phi}{2\epsilon \tanh \frac{1}{2\sqrt{\epsilon}}}, \qquad a_2 = \frac{\Delta\Phi}{2\epsilon}, \qquad a_3 = 0, \qquad a_4 = \frac{\Phi_1 + \Phi_2}{2} \tag{4.76}$$

We can now use these coefficients to formulate the steady-state solution to the internal potential function $\phi_{ss}(x)$. Substituting these coefficient expressions into equation 4.61 we get,

$$\phi_{ss}(x) = \frac{1}{2} \left[\left(\frac{\Delta\Phi}{\tanh \frac{1}{2\sqrt{\epsilon}}} \right) \sinh \frac{x}{\sqrt{\epsilon}} - \Delta\Phi \cosh \frac{x}{\sqrt{\epsilon}} + \Phi_1 + \Phi_2 \right] \tag{4.77}$$

The individual components of this expression (primarily $\frac{\Delta\Phi}{\tanh \frac{1}{2\sqrt{\epsilon}}} \sinh \frac{x}{\sqrt{\epsilon}}$ and $-\Delta\Phi \cosh \frac{x}{\sqrt{\epsilon}}$) go off to $\pm\infty$ as x approaches 1. When summed together the analytical expression goes to Φ_2, however numerical errors tend to drive the simulation to 0 at $x = 1$. Therefore we consider the simplified expression that is obtained by multiplying through

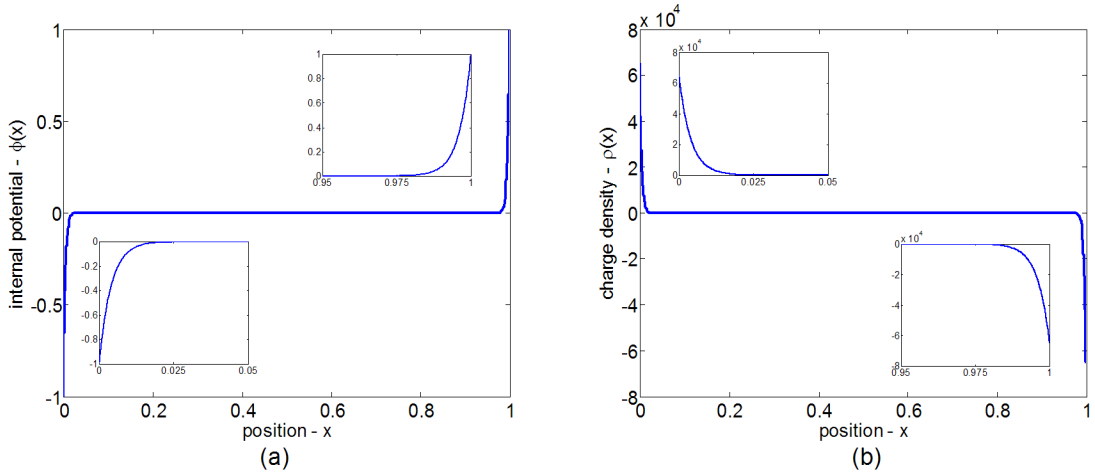

Figure 4.4: The steady-state response of the IPT. This figure illustrates the (a) internal potential and (b) charge density through the material thickness.

by $\frac{\sinh\frac{1}{2\sqrt{\epsilon}}}{\sinh\frac{1}{2\sqrt{\epsilon}}}$ and imposing the hyperbolic identity for $\sinh(x+y)$. This yields the solution

$$\phi_{ss}(x) = \frac{1}{2}\left[(\Phi_2+\Phi_1) - \frac{\Delta\Phi}{\sinh\frac{1}{2\sqrt{\epsilon}}}\left(\sinh\frac{1}{2\sqrt{\epsilon}}\cosh\frac{x}{\sqrt{\epsilon}} - \cosh\frac{1}{2\sqrt{\epsilon}}\sinh\frac{x}{\sqrt{\epsilon}}\right)\right]$$

$$\phi_{ss}(x) = \frac{1}{2}\left[(\Phi_2+\Phi_1) - \frac{\Delta\Phi}{\sinh\frac{1}{2\sqrt{\epsilon}}}\sinh\frac{1-2x}{2\sqrt{\epsilon}}\right] \tag{4.78}$$

From this solution for the internal potential, we can impose the field relationships to yield an expression that describes the steady-state charge density $\rho_{ss}(x)$. In the nondimensional form this relationship is governed by the equation $\rho_{ss}(x) = -\frac{d^2\phi_{ss}(x)}{dx^2}$. Imposing this relationship yields the steady-state solution $\rho_{ss}(x)$,

$$\rho_{ss} = \frac{\Delta\Phi}{2\epsilon\sinh\frac{1}{2\sqrt{\epsilon}}}\sinh\frac{1-2x}{2\sqrt{\epsilon}} \tag{4.79}$$

These steady-state profiles are shown in detail in Figure 4.4. From this figure it is apparent that the internal potential and charge density profiles are dominated by the $\sinh\frac{1-2x}{2\sqrt{\epsilon}}$ term in equations 4.78 and 4.79. These figures also illustrate the boundary layer effect that is predicted to develop within the IPT under a constant applied potential. The charge density result is consistent with predictions of Nemat-Nasser [59], while Figure 4.4a extends Nemat-Nasser's results to provide a corresponding prediciton of the internal potential as well.

In addition to a qualitative understanding of the IPT response, we can extend our analysis to focus on the theoretical potential limit that would correspond to a full depletion of cations near the anode. Following the analysis used to generate Figure 4.4, we focus on the cation depletion that is expected to develop near the anode at $x = 1$. In this region of the polymer it is evident that the charge density expriences a rapid loss in the number of cations

within the boundary layer at $x = 1$. As more cations migrate out of this region, the charge density is expected to approach a saturation limit imposed by the anionic nature of the base ionomer itself. The chemical composition of the ionic polymer restricts the minimal charge density to a level corresponding to $\hat{\rho} = -FC^{-}$. In the nondimensional coordinate this saturation limit corresponds to $\rho = -\frac{L^2 FC^{-}}{\kappa \Phi_m}$. Therefore if we apply this saturation constraint to the steady state charge density it is possible to identify a critical potential which will correspond to a full depletion of the cations near the anode. Thus we begin by considering the case where

$$\frac{\Delta\Phi}{2\epsilon \sinh \frac{1}{2\sqrt{\epsilon}}} \sinh \frac{-1}{2\sqrt{\epsilon}} = -\frac{L^2 FC^{-}}{\kappa \Phi_m} \tag{4.80}$$

This yields the case where

$$\frac{-\Delta\Phi}{2\epsilon} = -\frac{L^2 FC^{-}}{\kappa \Phi_m} \tag{4.81}$$

Imposing the definition for $\Delta\Phi$ in terms of $\hat{\Phi}_1$, $\hat{\Phi}_2$ and Φ_m, we get an expression in terms of the physical potentials $\hat{\Phi}_1$ and $\hat{\Phi}_2$,

$$\frac{\left(\hat{\Phi}_2 - \hat{\Phi}_1\right)}{2\epsilon \Phi_m} = \frac{L^2 FC^{-}}{\kappa \Phi_m} \tag{4.82}$$

We define this critical potential difference as $\Delta\hat{\Phi}_{crit} = \hat{\Phi}_2 - \hat{\Phi}_1$. Solving for this value we find

$$\Delta\hat{\Phi}_{crit} = \frac{2\epsilon L^2 FC^{-}}{\kappa} = \frac{2L^2 FC^{-}}{\kappa L^2 \gamma^2} = \frac{2FC^{-}}{\kappa \frac{F^2 C^{-}}{\kappa RT}}$$
$$\Delta\hat{\Phi}_{crit} = \frac{2RT}{F} \tag{4.83}$$

One of the most interesting features of this critical potential is that it relies solely on the ambient temperature T. For experiments conducted in the lab, this temperature corresponds to 300K, producing a critical transition potential of

$$\Delta\hat{\Phi}_{crit} = 51.8\mathrm{mV} \tag{4.84}$$

This critical potential assumes that the charge density has reached a steady-state profile following the application of a step voltage across the material thickness. Such a response offers insight into the boundary layer development near each of the electrodes at $x = 0$ and $x = 1$ as shown in Figure 4.4. Next we want to consider the effects of frequency on the charge density response within the IPT. In the next section we redevelop the internal potential, this time considering a harmonic excitation of the form $\Phi_n \sin \Omega t$

4.5 Forced response - harmonic excitation

At this point we consider the response to a harmonic electric potential applied at the boundaries. Considering the long term performance, we assume the forced response to be the sum of forced and resonant components,

$$\phi(x,t) = F\psi(x)\sin\Omega t + F\delta(x)\cos\Omega t + u(x,t) \tag{4.85}$$

where F is equal to $\frac{\Delta\Phi}{2}$ or $\frac{\Phi_2-\Phi_1}{2}$. $\psi(x)$ and $\delta(x)$ are the forced modal components. Now we consider the linear PDE

$$\dot{\phi}^{''} - \epsilon\phi^{iv} + \phi^{''} = 0 \tag{4.86}$$

Substituting the assumed solution for the potential into this linear PDE we have

$$\begin{aligned}\left(F\psi^{''}(x)\Omega\cos\Omega t - F\delta^{''}(x)\Omega\sin\Omega t + \dot{u}^{''}\right) - \epsilon\left(F\psi^{iv}(x)\sin\Omega t + F\delta^{iv}(x)\cos\Omega t + u^{iv}\right) \\ + \left(F\psi^{''}(x)\sin\Omega t + F\delta^{''}(x)\cos\Omega t + u^{''}\right) &= 0\end{aligned} \tag{4.87}$$

For now we define the resonant component to be zero. Applying this assumption and grouping $\sin\Omega t$ and $\cos\Omega t$ terms,

$$F\left[\left(-\delta^{''}(x)\Omega - \epsilon\psi^{iv}(x) + \psi^{''}(x)\right)\sin\Omega t + \left(\psi^{''}(x)\Omega - \epsilon\delta^{iv}(x) + \delta^{''}(x)\right)\cos\Omega t\right] = 0 \tag{4.88}$$

to satisfy this expression, we formulate a set of coupled ODEs in terms of ψ and δ,

$$\begin{aligned}-\epsilon\psi^{iv}(x) + \psi^{''}(x) &= \Omega\delta^{''}(x) \\ -\epsilon\delta^{iv}(x) + \delta^{''}(x) &= -\Omega\psi^{''}(x)\end{aligned} \tag{4.89}$$

Dividing through by ϵ, we define the constants a and b such that $\tilde{a} = \frac{-1}{\epsilon}$ and $\tilde{b} = \frac{-\Omega}{\epsilon}$. Thus the coupled ODEs have the form

$$\begin{aligned}\psi^{iv}(x) - \tilde{a}\psi^{''}(x) &= -\tilde{b}\delta^{''}(x) \\ \delta^{iv}(x) - \tilde{a}\delta^{''}(x) &= \tilde{b}\psi^{''}(x)\end{aligned} \tag{4.90}$$

From this we can solve for a set of general solutions to $\psi(x)$ and $\delta(x)$. The solutions are composed of eight unknown constant coefficients which may be solved for through the boundary conditions at $x = 0$ and $x = 1$. The general

solutions for $\psi(x)$ and $\delta(x)$ are,

$$\begin{aligned}\psi(x) &= c_6 + c_7 x - \frac{a}{A\bar{A}}(c_8 + c_1 x) - \frac{b}{A\bar{A}}(c_5 + c_2 x) + \frac{c_1 + ic_2}{2A^{3/2}}\sinh\sqrt{A}x + \frac{c_1 - ic_2}{2\bar{A}^{3/2}}\sinh\sqrt{\bar{A}}x \\ &\quad + \frac{c_8 + ic_5}{2A}\cosh\sqrt{A}x + \frac{c_8 - ic_5}{2\bar{A}}\cosh\sqrt{\bar{A}}x \end{aligned} \tag{4.91}$$

and,

$$\begin{aligned}\delta(x) &= c_3 + c_4 x - \frac{a}{A\bar{A}}(c_5 + c_2 x) + \frac{b}{A\bar{A}}(c_8 + c_1 x) + \frac{c_2 - ic_1}{2A^{3/2}}\sinh\sqrt{A}x + \frac{c_2 + ic_1}{2\bar{A}^{3/2}}\sinh\sqrt{\bar{A}}x \\ &\quad + \frac{c_5 - ic_8}{2A}\cosh\sqrt{A}x + \frac{c_5 + ic_8}{2\bar{A}}\cosh\sqrt{\bar{A}}x \end{aligned} \tag{4.92}$$

where A and $\bar{A}$ are defined as $A = \frac{-1}{\epsilon}(1 + i\Omega)$ and $\bar{A} = \frac{-1}{\epsilon}(1 - i\Omega)$. At this point we consider the boundary conditions associated with the potential boundary condition, still leaving out the nonlinear terms in the flux boundary condition. As we consider these boundary conditions, we first formulate spatial derivatives of $\psi(x)$,

$$\psi'(x) = c_7 - \frac{ac_1 + bc_2}{A\bar{A}} + \frac{1}{2}\left[\frac{c_1 + ic_2}{A}\cosh\sqrt{A}x + \frac{c_1 - ic_2}{\bar{A}}\cosh\sqrt{\bar{A}}x + \frac{c_8 + ic_5}{\sqrt{A}}\sinh\sqrt{A}x + \frac{c_8 - ic_5}{\sqrt{\bar{A}}}\sinh\sqrt{\bar{A}}x\right] \tag{4.93}$$

$$\psi''(x) = \frac{1}{2}\left[\frac{c_1 + ic_2}{\sqrt{A}}\sinh\sqrt{A}x + \frac{c_1 - ic_2}{\sqrt{\bar{A}}}\sinh\sqrt{\bar{A}}x + (c_8 + ic_5)\cosh\sqrt{A}x + (c_8 - ic_5)\cosh\sqrt{\bar{A}}x\right] \tag{4.94}$$

$$\psi'''(x) = \frac{1}{2}\left[(c_1 + ic_2)\cosh\sqrt{A}x + (c_1 - ic_2)\cosh\sqrt{\bar{A}}x + \sqrt{A}(c_8 + ic_5)\sinh\sqrt{A}x + \sqrt{\bar{A}}(c_8 - ic_5)\sinh\sqrt{\bar{A}}x\right] \tag{4.95}$$

as well as those for the forced modeshape $\delta(x)$,

$$\delta'(x) = c_4 - \frac{ac_2 - bc_1}{A\bar{A}} + \frac{1}{2}\left[\frac{c_2 - ic_1}{A}\cosh\sqrt{A}x + \frac{c_2 + ic_1}{\bar{A}}\cosh\sqrt{\bar{A}}x + \frac{c_5 - ic_8}{\sqrt{A}}\sinh\sqrt{A}x + \frac{c_5 + ic_8}{\sqrt{\bar{A}}}\sinh\sqrt{\bar{A}}x\right] \tag{4.96}$$

$$\delta''(x) = \frac{1}{2}\left[\frac{c_2 - ic_1}{\sqrt{A}}\sinh\sqrt{A}x + \frac{c_2 + ic_1}{\sqrt{\bar{A}}}\sinh\sqrt{\bar{A}}x + (c_5 - ic_8)\cosh\sqrt{A}x + (c_5 + ic_8)\cosh\sqrt{\bar{A}}x\right] \tag{4.97}$$

$$\delta'''(x) = \frac{1}{2}\left[(c_2 - ic_1)\cosh\sqrt{A}x + (c_2 + ic_1)\cosh\sqrt{\bar{A}}x + \sqrt{A}(c_5 - ic_8)\sinh\sqrt{A}x + \sqrt{\bar{A}}(c_5 + ic_8)\sinh\sqrt{\bar{A}}x\right] \tag{4.98}$$

From this we can address both the potential and flux boundary conditions. First we consider the potential function as,

$$\phi(x,t) = F\psi(x)\sin\Omega t + F\delta(x)\cos\Omega t \tag{4.99}$$

Applying the potential boundary conditions to this assumed solution, we find that

$$\begin{aligned} \phi(0) &= F\psi(0)\sin\Omega t + F\delta(0)\cos\Omega t = -F\sin\Omega t \\ &\rightarrow \quad \psi(0) = -1 \qquad \delta(0) = 0 \end{aligned} \tag{4.100}$$

$$\begin{aligned} \phi(L) &= F\psi(L)\sin\Omega t + F\delta(L)\cos\Omega t = F\sin\Omega t \\ &\rightarrow \quad \psi(L) = 1 \qquad \delta(L) = 0 \end{aligned} \tag{4.101}$$

Similarly we apply the flux boundary conditions,

$$\begin{aligned} J(0) &= N_1\left[\epsilon\left(F\psi^{'''}(0)\sin\Omega t + F\delta^{'''}(0)\cos\Omega t\right) - \left(F\psi^{'}(0)\sin\Omega t + F\delta^{'}(0)\cos\Omega t\right)\right] = 0 \\ &\rightarrow \quad \epsilon\psi^{'''}(0) - \psi^{'}(0) = 0 \qquad \epsilon\delta^{'''}(0) - \delta^{'}(0) = 0 \end{aligned} \tag{4.102}$$

$$\begin{aligned} J(L) &= N_1\left[\epsilon\left(F\psi^{'''}(L)\sin\Omega t + F\delta^{'''}(L)\cos\Omega t\right) - \left(F\psi^{'}(L)\sin\Omega t + F\delta^{'}(L)\cos\Omega t\right)\right] = 0 \\ &\rightarrow \quad \epsilon\psi^{'''}(L) - \psi^{'}(L) = 0 \qquad \epsilon\delta^{'''}(L) - \delta^{'}(L) = 0 \end{aligned} \tag{4.103}$$

Thus, applying the four boundary conditions produces a set of eight equations that can be applied to our expressions for $\psi(x)$ and $\delta(x)$ to solve for coefficients $c_1 - c_8$. Mathematica is employed to solve for these coefficients, yielding a set of solutions

$$c_1 = \frac{2\left[A^{3/2}\sinh^2\frac{\sqrt{A}}{2}\sinh\sqrt{A} + \sqrt{A}\sinh\frac{\sqrt{A}}{2}\sinh\sqrt{A}\left(\sqrt{A}\left(\epsilon A\bar{A} - a\right)\cosh\frac{\sqrt{A}}{2} + \bar{A}\sinh\frac{\sqrt{A}}{2}\right)\right]}{2\Upsilon_h\sinh\frac{\sqrt{A}}{2}\sinh\frac{\sqrt{A}}{2}} \tag{4.104}$$

$$c_2 = \frac{\left[iA^{3/2}\sinh^2\frac{\sqrt{A}}{2}\sinh\sqrt{A} + \sqrt{A}\sinh\frac{\sqrt{A}}{2}\sinh\sqrt{A}\left(-\sqrt{A}b\cosh\frac{\sqrt{A}}{2} + i\bar{A}\sinh\frac{\sqrt{A}}{2}\right)\right]}{\Upsilon_h\sinh\frac{\sqrt{A}}{2}\sinh\frac{\sqrt{A}}{2}} \tag{4.105}$$

$$c_3 = 0 \tag{4.106}$$

$$c_4 = \frac{\epsilon\left[iA^{3/2}\sinh^2\frac{\sqrt{A}}{2}\sinh\sqrt{A} + \sqrt{A}\sinh\frac{\sqrt{A}}{2}\sinh\sqrt{A}\left(-\sqrt{A}b\cosh\frac{\sqrt{A}}{2} + i\bar{A}\sinh\frac{\sqrt{A}}{2}\right)\right]}{\Upsilon_h\sinh\frac{\sqrt{A}}{2}\sinh\frac{\sqrt{A}}{2}} \tag{4.107}$$

$$c_5 = \Big[\cosh\sqrt{\bar{A}}\left(4b\left(1-\cosh\sqrt{A}\right) - i\bar{A}\sqrt{A}\left((\epsilon A-1)\sinh\sqrt{A}\right) + i\left(4ib + \bar{A}\sqrt{A}\left(\epsilon A-1\right)\sinh\sqrt{A}\right.\right. \tag{4.108}$$
$$\left.\left. -A\sqrt{\bar{A}}\left(\epsilon\bar{A}-1\right)\sinh\sqrt{\bar{A}}\right) + \cosh\sqrt{A}\left(4b + iA\sqrt{\bar{A}}\left(\epsilon\bar{A}-1\right)\sinh\sqrt{\bar{A}}\right)\Big] \Big/ \left(4\Upsilon_h \sinh\frac{\sqrt{A}}{2}\sinh\frac{\sqrt{\bar{A}}}{2}\right)$$

$$c_6 = -1 \tag{4.109}$$

$$c_7 = \frac{2\epsilon\left[A^{3/2}\sinh^2\frac{\sqrt{A}}{2}\sinh\sqrt{A} + \sqrt{\bar{A}}\sinh\frac{\sqrt{A}}{2}\sinh\sqrt{\bar{A}}\left(\sqrt{A}\left(\epsilon A\bar{A}-a\right)\cosh\frac{\sqrt{A}}{2} + \bar{A}\sinh\frac{\sqrt{A}}{2}\right)\right]}{2\Upsilon_h \sinh\frac{\sqrt{A}}{2}\sinh\frac{\sqrt{\bar{A}}}{2}} \tag{4.110}$$

$$c_8 = \Big[4a + \bar{A}\sqrt{A}\sinh\sqrt{A} - \epsilon\bar{A}A^{3/2}\sinh\sqrt{A} + \cosh\sqrt{\bar{A}}\left(4a\left(\cosh\sqrt{A}-1\right) + \bar{A}\sqrt{A}\left(\epsilon A-1\right)\sinh\sqrt{A}\right) \tag{4.111}$$
$$+\ A\sqrt{\bar{A}}\sinh\sqrt{\bar{A}} - \epsilon A\bar{A}^{3/2}\sinh\sqrt{\bar{A}} + \cosh\sqrt{A}\left(-4a + A\sqrt{\bar{A}}\left(\epsilon\bar{A}-1\right)\sinh\sqrt{\bar{A}}\right)\Big] \Big/ \left(4\Upsilon_h \sinh\frac{\sqrt{A}}{2}\sinh\frac{\sqrt{\bar{A}}}{2}\right)$$

where the term Υ_h represents the common denominator for coefficients $c_3 - c_8$. This denominator term has the form

$$\Upsilon_h = \left(\sqrt{A}\left(\epsilon A-1\right)\cosh\frac{\sqrt{A}}{2} + 2\sinh\frac{\sqrt{A}}{2}\right)\left(\sqrt{\bar{A}}\left(\epsilon\bar{A}-1\right)\cosh\frac{\sqrt{\bar{A}}}{2} + 2\sinh\frac{\sqrt{\bar{A}}}{2}\right) \tag{4.112}$$

Applying these constants to the forced modeshapes of equations 4.91 - 4.92 and simplifying, we obtain a set of expressions for $\psi(x)$ and $\delta(x)$. Substituting these constants into equations 4.91 - 4.92 and simplifying yields an in-phase forced modeshape $\psi(x)$ of the form,

$$\begin{aligned}\psi(x) \quad = \quad & \frac{1}{\sqrt{\bar{A}}\Upsilon_h}\left(\sqrt{\bar{A}}\sinh\frac{\sqrt{\bar{A}}}{2}\left[-2\sinh\frac{\sqrt{A}}{2}\left(\cosh\sqrt{A}x + \cosh\sqrt{\bar{A}}x\right) + \cosh\frac{\sqrt{A}}{2}\left(\sqrt{A}\left(\epsilon A-1\right)(2x-1)\right.\right.\right. \\ & \left. - \sqrt{A}\left(\epsilon A-1\right)\cosh\sqrt{\bar{A}}x + 2\sinh\sqrt{A}x\right)\Big] + \cosh\frac{\sqrt{A}}{2}\left[\sinh\frac{\sqrt{A}}{2}\left(\bar{A}\left(\epsilon\sqrt{\bar{A}}-1\right)(2x-1)\right.\right. \\ & -\bar{A}\left(\epsilon\bar{A}-1\right)\cosh\sqrt{A}x + 2\sqrt{\bar{A}}\sinh\sqrt{\bar{A}}x\Big) + \cosh\frac{\sqrt{A}}{2}\left(\sqrt{A}\sqrt{\bar{A}}\left(\epsilon A-1\right)\sinh\sqrt{\bar{A}}x\right. \\ & \left.\left.\left.\left.+\bar{A}\left(\epsilon\bar{A}-1\right)\left(\sqrt{A}\left(\epsilon A-1\right)(2x-1) + \sinh\sqrt{A}x\right)\right)\right]\right)\end{aligned} \tag{4.113}$$

with the out-of-phase modeshape forced $\delta(x)$ defined as

$$\begin{aligned}\delta(x) \quad = \quad & \frac{1}{\sqrt{\bar{A}}\Upsilon_h}\left(\sqrt{\bar{A}}\sinh\frac{\sqrt{\bar{A}}}{2}\left[-2\left(A\cosh\sqrt{A}x + \bar{A}\cosh\sqrt{\bar{A}}x\right)\sinh\frac{\sqrt{A}}{2} + \cosh\frac{\sqrt{A}}{2}\left(2A\sinh\sqrt{A}x\right.\right.\right. \\ & \left.\left. -\bar{A}\sqrt{A}\left(\epsilon A-1\right)\cosh\sqrt{\bar{A}}x\right)\Big] + \cosh\frac{\sqrt{\bar{A}}}{2}\left[\sinh\frac{\sqrt{A}}{2}\left(-A\bar{A}\left(\epsilon\bar{A}-1\right)\cosh\sqrt{A}x + 2\bar{A}^{3/2}\sinh\sqrt{\bar{A}}x\right)\right. \\ & \left.\left. + \cosh\frac{\sqrt{A}}{2}\left(A\bar{A}\left(\epsilon A-1\right)\sinh\sqrt{A}x + \sqrt{A}\bar{A}^{3/2}\left(\epsilon A-1\right)\sinh\sqrt{\bar{A}}x\right)\Big]\right)\end{aligned} \tag{4.114}$$

Figure 4.5 presents the in-phase $\psi(x)$ and out-of-phase $\delta(x)$ modal components of the electric potential. From these figures it can be seen that the modeshape $\psi(x)$ associated with the in-phase component $F\sin\Omega t$ is primarily linear, and constant with applied frequency ω (where ω corresponds to the dimensional frequency in hertz). This function

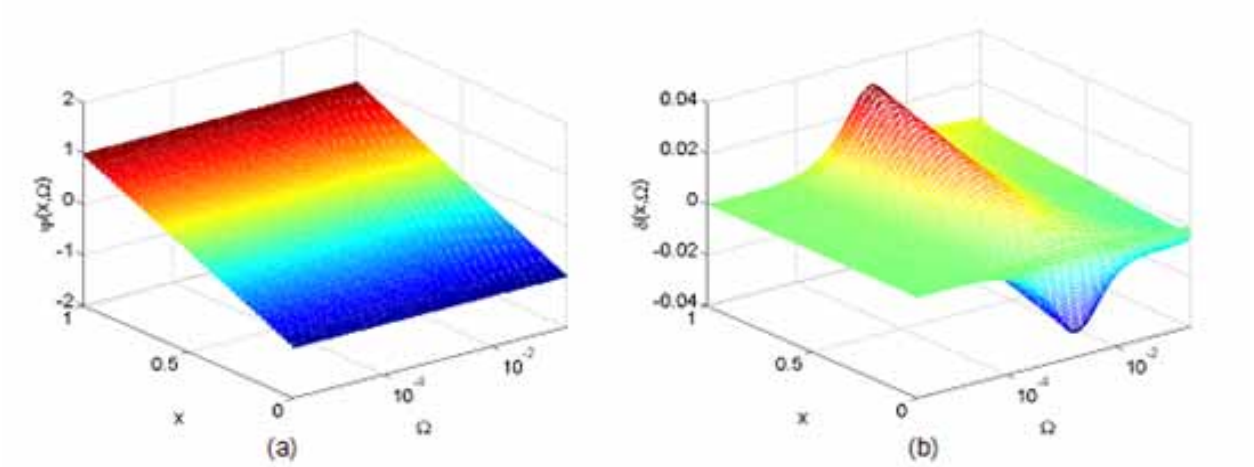

Figure 4.5: The spatial response for $\psi(x,\Omega)$ and $\delta(x,\Omega)$ as a function of frequency and position through the transducer's thickness.

is linear through the polymer thickness, matching the potential boundary conditions for a 1V applied potential. The out-of-phase modeshape $delta(x)$ is shown in Figure 4.5b is of much lower magnitude, however it does show a frequency dependent response, with a maximum response near $\omega = 0.08$Hz and an inflection point near $\omega = 0.65$Hz.

4.5.1 Forced internal potential

These two modeshapes are the basis for our forced electric potential profile defined in equation 4.85. Substituting these definitions for $\psi(x)$ and $\delta(x)$ into this equation, we develop the expression for $\phi(x,t)$,

$$\begin{aligned}
\phi_f(x,t) \quad = \quad & \frac{\Delta\Phi}{2\sqrt{\bar{A}}\Upsilon_h}\left\{\sin\Omega t\left(\sqrt{\bar{A}}\sinh\frac{\sqrt{\bar{A}}}{2}\left[-2\sinh\frac{\sqrt{A}}{2}\left(\cosh\sqrt{\bar{A}}x+\cosh\sqrt{\bar{A}}x\right)+\cosh\frac{\sqrt{A}}{2}\left(\sqrt{A}\left(\epsilon A-1\right)\left(2x-1\right)\right.\right.\right.\right. \\
& \left.\left.\left.\left.-\sqrt{A}\left(\epsilon A-1\right)\cosh\sqrt{\bar{A}}x+2\sinh\sqrt{A}x\right)\right]+\cosh\frac{\sqrt{\bar{A}}}{2}\left[\sinh\frac{\sqrt{A}}{2}\left(\bar{A}\left(\epsilon\sqrt{\bar{A}}-1\right)\left(2x-1\right)\right.\right.\right. \\
& \left.\left.\left.-\bar{A}\left(\epsilon\bar{A}-1\right)\cosh\sqrt{A}x+2\sqrt{\bar{A}}\sinh\sqrt{\bar{A}}x\right)+\cosh\frac{\sqrt{A}}{2}\left(\sqrt{A}\sqrt{\bar{A}}\left(\epsilon A-1\right)\sinh\sqrt{\bar{A}}x\right.\right.\right. \\
& \left.\left.\left.+\bar{A}\left(\epsilon\bar{A}-1\right)\left(\sqrt{A}\left(\epsilon A-1\right)\left(2x-1\right)+\sinh\sqrt{A}x\right)\right)\right]\right) \\
& +\cos\Omega t\left(\sqrt{\bar{A}}\sinh\frac{\sqrt{\bar{A}}}{2}\left[-2\left(A\cosh\sqrt{A}x+\bar{A}\cosh\sqrt{\bar{A}}x\right)\sinh\frac{\sqrt{A}}{2}+\cosh\frac{\sqrt{A}}{2}\left(2A\sinh\sqrt{A}x\right.\right.\right. \\
& \left.\left.\left.-\bar{A}\sqrt{A}\left(\epsilon A-1\right)\cosh\sqrt{\bar{A}}x\right)\right]+\cosh\frac{\sqrt{\bar{A}}}{2}\left[\sinh\frac{\sqrt{A}}{2}\left(-A\bar{A}\left(\epsilon\bar{A}-1\right)\cosh\sqrt{A}x+2\bar{A}^{3/2}\sinh\sqrt{\bar{A}}x\right)\right.\right. \\
& \left.\left.\left.+\cosh\frac{\sqrt{A}}{2}\left(A\bar{A}\left(\epsilon A-1\right)\sinh\sqrt{A}x+\sqrt{A}\bar{A}^{3/2}\left(\epsilon A-1\right)\sinh\sqrt{\bar{A}}x\right)\right]\right)\right\} \qquad (4.115)
\end{aligned}$$

The internal potential is presented with respect to space and time in Figure 4.6a. This plot corresponds to an applied harmonic potential of $\pm\frac{\Delta\Phi}{2}\sin\Omega t$ at each of the electrode surfaces. In this case the potential is of unity magnitude

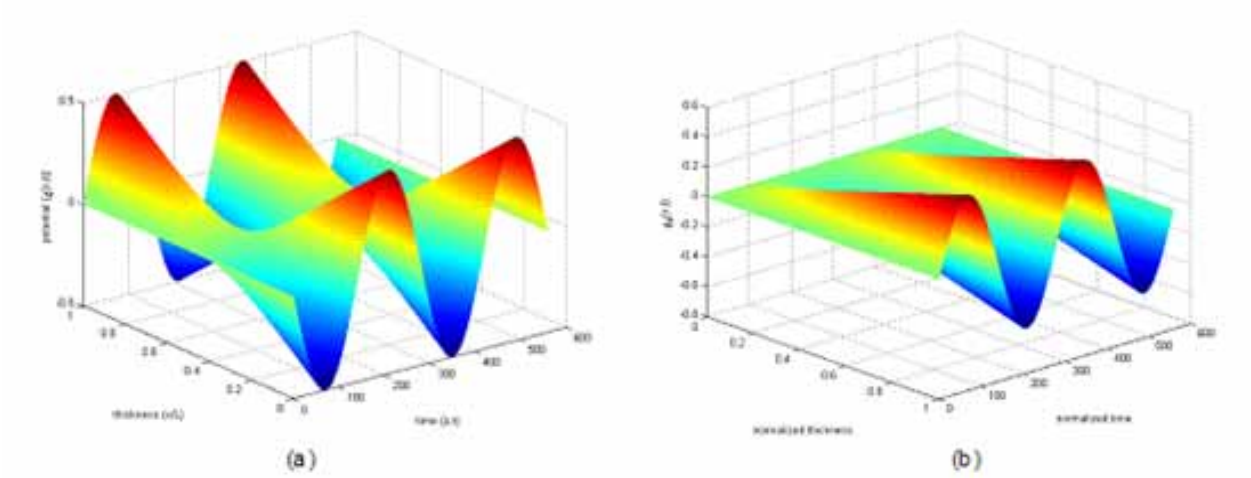

Figure 4.6: The electric potential response to an applied harmonic excitation. Figure (a) presents the response to a harmonic excitation at both electrodes, while (b) presents the response to a harmonic excitation at only one electrode. All excitations have unity amplitude and a frequency of 1 Hz.

and a frequency Ω of $\frac{1}{\lambda}$ or $\frac{1}{d\gamma^2}$. This figure shows a nearly linear profile through the material thickness. Slight variations do exist in the spatial profile, most evident in the out-of-phase component of Figure 4.5b. In addition to the symmetrically applied potential, Figure 4.6b depicts the internal potential response to a harmonic potential applied at one electrode while the other is continually held a 0.

4.5.2 Forced internal charge density

Using the electric field relationships we can develop an expression for the forced charge density $\rho_f(x,t)$ as well as teh isothermal transient ionic current (ITIC). First however we must formulate the nondimensional form of the of the potential to charge density relationship. Applying the normalization relationships of equation 4.23 to the field relationships of equation 4.14 we get the charge density relationship,

$$\hat{\rho}(\hat{x},\hat{t}) = -\kappa \frac{\partial^2 \hat{\phi}(\hat{x},\hat{t})}{\partial \hat{x}^2} \tag{4.116}$$

Applying the nondimensionalization of $\hat{\phi}(\hat{x},\hat{t})$, $\hat{\rho}(\hat{x},\hat{t})$ can be written as

$$\hat{\rho}(\hat{x},\hat{t}) = \frac{-\kappa\Phi_m}{L^2}\frac{\partial^2 \phi(x,t)}{\partial x^2} \tag{4.117}$$

Therefore, we can nondimensionalize $\hat{\rho}$ by dividing through by $\frac{\kappa\Phi_m}{L^2}$, producing a nondimensional $\rho(x,t)$ defined as

$$\rho(x,t) = \frac{L^2}{\kappa\Phi_m}\hat{\rho}(\hat{x},\hat{t}) = -\frac{\partial^2 \phi(x,t)}{\partial x^2} \tag{4.118}$$

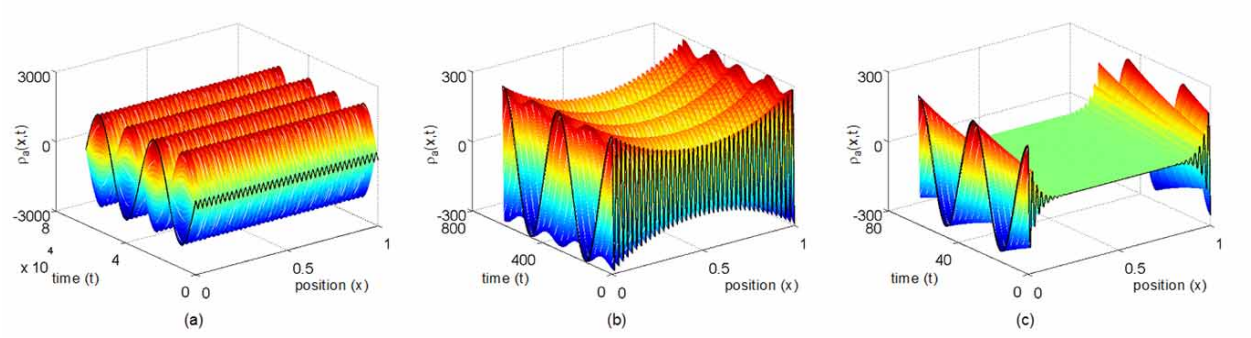

Figure 4.7: The charge density response to an applied harmonic excitation. Three separate excitation frequencies are considered: (a) corresponds to $\Omega = 0.002$, (b) corresponds to $\Omega = 0.02$ while (c) corresponds to $\Omega = 0.2$, where Ω corresponds to the frequency normalized by the characteristic time λ. All excitations are 0 at $x = 0$ and harmonic with amplitude 1 at $x = 1$.

From this expression we can develop the charge density relationship resulting from an applied harmonic potential at each of the IPT surfaces. This applied voltage induces the internal potential of equation 4.115, which when applied to the above charge density expression yields the forced charge density $\rho_f(x,t)$,

$$\begin{aligned}\rho_f(x,t) = \frac{-\Delta\Phi}{2\sqrt{\bar{A}}\Upsilon_h}\Bigg[&\sin\Omega t\left(\sqrt{\bar{A}}\sinh\frac{\sqrt{\bar{A}}}{2}\left[-2\sinh\frac{\sqrt{A}}{2}\left(A\cosh\sqrt{A}x+\bar{A}\cosh\sqrt{\bar{A}}x\right)+\cosh\frac{\sqrt{A}}{2}\left(2A\sinh\sqrt{A}x\right.\right.\right.\\&\left.\left.\left.-\bar{A}\sqrt{A}\left(\epsilon A-1\right)\cosh\sqrt{\bar{A}}x+\right)\right]+\cosh\frac{\sqrt{\bar{A}}}{2}\left[\sinh\frac{\sqrt{\bar{A}}}{2}\left(-A\bar{A}\left(\epsilon\bar{A}-1\right)\cosh\sqrt{A}x\right.\right.\\&\left.\left.+2\bar{A}^{3/2}\sinh\sqrt{\bar{A}}x\right)+\cosh\frac{\sqrt{A}}{2}\left(A\bar{A}\left(\epsilon\bar{A}-1\right)\sinh\sqrt{A}x+\bar{A}^{3/2}\sqrt{A}\left(\epsilon A-1\right)\sinh\sqrt{\bar{A}}x\right)\right]\Bigg)\\&+i\cos\Omega t\left(\sinh\frac{\sqrt{A}}{2}\left[-2\sqrt{\bar{A}}\sinh\frac{\sqrt{A}}{2}\left(-A\cosh\sqrt{A}x+\bar{A}\cosh\sqrt{\bar{A}}x\right)+\cosh\frac{\sqrt{A}}{2}\left(2\bar{A}^{3/2}\sinh\sqrt{\bar{A}}x\right.\right.\right.\\&\left.\left.+A\bar{A}\left(\epsilon A-1\right)\cosh\sqrt{A}x\right)+\cosh\frac{\sqrt{A}}{2}\left(\sqrt{\bar{A}}\sinh\frac{\sqrt{\bar{A}}}{2}\left(\bar{A}\sqrt{A}\left(\epsilon A+1\right)\cosh\sqrt{\bar{A}}x\right.\right.\\&\left.\left.\left.-2A\sinh\sqrt{A}x\right)+\cosh\frac{\sqrt{A}}{2}\left(-A\bar{A}\left(\epsilon\bar{A}-1\right)\sinh\sqrt{A}x+\bar{A}^{3/2}\sqrt{A}\left(\epsilon A-1\right)\sinh\sqrt{\bar{A}}x\right)\right)\right]\end{aligned} \tag{4.119}$$

This expression describes the ion distribution throughout the IPT with respect to space and time, as well as the frequency of the external potential. Figure 4.7 presents the predicted charge density associated with three different driving frequencies, ranging from $\Omega = 0.0002$ to $\Omega = 0.2$. As before Ω corresponds to the nondimensional frequency that results from normalizing the applied frequency ω in Hz by the characteristic time λ. At low frequencies the termporal response is in-phase with the applied potential as shown in Figure 4.7a. As this excitation frequency increases the charge density gradually becomes out-of-phase with the input signal, illustrated in Figures 4.7b-c. Considering the physical performance of the polymer itself, this behavior is expected in the time response. Since the material exhibits capacitive properties at low frequencies and resistive properties at higher frequencies, it is natural

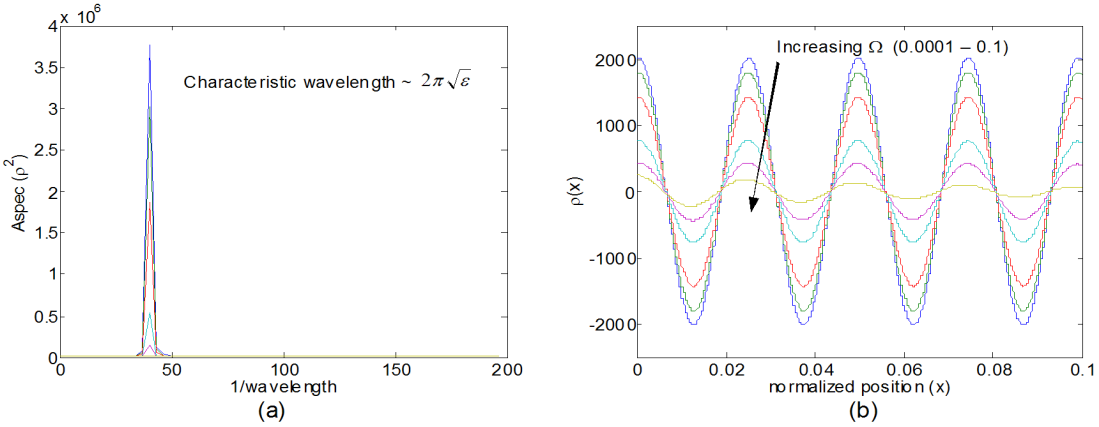

Figure 4.8: Wavelength analysis of the charge density's spatial response to low frequency harmonic excitation ($0.0001 \leq \Omega \leq 0.1$). An autospectrum of the data shows that the characteristic wavelength is $\approx 2\pi\sqrt{\epsilon}$. Plot (b) depicts the charge density near the boundary from $0 \leq x \leq 0.1$.

to expect a shift in the phase with faster signals. Since the charge density is proportional to the surface charge, it is expected that $\rho_f(x,t)$ will be in-phase with the applied potential at low frequencies to emulate a capacitive response. Similarly we expect while the more resistive, high frequency response to be 90^o out-of-phase with the applied potential, as seen in Figure 4.7c.

In addition to the termporal response of the IPT, the spatial response also exhibits a harmonic profile through the material thickness. At low frequencies this spatial profile has a nearly uniform peak amplitude throughout the polymer. As this excitation frequency increases the magnitude begins to decay near the center of the polymer. This behavior becomes more pronounced as the excitation frequency increases further, and is apparent in Figure 4.7c. Figure 4.8 considers the spatial response and its characteristic wavelength as they vary exclusively with x and the driving frequency Ω. The spatial profiles of 4.8b correspond to the time t in which $\rho(x,t)$ is maximized at $x = 0$. Six separate excitation frequencies are considered in this plot, ranging from $\Omega = 0.0001$ to $\Omega = 0.1$. An autospectrum of this data quantifies the characteristic wavelength for each driving frequency, indicating that it is nearly proportional to $2\pi\sqrt{\epsilon}$ at low exitation frequencies. As the applied frequency increases beyond $\Omega = 0.1$, a noticable shift in the autospectrums becomes evident. Figure 4.9a presents this shfit in wavelength, illustrating that the characteristic wavelength increases with applied frequency Ω. Further analysis indicates that this wavelength scales with $2\pi\sqrt{\frac{\epsilon}{1+\Omega}}$, the characteristic length scale in both $\psi(x)$ and $\delta(x)$ of the spatial analysis.

The spatial response of Figre 4.9b indicates a significant spatial decay in the charge density through the polymer thickness at higher excitation frequencies. Such behavior beomes intuitive as we consider the fundamental nature of the ion-transport membrane. Within the ionomer, ion motion is limited by the material's inherent time constant, which in turn is governed by the diffusion coefficient of the membrane. At low frequencies cations have a significant amount of time to redistribute throughout the transducer's thickness. As this excitation frequency

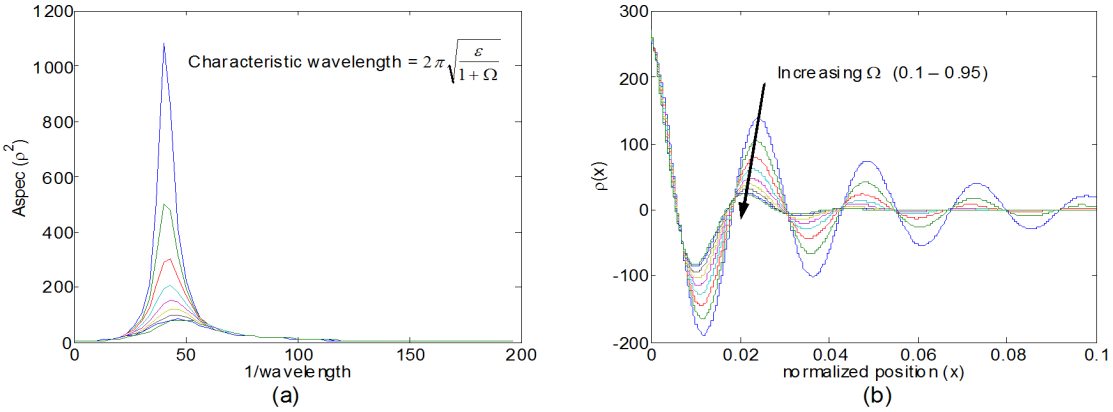

Figure 4.9: Wavelength analysis of the charge density's spatial response to low frequency harmonic excitation ($0.1 \leq \Omega \leq 0.95$). An autospectrum of the data shows that the characteristic wavelength is equal to $2\pi\sqrt{\frac{\epsilon}{1+\Omega}}$. Plot (b) presents the charge density simulations near the boundary of $x = 0$.

increases cations have less time to migrate through the polymer thickness, and as a result changes in charge density are limited to regions directly adjacent to the electrodes. This localization effect emphasizes the boundary layer region near the polymer surfaces at $x = 0$ and $x = 1$. At low frequencies we notice that the boundary layer is defined by the small scale parameter ϵ, just as it had been in the case of the step excitation discussed previously. As the excitation frequency increases further the boundary layer shifts closer toward the electrode surface, becoming smaller as a function of the driving frequency Ω through the relationship of $\frac{\epsilon}{1+\Omega}$.

Saturation limit as a function of frequency and potential

From thie induced charge density we can extend our analysis to examine the effects of harmonic excitation on the saturation phenomena that develops at higher excitation levels. In the previous case we considered the saturation effect purely as a function of the applied voltage associated with a step excitation. In the case of a harmonic driving signal we can integrate the effects of excitation frequency into our analysis of the saturation region as well. As in our analysis of the step excitation we define saturation to be the level at which the charge density near the anode reaches $\hat{\rho}(\hat{x}, \hat{t}) = -FC^{-}$. For a simple step change in the applied voltage, this saturation region was shown to form solely as a function of the applied voltage. In the case of a harmonic excitation frequency is expected to play a key role in determing the saturation level near the anode. Since cation motion is limited by the diffusion coefficient of the polymer, the excitation frequency will determine the time duration cations have to accumulate near the cathode. Thus at lower frequencies cations have longer to migrate through the polymer, resulting in a lower threshold voltage necessary to induce saturation at the IPT anode. Conversely, we expect higher frequencies to require larger applied voltages in order to achieve the same saturation effect.

To analyze the saturation phenomena we begin by considering the peak charge density as a function of

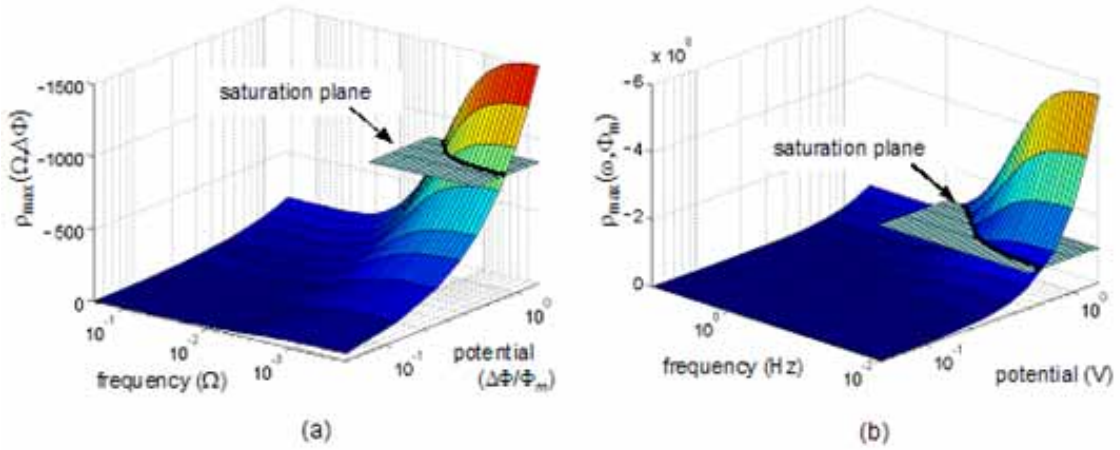

Figure 4.10: Peak charge density as a function of applied voltage and frequency. This figure includes both (a) nondimensional and (b) dimensional predictions of the saturation region. Dimensional simulations correspond to a Nafion-117 based transducer in Li^+ form.

the applied potential and driving frequency. The results of this analysis are presented for the nondimensional system in Figure 4.10a, and for the dimensional system in Figure 4.10b (Note the negative axes). Superimposed upon each of these figures is a saturation plane that corresponds to the critical charge density corresponding to $\rho_{\text{sat}}(x,t) = \frac{-L^2FC^-}{\kappa\Phi_m}$ in the nondimensional case, and to $\hat{\rho}_{\text{sat}}(\hat{x},\hat{t}) = -FC^-$ in the dimensional case. As the saturation plane intersects the peak charge density, a curve develops which corresponds to the critical frequency-potential relationship that induces saturation at the anode. To formulate this expression we begin with the forced charge density of equation 4.120,

$$\rho_f(x,t) = \frac{-\Delta\Phi}{2\sqrt{\bar{A}}\Upsilon_h}\left[\tilde{\psi}(x)\sin\Omega t + \tilde{\delta}(x)\cos\Omega t\right] \tag{4.120}$$

where $\tilde{\psi}(x)$ and $\tilde{\delta}(x)$ represent the spatial coefficients of the in-phase and out-of-phase terms of $\rho_f(x,t)$. Equating this with the saturation term $\rho_{\text{sat}}(x,t)$

$$\frac{-\Delta\Phi}{2\sqrt{\bar{A}}\Upsilon_h}\left[\tilde{\psi}(x)\sin\Omega t + \tilde{\delta}(x)\cos\Omega t\right] = \frac{-L^2FC^-}{\kappa\Phi_m} \tag{4.121}$$

Imposing the definition $\Delta\Phi = \frac{\hat{\Phi}_2 - \hat{\Phi}_1}{\Phi_m}$, we can solve for the critical potential difference $\Delta\hat{\Phi} = \hat{\Phi}_2 - \hat{\Phi}_1$ as,

$$\Delta\hat{\Phi} = \frac{2\sqrt{\bar{A}}\Upsilon_h L^2FC^-}{\kappa\left[\tilde{\psi}(x)\sin\Omega t + \tilde{\delta}(x)\cos\Omega t\right]} \tag{4.122}$$

This expression describes the critical potential difference as a function of space x, time t and the driving frequency

Ω. In this analysis we are most concerned with the potential corresponding to the peak charge density induced at the anode. Therefore we express the critical potential as a function of applied frequency by evaluating equation 4.122 at $x = x_{\text{anode}}$ and at the peak time $t = t_p$,

$$\Delta\hat{\Phi} = \left. \frac{2L^2 FC^{-}\sqrt{A}\Upsilon_h}{\kappa\left(\tilde{\psi}(x)\sin\Omega t + \tilde{\delta}(x)\cos\Omega t\right)} \right|_{\substack{t\,=\,t_p \\ x\,=\,x_{\text{anode}}}} \tag{4.123}$$

The peak time aluded to in this expression is a function of frequency, and will therefore change with Ω. This phase shift is evident in Figure 4.7 and ranges between 0^o and -90^o depending on the excitation frequency Ω. This phase relationship becomes very important in the next analysis which models the surface charge and current that develops at the IPT electrodes.

4.5.3 Developing surface charge and current models

In addition to the saturation analysis, we can use the internal charge density to develop models of the surface current that would be measurable at the outer surfaces of the polymer. Greeuw and Hoenders [28] present an anlytical approach to describe the transient ionic current that develops in a dielectric medium subject to an external voltage. Using this work as a basis, we define the general form of the isothermal transient ionic charge $Q_{it}(t)$ to be the spatial integral of $\hat{x}$ times the charge density $\hat{\rho}(\hat{x},\hat{t})$ through the material thickness.

$$\hat{Q}_{it}(\hat{t}) \quad = \quad \frac{1}{L}\int_0^L \hat{x}\,\hat{\rho}(\hat{x},\hat{t})d\hat{x}$$

This definition corresponds to the physical system, and therefore has not been nondimensionalized. Using the coordinate transformations outlined in equations 4.23 and 4.118, we express the transient charge as

$$\hat{Q}_{it}(\hat{t}) \quad = \quad \frac{1}{L}\int_0^1 Lx\,\frac{\kappa\Phi_m}{L^2}\rho(x,t)Ldx \quad = \quad \frac{\kappa\Phi_m}{L}\int_0^1 x\,\rho(x,t)dx$$

To formulate a unitless form of charge density, $Q_{it}(t)$, we impose a normalization of

$$Q_{it}(t) = \frac{L}{\kappa\Phi_m}\hat{Q}_{it}(\hat{t}) \tag{4.124}$$

Thus, we can express the nondimensional isothermal transient ionic charge as a function of either the charge density $\rho(x,t)$ or the internal potential $\phi(x,t)$,

$$Q_{it}(t) \quad = \quad \int_0^1 x\,\rho(x,t)dx \quad = \quad -\int_0^1 x\frac{\partial^2\phi(x,t)}{\partial x^2}dx \tag{4.125}$$

Similarly we must consider the isothermal transient ionic current (ITIC) in its nondimensional form. Since current is defined as the time derivative of charge, the ITIC will have the form

$$\hat{I}_{it}(\hat{t}) = \frac{d\hat{Q}_{it}(\hat{t})}{d\hat{t}} \tag{4.126}$$

Substituting our definitions for $\hat{Q}$ and $\frac{d}{dt}$ into this expression, we find that the current has the form

$$\hat{I}_{it}(\hat{t}) = \frac{\kappa\lambda\Phi_m}{L}\frac{dQ_{it}(t)}{dt} \tag{4.127}$$

Therefore, we nondimensionalize $I_{it}(t)$ by $\frac{L}{\kappa\lambda\Phi_m}$ to give us a unitless form of the ITIC,

$$I_{it}(t) \quad = \quad \frac{dQ_{it}(t)}{dt} \quad = \quad \frac{d}{dt}\left(\int_0^1 x\rho(x,t)\,dx\right) \quad = \quad -\frac{d}{dt}\left(\int_0^1 x\frac{\partial^2\phi(x,t)}{\partial x^2}dx\right) \tag{4.128}$$

The isothermal current defined in this expression represents the surface current as a function of the induced charge density within the IPT. Applying the forced charge density relationship $\rho_f(x,t)$ from equation 4.120 we get the isothermal transient ionic current,

$$\begin{aligned} I_{it}(t) \quad = \quad & \frac{-\Delta\Phi}{\sqrt{A}\,\Upsilon_h}\left(\cosh\frac{\sqrt{A}}{2}\sqrt{\bar{A}}\left[A\cosh\frac{\sqrt{A}}{2}\left((\epsilon a-1)\,\Omega\cos\Omega t + b\epsilon\Omega\sin\Omega t\right) - \sqrt{A}\sinh\frac{\sqrt{A}}{2}\left(2\epsilon\bar{A}\Omega\cos\Omega t + i\epsilon\bar{A}\Omega\sin\Omega t\right)\right]\right. \\ & \left. -\,\sin\frac{\sqrt{\bar{A}}}{2}\left[A\cosh\frac{\sqrt{A}}{2}\left(\Omega\left(\epsilon A-2\right)\cos\Omega t - i\epsilon A\Omega\sin\Omega t\right) + 4\sqrt{A}\sinh\frac{\sqrt{A}}{2}\left(\Omega\cos\Omega t\right)\right]\right) \end{aligned} \tag{4.129}$$

Physically this surface current represents the measurable current generated by an external potential that is applied across the ionic polymer's thickness. With this expression it is possible to construct an equivalent admittance model of the IPT by relating the input voltage to the predicted surface current. Consequently, we can invert this admittance model to produce an impedance model of the ionic polymer. Thus it is possible to sweep through a series of applied frequencies, noting the magnitude and phase of $I_{it}(t)$ and $\Phi(t)$ to generate an impedance response of the polymer, as shown in Figure 4.11. The response itself is indicative of a first order system, similar to the RC circuit analyzed in Figure 4.1. Using this simple RC system as an analogy, we can expand our analysis of the IPT to investigate the equivalent resistance and capacitance mechanisms that govern the impedance response of Figure 4.11.

Since the polymer in our model is driven by a sinusoidal excitation of the form $\Phi(t) = \frac{1}{2}\Delta\Phi\sin\Omega t$, it is evident that there are two principle components in the current response of equation 4.129: an in-phase term related to $\sin\Omega t$, and an out-of-phase term corresponding to $\cos\Omega t$. Separating the ITIC in this manner yields the in-phase $I_{ip}(t)$ component,

$$I_{ip}(t) \quad = \quad \frac{-\epsilon\Delta\Phi\Omega}{\sqrt{A}\,\Upsilon_h}\left(\cosh\frac{\sqrt{A}}{2}\sqrt{\bar{A}}\left[A\,b\cosh\frac{\sqrt{A}}{2} - i\sqrt{A}\sqrt{\bar{A}}\sinh\frac{\sqrt{A}}{2}\right] + iA^2\cosh\frac{\sqrt{A}}{2}\sinh\frac{\sqrt{A}}{2}\right)\sin\Omega t \tag{4.130}$$

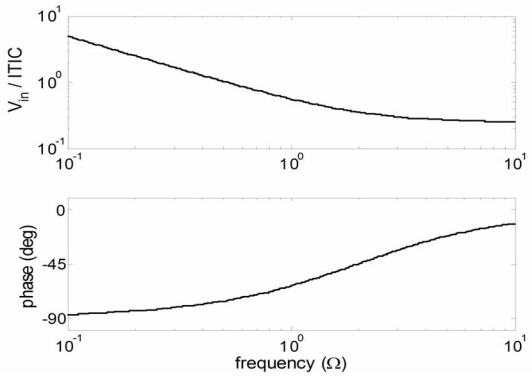

Figure 4.11: Frequency response predictions for the electrical impedance of the IPT. This plot relates the predicted ITIC to the applied voltage.

as well as the out-of-phase $I_{op}(t)$ component,

$$I_{op}(t) = \frac{-\Delta\Phi\Omega}{\sqrt{A}\ \Upsilon_h}\left(\cosh\frac{\sqrt{A}}{2}\sqrt{A}\left[A\left(\epsilon a-1\right)\cosh\frac{\sqrt{A}}{2}-\sqrt{A}\left(\epsilon\bar{A}-2\right)\sinh\frac{\sqrt{A}}{2}\right]\right.$$
$$\left.+\ \sinh\frac{\sqrt{A}}{2}\left[A\left(\epsilon A-2\right)\cosh\frac{\sqrt{A}}{2}-4\sqrt{A}\sinh\frac{\sqrt{A}}{2}\right]\right)\cos\Omega t \tag{4.131}$$

Using a simple RC analogy for the polymer, similar to that shown in Figure 4.1a, we can conceptually associate the in-phase component with the pseudo-conductance (R^{-1}) of the polymer. Similarly, we can correlate the out-of-phase component with the pseudo-susceptance ($2\pi fC$) of the system. The nomenclature of conductance and susceptance are used in this case because the polymer is being driven by the applied voltage $\Phi(t)$, resulting in an induced current $I_{it}(t)$. The corresponding admittance can be expressed as

$$Y = \sqrt{G^2+B^2} = \frac{I}{V} = \frac{I_{ip}(t)+I_{op}(t)}{\Phi(t)} \tag{4.132}$$

where G is the conductance and B is the susceptance of the polymer. From this expression we see that the conductance and susceptance cannot simply be taken as the ratios $\frac{I_{ip}(t)}{\Phi(t)}$ or $\frac{I_{op}(t)}{\Phi(t)}$, respectively. Expanding the admittance from equation 4.132 we see that G and B are related to the in-phase and out-of-phase terms of the ITIC through the expression,

$$G^2+B^2 = \frac{\left(I_{ip}(t)+I_{op}(t)\right)^2}{\Phi^2(t)} = \frac{I_{ip}^2(t)+2I_{ip}(t)I_{op}(t)+I_{op}^2(t)}{\Phi^2(t)} \tag{4.133}$$

From this the conductance G is defined as the component of $I_{ip}^2(t)+2I_{ip}(t)I_{op}(t)+I_{op}^2(t)$ that is in-phase with the applied potential, while the susceptance is defined as the out-of-phase component of $I_{ip}^2(t)+2I_{ip}(t)I_{op}(t)+I_{op}^2(t)$. At this point the coupling term $2I_{ip}(t)I_{op}(t)$ becomes important in determining the equivalent resistance and capacitance of the polymer. Since this term is related to G^2+B^2, the actual conductance and susceptance will be related to

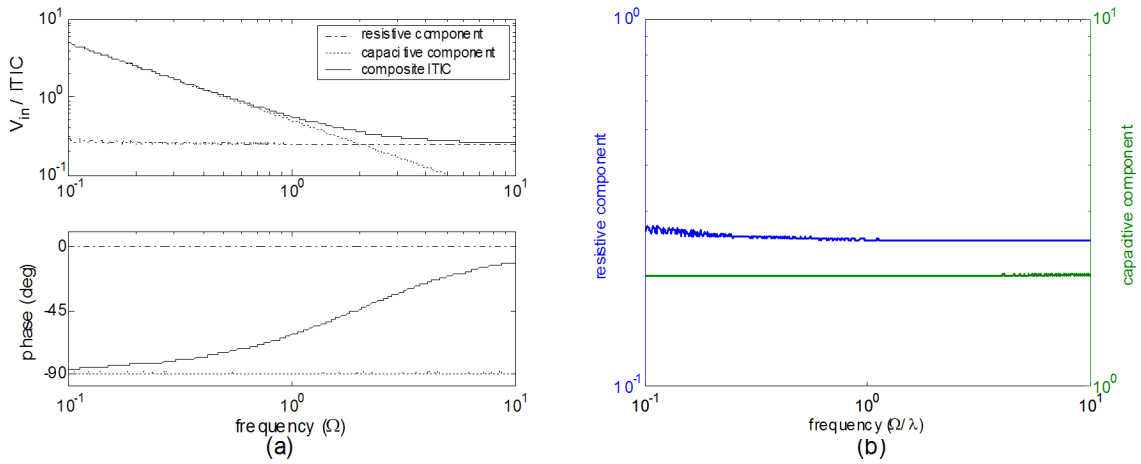

Figure 4.12: Impedance response broken into equivalent resistance and capacitance components. Results correspond to the nondimensional model and rely upon the equivalent circuit model $Z = R + \frac{1}{j\omega C}$.

$\sqrt{2I_{ip}(t)I_{op}(t)}$. Looking closely at this term we find that it cycles between real and imaginary values with time, while also introducing a phase shift of -45^o into the analysis. The presence of this term greatly complicates the analytical analysis, and therefore we redirect our focus to consider a complex impedance method to describe the equivalent resistance and capacitance of the model. In this manner we define the impedance to be the inverse of the admittance $Z = \frac{1}{Y}$ in accordance to fundamental electrical theory, giving us the relationship,

$$Z \quad = \quad = \frac{V}{I} \quad = \quad \frac{\Phi(t)}{I_{it}(t)} \tag{4.134}$$

Using a sine-dwell approach, we progress through the impedance analysis extracting magnitude and phase information between $\Phi(t)$ and $I_{it}(t)$, as functions of the applied frequency Ω. From this magnitude and phase information we construct a complex impedance representation defined as $Z = \bar{Z}e^{i\theta}$, where $\bar{Z}$ is the ratio of peak magnitudes of $\Phi(t)$ and $I_{it}(t)$, and θ defines the phase between $\Phi(t)$ and $I_{it}(t)$.

The complex impedance developed using this technique contains the same information used to generate the impedance response of Figure 4.11. The benefit of this representation is that we can now employ equivalent circuit models to extract profiles for the equivalent resistance and capacitance. Using the series representation $Z = R + \frac{1}{j\omega C}$ we extract the equivalent R and C components shown in Figure 4.12. The frequency response shown in Figure 4.12a presents the resistive (Z_r), capacitive (Z_c) and total (Z) impedance curves based upon the series representation of an equivalent RC circuit. From this figure we see that the total impedance tracks the capacitive response at low frequencies, then transitions to a resistive response beyond $\Omega = 2$. From the resistive Z_r and capacitive Z_c impedance profiles, we can extract equivalent $R = Z_r$ and $C = \frac{-1}{\Omega Z_c}$ values for the system. Figure 4.12b illustrates that the equivalent R and C values change very little with respect to driving frequency Ω. The capacitive response

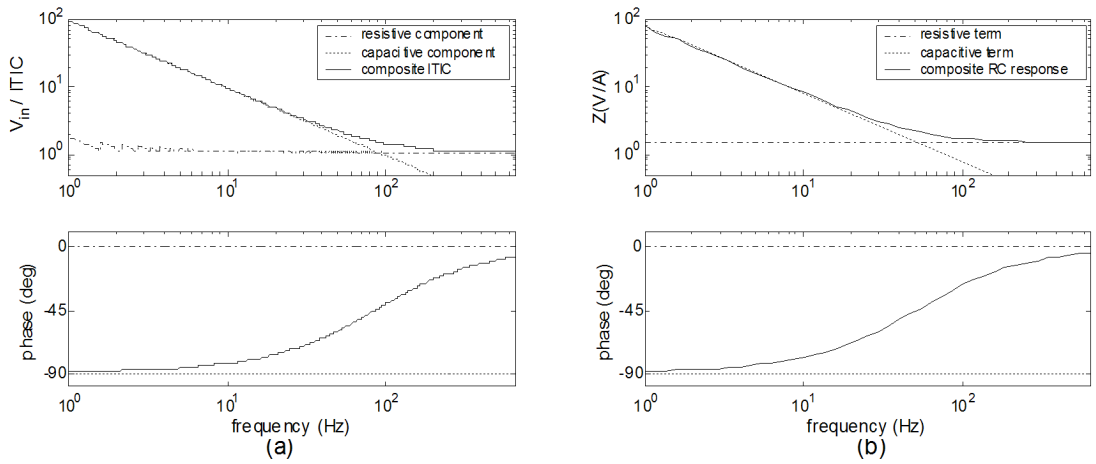

Figure 4.13: Impedance response broken into resistive and capacitive. Results correspond to a dimensional study of (a) the IPT model and (b) the simple RC circuit from Figure 4.1.

is nearly constant, while the resistance does exhibit a slight decay with increased frequency. There does appear to be a slight ripple in the low frequeny resistance response, most evident in the region $\Omega \leq 0.5$. This feature diminishes with higher resolution in the time simulations, and is therefore attributed to the step size used to evaluate the $\Phi(t)$ and $I_{it}(t)$ expressions.

We can extend this complex impedance method to consider the physical system by redimensionalizing the $I_{it}(t)$ and $\Phi(t)$ expressions. For this dimensional system the equivalent resistance is estimated to be 1.2 Ohms at high frequencies, with and equivalent capacitance estimated at 2 mF. Figure 4.13a presents the impedance response using physical values from Table 2.2. Figure 4.13b presents the response of a simple RC model whose resistance and capacitance values were chosen to correspond to the equivalent R and C values from the IPT simulation. The general form of this RC circuit is given in Figure 4.1a. Comparison of these simulations reveal almost identical results for the polymer-based impedance and the simple RC-circuit impedance.

4.5.4 Model v. experiment

At this point we extend our analysis to consider how well the analytic model compares to the measured response of an actual ionic polymer transducer. The model developed thus far in this chapter has focused on the nondimensional expressions for potential, charge density, surface charge and surface current. Therefore, it is necessary to consider the dimensional form of the model in order to compare simulation results with experimental data. To accomplish this dimensionalization we use the relationships outlined in Table 4.1 to extablish physical equivalents of the current and impedance models. Figure 4.14a presents the modeled impedance response based upon the physical values presented in Table 2.2. Next to these analytical predictions, the measured impedance response of a Nafion-based

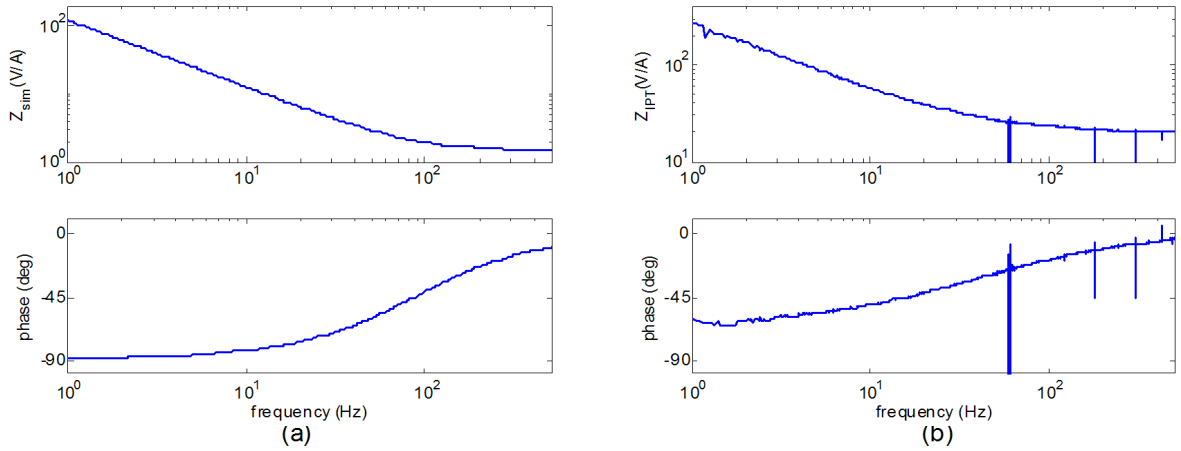

Figure 4.14: Comparison of the (a) predicted and (b) experimentally measured impedance response.

ionic polymer transducer is presented in Figure 4.14b. The values used in the simulation correspond to general parameters measured for Nafion and have not been adjusted or tuned to match those of the experimental sample tested in Figure 4.14b. While there exists some discrepancy between the high frequency magnitude of the predicted and measured impedance, there does appear to be good agreement in the general form of the responses. Time constants appear to correspond to frequencies between 70Hz and 80Hz in each case and the phase asymptotes to 0^o at higher frequencies. At lower frequencies the results of Figure 4.14 a & b begin to diverge as the experimental data exhibits a lower slope in the magnitude response, with the phase leveling off near 60^o. These features are attributed to a low frequency resistance associated with the poly-dispersed electrode of the experimental sample. The model does not address this electrode region, and therefore is not expected to capture the low frequency features of the experimental response.

To address the variations between the predicted and measured impedance responses, it is beneficial to consider the equivalent resistance and capacitance of the experimental data. To accomplish this we begin by imposing the simple equivalent impedance model $Z = R + \frac{1}{i\omega C}$ to extract frequency dependent R and C components from the experimental data. This model assumes an overall transducer resistance and capacitance, each of which are

Table 4.1: Relationship between physical and the nondimensional terms used in this analysis.

Quantity	Physical Variable	Dimensionless Expression	Quantity	Physical Variable	Dimensionless Expression
Position	$\hat{x}$	$x = \frac{\hat{x}}{L}$	Charge density	$\hat{\rho}(\hat{x},\hat{t})$	$\rho(x,t) = \frac{L^2}{\kappa\Phi_m}\hat{\rho}(\hat{x},\hat{t})$
Time	$\hat{t}$	$t = \lambda\hat{t}$	Surface charge	$\hat{Q}_{it}(\hat{t})$	$Q_{it}(t) = \frac{L}{\kappa\Phi_m}\ \hat{Q}_{it}(\hat{t})$
Potential	$\hat{\phi}(\hat{x},\hat{t})$	$\phi(x,t) = \frac{\phi(\hat{x},\hat{t})}{\Phi_m}$	Surface current	$\hat{I}_{it}(\hat{t})$	$I_{it}(t) = \frac{L}{\kappa\lambda\Phi_m}\ \hat{I}_{it}(\hat{t})$

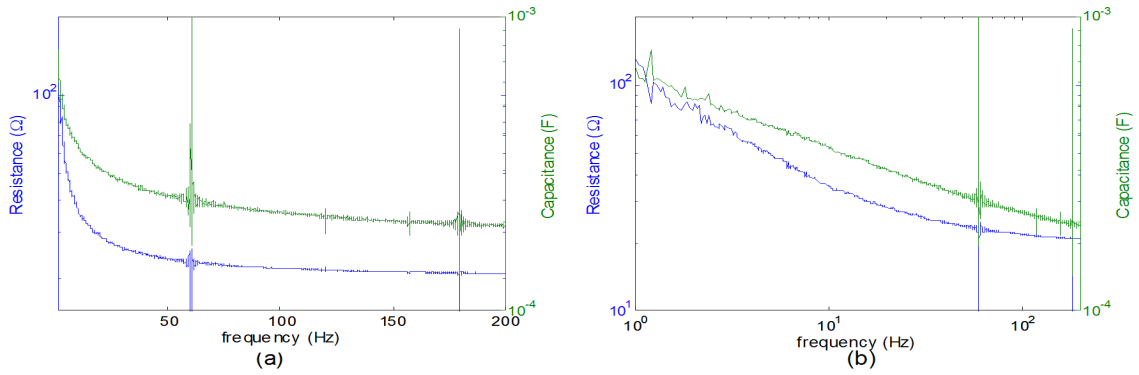

Figure 4.15: Equivalent resistive and capacitive components of the experimental data using a series RC equivalence model $Z = R + \frac{1}{j\omega C}$. Results are plotted with respect to (a) linear and (b) logrithmic frequency.

shown in Figure 4.15. Based upon the simple equivalence model used in this analysis, the results indicate that the poly-dispersed electrode introduces high DC resistance and capacitance, both of which decay at higher excitation frequencies. Relative to the overall impedance of the experimental sample, the high DC resistance is associated with the low frequency magnitude and phase response of the experimental impedance in Figure 4.14b. While this simple model does provide some insight into the overall resistance and capacitance of the physical transducer, it does not distinguish between the electrode and polymer regions. If we want to focus solely on the electroded region of the polymer, we must use a more detailed equivalence model to describe the experimental sample. To accomplish this we use a model similar to that proposed by Paquette *et al.* [73] (shown in Figure 4.2), defining the overall impedance to be

$$Z = R_m + \frac{2R_e}{1 + \omega^2 R_e^2 C_e^2} - i\frac{2\omega R_e^2 C_e}{1 + \omega^2 R_e^2 C_e^2} \tag{4.135}$$

where R_m is the membrane resistance, R_e is the electrode resistance and C_e is the electode capacitance. From this impedance relationship we can equate the real and imaginary components of the measured impedance with the real and imaginary components of equation 4.135. In this manner we can solve for the electrode resistance and capacitance in terms of the measured impedance $Z = Z_r + iZ_i$ and the membrane resistance R_m. This yields the solution

$$R_e = \frac{Z_r^2 + Z_i^2 + R_m^2 - 2R_m Z_r}{2\left(Z_r - R_m\right)} \qquad C_e = \frac{-2Z_i/\omega}{Z_r^2 + Z_i^2 + R_m^2 - 2R_m Z_r} \tag{4.136}$$

In the circuit diagram from Figure 4.2 we recognize that the electrode capacitance will act as a short circuit at high frequencies, enabling us to approximate R_m as the high frequency impedance of the system. With this value for R_m we can generate the equivalent electrode resistance and capacitance terms presented in Figure 4.16. In this

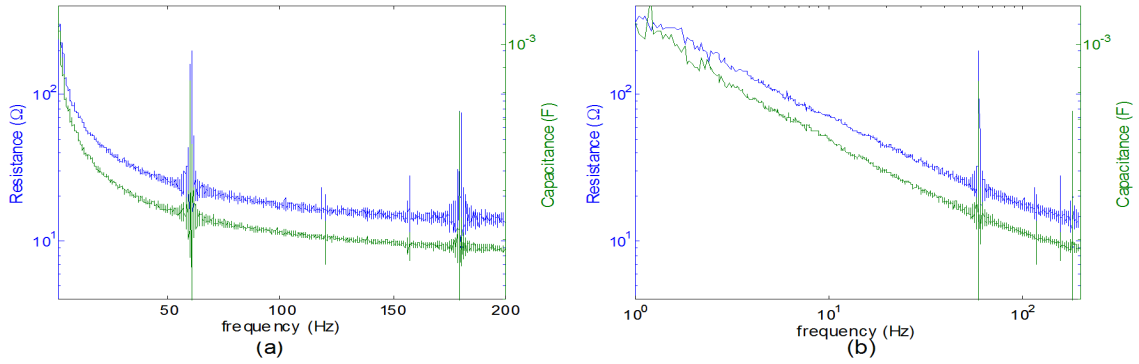

Figure 4.16: Equivalent resistive and capacitive components of the experimental data using the equivalent circuit model of equation 4.135. Results are plotted with respect to (a) linear and (b) logrithmic frequency.

case the membrane resistance is taken to be 20.2 Ohms and is assumed constant with frequency in accordance with the predictions of Figure 4.12b. The advantage of the equivalent impedance model from equation 4.135 is that it allows us to estimate the membrane resistance, and consequently it enables us to characterize the effects of the poly-dispersed electrode on the measured impedance. From Figure 4.16 we see that the electrode still exhibits a frequency dependent decay in R_e and C_e, however it is now noted that the decay rate is consistent for both the resistive and capacitive components of the electrode.

4.5.5 Parameter study

Through the model development of this chapter we have constructed a set of equations that enable us to predict the ionomer's induced current and subsequently the electrical impedance as a function of an applied potential. With this modeling capability, we now want to consider the influence of material and environmental parameters on the voltage to current relationship within the ionic polymer transducer. We begin this analysis by identifying three primary variables of interest: the diffusion coefficient d, the electrical permittivity κ and the ambient temperature T. The first two variables are chosen because they govern the polymer's ability to transport ions (d) and its ability to store charge (κ). The third variable is chosen because it relates to the ionomer's interaction with its environment.

In this manner we begin our parametric study with the membrane's diffusion coefficient d, results shown in Figure 4.17. Since this term defines the cation's ability to move within and through the transport membrane, variations in this parameter are expected to influence the resistive nature of the IPT. As a reference value the diffusion coefficient is taken to be the self-diffusion rate of a hydrated Nafion-117 membrane in Li^+ form. The nominal value for this diffusion coefficient is $d = 1.389 * 10^{-10} \frac{m^2}{s}$ [**?**]. Figure 4.17 presents the IPT impedance response for five variations in the diffusion coefficient, spanning from $0.01\ d$ to $100\ d$. In the nondimensional case of Figure 4.17a there is no measureable difference between the predicted impedance calculated for each diffusion coefficient. This

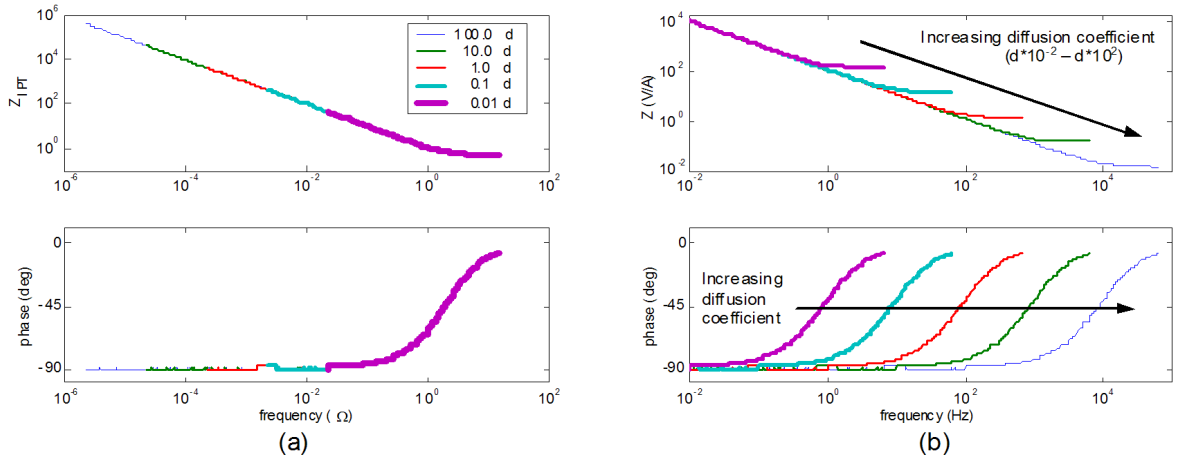

Figure 4.17: Impedance response as a function of the diffusion coefficient d. The effect of the diffusion coefficient is not very evident in the nondimensional case (a). However the dimensional case (b) indicates shifts in both magnitude and break frequency as a function of the d.

invariance to the diffusion coefficient is a result of the normalization process used to nondimensionalize the general continuity expression. Through normalizing the temporal coefficient by the system time constant $\lambda = d\frac{F^2C^-}{\kappa RT}$, we effectively remove the diffusion coefficient from the nondimensional analysis. Therefore we must consider the dimensional, or physical, representation of the ITIC if we want to study the effects of d on the transducer's impedance response. As we consider the dimensional response of Figure 4.17b it becomes evident that the resistive component changes dramatically as a function of d. As the diffusion coefficient increases we see a steady decline in the material's resistive behavior. In this manner the capacitive nature of the polymer dominates over a larger frequency band, driving the cut off frequency higher as the diffusion coefficient increases. Looking at this result from a physical standpoint we see that the behavior makes sense with respect to our shifts in the diffusion coefficient d. Specifically, an increased diffusion coefficient means that cations can diffuse through the material at a higher rate. Thus there is less opposition to the cation motion through the membrane and therefore lower resistance at higher diffusion coefficients.

The second parameter considered in this analysis is the effective permittivity κ of the transducer. Figure 4.18a presents the impedance response for four scalings of the permittivity, from 1 κ to 1000 κ, where κ is taken to be 2 mF/m. As in the case of the diffusion coefficient, the nondimensionalization process removes any influence that the permittivity has on the nondimensional response. Therefore the results presented Figure 4.18a only consider the physical, or dimensioned, system. From this figure it can be seen that κ scales the capacitive component of the impedance response, while maintaining a constant high frequency resistance value. Since the permittivity of a pure dielectric is directly related to capacitance, it makes sense that κ's predominant effect is on the low frequency capacitance of the ionic polymer. This shift in the material's capacitance causes a significant shift in the time constant

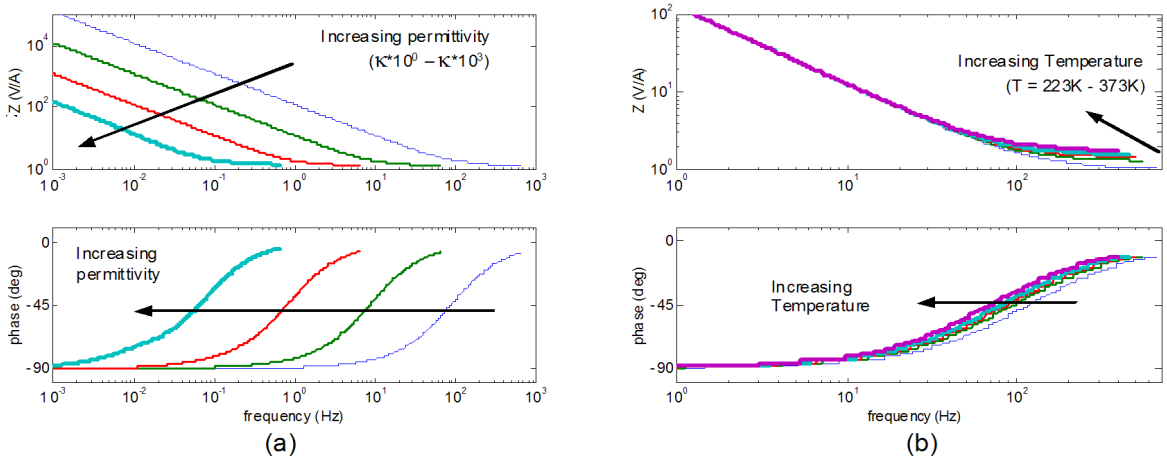

Figure 4.18: Impedance response as a function of (a) the electrical permittivity κ and (b) the ambient temperature T. Results are presented for the dimensional case.

of the polymer. The time constant itself, $\lambda = \frac{dF^2C^-}{\kappa RT}$, is inversely related to the effective permittivity, indictating that higher values of κ should result in a decrease in λ. This trend is evident in Figure 4.18a as the corner frequency of the polymer decreases steadily with increasing permittivity. In terms of the overall modeling approach, the effective permittivity provides a capacitance related term that functions independently from the diffusion coefficient considered in the previous analysis. While each of these parameters effect the transducer's time constant, the scale the overall shape of the impedance in distinctly different ways. Therefore, the parameters d and κ provide us with the ability to tune the resistive and capacitive characteristics of the impedance response independently, a feature which will be beneficial in predicting the effective properties of experimental measurement in Chapter 6.

The final parameter considered in this analysis is the ambient temperature T. While holding the other coefficients constant, we notice that the effects of temperature are very consistent with those of the electric permittivity discussed in the previous case. Figure 4.18b illustrates the impedance response as a function of temperature. Since the scalability of temperature is limited to a relatively small range, we consider temperature variations from 223K to 373K. We see that the system's time constant λ scales inversely with T, in much the same manner as it did with κ. Similarly we note that the polymer becomes more resistive with increasing temperature, and that λ subsequently decreases as well. While these results come directly from the model development, we must recognize that the predictions do not follow trends observed in initial experimental results. Several initial experiments indicate that the IPT's high frequency resistance actually decreases with a rise in temperature, contrary to the predictions of the model. To account for this discrepancy we revisit our model, incorporating interactions between the ambient temperature T and the diffusion coefficient d. Yeager *et al.* [98, 99] conducted several experimental studies that looked at the self-diffusion coefficient of $Na^+$and Cs^+through Nafion as a function of the ambient temperature. Yeager *et al.* found that the diffusion coefficient had a strong dependence on temperature for each of the counterions considered.

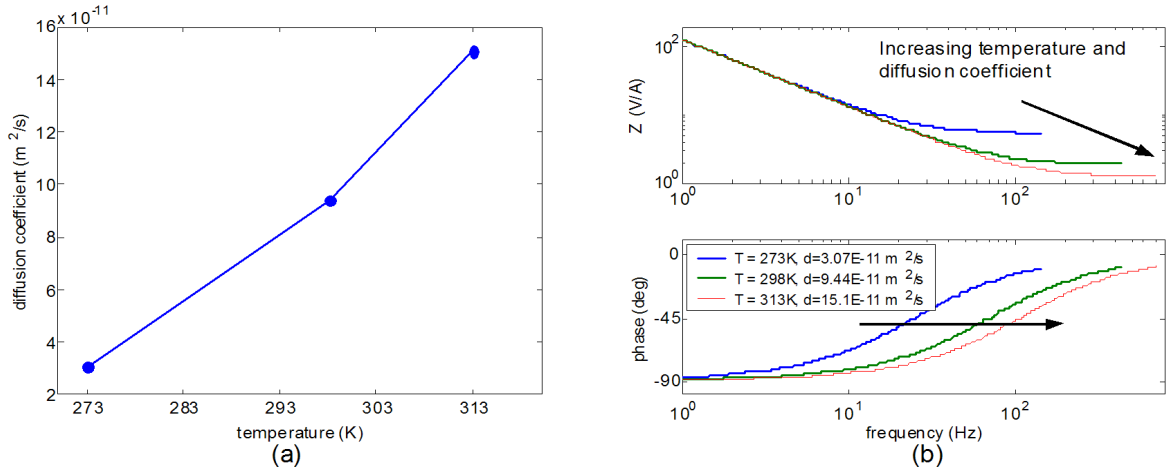

Figure 4.19: Impedance response as a function of the external temperature T and a temperature dependent diffusion coefficient d. This figure considers the response of a membrane in Na^+form. The figure includes (a) diffusion as a function of temperature and (b) the predicted impedance as a function of T and d.

A table of their results is shown in Table 4.2, and those values for the Na^+coutnerion are shown graphically in Figure 4.19a. Using the values of Yeager *et al.* we now consider the polymer's impedance as a function of temperature while incorporating the temperature variant diffusion coefficient for Na^+. The results shown in Figure 4.19b indicate that the temperature changes in the diffusion coefficient actually cause d to dominate the impedance response of the polymer. Figure 4.19b illustrates that the high frequency resistance should decrease with rising temperature due to coinciding increases in the diffusion coefficient. This response in particular will be investigated further in the experimental study of Chapter 6, at which point direct comparisons will be made between analytical predictions and experimental results.

Table 4.2: Diffusion coefficients as a function of temperature. Values are from work by Yeager and Steck [99].

		Diffusion Coefficient (m^2/s) - From Yeager and Steck [99]			
Ion	Temp (^{o}C)	I^a	I^b	I^c	II^d
Na^+	0	$3.07x10^{-11}$	$2.78x10^{-11}$		$3.18x10^{-11}$
	25	$9.44x10^{-11}$	$11.2x10^{-11}$		$9.83x10^{-11}$
	40	$15.1x10^{-11}$	$14.9x10^{-11}$		$14.8x10^{-11}$
Cs^+	0	$3.84x10^{-13}$	$3.80x10^{-13}$	$4.46x10^{-12}$	$3.63x10^{-12}$
	25	$5.20x10^{-12}$	$1.70x10^{-11}$	$2.38x10^{-11}$	$1.88x10^{-11}$
	40	$1.58x10^{-11}$	$3.37x10^{-11}$	$3.01x10^{-11}$	$2.67x10^{-11}$

4.6 Chapter summary

In this chapter the development of an induced current and impedance model for ionic polymer transducers has been presented. The modeling process began through electrostatic models of ion transport in ionomer membranes, relating the rate of cation motion to the Nernst-Planck equation for ion flux. From this continuity relationship the internal potential was derived as a function of an applied voltage at the transducer's boundaries. Next, field relationships were imposed to develop the induced steady-state charge density for both step and harmonic excitations. Saturation effects were also considered in each case as relationships were developed to describe the critical voltages that would induce saturation for both step and harmonic potentials. The charge density was then used to derive the isothermal transient ionic current induced by an applied potential. From this we could simulate the induced current measurable at the polymer's outer surfaces. With this relationship we could simply compare the induced current to the applied potential to develop a characteristic impedance response for the ionic polymer transducer. Comparing this relationship to experimental data we find good qualitative correlation in the polymer's transition from capacitive to resistive behavior as a function of frequency. From this model a parameter study was conducted to identify the effects that the diffusion coefficient d, electrical permittivity κ and temperature T have on the polymer's characteristic impedance. Results indicate that the transducer's high frequency resistance is most affected by these parameter. Increases in the diffusion coefficient d had the effect of decreasing the polymer's high frequency resistance, while also increasing the time constant λ. The permittivity κ showed an inverse effect on the IPT impedance. Increasing values of κ resulted in increased high frequency impedance, while also lowering the system's characteristic time λ. Temperature effects showed an interesting response. If all other coefficients are held constant, and T is the only variable considered, the polymer's impedance scales in the same manner as it did with variations in κ. From initial experimental testing this prediction counters physical data for the polymer. To address this discrepancy, studies by Yeager *et al.* [98, 99] were used to incorporate the temperature variation in the diffusion coefficient d. Thus the temperature study was altered slightly to incorporate temperature variations in d. These results showed that the changes in d outweighed those of T, causing the high frequency impedance of the polymer to decrease with increasing temperature. This result agrees qualitatively with experimental results and will be expanded upon further in Chapter 6.

Chapter 5

Effect of nonlinear components on the steady-state boundary layer

Most of the electrostatic models of ionic polymer transducers begin in the same manner presented in the impedance model of Chapter 4. Using basic transport theory, a nonlinear expression for ion flux is derived in accordance with the Nernst-Planck relationship. The spatial gradient of this ion flux is then related to the rate of cation motion within the polymer to produce a nonlinear continuity expression for the transducer. At this point the nonlinear term is considered to be negligible by relating the magnitude of coefficients on the linear and nonlinear terms. This reduces the system to a linearized continuity expression that is subject to potential and linear flux boundary conditions. The linearization simplifies much of the analysis, particularly in terms of the steady-state response for both step and harmonic exciations, as discussed in the previous chapter. The main limitation in this approach is the inability to extend the analysis to consider the transient response of the internal charge density.

In our development of the impedance response in chapter 4, numerous methods were used to investigate the linear transport model, trying to incorporate both transient and steady-state response characteristics into the analysis. In each of the methods a divergent expression was obtained for the transient charge density response. The eigenfuctions that result from the linear analysis remain bounded with respect to the potential function, but are subject to positive, periodic coefficients when used to develop the corresponding charge density. This effect produces a set of modeshapes that do not converge with the number of modes in the modal summation of $\rho(x,t)$. Thus, the charge density is seen to grow steadily larger as more modes are incorporated in the summation series that describes the linear transient analysis. This behavior is especially evident in the boundary layers that develop near the outer edges of the transducer. Looking again at the original nonlinear continuity expression,

$$\dot{\phi}^{''} - \varepsilon\phi^{iv} - \varepsilon N_2 \left[\phi^{'''}\phi^{'} + \left(\phi^{''}\right)^2\right] + \phi^{''} = 0 \tag{5.1}$$

we see that the nonlinearities correspond to $\phi^{'''}\phi^{'}$ and $\left(\phi^{''}\right)^2$. In terms of charge density, these nonlinearities can be expressed as $-\rho^{'}\phi^{'}$ and ρ^2. If we consider the saturation value that defines the limits of the symmetric model from Chapter 4, we see that the critical charge density has a value on the order of $1.5\text{x}10^3$ for the nondimensional system and 10^8 for the physical system. These values correspond to the charge density within the boundary layer and they indicate that the nonlinear terms may become influencial at these regions of large charge density. We also observe that the highest spatial derivative of the nonlinear continuity expreesion is subject to the small scale parameter ϵ. This feature is indicative of a boundary layer problem, similar to those studied by Nayfeh [57, 58]. In addition to this observation, we also note that the highest deriviative ϕ^{iv} is two orders higher than the linear term $\phi^{''}$ indicating that two boundary layers are expect to develop near the outer surfaces of the polymer.

In addition to the work by Nemat-Nasser *et al.* [61, 59], Wallmersperger *et al.* [89, 91, 47] have investigated the transport system, idtentifying boundary layer developments within ionic gels and polymers. The principle difference between Wallmersperger's and Nemat-Nasser's work is that Wallmersperger uses a numerical approach to approximate the full nonlinear continuity equation analogous to equation 5.1. The technique of Walmersperger *et al.* is developed for ionic gels and allows for ion motion in either the cation or the anion. For modeling of the ionic polymer, the anion concentration is constrained to be constant and the potential and charge density are solved for with respect to a spatial and time varying cation concentration. The key ability of their results are that they can predict the response of the full nonlinear system, simulating the induced potential and charge density responses for step and harmonic excitations. Work by Kothera and Leo [40, 41] have investgiated the effect and presence of nonlinearities in the ionic polymer's voltage to strain and current to strain relationships. Using experimental data Kothera and Leo separate the response into a voltage to current relationship and the current to strain relationship. From their analysis the polymer exhibits quadratic and cubic nonlinearities in the voltage to current relationship at low frequencies.

These results provide motivation as we extend our analysis to consider perturbation techniques that will enable us to analyze the boundary layer development for the linear and nonlinear form of the continuity expression. The method that will be considered in this analysis is the method of Matched Asymptotes as described by Nayfeh [57, 58]. This techique enables us to define three distinct regions within the polymer, one which describes the bulk of the polymer and two others which magnify the regions around the polymer's outer surfaces. The boundary conditions are then applied to the magnified regions near the outer surfaces, while the interface between each region is matched to produce an overall solution that describes the overall potential response throughout the ionic polymer. This approach will be applied to three variations of equation 5.1. These variations will each focus on the steady-state

response ($\dot{\phi} \rightarrow 0$), and look at 1.) the linear continuity equation (LCE) with linear boundary conditions, 2.) the LCE with nonlinear boundary conditions and 3.) the nonlinear continuity equation (NLCE) with nonlinear boundary conditions. The next section focuses on the steady-state form of this of the general continuity expression.

5.1 Method of Matched Asymptotes - Steady-State Solution

In this analysis we use the method of Matched Asymptotes to consider the boundary layer development that arises for linear and nonlinear forms of the steady-state continuity equation (SSCE). Thus we assume that the rate term $\dot{\phi}'' = 0$, giving us the SSCE,

$$-\epsilon\phi^{iv} - \epsilon N_2 \left[\phi''' \phi' + \left(\phi''\right)^2\right] + \phi'' = 0 \tag{5.2}$$

Since the highest order term is a function of the small scale parameter ϵ, this problem is expected to possess boundary layers. And the fact that there are two orders between the highest and the next highest linear term, we expect two distinct boundary layers to develop within the transducer. These boundary regions will be subject to the boundary conditions,

$$\begin{aligned} \phi|_{x=0} &= \Phi_1 \qquad \epsilon\phi''' - \phi' + \epsilon N_2 \phi'' \phi' \Big|_{x=0} = 0 \\ \phi|_{x=1} &= \Phi_2 \qquad \epsilon\phi''' - \phi' + \epsilon N_2 \phi'' \phi' \Big|_{x=1} = 0 \end{aligned} \tag{5.3}$$

From this set of equations we begin our examination of the boundary layers that develop within the potential profile. This section will consider three distinct formulations of the system. The first will consider the linear continuity equation (LCE) subject to the a set of linearized flux boundary conditions. The second will consider the LCE with nonlinear flux boundary conditions while the third will focus on the nonlinear continuity equation (NLCE) and the nonlinear flux boundary conditions. The subsequent simplifications and assumptions corresponding to each of these formulations will be presented in the following sections.

5.2 LCE subject to linear flux boundary conditions

The first of these formulations focuses on the linear form of equations 5.2 and 5.3. Neglecting the nonlinear terms in these equations we develop the linear continuity expression

$$-\epsilon\phi^{iv} + \phi'' = 0 \tag{5.4}$$

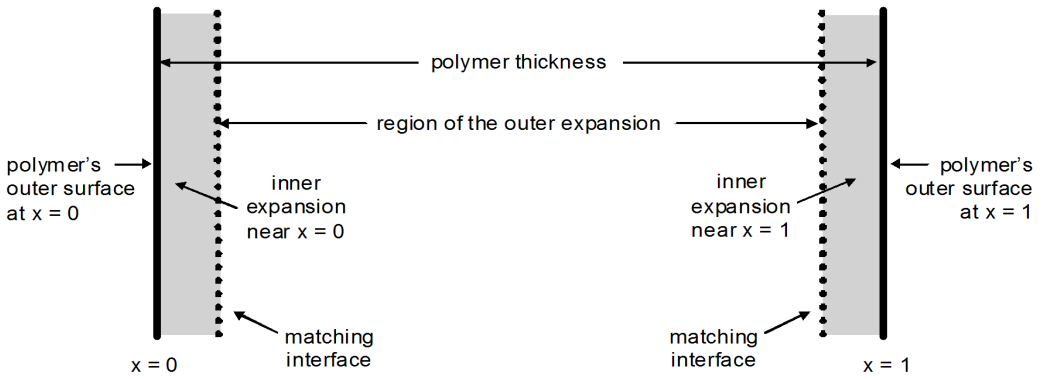

Figure 5.1: Diagram explaining the different regions refered to in the matched asymptotes analysis.

with boundary conditions,

$$\phi|_{x=0} = \Phi_1, \qquad \epsilon\phi''' - \phi'\Big|_{x=0} = 0, \qquad \phi|_{x=1} = \Phi_2, \qquad \epsilon\phi''' - \phi'\Big|_{x=1} = 0 \tag{5.5}$$

This expression is of fourth order and the highest order derivative is multiplied by the small parameter ϵ, indicating that it most likely contains at least one boundary layer. Since the highest order derivative is two orders higher than the next we expect two boundary layers to develop, one at each of the electrode interfaces at $x = 0$ and $x = 1$.

5.2.1 Outer expansion - LCE with *Linear BCs*

The first step in this analysis is to examine the expansion that exists between the boundary layers at $x = 0$ and $x = 1$. Looking at the diagram in Figure 5.1, this region corresponds to the bulk of the polymer that does not encompass the boundary layers near $x = 0$ and $x = 1$. This region is referred to as the outer expansion in accordance with the nomenclature of Nayfeh [57]. We begin by imposing a two-term outer expansion of the form,

$$\phi^o = \varphi_0(x) + \delta(\epsilon)\varphi_1(x) + ... \tag{5.6}$$

where $\delta(\epsilon)$ is defined such that $\delta(\epsilon) \to 0$ as $\epsilon \to 0$. For our specific system this function must have the form $\sqrt{\epsilon}$ to properly facilitate matching between the outer and inner expansions. The rationale for this form of $\delta(\epsilon)$ will become apparent as we introduce the stretching transformations in the inner expansions. For now however we will simply note that $\delta(\epsilon) = \sqrt{\epsilon}$. At this point we apply this definition and substitute the outer expansion into the LCE.

$$\epsilon\left(\varphi_0^{iv}(x) + \sqrt{\epsilon}\varphi_1^{iv}(x) + ...\right) - \left(\varphi_0''(x) + \sqrt{\epsilon}\varphi_1''(x) + ...\right) = 0 \tag{5.7}$$

This expression contains terms that are of varying order of ϵ. To satisfy this expresssion it is helpful to group like powers of ϵ and equate them to the corresponding powers of ϵ on the right-hand side of the equation, namely order $\left(\epsilon^0\right)$, order $\left(\epsilon^{1/2}\right)$ and so forth. Thus, by equating like powers of ϵ we develop a set of differential equations in terms of φ_0 and φ_1 which have the form,

$$\begin{aligned} \mathcal{O}\left(\epsilon^0\right) &\rightarrow \varphi_0'' = 0 \\ \mathcal{O}\left(\epsilon^{1/2}\right) &\rightarrow \varphi_1'' = 0 \end{aligned}$$

Focusing first on the $\mathcal{O}(\epsilon^0)$ equation, the general solution for φ_0 has the form

$$\varphi_0 = A_0 x + B_0 \tag{5.8}$$

Since the $\mathcal{O}\left(\epsilon^0\right)$ expression is not coupled with the $\mathcal{O}\left(\epsilon^{1/2}\right)$, but nonetheless has the same form, we can write the general solution for φ_1 as,

$$\varphi_1 = A_1 x + B_1 \tag{5.9}$$

Substituting the general solutions for φ_0 and φ_1 back into the outer expansion, it is possible to formulate the overall expression for ϕ^o,

$$\phi^o = A_0 x + B_0 + \sqrt{\epsilon}\left(A_1 x + B_1\right) + ... \tag{5.10}$$

Since this outer expansion does not extend to either of the surfaces of the polymer, it is not expected to necessarily satisfy either of the boundary conditions explicitly. Therefore it is necessary to extend the analysis to incorporate the two inner expansions near $x = 0$ and $x = 1$ in order to gain additional insight into each of the boundary layers from Figure 5.1.

5.2.2 Inner expansion near $x = 0$ - LCE with *Linear BCs*

Next we consider the inner expansion near $x = 0$. As we consider this inner expansion it is necessary to introduce a stretching transformation that will allow us to magnify the region around the left boundary from Figure 5.1. In terms of the general system from equation 5.4, the small parameter ϵ can be viewed as a characteristic length of the LCE. Therefore it is beneficial to formulate the stretched coordinate in terms of this ϵ term, yielding the stretching transformation,

$$\xi = \frac{x}{\epsilon^\nu} \quad \text{or} \quad x = \epsilon^\nu \xi \tag{5.11}$$

where ν is a general parameter defined such that $\nu > 0$. Applying this transformation to the potential function, we can formulate ϕ and its derivatives in the form

$$\phi(x) = \epsilon^{\nu}\xi, \qquad \frac{\partial^n \phi}{\partial x^n} = \epsilon^{-n}\frac{\partial^n \phi^i}{\partial \xi^n} \tag{5.12}$$

From this information it is possible to transform the linear differential equation 5.4 in terms of the magnified coordinate ξ,

$$\epsilon^{1-4\nu}\frac{d^4\phi^i}{d\xi^4} - \epsilon^{-2\nu}\frac{d^2\phi^i}{d\xi^2} = 0. \tag{5.13}$$

Next we consider what happens as the parameter becomes significantly small, to the limit where $\epsilon \to 0$. In this case the distinguished limit of equation 5.13 corresponds to the case where $1 - 4\nu = -2\nu$, or specifically where $\nu = \frac{1}{2}$. From this, the stretching transformation for the system has the form $\xi = \frac{x}{\sqrt{\epsilon}}$, and consequently the inner expansion ϕ^i is governed by the expression

$$\epsilon^{-1}\left(\frac{d^4\phi^i}{d\xi^4} - \frac{d^2\phi^i}{d\xi^2}\right) \quad = \quad \frac{d^4\phi^i}{d\xi^4} - \frac{d^2\phi^i}{d\xi^2} \quad = \quad 0 \tag{5.14}$$

At this point we consider a two term expansion for ϕ^i,

$$\phi^i = \psi_0(\xi) + \sqrt{\epsilon}\,\psi_1(\xi) + ... \tag{5.15}$$

Substituting this two-term expansion back into the governing differential equation for ϕ^i from equation 5.14 we find,

$$\left(\psi_0^{iv}(\xi) + \sqrt{\epsilon}\psi_1^{iv}(\xi) + ...\right) - \left(\psi_0^{''}(\xi) + \sqrt{\epsilon}\psi_1^{''}(\xi) + ...\right) \quad = \quad 0 \tag{5.16}$$

As in the case of the outer expansion we group like powers of ϵ, developing a set of partial differential equations that describe ψ_0 and ψ_1. Equating orders of ϵ^0 and $\epsilon^{1/2}$ we obtain the system of equations

$$\mathcal{O}(\epsilon^0) \quad \to \quad \psi_0^{iv} - \psi_0^{''} \quad = \quad 0 \tag{5.17}$$

$$\mathcal{O}(\epsilon^{1/2}) \quad \to \quad \psi_1^{iv} - \psi_1^{''} \quad = \quad 0 \tag{5.18}$$

Next, we consider the boundary conditions as they correspond to the inner expansion at $\xi = 0$. We accomplish this by first transforming the boundary conditions at $x = 0$ to the magnified coordinate ξ. Since $\xi = 0$ when $x = 0$, the potential boundary condition $\phi_{x=0} = \Phi_1$ can be written in terms of the magnified coordinate as

$$\phi^i(0) = \Phi_1 \tag{5.19}$$

To formulate the flux boundary condition in terms of the innner expansion, it is helpful to define the spatial derivatives in terms of the stretching parameter for $\nu = \frac{1}{2}$. In this manner we can relate $\frac{d^n\phi^i}{dx^n}$ to $\frac{d^n\phi^i}{d\xi^n}$ as

$$\frac{d^n\phi^i}{dx^n} = \frac{1}{\epsilon^{n/2}}\frac{d^n\phi^i}{d\xi^n}. \tag{5.20}$$

Applying this definition to the flux boundary condition, we can rephase the second expression from equation 5.5 in terms of the magnified coordinate ξ,

$$\begin{aligned}\epsilon \cdot \frac{1}{\epsilon^{3/2}}\frac{d^3\phi^i}{d\xi^3} - \frac{1}{\epsilon^{1/2}}\frac{d\phi^i}{d\xi}\bigg|_{\xi=0} &= \frac{1}{\epsilon^{1/2}}\left[\frac{d^3\phi^i}{d\xi^3} - \frac{d\phi^i}{d\xi}\right]_{\xi=0} = 0, \\ \frac{d^3\phi^i}{d\xi^3} - \frac{d\phi^i}{d\xi}\bigg|_{\xi=0} &= 0.\end{aligned} \tag{5.21}$$

Substituting the inner expansion for ϕ^i from equation 5.15 into the boundary conditions of the magnified coordinate ξ we get

$$\psi_0 + \sqrt{\epsilon}\psi_1 = \Phi_1, \qquad \psi_0^{'''} + \sqrt{\epsilon}\psi_1^{'''} - \psi_0^{'} - \sqrt{\epsilon}\psi_1^{'} = 0. \tag{5.22}$$

Equating like powers of ϵ yields a set of four boundary conditons at $\xi = 0$, defined as

$$\mathcal{O}(\epsilon^0) \quad \rightarrow \quad \psi_0(0) = \Phi_1 \qquad \psi_0^{'''}(0) - \psi_0^{'}(0) = 0, \tag{5.23}$$

$$\mathcal{O}(\epsilon^{1/2}) \quad \rightarrow \quad \psi_1(0) = 0 \qquad \psi_1^{'''}(0) - \psi_1^{'}(0) = 0 \tag{5.24}$$

In this set of expressions we recognize that the potential boundary condition Φ_1 is applied to the zeroth order term, and that no additional information is added through the first order boundary conditions applied in the $\mathcal{O}\left(\epsilon^{1/2}\right)$ case. Since the first order term does not add any additional information, it may be sufficient to simply consider a one term expansion for ϕ^i. However, for generality we will continue our development while including φ_1 and discuss it's effects at the conclusion of this derivation. Thus we consider the general solutions for ψ_0 and ψ_1, each having the form,

$$\psi_0 = a_0 + b_0\xi + c_0e^{-\xi} + d_0e^{\xi} \qquad \psi_1 = a_1 + b_1\xi + c_1e^{-\xi} + d_1e^{\xi} \tag{5.25}$$

Since the exponential terms e^{ξ} grow unbounded, we define their coefficients d_0 and d_1 to be 0, giving us the solutions

$$\psi_0 = a_0 + b_0\xi + c_0e^{-\xi} \qquad \psi_1 = a_1 + b_1\xi + c_1e^{-\xi} \tag{5.26}$$

We now want to apply the boundary conditions from equations 5.23 and 5.24 to each of these solutions. This yields the conditions

$$\psi_0(0) = a_0 + c_0 = \Phi_1 \quad \rightarrow a_0 = \Phi_0 - c_0, \qquad \psi_0^{'''}(0) - \psi_0^{'}(0) = -c_0 - (b_0 - c_0) = 0 \quad \rightarrow b_0 = 0$$
$$\psi_1(0) = a_1 + c_1 = 0 \quad \rightarrow a_1 = -c_1, \qquad \psi_1^{'''}(0) - \psi_1^{'}(0) = -c_1 - (b_1 - c_1) = 0 \quad \rightarrow b_1 = 0$$

From which we can formulate the general solution for the inner expansion ϕ^i

$$\phi^i = \Phi_1 - c_0\left(1 - e^{-\xi}\right) - \sqrt{\epsilon}c_1\left(1 - e^{-\xi}\right) \tag{5.27}$$

Matching the two-term inner and outer expansions near x = 0

With the inner expansion defined near $x = 0$ we now consider matching the inner and outer expansions in this region. The matching process begins by considering the outer/inner expansions and rewriting them in terms of the inner/outer variable, respectively. This transformation enables us to group like powers of ϵ and analyze the system as ϵ becomes small. Therefore we begin the matching process by considering the outer expansion,

- Two-term outer expansion: $\phi^o \sim A_0 x + B_0 + \sqrt{\epsilon}\left(A_1 x + B_1\right)$
- Rephrase in terms of inner variable: $= \sqrt{\epsilon}A_0\xi + B_0 + \epsilon A_1 x + \sqrt{\epsilon}B_1$
- Expanding for small ϵ: $= B_0 + \sqrt{\epsilon}\left(A_0\xi + B_1\right) + \epsilon A_1\xi$
- Two-term inner expansion: $= B_0 + \sqrt{\epsilon}\left(A_0\xi + B_1\right)$

This defines the first matching point between the outer and inner expansions. To continue this analysis we transform the inner expansion into the outer variable,

- Two-term inner expansion: $\phi^i \sim \Phi_1 - c_0\left(1 - e^{-\xi}\right) - \sqrt{\epsilon}c_1\left(1 - e^{-\xi}\right)$
- Rephrase in terms of outer variable: $= \Phi_1 - c_0\left(1 - e^{-x/\sqrt{\epsilon}}\right) - \sqrt{\epsilon}c_1\left(1 - e^{-x/\sqrt{\epsilon}}\right)$
- Expanding for small ϵ: $= \Phi_1 - c_0 + c_0 e^{-x/\sqrt{\epsilon}} - \sqrt{\epsilon}c_1 + \sqrt{\epsilon}c_1 e^{-x/\sqrt{\epsilon}}$
- Two-term outer expansion: $= \Phi_1 - c_0 - \sqrt{\epsilon}c_1$

At this point we equate the two-term inner and outer expansions,

$$B_0 + \sqrt{\epsilon}\left(A_0\xi + B_1\right) = \Phi_1 - c_0 - \sqrt{\epsilon}c_1 \tag{5.28}$$

Re-expressed in terms of x,

$$B_0 + A_0 x + \sqrt{\epsilon} B_1 = \Phi_1 - c_0 - \sqrt{\epsilon} c_1 \tag{5.29}$$

we can now equate coefficients of x and $\sqrt{\epsilon}$ to yield a set of relationships between coefficients of the inner and outer expansions

$$B_0 = \Phi_1 - c_0 \qquad A_0 = 0 \qquad B_1 = -c_1 \tag{5.30}$$

5.2.3 Inner expansion near $x = 1$ - LCE with *Linear BCs*

The next step in our analysis focuses on matching the inner and outer expansions near $x = 1$ for the linear continuity equation. The matching process follows the same procedure as in the expansion near $x = 0$, and will be considered repeatedly in the developments of the LCE with nonlinear boundary conditions and the nonlinear continuity equation (NLCE) with nonlinear boundary conditions. To help organize their presentation, the matching process will be presented side-by-side so that the outer and inner expansions can be compared more directly. Four principle steps will be conducted on each expansion and are outlined in the following manner,

	Outer expansion	Inner expansion
1.)	Two-term outer expansion	Two-term inner expansion
2.)	Rewrite in inner variable	Rewrite in outer variable
3.)	Expand for small ϵ	Expand for small ϵ
4.)	Two-term inner expansion	Two-term outer expansion

In the previous section we considered the outer and inner expansions near the left boundary of the polymer transducer depicted in Figure 5.1. Next we consider the inner expansion near $x = 1$. As in the inner expansion near $x = 0$, we introduce a stretching parameter which magnifies the spatial region near the boundary of the polymer. Near $x = 1$ we introduce the stretching coordinate ζ

$$\zeta = \frac{1 - x}{\epsilon^\nu} \quad \text{or} \quad x = 1 - \epsilon^\nu \zeta \quad \text{where} \quad \nu > 0. \tag{5.31}$$

Again we consider the derivatives associated with this transformation, expressing the n^{th} derivative as $\frac{\partial^n \phi^I}{\partial x^n} = \left(\frac{-1}{\epsilon^\nu}\right)^n \frac{\partial^n \phi^I}{\partial \zeta^n}$. Applying this transformation to the linear differential expression from equation 5.6,

$$\epsilon^{1-4\nu} \frac{\partial^4 \phi^I}{\partial \zeta^4} - \epsilon^{-2\nu} \frac{\partial^2 \phi^I}{\partial \zeta^2} = 0 \tag{5.32}$$

As in the expansion near $x = 0$, the distinguishing limit occurs when $\nu = \frac{1}{2}$. Thus the inner expansion of the linear differential equation near $x = 1$ has the form

$$\frac{\partial^4 \phi^I}{\partial \zeta^4} - \frac{\partial^2 \phi^I}{\partial \zeta^2} = 0 \tag{5.33}$$

We express the two-term inner expansion for ϕ^I in the form

$$\phi^I = \tilde{\psi}_0(\zeta) + \sqrt{\epsilon}\,\tilde{\psi}_1(\zeta) + ... \tag{5.34}$$

Substituting this into equation 5.33 and equating like powers of ϵ,

$$\mathcal{O}(\epsilon^0) \quad \rightarrow \quad \tilde{\psi}_0^{iv} - \tilde{\psi}_0'' \quad = \quad 0 \tag{5.35}$$

$$\mathcal{O}(\epsilon^{1/2}) \quad \rightarrow \quad \tilde{\psi}_1^{iv} - \tilde{\psi}_1'' \quad = \quad 0 \tag{5.36}$$

At this point we consider the boundary conditions at $x = 1$ as they correspond to the stretched region of the inner expansion. The first thing that must be done is to consider how the originial boundary condition translates into the magnified coordinate ζ. We recognize that $x = 1$ corresponds to $\zeta = 0$ through our definition of the stretching transformation, enabling us to define the potential boundary condition $\phi|_{x=1} = \Phi_2$ as

$$\phi^I\big|_{\zeta=0} = \Phi_2 \tag{5.37}$$

Applying the stretching transformation to the flux boundary conditions yields the expression

$$\frac{d^3\phi^I}{d\zeta^3} - \frac{d\phi^I}{d\zeta}\bigg|_{\zeta=0} \quad = \quad 0. \tag{5.38}$$

Substituting the inner expansion of ϕ^I from equation 5.34 into these boundary conditions produces the set of relationships

$$\tilde{\psi}_0 + \sqrt{\epsilon}\tilde{\psi}_1 = \Phi_2 \qquad\qquad \tilde{\psi}_0''' + \sqrt{\epsilon}\tilde{\psi}_1''' - \psi_0' - \sqrt{\epsilon}\tilde{\psi}_1' = 0. \tag{5.39}$$

Equating powers of ϵ produces a set of four boundary conditons at $\zeta = 1$, defined as

$$\mathcal{O}(\epsilon^0) \quad \rightarrow \quad \tilde{\psi}_0(0) = \Phi_2 \qquad \tilde{\psi}_0'''(0) - \tilde{\psi}_0'(0) = 0, \tag{5.40}$$

$$\mathcal{O}(\epsilon^{1/2}) \quad \rightarrow \quad \tilde{\psi}_1(0) = 0 \qquad \tilde{\psi}_1'''(0) - \tilde{\psi}_1'(0) = 0. \tag{5.41}$$

At this point we return to the differential equations 5.35 and 5.36 which constitute the inner expansion near $x = 1$. As in the case of the expansion near $x = 0$ the solutions have the form

$$\tilde{\psi_0} = \tilde{a}_0 + \tilde{b}_0\zeta + \tilde{c}_0 e^{-\zeta}, \qquad \tilde{\psi_1} = \tilde{a}_0 + \tilde{b}_0\zeta + \tilde{c}_1 e^{-\zeta} \tag{5.42}$$

where the exponentially growing terms have again been ignored. Imposing the boundary conditions and solving for the constants enables us to express the two-term inner expansion as

$$\phi^I = \Phi_2 - \tilde{c}_0\left(1 - e^{-\zeta}\right) - \sqrt{\epsilon}\tilde{c}_1\left(1 - e^{-\zeta}\right) + ... \tag{5.43}$$

Performing matching of the two-term outer and inner expansions yields

	Outer expansion			Inner expansion		
1.)	$\psi^o \sim$	$A_0 x + B_0 + \sqrt{\epsilon}(A_1 x + B_1)$	$\psi^i \sim$	$\Phi_2 - \tilde{c}_0\left(1 - e^{-\zeta}\right) - \sqrt{\epsilon}\tilde{c}_1\left(1 - e^{-\zeta}\right)$	
2.)	$=$	$A_0(1 - \sqrt{\epsilon}\zeta) + B_0 + \sqrt{\epsilon}\left(A_1(1 - \sqrt{\epsilon}\zeta) + B_1\right)$	$=$	$\Phi_2 - \tilde{c}_0\left(1 - e^{\frac{-(1-x)}{\sqrt{\epsilon}}}\right) - \sqrt{\epsilon}\tilde{c}_1\left(1 - e^{\frac{-(1-x)}{\sqrt{\epsilon}}}\right)$	
3.)	$=$	$A_0 + B_0 + \sqrt{\epsilon}(A_1 + B_1 - A_0\zeta) + \epsilon A_1\zeta$	$=$	$\Phi_2 - \tilde{c}_0 + \tilde{c}_0 e^{\frac{-(1-x)}{\sqrt{\epsilon}}} - \sqrt{\epsilon}\tilde{c}_1 + \sqrt{\epsilon}\tilde{c}_1 e^{\frac{-(1-x)}{\sqrt{\epsilon}}}$	
4.)	$=$	$A_0 + B_0 + \sqrt{\epsilon}(A_1 + B_1 - A_0\zeta)$	$=$	$\Phi_2 - \tilde{c}_0 - \sqrt{\epsilon}\tilde{c}_1$	

Comparing the results of the two-term matching at $x = 1$ we find

$$\begin{aligned} A_0 + B_0 + \sqrt{\epsilon}(A_1 + B_1 - A_0\zeta) &= \Phi_2 - \tilde{c}_0 - \sqrt{\epsilon}\tilde{c}_1 \\ A_0 + B_0 + \sqrt{\epsilon}(A_1 + B_1 - A_0\frac{1-x}{\sqrt{\epsilon}}) &= \Phi_2 - \tilde{c}_0 - \sqrt{\epsilon}\tilde{c}_1 \\ B_0 + A_0 x + \sqrt{\epsilon}(A_1 + B_1) &= \Phi_2 - \tilde{c}_0 - \sqrt{\epsilon}\tilde{c}_1 \end{aligned} \tag{5.44}$$

From this we can solve for the relationship between coefficients of the inner and outer expansions

$$B_0 = \Phi_2 - \tilde{c}_0, \qquad A_0 = 0, \qquad A_1 + B_1 = \tilde{c}_1 \tag{5.45}$$

Combining these results with the matching conducted near $x = 0$

$$\begin{aligned} c_0 &= \Phi_1 - B_0 \qquad & c_1 &= B_1 \\ \tilde{c}_0 &= \Phi_2 - B_0 \qquad & \tilde{c}_1 &= A_1 + B_1 \end{aligned} \tag{5.46}$$

The composite solution for this problem will have the form

$$\begin{aligned}\phi^c &= \phi^o + \phi^i + \phi^I - \left(\phi^i\right)^o - \left(\phi^I\right)^o \\ &= B_0 + \sqrt{\epsilon}(A_1 x + B_1) + \Phi_1 - (\Phi_1 - B_0)\left(1 - e^{-\xi}\right) - \sqrt{\epsilon}B_1\left(1 - e^{-\xi}\right) \\ &\quad + \Phi_2 - (\Phi_2 - B_0)\left(1 - e^{-\zeta}\right) - \sqrt{\epsilon}(A_1 + B_1)\left(1 - e^{-\zeta}\right) \\ &\quad - \left(\Phi_1 - (\Phi_1 - B_0) - \sqrt{\epsilon}B_1\right) - \left(\Phi_2 - (\Phi_2 - B_0) - \sqrt{\epsilon}(A_1 + B_1)\right)\end{aligned} \tag{5.47}$$

$$\phi^c = B_0 + (\Phi_1 - B_0)\, e^{-\xi} + (\Phi_2 - B_0)\, e^{-\zeta} + \sqrt{\epsilon}\left(A_1 x + B_1 + B_1 e^{-\xi} + (A_1 + B_1)e^{-\zeta}\right) \tag{5.48}$$

At this point we note that there is not enough information to solve for the constants B_0, A_1 or B_1. This breakdown in the solution process comes about primarily because the flux boundary conditions do not provide enough information with regard to the inner expansions near $x = 0$ and $x = 1$. If the inner expansions were considered solely as one-term expansions then the constants A_1 and B_1 would be 0, producing a composite solution

$$\phi^c = B_0 + (\Phi_1 - B_0)\, e^{-\xi} + (\Phi_2 - B_0)\, e^{-\zeta} \tag{5.49}$$

This method still does not provide us with enough information to solve for the constant B_0, a result of the manner in which the flux boundary conditions effect the system. In the formulation of the LCE, it is seen that the continuity expression is simply the derivative of the flux condition, and thus the second flux boundary condition is redundant, offering no additional information to the system. This in turn reduces the number of availale conditions on the system, making the system underconstrained in this formulation. Therefore, we must introduce another condition on the problem to solve for this remaining coefficient.

The additional constraint considered in this analysis focuses on the overall ion distribution within the polymer. In the development of Chapter 4 the ionic polymer is considered to be a closed system with regard to cation motion, restricting ion motion into or out of the system . This restriction can be represented analytically through the simple integral,

$$\int_0^1 \rho(x,t)dx = \int_0^1 \frac{\partial^2 \phi(x,t)}{\partial x^2} dx = 0 \tag{5.50}$$

Applying this conservation of charge constraint to the composite soluiton of equation 5.49, and solving for B_0 we find that

$$B_0 = \frac{1}{2}\left(\Phi_1 + \Phi_2\right) \tag{5.51}$$

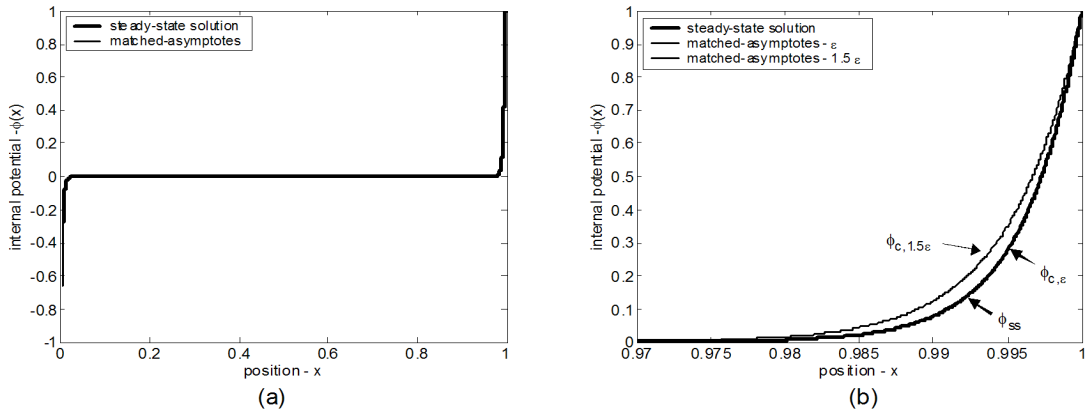

Figure 5.2: Comparison of the matched-asymptotes solution for the LCE system with linear boundary conditions to the steady-state solution derived in Chapter 4. Plot (a) shows a comparison for $\epsilon_{ma} = \epsilon_{ss}$ while (b) illustrates the influence ϵ has on the matched-asymptote system, showing plots for $\epsilon_{ma} = \epsilon_{ss}$ and $\epsilon_{ma} = 1.5\epsilon_{ss}$.

Substituting this into the composite solution yields the approximate potential profile

$$\frac{1}{2}\left[(\Phi_2 + \Phi_1) - \Delta\Phi e^{-\xi} + \Delta\Phi e^{-\zeta}\right] \tag{5.52}$$

where $\Delta\Phi$ is equal to $\Phi_2 - \Phi_1$. The profile predicted in this approximation is shown in Figure 5.2 along with the steady-state solution derived in equation 4.78 from Chapter 4. Figure 5.2a presents the potential profile through the thickness of the polymer membrane. The boundary layer near $x = 1$ is shown in more detail in Figure 5.2b. This expanded view presents the potential profile for the exact steady-state soluiton, the approximate solution using matched asymptotes and a slightly perturbed composite solution with the small parameter approximated as 1.5ϵ. Comparison of the exact and approximate solutions yield extremely good correlation. The perturbed solution indicates the sensitivity of the composite solution to variations in the small parameter ϵ, resulting in a broader boundary layer for larger values of ϵ. This finding is consistent with the physical interpretation since the small scale parameter ϵ is representative of the natural length scale of the IPT. Consequently, a larger value of ϵ would correspond to a larger boundary layer near the outer surfaces of the ionic polymer. Thus, we have shown that the matched asymptotes method can be applied to obtain an approximate for the linearized transport problem associated with the ionic polymer transducer. This method will now be implemented to analyze the effects introduced by considering the nonlinear flux as applied to the linear and nonlinear continuity expressions.

5.3 LCE subject to nonlinear flux boundary conditions

The second development in this series builds upon the LCE, considering the effects of nonlinear flux boundary condition on the linearized continuity equation. We begin this analysis by considering the linear form of the continuity equation 5.2, but maintain the nonlinear boundary conditions of equation 5.3. In this development the polymer is again thought to be composed of three regions, defined as the outer expansion and the inner expansions near $x = 0$ and $x = 1$ as shown in Figure 5.1. Since the outer expansion is independent of the boundary conditions and we are again considering the LCE, the general solution for the outer expansion remains unchanged from the previous development,

$$\phi^o = A_0 x + B_0 + \sqrt{\epsilon}\,(A_1 x + B_1) + ... \tag{5.53}$$

This expansion results from a two term expansion of the LCE from equation 5.4. Now with this expansion defined, we move toward the inner expansion near $x = 0$.

5.3.1 Inner expansion near $x = 1$ - LCE with *Nonlinear BCs*

In the region of the inner expansion near $x = 0$ a stretching parameter is introduced in the same manner as it was in the previous formulation. Due to the similarities in these formulations, we can refer to the development of equations 5.11 - 5.19 as they are the same steps used in this system. The principle difference appears when we consider the flux boundary condition for the LCE with *nonlinear* boundary conditions. When taking the new flux BC into consideration, and applying the two-term expansion in terms of ξ we get a system of four boundary conditions,

$$\begin{aligned} \mathcal{O}\left(\epsilon^0\right) \quad &\rightarrow \quad \psi_0 = \Phi_1 \qquad \psi_0^{'''} - \psi_0^{'} = -N_2 \psi^{''} \psi_0^{'} \\ \mathcal{O}\left(\epsilon^{1/2}\right) \quad &\rightarrow \quad \psi_1 = 0 \qquad \psi_1^{'''} - \psi_1^{'} = -N_2 \psi^{''} \psi_1^{'} \end{aligned} \tag{5.54}$$

Thus when we consider the general solution for ψ_0 and ψ_1 we must impose these nonlinear flux conditions. Again, we consider the general solutions,

$$\psi_0 = a_0 + b_0 \xi + c_0 e^{-\xi} \qquad\qquad \psi_1 = a_1 + b_1 \xi + c_1 e^{-\xi} \tag{5.55}$$

Imposing the boundary conditions to these general solutions we find

$$a_0 = \Phi_1 - c_0, \qquad b_0 = \frac{N_2 c_0^2}{N_2 c_0 - 1}, \qquad a_1 = -c_1, \qquad b_1 = \frac{N_2 c_1^2}{N_2 c_1 - 1} \tag{5.56}$$

Applying these results to the general expressions for ψ_0 and ψ_1, we can formulate the inner expansion as $\phi^i = \psi_0 + \sqrt{\epsilon}\psi_1$. This yields the two-term inner expansion of the form

$$\phi^i = \Phi_1 - c_0\left(1 - \frac{N_2 c_0}{N_2 c_0 - 1}\xi - e^{-\xi}\right) - \sqrt{\epsilon}c_1\left(1 - \frac{N_2 c_1}{N_2 c_1 - 1}\xi - e^{-\xi}\right) \tag{5.57}$$

With this inner expansion we can now consider matching the two regions defined by equations 5.53 and 5.57. Using the notation outlined in the previous section, we sumarize the matching process as follows:

	Outer expansion		Inner expansion	
1.)	$\psi^o \sim$	$A_0 x + B_0 + \sqrt{\epsilon}(A_1 x + B_1) + ...$	$\psi^i \sim$	$\Phi_1 - c_0\left(1 - \frac{N_2 c_0}{N_2 c_0 - 1}\xi - e^{-\xi}\right) - \sqrt{\epsilon}c_1\left(1 - \frac{N_2 c_1}{N_2 c_1 - 1}\xi - e^{-\xi}\right)$
2.)	$=$	$\sqrt{\epsilon}A_0\xi + B_0 + \epsilon A_1\xi + \sqrt{\epsilon}B_1 + ...$	$=$	$\Phi_1 - c_0\left(1 - \frac{N_2 c_0}{N_2 c_0 - 1}\frac{x}{\sqrt{\epsilon}} - e^{\frac{-x}{\sqrt{\epsilon}}}\right) - \sqrt{\epsilon}c_1\left(1 - \frac{N_2 c_1}{N_2 c_1 - 1}\frac{x}{\sqrt{\epsilon}} - e^{\frac{-x}{\sqrt{\epsilon}}}\right)$
3.)	$=$	$B_0 + \sqrt{\epsilon}(A_0\xi + B_1) + \epsilon A_1\xi + ...$	$=$	$(\Phi_1 - c_0) + \frac{N_2 c_1 2}{N_2 c_1 - 1}x + \frac{N_2 c_0^2}{N_2 c_0 - 1}\frac{x}{\sqrt{\epsilon}} + \left(c_0 + \sqrt{\epsilon}c_1\right)e^{\frac{-x}{\sqrt{\epsilon}}} - \sqrt{\epsilon}c_1$
4.)	$=$	$B_0 + \sqrt{\epsilon}(A_0\xi + B_1)$	$=$	$\Phi_1 + \frac{N_2 c_1^2}{N_2 c_1 - 1}x - \sqrt{\epsilon}c_1$ if $c_0 = 0$
			$=$	$\frac{N_2 c_0^2}{N_2 c_0 - 1}\frac{x}{\sqrt{\epsilon}}$ if $c_0 \neq 0$

In this case c_0 must be defined as zero in order to uphold the matching process. From this we equate the inner and outer expansions to develop relationships between the coefficients of the two expansions,

$$\begin{aligned} B_0 + \sqrt{\epsilon}(A_0\xi + B_1) &= \Phi_1 + \frac{N_2 c_1^2}{N_2 c_1 - 1}x - \sqrt{\epsilon}c_1 \\ B_0 + A_0 x + \sqrt{\epsilon}B_1 &= \Phi_1 + \frac{N_2 c_1^2}{N_2 c_1 - 1}x - \sqrt{\epsilon}c_1 \end{aligned} \tag{5.58}$$

Equating coefficients, we conclude that

$$B_0 = \Phi_1, \qquad A_0 = \frac{N_2 c_1^2}{N_2 c_1 - 1}, \qquad B_1 = -c_1 \tag{5.59}$$

These relationships describe how the inner expansion near $x = 0$ relates to the outer expansion in this region. We now extend this analysis to consider the region near $x = 1$.

5.3.2 Inner expansion near $x = 1$ - LCE with *Nonlinear BCs*

We now consider the inner expansion near $x = 1$. As in the previous formulation we introduce the stretching parameter ζ to magnify the region around this boundary layer. This analysis follows the same derivation given in equations 5.31 - 5.37, covering the development of a two-term expansion for the linear continuity equation in terms of ζ through the development of the potential boundary condition at $x = 1$ in terms of ζ. Using the same technique considered in the case of the linear boundary condiiton, we develop the nonlinear flux in terms of the stretched coordinate ζ as it cooresponds to $x = 1$. Taking into consideration the two-term expansion for ϕ^I and the potential

boundary conditions, we formulate a set of four boundary conditions corresponding to $\zeta = 0$,

$$\mathcal{O}(\epsilon^0) \quad \rightarrow \quad \tilde{\psi}_0(0) = \Phi_2 \qquad \tilde{\psi}_0''' - \tilde{\psi}_0' = -N_2 \tilde{\psi}_0'' \tilde{\psi}_0' \tag{5.60}$$

$$\mathcal{O}(\epsilon^{1/2}) \quad \rightarrow \quad \tilde{\psi}_1(0) = \Phi_2 \qquad \tilde{\psi}_1''' - \tilde{\psi}_1' = -N_2 \tilde{\psi}_1'' \tilde{\psi}_1' \tag{5.61}$$

The assumed solutions for $\tilde{\psi}_0$ and $\tilde{\psi}_1$ have the form

$$\tilde{\psi}_0 = \tilde{a}_0 + \tilde{b}_0 \zeta + \tilde{c}_0 e^{-\zeta} \qquad\qquad \tilde{\psi}_1 = \tilde{a}_1 + \tilde{b}_1 \zeta + \tilde{c}_1 e^{-\xi} \tag{5.62}$$

We can apply the boundary conditions from equations 5.60 and 5.61 to solve for the coefficients $\tilde{a}_0$, $\tilde{a}_1$, $\tilde{b}_0$ and $\tilde{b}_1$ in terms of $\tilde{c}_0$ and $\tilde{c}_1$,

$$\tilde{a}_0 = \Phi_2 - \tilde{c}_0, \qquad \tilde{b}_0 = \frac{N_2 \tilde{c}_0^2}{N_2 \tilde{c}_0 - 1}, \qquad \tilde{a}_1 = -\tilde{c}_1, \qquad \tilde{b}_1 = \frac{N_2 \tilde{c}_1^2}{N_2 \tilde{c}_1 - 1} \tag{5.63}$$

Substituting these relationships into the inner expansion ϕ^I,

$$\phi^I = \Phi_2 - \tilde{c}_0 \left(1 - \frac{N_2 \tilde{c}_0}{N_2 \tilde{c}_0 - 1}\zeta - e^{-\zeta}\right) - \sqrt{\epsilon}\tilde{c}_1 \left(1 - \frac{N_2 \tilde{c}_1}{N_2 \tilde{c}_1 - 1}\zeta - e^{-\zeta}\right) \tag{5.64}$$

We can now relate this inner expansion ϕ^I defined in equation 5.64 to the outer expansion ϕ^o defined in equation 5.53. Using the table notation defined previously we find

	Outer expansion		Inner expansion	
1.)	$\psi^o \sim$	$A_0 x + B_0 + \sqrt{\epsilon}(A_1 x + B_1) + ...$	$\psi^i \sim$	$\Phi_2 - \tilde{c}_0 \left(1 - \frac{N_2 \tilde{c}_0 \zeta}{N_2 \tilde{c}_0 - 1} - e^{-\zeta}\right) - \sqrt{\epsilon}\tilde{c}_1 \left(1 - \frac{N_2 \tilde{c}_1 \zeta}{N_2 \tilde{c}_1 - 1} - e^{-\zeta}\right)$
2.)	$=$	$A_0(1 - \sqrt{\epsilon}\zeta) + B_0 + \sqrt{\epsilon}(A_1(1 - \sqrt{\epsilon}\zeta) + B_1)$	$=$	$\Phi_2 - \tilde{c}_0 \left(1 - \frac{N_2 \tilde{c}_0}{N_2 \tilde{c}_0 - 1} \frac{1-x}{\sqrt{\epsilon}} - e^{-\frac{1-x}{\sqrt{\epsilon}}}\right)$ $-\sqrt{\epsilon}\tilde{c}_1 \left(1 - \frac{N_2 \tilde{c}_1}{N_2 \tilde{c}_1 - 1} \frac{1-x}{\sqrt{\epsilon}} - e^{-\frac{1-x}{\sqrt{\epsilon}}}\right)$
3.)	$=$	$A_0 + B_0 + \sqrt{\epsilon}(A_1 + B_1 - A_0\zeta) + \epsilon A_1 \zeta$	$=$	$(\Phi_2 - \tilde{c}_0) + \frac{N_2 \tilde{c}_1^2}{N_2 \tilde{c}_1 - 1} - \frac{N_2 \tilde{c}_1^2}{N_2 \tilde{c}_1 - 1} x - \sqrt{\epsilon}\tilde{c}_1 + \frac{N_2 \tilde{c}_0^2}{N_2 \tilde{c}_0 - 1} \frac{(1-x)}{\sqrt{\epsilon}}$ $+ \left(\tilde{c}_0 + \sqrt{\epsilon}\tilde{c}_1\right) e^{-\frac{1-x}{\sqrt{\epsilon}}}$
4.)	$=$	$(A_0 + B_0) + \sqrt{\epsilon}(A_1 + B_1 - A_0\zeta)$	$=$	$\left(\Phi_2 + \frac{N_2 \tilde{c}_1^2}{N_2 \tilde{c}_1 - 1}\right) - \frac{N_2 \tilde{c}_1^2}{N_2 \tilde{c}_1 - 1} x - \sqrt{\epsilon}\tilde{c}_1$ if $\tilde{c}_0 = 0$
			$=$	$\frac{N_2 \tilde{c}_0^2}{N_2 \tilde{c}_0 - 1} \frac{1-x}{\sqrt{\epsilon}}$ if $\tilde{c}_0 \neq 0$

As in the expansion near $x = 0$ we must define the coefficient $\tilde{c}_0$ to be zero in order to uphold matching. Equating the inner and outer expansions we produce the relationship between ϕ^o and ϕ^I,

$$\begin{aligned} (A_0 + B_0) + \sqrt{\epsilon}(A_1 + B_1 - A_0\zeta) &= \left(\Phi_2 + \frac{N_2 \tilde{c}_1^2}{N_2 \tilde{c}_1 - 1}\right) - \frac{N_2 \tilde{c}_1^2}{N_2 \tilde{c}_1 - 1} x - \sqrt{\epsilon}\tilde{c}_1 \\ B_0 + A_0 x + \sqrt{\epsilon}(A_1 + B_1) &= \left(\Phi_2 + \frac{N_2 \tilde{c}_1^2}{N_2 \tilde{c}_1 - 1}\right) - \frac{N_2 \tilde{c}_1^2}{N_2 \tilde{c}_1 - 1} x - \sqrt{\epsilon}\tilde{c}_1 \end{aligned} \tag{5.65}$$

From this expression we can equate coefficients and solve for the variables of the outer expansion.

$$B_0 = \Phi_2 + \frac{N_2\tilde{c}_1^2}{N_2\tilde{c}_1 - 1}, \qquad A_0 = \frac{-N_2\tilde{c}_1^2}{N_2\tilde{c}_1 - 1}, \qquad A_1 + B_1 = -\tilde{c}_1 \tag{5.66}$$

Combining these with the results of the expansion near $x = 0$ we find

$$c_1 = \frac{N_2\Delta\Phi \pm \sqrt{N_2\Delta\Phi}\sqrt{N_2\Delta\Phi - 4}}{2N_2} \qquad \tilde{c}_1 = \frac{-N_2\Delta\Phi \pm \sqrt{N_2\Delta\Phi}\sqrt{N_2\Delta\Phi + 4}}{2N_2}$$
$$A_0 = \Delta\Phi, \qquad B_0 = \Phi_1, \qquad B_1 = -c_1, \qquad A_1 = c_1 - \tilde{c}_1 \tag{5.67}$$

Now we consider the composite profile φ^c,

$$\phi^c \quad = \quad \phi^o + \phi^i + \phi^I - \left(\phi^i\right)^o - \left(\phi^I\right)^o$$

Imposing the results of our matching process we have,

$$\begin{aligned}\phi^c = {} & (\Phi_2 - \Phi_1)\, x + \Phi_1 + \sqrt{\epsilon}\left[(c_1 - \tilde{c}_1)\, x - c_1\right] + \Phi_1 - \sqrt{\epsilon}\left(c_1 - \frac{N_2 c_1^2}{N_2 c_1 - 1}\xi - c_1 e^{-\xi}\right) + \Phi_2 \\ & - \sqrt{\epsilon}\left(\tilde{c}_1 - \frac{N_2\tilde{c}_1^2}{N_2\tilde{c}_1 - 1}\zeta - \tilde{c}_1 e^{-\zeta}\right) - \left(\Phi_1 + \frac{N_2 c_1^2}{N_2 c_1 - 1}x - \sqrt{\epsilon}c_1\right) \\ & - \left(\Phi_2 + \frac{N_2\tilde{c}_1^2}{N_2\tilde{c}_1 - 1} - \frac{N_2\tilde{c}_1^2}{N_2\tilde{c}_1 - 1}x - \sqrt{\epsilon}\tilde{c}_1\right)\end{aligned} \tag{5.68}$$

where c_1 and $\tilde{c}_1$ are defined above. The resulting composite profile for the electric potential is shown in Figure 5.3. The formulation predicts a linear potential profile through the outer expansion with slight boundary effects near the polymer's outer surfaces. Figure 5.3a presents the potential profile through the entire polymer thickness while Figure 5.3b focuses on the boundary response near $x = 0$. Through most of the polymer the spatial response is governed by the linear function $(\Phi_2 - \Phi_1)\, x + \Phi_1 + \sqrt{\epsilon}\left[(c_1 - \tilde{c}_1)\, x - c_1\right]$ described by the outer expansion. Within the boundary layer the exponential terms of the inner expansions govern the response, forcing the slope of the spatial solution toward zero as $x \to 0$ at the left boundary and as $x \to 1$ at the right boundary.

The presence of the nonlinear flux boundary condition has a significant effect on the potential response when compared to the response derived in section 5.2 for the linearized flux conditons at $x = 0$ and $x = 1$. The source of this variation arises from the linear terms $b_1\xi$ and $\tilde{b}_1\zeta$ of the inner expansions and their interaction with the flux boundary conditions. When subject to the linearized flux condition b_1 and $\tilde{b}_1$ must equal 0 to satisfy the constraints and therefore drop out of the inner expansion solutions. The absence of these linear terms in the inner expansions of section 5.2 translates into a slope $A_0 = 0$ in the outer expansion. The linear flux also fails to provide enough information to explicitly solve for all of the system coefficients. This feature results from the fact that the steady-state LCE is simply the spatial derivative of the flux boundary condition. Therefore, if we integrate the LCE

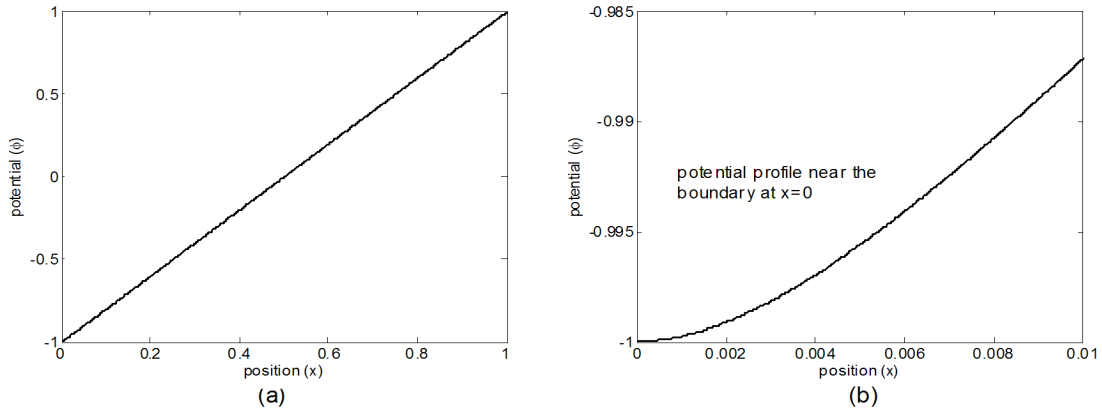

Figure 5.3: The composite solution for the matched-asymptotes analysis of the steady-state LCE with nonlinear boundary conditions. Plot (a) shows the profile through the entire polymer thickness while (b) presents the potential profile near the boundary at $x = 0$.

we get the condition

$$\frac{d}{dx}\left(\epsilon\phi''' - \phi'\right) = 0$$
$$\epsilon\phi''' - \phi' = C$$

where C is a constant of integration. Once the flux boundary condition is imposed at $x = 0$ the constant C is constrained to be 0, effectively making the boundary condition at $x = 1$ redundant. The redundancy in this second flux boundary condition requires that we introduce the conservation of charge condition $\int_0^1 \frac{\partial^2 \phi^c}{\partial x^2} dx$ to solve for the remaining coefficient B_0 in the development of section 5.2. Conversely, the nonlinear flux provides enough additional information to the system to solve for the entire soluiton. The presence of this nonlinear flux results in nonzero b_1 and $\tilde{b}_1$ coefficients, in turn producing the nonzero slope A_0 in the outer expansion. The next section in this chapter extends our analysis to consider the full nonlinear continuity equation when subject to potential and nonlinear flux boundary conditions.

5.4 Nonlinear continuity equation with nonlinear boundary conditions

The final steady-state development considered in this analysis focuses on the full nonlinear system with nonlinear boundary conditions. Therefore, we refocus our attention on the nonlinear continuity equation 5.2 subject to the potential and nonlinear flux boundaray conditions defined in equation 5.3. As in the previous two developments, we begin our analysis by considering the outer expansion of the system.

5.4.1 Outer expansion - NLCE with *Nonlinear BCs*

We formulate the outer expansion of the NLCE in the same manner that was used to formulate ϕ^0 for the linear continuity equation in sections 5.2 and 5.3. A general two-term expansion is assumed for the outer expansion, yielding the general expression for ϕ^o,

$$\phi^o = \varphi_0(x) + \delta(\epsilon)\varphi_1 + ... \tag{5.69}$$

where $\delta(\epsilon)$ is again taken to be $\sqrt{\epsilon}$ so that it corresponds to inner expansions near $x = 0$ and $x = 1$. Substituting the general expansion into the steady-state nonlinear continuity equation 5.2 we have

$$-\epsilon\left(\varphi_0^{iv} + \sqrt{\epsilon}\varphi_1^{iv}\right) - \epsilon N_2\left[\left(\varphi_0^{'''} + \sqrt{\epsilon}\varphi_1^{'''}\right)\left(\varphi_0^{'} + \sqrt{\epsilon}\varphi_1^{'}\right) - \left(\varphi_0^{''} + \sqrt{\epsilon}\varphi_1^{''}\right)^2\right] + \left(\varphi_0^{''} + \sqrt{\epsilon}\varphi_1^{''}\right) = 0 \tag{5.70}$$

At this point we equate powers of ϵ to yield simple differential equations for the functions φ_0 and φ_1. Grouping terms that are of order ϵ^0 and $\epsilon^{1/2}$ we get

$$\begin{aligned} \mathcal{O}(\epsilon^0) &\rightarrow \varphi_0^{''} = 0 \\ \mathcal{O}\left(\epsilon^{1/2}\right) &\rightarrow \varphi_1^{''} = 0 \end{aligned} \tag{5.71}$$

From the form of each of these expressions we expect a linear profile for both φ_0 and φ_1. Thus, we write the outer expansion as

$$\phi^o = A_0 x + B_0 + \sqrt{\epsilon}\,(A_1 x + B_1) \tag{5.72}$$

5.4.2 Inner expansion near $x = 0$ - NLCE with *Nonlinear BCs*

The next step in the analysis is to consider the inner expansion near $x = 0$. As in the previous cases we introduce the stretching parameter ϵ^ν to magnify inner expansion near $x = 0$. In this region we define the stretching transformation to have the general form,

$$\xi = \frac{x}{\epsilon^\nu} \quad \text{or} \quad x = \epsilon^\nu \xi \quad \text{where} \quad \nu > 0. \tag{5.73}$$

In the previous cases we considered the linearized form of equation 5.2. Since we are now focusing on the nonlinear problem, it may be necessary to scale the dependent variable. This scaling will allow us to consider different scales

of the nonlinear component. Thus, we will express the inner expansion as

$$\phi^i = \psi(\xi;\epsilon) + ... = \frac{\phi(x;\epsilon)}{\epsilon^\varsigma} \qquad\qquad \phi(x;\epsilon) = \phi^i e^\varsigma \tag{5.74}$$

Based on the scaling terms, we can express the subsequent derivatives as $\frac{\partial^n \phi}{\partial x^n} = \epsilon^{-n\nu}\frac{\partial^n \epsilon^\varsigma \phi^i}{\partial \xi^{n\nu}}$. Applying this transform to the nonlinear continuity expression from equation 5.2 we can formulate the NLCE in terms of the magnified coordinate ξ,

$$\epsilon^{\varsigma+1-4\nu}\frac{d^4\phi^i}{d\xi^4} + \epsilon^{2\varsigma+1-4\nu}N_2\left[\frac{d^3\phi^i}{d\xi^3}\frac{d\phi^i}{d\xi} + \left(\frac{d^2\phi^i}{d\xi^2}\right)^2\right] - \epsilon^{\varsigma-2\nu}\frac{d^2\phi^i}{d\xi^2} = 0. \tag{5.75}$$

Dividing through by $\epsilon^{\varsigma+1-4\nu}$ this equation 5.75 has the form,

$$\frac{d^4\phi^i}{d\xi^4} + \epsilon^\varsigma N_2\left[\frac{d^3\phi^i}{d\xi^3}\frac{d\phi^i}{d\xi} + \left(\frac{d^2\phi^i}{d\xi^2}\right)^2\right] - \epsilon^{2\nu-1}\frac{d^2\phi^i}{d\xi^2} = 0. \tag{5.76}$$

Since ς and ν are applied to the nonlinear $N_2\left[\frac{d^3\phi^i}{d\xi^3}\frac{d\phi^i}{d\xi} + \left(\frac{d^2\phi^i}{d\xi^2}\right)^2\right]$ and linear $\frac{d^2\phi^i}{d\xi^2}$ terms in an independent manner, we can consider three distinct cases with different distinguished limits. *Case 1* corresponds to $\varsigma > 0$ and $\nu = \frac{1}{2}$, which results in the distinguished limit,

$$\frac{d^4\phi^i}{d\xi^4} - \frac{d^2\phi^i}{d\xi^2} = 0 \tag{5.77}$$

If $\varsigma = 0$ and $\nu > \frac{1}{2}$ then we get the distinguished limit of *Case 2*,

$$\frac{d^4\phi^i}{d\xi^4} + N_2\left[\frac{d^3\phi^i}{d\xi^3}\frac{d\phi^i}{d\xi} + \left(\frac{d^2\phi^i}{d\xi^2}\right)^2\right] = 0 \tag{5.78}$$

The final variation *Case 3* corresponds to $\varsigma = 0$ and $\nu = \frac{1}{2}$, resulting in the distinguished limit

$$\frac{d^4\phi^i}{d\xi^4} + N_2\left[\frac{d^3\phi^i}{d\xi^3}\frac{d\phi^i}{d\xi} + \left(\frac{d^2\phi^i}{d\xi^2}\right)^2\right] - \frac{d^2\phi^i}{d\xi^2} = 0 \tag{5.79}$$

In *Case 1* the potential function ϕ from equation 5.81 is of order ϵ^ς where $\varsigma > 0$. If ς is taken to be $\frac{1}{2}$ then the nonlinearity will appear in the first order expansion, whereas if $\varsigma > \frac{1}{2}$ then the system will be reduced to the linear expansion of section 5.2. In *Case 2* ϕ is of $\mathcal{O}(1)$ and the linear second-order term drops out of the equation. This expression only considers the small-scale components of the original nonlinear continuity expression described in equation 5.2. *Case 3* is also ϕ is of $\mathcal{O}(1)$ and the distinguished limit is equivalent to the original differential equation. In order to solve for this last case we would need to numerically integrate the system to yield a solution,

and we would not obtain any simplifications in this analysis. Therefore, we focus our attention on the approximate systems of *Case 1* (with $\varsigma = \frac{1}{2}$) and *Case 2*.

Before we delve into the analysis of *Case 1* and *Case 2* we will consider how each case develops with respect to the inner expansion near the right boundary at $x = 1$. This will enable us to fully develop each case without needing to switch between formulations.

5.4.3 Inner expansion near $x = 1$ - NLCE with *Nonlinear BCs*

In the region of the inner expansion near $x = 0$ we once again introduce the stretching parameter ϵ^ν to magnify the region near this boundary. The stretching transformation is therefore defined as,

$$\zeta = \frac{1-x}{\epsilon^\nu} \quad \text{or} \quad x = 1 - \epsilon^\nu \zeta \quad \text{where} \quad \nu > 0. \tag{5.80}$$

We also introduce the scaling parameter ϵ^ς which will enable us to scale the dependent variable. Thus, the inner expansion can be written as,

$$\phi^I = \tilde{\psi}(\zeta;\epsilon) + ... = \frac{\phi(x;\epsilon)}{\epsilon^\varsigma} \qquad \phi(x;\epsilon) = \phi^I e^\varsigma \tag{5.81}$$

Applying this transform to the NLCE, we find

$$\frac{d^4\phi^I}{d\zeta^4} + \epsilon^\varsigma N_2 \left[\frac{d^3\phi^I}{d\zeta^3}\frac{d\phi^I}{d\zeta} + \left(\frac{d^2\phi^I}{d\zeta^2}\right)^2 \right] - \epsilon^{2\nu-1}\frac{d^2\phi^I}{d\zeta^2} = 0. \tag{5.82}$$

From this we see that the expansion near $x = 1$ has the same distinguished limits as the inner expansion near $x = 0$ and the limits correspond to the same values of ς and ν. Since we will neglect the full nonlinear expression of *Case 3* which would require numerical integration, we focus instead on the first two cases corresponding to $\varsigma = \frac{1}{2},\ \nu = \frac{1}{2}$ and $\varsigma = 0,\ \nu > \frac{1}{2}$. Specifically, these cases can be defined as,

$$Case\ 1 - \varsigma = \frac{1}{2},\ \nu = \frac{1}{2} \qquad \frac{d^4\phi^I}{d\zeta^4} - \frac{d^2\phi^I}{d\zeta^2} = 0 \tag{5.83}$$

$$Case\ 2 - \varsigma = 0,\ \nu > \frac{1}{2} \qquad \frac{d^4\phi^I}{d\zeta^4} + N_2 \left[\frac{d^3\phi^I}{d\zeta^3}\frac{d\phi^I}{d\zeta} + \left(\frac{d^2\phi^I}{d\zeta^2}\right)^2 \right] = 0 \tag{5.84}$$

In this manner we have defined the inner expansions near both $x = 0$ and $x = 1$ for both *Case 1* and *2* of the NLCE. Therefore, we continue the our development by first considering the boundary layer development for the distinguished limit of *Case 1*.

5.4.4 Matched-Asymptotes of the NLCE - *Case 1*

When we consider the system defined in *Case 1* we see that the distinguished limit resembles the linearized continuity expression studied in sections 5.2 and 5.3. In the definition of *Case 1* the scales of ϵ are defined such that $\varsigma \geq 0$ and $\nu = \frac{1}{2}$. In order for the nonlinearity to influence the system we must consider at least a two-term expansion for ϕ^i. In this manner the expansions will be of $\mathcal{O}\left(\epsilon^{n\nu}\right)$ where $n = 0, 1, 2, ...$ For the sake of our analysis we will choose a two-term expansion,

$$\phi^i = \psi_0(\xi) + \sqrt{\epsilon}\psi_1(\xi) + ... \qquad \phi^I = \tilde{\psi}_0(\zeta) + \sqrt{\epsilon}\tilde{\psi}_1(\zeta) + ... \tag{5.85}$$

If ς is defined to be *greater than* $\varsigma = \frac{1}{2}$ then the two-term expansion will have a form identical to the linearized system of section 5.2. However, if ς is defined to be *equal to* $\frac{1}{2}$ then the nonlinearity will occur in the first-order terms $\psi_1(\xi)$ and $\tilde{\psi}_1(\zeta)$. The influence of this nonlinearity on the first-order term differentiates this development from the LCE based studies of sections 5.2 and 5.3. Therefore, we continue our formulation of *Case 1* by focusing on the inner expansion near $x = 0$, followed by an analysis of the inner expansion near $x = 1$.

Inner expansion near $x = 0$ - NLCE *Case 1*

As stated above, the nonlinear component is of order $\sqrt{\epsilon}$ based upon the development of our system in *Case 1*. In terms of the magnified coordinate ξ near $x = 0$ the governing expression has the form,

$$\frac{d^4\phi^i}{d\xi^4} + \sqrt{\epsilon}N_2\left[\frac{d^3\phi^i}{d\xi^3}\frac{d\phi^i}{d\xi} + \left(\frac{d^2\phi^i}{d\xi^2}\right)^2\right] - \frac{d^2\phi^i}{d\xi^2} = 0 \tag{5.86}$$

Applying the stretching transformation to the boundary conditions we find

$$\phi^i(0) = \Phi_1 \qquad \frac{d^3\phi^i}{d\xi^3} + \sqrt{\epsilon}N_2\left[\frac{d^2\phi^i}{d\xi^2}\frac{d\phi^i}{d\xi}\right] - \left.\frac{d\phi^i}{d\xi}\right|_{\xi=0} = 0 \tag{5.87}$$

At this point we assume a general two term expansion for ϕ^i

$$\phi^i = \psi_0(\xi) + \sqrt{\epsilon}\psi_1(\xi) + ... \tag{5.88}$$

Substituting this expansion into equation 5.86 we find

$$\begin{aligned}\left(\psi_0^{iv}(\xi) + \sqrt{\epsilon}\psi_1^{iv}(\xi)\right) + \sqrt{\epsilon}N_2\Big[&\left(\psi_0^{'''}(\xi) + \sqrt{\epsilon}\psi_1^{'''}(\xi)\right)\left(\psi_0^{'}(\xi) + \sqrt{\epsilon}\psi_1^{'}(\xi)\right) \\ &+ \left(\psi_0^{''}(\xi) + \sqrt{\epsilon}\psi_1^{''}(\xi)\right)^2\Big] - \left(\psi_0^{''}(\xi) + \sqrt{\epsilon}\psi_1^{''}(\xi)\right) = 0\end{aligned} \tag{5.89}$$

Grouping like powers of ϵ

$$\begin{aligned} \mathcal{O}(\epsilon^0): &\qquad \psi_0^{iv} - \psi_0^{''} = 0 \\ \mathcal{O}(\epsilon^{1/2}): &\qquad \psi_1^{iv} - \psi_1^{''} = -N_2 \left[\psi_0^{'''} \psi_0^{'} + \left(\psi_0^{''} \right)^2 \right] \end{aligned} \tag{5.90}$$

If we apply the general two-term expansion for ϕ^i to the boundary conditions, we can equate powers of ϵ to yield a set of four boundary conditions

$$\begin{aligned} \mathcal{O}(\epsilon^0): &\qquad \psi_0 = \Phi_1, \qquad \psi_0^{iv} - \psi_0^{''} = 0 \\ \mathcal{O}(\epsilon^{1/2}): &\qquad \psi_1 = 0, \qquad \psi_1^{'''} - \psi_1^{'} = -N_2 \left[\psi_0^{''} \psi_0^{'} \right] \end{aligned} \tag{5.91}$$

From these equations we can consider the general solution for ψ_0.

$$\psi_0 = a_0 + b_0 \xi + c_0 e^{-\xi} \tag{5.92}$$

where the exponentially growing term has again been ignored as it was in sections 5.2 and 5.3. Applying the $\mathcal{O}(\epsilon^0)$ boundary conditions we find

$$\psi_0(0) = a_0 + c_0 = \Phi_1 \quad \rightarrow a_0 = \Phi_0 - c_0, \qquad \psi_0^{'''}(0) - \psi_0^{'}(0) = -c_0 - (b_0 - c_0) = 0 \quad \rightarrow b_0 = 0$$

which yields the zeroth order term ψ_0

$$\psi_0 = \Phi_1 - c_0 \left(1 - e^{-\xi} \right) \tag{5.93}$$

With this expression for ψ_0 we can now formulate the first order term ψ_1. The general differential equation in terms of ψ_1 has the form

$$\psi_1^{iv} - \psi_1^{''} = -2 N_2 c_0^2 e^{-2\xi} \tag{5.94}$$

which has the general solution (neglecting exponentially growing terms),

$$\psi_1 = a_1 + b_1 \xi + c_1 e^{-\xi} - \frac{N_2 c_0^2}{6} e^{-2\xi} \tag{5.95}$$

Imposing the first order boundary conditions from equation 5.91 we find that

$$\psi_1(0) = a_1 + c_1 - \frac{N_2 c_0^2}{6} = 0 \quad \rightarrow a_1 = \frac{N_2 c_0^2}{6} - c_1,$$
$$\psi_1'''(0) - \psi_1'(0) + N_2\left[\psi_0'' \psi_0'\right] = -c_1 + \frac{4N_2 c_0^2}{3} - (b_1 - c_1 + \frac{N_2 c_0^2}{3}) + N_2 c_0^2 = 0 \quad \rightarrow b_1 = 2N_2 c_0^2$$

Substituting these results into equation 5.95 yields the solution for ψ_1

$$\psi_1 = N_2 c_0^2 \left(\frac{1}{6} + 2\xi + \frac{1}{6} e^{-2\xi}\right) - c_1\left(1 - e^{-\xi}\right) \tag{5.96}$$

Combining this with the solution for ψ_0 we obtain the inner expansion

$$\phi^i = \Phi_1 - c_0\left(1 - e^{-\xi}\right) + \sqrt{\epsilon}\left[N_2 c_0^2 \left(\frac{1}{6} + 2\xi + \frac{1}{6} e^{-2\xi}\right) - c_1\left(1 - e^{-\xi}\right)\right] \tag{5.97}$$

At this point we consider the inner expansion expressed in terms of the outer variable x. This yields the outer expansion ϕ^i near $x = 0$,

$$\left(\phi^i\right)^o = \Phi_1 - c_0\left(1 - e^{\frac{-x}{\sqrt{\epsilon}}}\right) + \sqrt{\epsilon}\left[N_2 c_0^2 \left(\frac{1}{6} + 2\frac{x}{\sqrt{\epsilon}} + \frac{1}{6} e^{\frac{-2x}{\sqrt{\epsilon}}}\right) - c_1\left(1 - e^{\frac{-x}{\sqrt{\epsilon}}}\right)\right] \tag{5.98}$$

As $\epsilon \rightarrow 0$ this equation reduces to

$$\left(\phi^i\right)^o = \Phi_1 - c_0 + 2N_2 c_0^2 x + \sqrt{\epsilon}\left[\frac{N_2 c_0^2}{6} - c_1\right] \tag{5.99}$$

As in the derivations of sections 5.2 and 5.3, we can match this with the inner expansion of the ϕ^o. Since the outer expansion for the NLCE is the same as it was for each of the LCE systems, we can write $\left(\phi^o\right)^i$ as

$$\left(\phi^o\right)^i = B_0 + \sqrt{\epsilon}\left(A_0 \xi + B_1\right) \tag{5.100}$$

Writing this expression in terms of x and equating to $\left(\phi^i\right)^o$,

$$B_0 + A_0 x + \sqrt{\epsilon} B_1 = \Phi_1 - c_0 + 2N_2 c_0^2 x + \sqrt{\epsilon}\left[\frac{N_2 c_0^2}{6} - c_1\right] \tag{5.101}$$

we can solve for the coefficients of the outer expansion in terms of those from the inner expansion. This yields a set of solutions of the form,

$$B_0 = \Phi_1 - c_0, \qquad A_0 = 2N_2 c_0^2, \qquad B_1 = \frac{N_2 c_0^2}{6} - c_1 \tag{5.102}$$

The next stage in this analysis is to now shift our focus to the region near the right boundary at $x = 1$.

Inner expansion near $x = 1$ - NLCE *Case 1*

The inner expansion in this region has almost the same form as the solution near $x = 0$. The principle difference lies in the fact that the stretching parameter is defined as $\zeta = \frac{1-x}{\sqrt{\epsilon}}$. However, when expressed in terms of ζ the development is almost identical to the development in ξ. Thus, we can write the system of equations as

$$\mathcal{O}(\epsilon^0): \qquad \tilde{\psi}_0^{iv} - \tilde{\psi}_0'' = 0, \qquad \tilde{\psi}_0 = \Phi_2, \quad \tilde{\psi}_0^{iv} - \tilde{\psi}_0'' = 0 \tag{5.103}$$

$$\mathcal{O}(\epsilon^{1/2}): \qquad \tilde{\psi}_1^{iv} - \tilde{\psi}_1'' = -N_2\left[\tilde{\psi}_0'''\tilde{\psi}_0' + \left(\tilde{\psi}_0''\right)^2\right], \qquad \tilde{\psi}_1 = 0, \quad \tilde{\psi}_1''' - \tilde{\psi}_1' = -N_2\left[\tilde{\psi}_0''\tilde{\psi}_0'\right] \tag{5.104}$$

The zeroth order term has a general solution,

$$\tilde{\psi}_0 = \tilde{a}_0 + \tilde{b}_0\zeta + \tilde{c}_0 e^{-\zeta} \tag{5.105}$$

which can be solved for in terms of Φ_2 and $\tilde{c}_0$ by imposing the boundary conditions of equaiton 5.103.

$$\tilde{\psi}_0 = \Phi_2 - \tilde{c}_0\left(1 - e^{-\zeta}\right) \tag{5.106}$$

If we apply this expression to the first order equation 5.104 we can determine the general solution for $\tilde{\psi}_1$ (neglecting exponentially growing terms),

$$\tilde{\psi}_1 = \tilde{a}_1 + \tilde{b}_1\zeta + \tilde{c}_1 e^{-\zeta} - \frac{N_2\tilde{c}_0^2}{6}e^{-2\zeta} \tag{5.107}$$

Using the boundary conditions defined in equation 5.103 we can solve for the solution to equation 5.107, yielding the expression for $\tilde{\psi}_1$,

$$\tilde{\psi}_1 = N_2\tilde{c}_0^2\left(\frac{1}{6} + 2\zeta + \frac{1}{6}e^{-2\zeta}\right) - \tilde{c}_1\left(1 - e^{-\zeta}\right) \tag{5.108}$$

Combining this with the solution for $\tilde{\psi}_0$ we obtain the inner expansion ϕ^I,

$$\phi^I = \Phi_2 - \tilde{c}_0\left(1 - e^{-\zeta}\right) + \sqrt{\epsilon}\left[N_2\tilde{c}_0^2\left(\frac{1}{6} + 2\zeta + \frac{1}{6}e^{-2\zeta}\right) - \tilde{c}_1\left(1 - e^{-\zeta}\right)\right] \tag{5.109}$$

At this point we consider the inner expansion expressed in terms of the outer variable x.

$$\left(\phi^I\right)^o = \Phi_2 - \tilde{c}_0\left(1 - e^{\frac{-(1-x)}{\sqrt{\epsilon}}}\right) + \sqrt{\epsilon}\left[N_2\tilde{c}_0^2\left(\frac{1}{6} + 2\frac{1-x}{\sqrt{\epsilon}} + \frac{1}{6}e^{\frac{-2(1-x)}{\sqrt{\epsilon}}}\right) - \tilde{c}_1\left(1 - e^{\frac{-(1-x)}{\sqrt{\epsilon}}}\right)\right] \tag{5.110}$$

As $\epsilon \to 0$ this equation yields the outer expansion of ϕ^I near $x = 1$,

$$\left(\phi^I\right)^o = \Phi_2 - \tilde{c}_0 + 2N_2\tilde{c}_0^2(1-x) + \sqrt{\epsilon}\left[\frac{N_2\tilde{c}_0^2}{6} - \tilde{c}_1\right] \tag{5.111}$$

We now consider the inner expansion of ϕ^o near $x = 1$. This expression has the same form as the equivalent expansion in sections 5.2 and 5.3. Using the same approach as these previous sections, $(\phi^0)^I$ will have the form $(\phi^0)^I = (A_0 + B_0) + \sqrt{\epsilon}\,(A_1 + B_1 - A_0\zeta)$. Equating this to the outer expansion of ϕ^I from equation 5.111 and expressing the system in terms of x, we have

$$B_0 + A_0 x + \sqrt{\epsilon}\,(A_1 + B_1) = \Phi_2 - \tilde{c}_0 + 2N_2\tilde{c}_0^2(1-x) + \sqrt{\epsilon}\left[\frac{N_2\tilde{c}_0^2}{6} - \tilde{c}_1\right] \tag{5.112}$$

Grouping coefficients, we can express A_0, B_0, A_1 and B_1 in terms of the coefficients of $(\phi^I)^o$. Combining these results with those of the inner expansion near $x = 0$, we get the set of conditions

$$B_0 = \Phi_1 - c_0, \qquad A_0 = 2N_2c_0^2, \qquad B_1 = \frac{N_2c_0^2}{6} - c_1 \tag{5.113}$$

$$B_0 = \Phi_2 - \tilde{c}_0 + 2N_2\tilde{c}_0^2, \qquad A_0 = -2N_2\tilde{c}_0^2, \qquad A_1 + B_1 = \frac{N_2\tilde{c}_0^2}{6} - \tilde{c}_1 \tag{5.114}$$

From these equations we can solve directly for the coefficients c_0, $\tilde{c}_0$, A_0 and B_0. Since the equations are quadratic in terms of c_0 and $\tilde{c}_0$, a set of solutions are obtained,

$$c_0 = \frac{(1 \pm i) \pm \sqrt{2i + 8N_2\Delta\Phi}}{4N_2}, \qquad \tilde{c}_0 = \frac{1 \pm \sqrt{1 - 8N_2\left(\Delta\Phi + c_0\right)}}{4N_2} \tag{5.115}$$

Expressing the remaining coefficients in terms of c_0 and $\tilde{c}_0$,

$$B_0 = \Phi_1 - c_0, \qquad A_0 = 2N_2c_0^2, \qquad B_1 = \frac{N_2c_0^2}{6} - c_1 \qquad A_1 = \frac{N_2\left(\tilde{c}_0^2 - c_0^2\right)}{6} - (\tilde{c}_1 - c_0) \tag{5.116}$$

At this point we recognize that we have solved for all but two of the system coefficients. The remaining unknowns c_1 and $\tilde{c}_1$ serve as the coefficients of the $\mathcal{O}(\epsilon^{1/2})$ terms in the inner expansions ϕ^i and ϕ^I, respectively. In order to solve for the remaining unknowns, we must impose two physical constraints on the system. The first of these constraints relies upon the idea of conservation of charge within the membrane. Since we assume that cations cannot cross the boundaries, then the integral of the charge density must equal 0 when evaluated through the thickness of the membrane. The second constraint comes out of this definition because we assume that a symmetric profile results for the system. Under this assumption, we conclude that the charge density must be zero at the center of the polymer thickness, i.e. where $x = \frac{1}{2}$. Due to the physical nature of these constraints, we must consider the solution

over the entire domain. Thus, we formulate the full composite solution for ϕ^c,

$$\begin{aligned}\phi^c = A_0 x + B_0 + \sqrt{\epsilon}\,(A_1 x + B_1) + \left(\Phi_1 - c_0\left(1 - e^{-\xi}\right) + \sqrt{\epsilon}\left[N_2 c_0^2\left(\frac{1}{6} + 2\xi + \frac{1}{6}e^{-2\xi}\right) - c_1\left(1 - e^{-\xi}\right)\right]\right) \\ + \left(\Phi_2 - \tilde{c}_0\left(1 - e^{-\zeta}\right) + \sqrt{\epsilon}\left[N_2 \tilde{c}_0^2\left(\frac{1}{6} + 2\zeta + \frac{1}{6}e^{-2\zeta}\right) - \tilde{c}_1\left(1 - e^{-\zeta}\right)\right]\right) \\ - \left(\Phi_1 - c_0 + 2N_2 c_0^2 x + \sqrt{\epsilon}\left[\frac{N_2 c_0^2}{6} - c_1\right]\right) - \left(\Phi_2 - \tilde{c}_0 + 2N_2 \tilde{c}_0^2(1-x) + \sqrt{\epsilon}\left[\frac{N_2 \tilde{c}_0^2}{6} - \tilde{c}_1\right]\right) \qquad (5.117)\end{aligned}$$

The composite charge density ρ^c is take to be proportional to the second spatial derivative of this potential expression. We can impose the conservation of charge by integrating ρ^c through the polymer thickness and equating it to 0. From this we can solve for one of the remaining unknowns, c_1, which will have the form

$$c_1 = \tilde{c}_1 - \left[\frac{c_0}{\sqrt{\epsilon}} + \frac{N_2 c_0^2}{3}\left(1 + e^{\frac{-1}{\sqrt{\epsilon}}}\right)\right] + \left[\frac{\tilde{c}_0}{\sqrt{\epsilon}} + \frac{N_2 \tilde{c}_0^2}{3}\left(1 + e^{\frac{-1}{\sqrt{\epsilon}}}\right)\right] \qquad (5.118)$$

We can also impose a constraint on the symmetry of charge density, or potential, by constraining the value at $x = \frac{1}{2}$ to be either $\rho^c = 0$ or $\phi^c = \frac{\Phi_1 + \Phi_2}{2}$. In this case we assume that the charge density is zero, and solve for the coefficient $\tilde{c}_1$,

$$\tilde{c}_1 = \frac{-\tilde{c}_0}{\sqrt{\epsilon}} + \frac{N_2}{6}\left[c_0^2\left(1 - e^{\frac{-1}{2\sqrt{\epsilon}}}\right)^2 - \tilde{c}_0^2\left(1 + e^{\frac{-1}{2\sqrt{\epsilon}}}\right)^2\right] \qquad (5.119)$$

With this we have defined all of the coefficients of the composite potential function from equation 5.117. Figure 5.4a presents this potential response through the polymer thickness. ϕ^c in this case is dominated by the linear component of both the inner and outer expansions. Even as we magnify the response near $x = 1$ we see that the potential response is predominately linear. However, if we are to consider the charge density, defined as $\rho^c = -\frac{\partial^2 \phi^c}{\partial x^2}$, we see that the potential response does contain some higher-order features near the boundaries, evident in the sharp boundary effects of the charge density. Due to the relationship between ρ^c and ϕ^c, the linear component falls out due to the second derivative, leaving only the exponential components of ϕ^c. This profile has some similarity with the LCE system subject to nonlinear boundary conditions in section 5.3. The primary difference lies in the response of the inner expansions near $x = 0$ and $x = 1$. In the LCE system of Figure 5.3 the exponential terms have a very pronounced effect on the boundary region. In the NLCE system of Figure 5.4 the exponential effects are much more subtle and we must look to the charge density response of Figure 5.4b to observe their influence. Now we move on to the second case of the NLCE system, looking at the effects of the nonlinear component when applied at $\mathcal{O}(\epsilon^0)$.

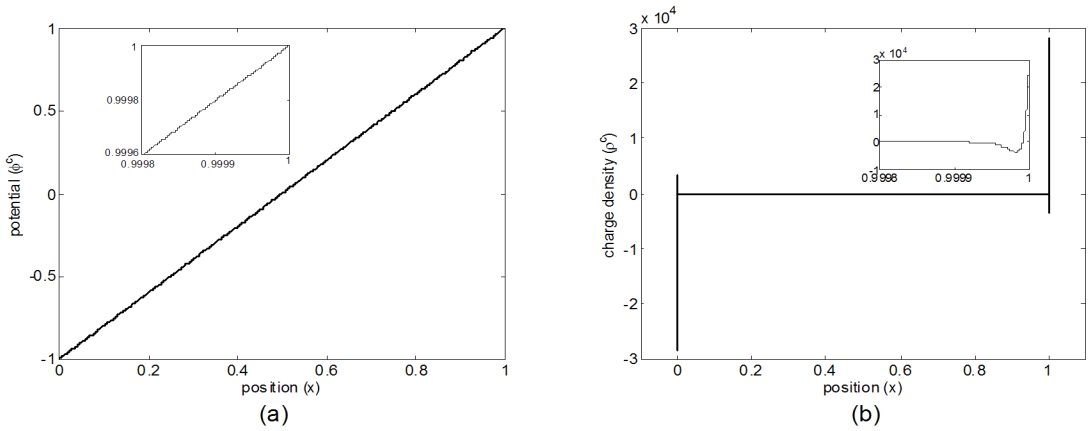

Figure 5.4: The composite solution for the matched-asymptotes analysis of *Case 1* of the steady-state NLCE problem with nonlinear boundary conditions. Plot (a) presents the potential profie through the polymer thickness, while (b) presents the composite charge density profile for NLCE *Case 1*.

5.4.5 Matched-Asymptotes of the NLCE for *Case 2*

The second case considered for the nonlinear continuity equation corresponds to the distinguished limit precipitated by the parameters $\varsigma = 0$ and $\nu > \frac{1}{2}$. Due to the relative complexity of this expression, we choose ν to be sufficiently larger than $\frac{1}{2}$, and simply consider a one-term approximation in the hopes of developing an analytical expression for ϕ^i and ϕ^I. Thus, the system will have inner expansions near $x = 0$ and $x = 1$ of the form,

$$\frac{d^4\phi^i}{d\xi^4} + N_2\left[\frac{d^3\phi^i}{d\xi^3}\frac{d\phi^i}{d\xi} + \left(\frac{d^2\phi^i}{d\xi^2}\right)^2\right] = 0 \qquad \frac{d^4\phi^I}{d\zeta^4} + N_2\left[\frac{d^3\phi^I}{d\zeta^3}\frac{d\phi^I}{d\zeta} + \left(\frac{d^2\phi^I}{d\zeta^2}\right)^2\right] = 0 \tag{5.120}$$

We begin our analysis by considering the inner expansion near $x = 0$ before moving on to the inner expansion near $x = 1$.

Inner expansion near $x = 0$ - NLCE for *Case 2*

In the region near $x = 0$ we assume the one-term expansion for ϕ^i of $\phi^i = \varphi + ...$ Expressing the approximate NLCE for *Case 2* in terms of this expansion,

$$\varphi^{iv} + N_2\left[\varphi'''\varphi' + \left(\varphi''\right)^2\right] = 0 \tag{5.121}$$

If we integrate both sides of this expression we find that

$$\varphi''' + N_2\left[\varphi''\varphi'\right] = b \tag{5.122}$$

where b is a constant of integration. At this point we recognize that this expression is very similar to the original flux boundary condition defined for the system. Therefore, we pause our development of the NLCE to consider the form of the general flux boundary condition in the region near $x = 0$. If we introduce the stretching transformation to the flux boundary condition and apply the constraints that $\varsigma = 0$ and $\nu > \frac{1}{2}$, then the flux can be expressed in terms of the inner coordinate as,

$$\frac{d^3\phi^i}{d\xi^3} + N_2 \left[\frac{d^2\phi^i}{d\xi^2}\frac{d\phi^i}{d\xi}\right]\Big|_{\xi=0} = 0, \qquad \text{or} \qquad \varphi^{'''} + \mathrm{N}_2 \left[\varphi^{''}\varphi^{'}\right]\Big|_{\xi=0} = 0 \tag{5.123}$$

Looking closely at this expression we see that it is equivalent to the integral of equation 5.121 evaluated at $\xi = 0$. In order for the system of equation 5.122 to satisfy this boundary condition, then the constant of integration b must be 0. Thus equation 5.122 can simply be written as $\varphi^{'''} + N_2 \left[\varphi^{''}\varphi^{'}\right] = 0$. At this point it is helpful to introduce a second change of coordinates, defining Υ to be equal to $\varphi^{'}$. This enables us to further simplify equation 5.122, expressing the system as

$$\Upsilon^{''} + N_2 \left[\Upsilon^{'}\Upsilon\right] = 0 \tag{5.124}$$

Now, if we integrate this expression we get

$$\Upsilon^{'} + \frac{N_2}{2}\Upsilon^2 = \frac{N_2}{2}k^2 \tag{5.125}$$

where $\frac{N_2}{2}k$ is again the constant of integration. This expression can also be written as

$$\frac{d\Upsilon}{d\xi} = \frac{N_2}{2}\left(k^2 - \Upsilon^2\right) \qquad \text{or} \qquad \frac{2\mathrm{d}\Upsilon}{(\mathrm{k}^2 - \Upsilon^2)} = \mathrm{N}_2\mathrm{d}\xi \tag{5.126}$$

When expressed in this form, the system is very similar to some nonlinear systems discussed by Nayfeh [57]. In his analysis he notes that there are two potential solutions, one corresponding to the case in which $\Upsilon^2 \leq k^2$ and the other in which $\Upsilon^2 \geq k^2$.

Case a: For the case in which $\Upsilon^2 \leq k^2$, we can assume a solution for Υ of the form,

$$\Upsilon = k\tanh\theta, \qquad\qquad d\Upsilon = k\ \mathrm{sech}^2\theta\mathrm{d}\theta$$

Substituting this into equation 5.126 we find

$$\frac{2k\ \mathrm{sech}^2\theta\mathrm{d}\theta}{\left(k^2 - k^2\tanh^2\theta\right)} = N_2 d\xi$$

At this point we recognize that $1 - \tanh^2\theta = \ \mathrm{sech}^2\theta$. Substituting this into the previous equation yields,

$$\frac{2}{k}d\theta = N_2 d\xi, \qquad d\theta = \frac{1}{2}kN_2 d\xi$$

Solving for θ,

$$\theta = \frac{1}{2}kN_2\left(\xi + m\right)$$

where m is a constant of integration. Substituting this expression back into Υ and integrating to yield φ, we get the one-term inner expansion of,

$$\phi_a^i = \varphi + ... = \frac{2}{N_2}\ln\left[\cosh\left(\frac{kN_2}{2}\left(\xi + m\right)\right)\right] + n + ... \tag{5.127}$$

where n is another constant of integration.

Case b: In the case where $\Upsilon^2 \geq k^2$, the solution is assumed to be

$$\Upsilon = k\coth\theta, \qquad\qquad d\Upsilon = k\ \ \mathrm{cosech}^2\theta \mathrm{d}\theta$$

Substituting this into equation 5.126 we find

$$\frac{2k\ \mathrm{cosech}^2\theta \mathrm{d}\theta}{\left(k^2 - k^2\coth^2\theta\right)} = N_2 d\xi = \frac{2}{k}d\theta$$

θ is solved for in the same manner as before, with $\theta = \frac{1}{2}kN_2\left(\xi + m\right)$, where m is again a constant of integration. Substituting this expression back into Υ and integrating to yield φ, we get the one-term inner expansion of,

$$\phi_b^i = \varphi + ... = k\ln\left[\sinh\left(\frac{kN_2}{2}\left(\xi + m\right)\right)\right] + n + ... \tag{5.128}$$

where n is another constant of integration. At this point we introduce the potential boundary condition at $\xi = 0$ to solve for the constant n in terms of the rest of the other coefficients. Imposing this boundary condition, we find that

$$Case\ \ a: \qquad \phi_a^i = k\ln\left[\cosh\left(\frac{kN_2}{2}\left(\xi + m\right)\right)\right] + \Phi_1 - k\ln\left[\cosh\left(\frac{kN_2}{2}m\right)\right] + ... \tag{5.129}$$

$$Case\ \ b: \qquad \phi_b^i = k\ln\left[\sinh\left(\frac{kN_2}{2}\left(\xi + m\right)\right)\right] + \Phi_1 - k\ln\left[\sinh\left(\frac{kN_2}{2}m\right)\right] + ... \tag{5.130}$$

We can also use the flux boundary condition to solve for one of the remaining constant coefficients. Imposing the

approximate flux condition from equation 5.123 to the solutions for *Cases a* and *b*, we find that

$$\textit{Case a:}\ \frac{k^4 N_2^3\,(kN_2-2)\tanh\left(\frac{kN_2 m}{2}\right)}{8\cosh^2\left(\frac{kN_2 m}{2}\right)}=0 \qquad \textit{Case b:}\ \frac{-k^4 N_2^3\,(kN_2-2)\coth\left(\frac{kN_2 m}{2}\right)}{8\sinh^2\left(\frac{kN_2 m}{2}\right)}=0$$

In order for these conditions to be satisfied, k must be defined as either 0 or $\frac{2}{N_2}$. Since $k=0$ is the trivial solution, we choose to consider the condition where $k=\frac{2}{N_2}$. Substituting this result into the definitions of ϕ_a^i and ϕ_b^i and considering the inner expansions in terms of the outer variable x, we develop the set of equations for *Case a* and *b*,

$$Case\ a: \qquad \left(\phi_a^i\right)^o=\frac{2}{N_2}\left(\ln\left[\cosh\left(\frac{x+m}{\sqrt{\epsilon}}\right)\right]-\ln\left[\cosh\left(\frac{m}{\sqrt{\epsilon}}\right)\right]\right)+\Phi_1+... \tag{5.131}$$

$$Case\ b: \qquad \left(\phi_b^i\right)^o=\frac{2}{N_2}\left(\ln\left[\sinh\left(\frac{x+m}{\sqrt{\epsilon}}\right)\right]-\ln\left[\sinh\left(\frac{m}{\sqrt{\epsilon}}\right)\right]\right)+\Phi_1+... \tag{5.132}$$

where we have rewritten the constant m in terms of $\sqrt{\epsilon}$ since it is simply a constant of integration whose form is somewhat arbitrary at the moment. Now we consider what happens as $\epsilon\to 0$. In the regions around $x=0$ the component $\ln\left[\sinh\left(\frac{x+m}{\sqrt{\epsilon}}\right)\right]$ is of the same order as $\ln\left[\sinh\left(\frac{m}{\sqrt{\epsilon}}\right)\right]$. Thus, we can express the outer expansions of ϕ_a^i and ϕ_b^i as

$$\textit{Case a:}\ \left(\phi_a^i\right)^o=\Phi_1 \qquad \text{and} \qquad \textit{Case b:}\ \left(\phi_{\mathrm{b}}^{\mathrm{i}}\right)^{\mathrm{o}}=\Phi_1 \tag{5.133}$$

Since we are only considering a one-term expansion for ϕ^i, we now equate the results of $\left(\phi_a^i\right)^o$ and $\left(\phi_b^i\right)^o$ with the one term inner expansion of ϕ^o. Equating these expansions we find,

$$A_0 x+B_0=\Phi_1 \qquad \rightarrow \qquad A_0=0, \qquad B_0=\Phi_1 \tag{5.134}$$

At this point we consider the inner expansion near $x=1$.

Inner expansion near $x=1$ - NLCE for *Case 2*

The development of the inner expansion near $x=1$ follows the same development as that near $x=0$. Therefore, we can express the expansion in terms of the stretching coordinate ζ

$$Case\ a: \qquad \phi_a^I=\frac{2}{N_2}\left(\ln\left[\cosh\left(\zeta+\frac{m}{\sqrt{\epsilon}}\right)\right]-\ln\left[\cosh\left(\frac{m}{\sqrt{\epsilon}}\right)\right]\right)+\Phi_2+... \tag{5.135}$$

$$Case\ b: \qquad \phi_b^I=\frac{2}{N_2}\left(\ln\left[\sinh\left(\zeta+\frac{m}{\sqrt{\epsilon}}\right)\right]-\ln\left[\sinh\left(\frac{m}{\sqrt{\epsilon}}\right)\right]\right)+\Phi_2+... \tag{5.136}$$

Next we consider the inner expansion in terms of the outer variable $x = 1$. Imposing the definition for the stretching coordinate $\zeta = \frac{1-x}{\sqrt{\epsilon}}$,

$$Case\ a: \qquad \left(\phi_a^I\right)^o = \frac{2}{N_2}\left(\ln\left[\cosh\left(\frac{(1-x)+m}{\sqrt{\epsilon}}\right)\right] - \ln\left[\cosh\left(\frac{m}{\sqrt{\epsilon}}\right)\right]\right) + \Phi_2 + ... \tag{5.137}$$

$$Case\ b: \qquad \left(\phi_b^I\right)^o = \frac{2}{N_2}\left(\ln\left[\sinh\left(\frac{(1-x)+m}{\sqrt{\epsilon}}\right)\right] - \ln\left[\sinh\left(\frac{m}{\sqrt{\epsilon}}\right)\right]\right) + \Phi_2 + ... \tag{5.138}$$

where we have rewritten the constant m in terms of $\sqrt{\epsilon}$ since it is simply a constant of integration whose form is somewhat arbitrary at the moment. Now we consider what happens as $\epsilon \to 0$. In the regions around $x = 0$ the component $\ln\left[\sinh\left(\frac{(1-x)+m}{\sqrt{\epsilon}}\right)\right]$ is of the same order as $\ln\left[\sinh\left(\frac{m}{\sqrt{\epsilon}}\right)\right]$. Thus, we can express the outer expansions of ϕ_a^I and ϕ_b^I as

$$\textit{Case a:}\ \left(\phi_a^i\right)^o = \Phi_2 \qquad \text{and} \qquad \textit{Case b:}\ \left(\phi_{\mathrm{b}}^{\mathrm{i}}\right)^{\mathrm{o}} = \Phi_2 \tag{5.139}$$

Since we are only considering a one-term expansion for ϕ^I, we now equate the results of $\left(\phi_a^I\right)^o$ and $\left(\phi_b^I\right)^o$ with the one term inner expansion of ϕ^o. Equating these expansions we find,

$$A_0 x + B_0 = \Phi_2 \qquad \rightarrow \qquad A_0 = 0, \qquad B_0 = \Phi_2 \tag{5.140}$$

Now if we compare these results with those obtained in matching the expansions near $x = 0$, we find that the slope A_0 is 0 in each case, however the intercept B_0 is discontinuous over the region of the outer expansion. In the matching process near $x = 0$ this constant term is determined to be Φ_1, whereas at $x = 1$ the constant B_0 is required to be Φ_2 to satisfy the matching criteria. The discontinuous nature of this solution indicates that the one-term expansion is insufficient for modeling the nonlinear system of *Case 2*. Some work was done to investigate higher order expansions of the system defined in equation 5.120, however an analytic solution could not be determined.

5.5 Comparison with numerical simulations

Another active researcher in the area of ionic polymer modeling is Thomas Wallmersperger [89, 90, 91, 47] of the Universität Stuttgart in Stuttgart, Germany. Much of Wallmersperger's work focuses on using numerical methods for modeling charge motion within ionic gels and membranes. We have had the opportunity to collaborate with Wallmersperger on numerous occations, applying his modeling techniques to electromechanical models of the IPT for comparison with experimental data [47], as well as using his simulation results for comparison with our analytical and approximate methods. Figure 5.5a presents the transient to stead-state development of the internal potential subject to a step voltage of 50mV across the polymer thickness (provided courtesy of Thomas Wallmersperger).

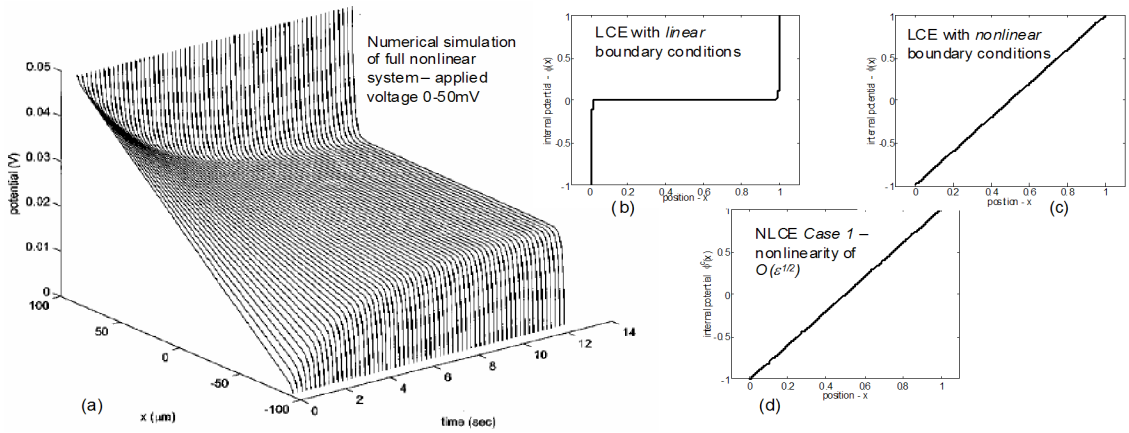

Figure 5.5: Comparison o fthe steady-state potential predictions with numerical simulations of Thomas Wallmersperger. Plot (a) presents the transient to steady-state simulation conducted by Wallmersperger for a 50mV step voltage. Plot (b) presents the approximate solution for the LCE with *linear* boundary conditions while (c) corresponds to the LCE with *nonlinear* boundary conditions and (d) presents the results of *Case 1* from the NLCE analysis.

This response is a numerical approximation to the full nonlinear transport equation similar to the nondimensional system of equation 5.1. This response predicts an initial linear potential distribution at time $t = 0$s, which gradually develops into a steady-state profile reminiscent of a hyperbolic sine distribtution beyond $t = 10$s.

In addition to the numerical simulations, the approximate solutions from sections 5.2 - 5.4 are also shown in Figure 5.5 b-d. Interestingly, we see that the linear approximation of equatuion 5.1 subject to the linear flux boundary conditions actually provides the best approximation of the steady-state response of Figure 5.5a. The responses of Figures 5.5 c and d show almost identical linear profiles, similar to the internal potential response at $t = 0$s. Looking into the specific constraints considered in the analysis from sections 5.2 - 5.4 we see that the variations in Figure 5.5 b-d must be tied to the flux boundary conditions imposed upon the transport equation. In the case of the LCE with linear boundary conditions the flux conditions was only a slight variation on the governing equation itself. Since we are considering the steady-state response, the LCE is simply the gradient of the linear ion flux expression. In this manner, the only variation between the flux and the LCE is the constant of integration discussed earlier in section 5.3.2. This relationship between the boundary condition and the LCE makes the second flux boundary condition redundant, such that it does not add any additional information to the problem. We circumvented this redundancy by introducing the conservation of charge condition to augment the loss of an effective constraint.

In the case of section 5.3, the nonlinear flux does not produce this redundancy. Instead the internal potential can be solved directly from the potential and flux boundary conditions and all of the coefficients of the inner and outer expansions can be determined through the matching process. The NLCE of section 5.4 has a similar effect. While the $\mathcal{O}\left(\epsilon^0\right)$ expression is equivalent to the LCE and is subject to linear flux conditions, the presence of the nonlinear flux relationshp at $\mathcal{O}\left(\epsilon^{1/2}\right)$ produces an additional term of $\mathcal{O}(\epsilon^0)$ in the matching process near $x = 1$. The

presence of this term $2N_2\tilde{c}_0^2$ enables us to solve for the $\mathcal{O}(\epsilon^0)$ coefficients. In each of these development (sections 5.3 & 5.4) the solution to the outer expansion produces the linear profiles in Figures 5.5 c & d. The linear nature of these profiles are a direct result of the nature of the flux boundary conditions and how they interact with the governing differential equation. If we extend this reasoning to the full nonlinear transport problem of equation 5.2, we recognize that the nonlinear boundary conditions of equation 5.3 are actually the integral of the NLCE. Thus, the application of one boundary condition is enough to prescribe the flux at both of the polymer's outer surfaces. This similarity between the linearized and the nonlinear transport problems is what produces the qualitative agreement in the steady-state response of Figures 5.5 a & b. And while the approximations of sections 5.3 and 5.4 do not provide definitive agreement with the full nonlinear transport equation, they do provide insight into the roll of the flux boundary condition on the internal potential response.

5.6 Chapter summary

This chapter has focused on the effect of nonlinear components in the transport equation and flux boundary condition on the internal potential response of the ionic polymer transducer. Three main formulations were considered in this development: (1) the linear continuity equation (LCE) with linear boundary conditions, (2) the LCE with nonlinear flux boundary conditions and (3) the nonlinear continuity equation (NLCE) with nonlinear boundary conditions. The third formulation was split into two distinct cases, each corresponding to a different weighting of the nonlinear component in the NLCE. The method of matched asymptotes was used to divide the polymer into three principle regions: two inner expansions which magnified the regions very near the polymer surface, and an outer expansion which defined the bulk of the polymer between the two inner expansions. Analysis of the LCE with linear boundary conditions was compared to the exact solution from Chapter 4, illustrating the effectiveness of the matched asymptotes method in predicting the steady-state spatial profile of the internal potential. Following the development of each formulation, a comparison was made with numerical simulations of the full NLCE with nonlinear flux boundary conditions provided by Thomas Wallmersperger. Comparison of these results illustrates the importance of the flux boundary condition on the predicted response. Interestingly, it was seen that the linearized system of section 5.2 actually produced the best agreement with the full NLCE response. This result is attributed to the interaction between the flux boundary condition and the continuity equation. In the case of the LCE and the full NLCE, the steady-state continuity equation is actually the gradient of the flux condtions, producing an interesting interaction between the boundary conditions and the transport equation under consideration. The special conditions considered in sections 5.3 and 5.4 failed to capture this relationship, resulting in profiles that were dominated primarily by a linear profile. While these approximations do not completely agree with simulations of the full nonlinear tranport problem, they offer a considerable amount of insight into the relationship that the flux boundary condition has on the system response. To try and improve our understanding further we will shift our focus to experimental results in which we

try to quantify the internal potential response through the polymer thickness.

Chapter 6

Experimental studies

The previous chapters have focused on the development of internal potential and electrical impedance models of the ionic polymer transducer, derived from basic transport theory. In addition to the analytical and numerical comparisons used in validating the modeing approach used in each of the preceeding chapters, a series of experimental studies have also been conducted to consider the effectiveness of the models. These experimental studies are considered in two distinct groups: (1) frequency domain analysis of the impedance response and (2) time domain analysis of layered transducers. The first set of experiments focus on the impedance response of ionic polymer transducers, considering the effect of temperature, solvent viscosity and pretension on the material's voltage to current relationship at the transducer's electrodes. For the solvent viscosity study we revisit the glycerol study of Chapter 3 and use the modeling approach of Chapter 4 to determine equivalent diffusion and permittivity values for the transdcuers swollen with varying glycerol concentration. In the second series of experiments a set of layered transducers are used to measure the internal potential at discrete points within the polymer for both step and harmonic voltage excitations.

6.1 Impedance response

The culmination of the modeling approach in Chapter 4 is the development of an expression for the isothermal transient ionic current (ITIC) in response to a harmonic voltage signal applied to the polymer's outer electrodes. This model of the surface current enables us to predict the polymer's electrical impedance as a function of five principle terms: anion concentration C^-, polymer thickness L, ambient temperature T, diffusion coefficient d, and the transducer's effective permittivity κ. A parametric study was conducted at the end of Chapter 4 considering the effects of d, κ and T on the predicted impedance response. In this chapter we shift our focus to the physical system, looking at the experimental impedance as a function of ambient temperature, solvent type and mechanical loading.

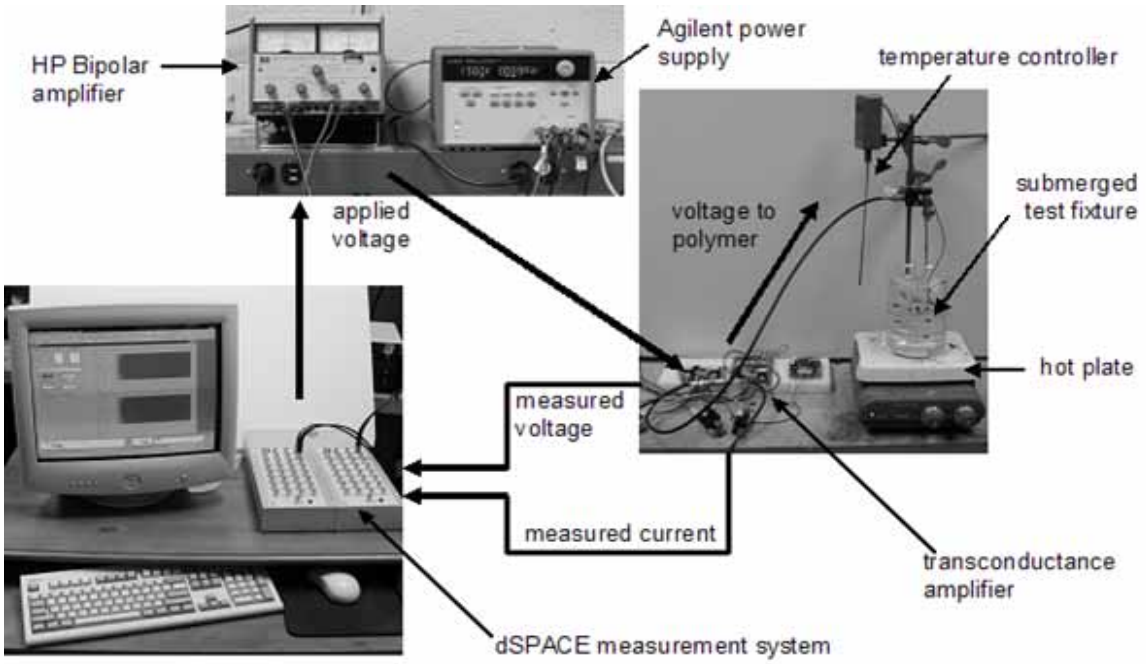

Figure 6.1: Test fixture used to test the ionic polymer's electrical impedance at various temperatures.

6.1.1 Impedance as a function of ambient temperature

Numerous studies of ionic polymers have shown that the transport properties vary as a function of the ambient temperature. Some of the first work performed in this area was conducted by Yeager *et al.* [98, 99] who investigated the self-diffusion properties of Nafion as a function solution temperatures. From their experimental work Yeager *et al.* found that the ion mobility goes down with temperature, resulting in lower diffusion coefficients at lower temperature scales. Paquette and Kim [70, 71, 72] went on to consider the effect of subzero temperatures on Nafion based ionic polymer-metal composites (IPMC). Focusing on the actuation response, Paquette and Kim found that the IPMC transducers still exhibit an actuation response below the freezing temperature of the solvent (water), however they found that the blocked force response declined with decreasing temperature. They attributed this feature to the formation of water crystals within the ionomer, a result offers agreement with findings of Asaka *et al.* [4].

In this chapter we consider the ionic polymer transducer's response to temperatures above and below room temperature. In the parametric study of Chapter 4, we recognized the importance of the relationship between diffusion properties and ambient temperatures in ionomer membranes. Integrating the diffusion results of Yeager *et al.* we found that the high frequency resistance is predicted to decrease with increasing temperature in the parametric study of Chapter 4. Now we consider how these predictions correlate with experimental measurements. Figure 6.1 presents the experimental set-up used in this investigation. A dSPACE 1005 controller with DS2103 DAC / DS2002/2003 MUX AD Boards was used for signal generation and measurement of the voltage and current responses of the ionic

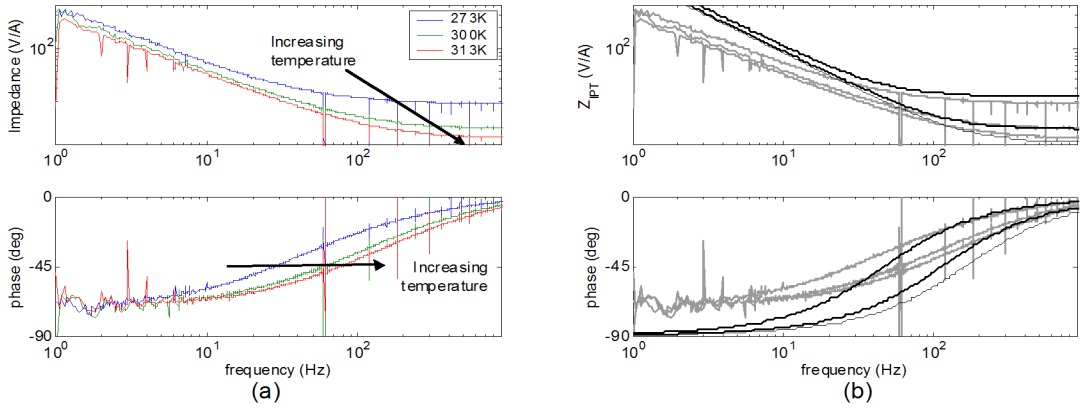

Figure 6.2: Impedance response of an IPT in Li^+ form as a function of temperature, ranging from 274K - 313K. Plot (a) presents the results measured directly from the experimement while (b) presents the results as normalized by the low frequency component of the sample at 274K. In the comparison of (b) the gray curves correspond to experimental data and black curves correspond to model predictions.

polymer sample. The transducer was driven with a chirp voltage signal of 0.5V, 0-1000 Hz through an HP 6825A Bipolar Power Supply / Amplifier. A transductance amplifier [65], powered by an Agilent E3648A Dual Output DC Power Supply, was used to condition the voltage signal into the ionic polymer, and to measure the current drawn by the polymer as the tests were run. The polymer itself was mounted between fixed electrodes in a fixture that was submerged in de-ionized water. Temperature of the water was controlled using a Corning hot plate and a feedback Corning Temperature Controller. An ice bath was used for measurements below room temperature. A standard mercury thermometer was used to verify the temperature of the water bath in each case. Three temperature levels were considered in these experiments, corresponding to 0^oC, 25^oC and 40^oC. These temperature levels were chosen to correspond to the diffusion studies of Yeager *et al.* summarized in Table 4.2.

In the testing process, the IPT was placed in a water bath as the temperature was regulated to the desired level. Once the water bath had reached the target temperature, the system was allowed to equilibrate for 30 minutes before testing began. The testing procedure began at 0^oC and then was increased to 25^oC and 40^oC, subsequently. All tests were run consecutively to minimize sample variation. The results of this analysis are shown in Figure 6.2a. From this set of experiments we see that the ambient temperature has a strong effect on the steady-state resistance of the IPT, showing strong agreement with the predictions of Figure 4.19 in Chapter 4. Looking closely at the low frequency response of Figure 6.2a, we see a slight shift in magnitude of the response. This feature is attributed to a increase in the capacative term in the impedance, which is directly related to the effective permittivity κ of the material. Thus, by looking at the frequency domain response of the electrical impedance we can note that the increased temperature must result in a rise in both the diffusion coefficient *and* the effective permittivity of the membrane. More specifically, we can also draw the conclusion that the increased temperature has a larger effect on d than it does on the permittivity κ. This observation is based primarily on the behavior of the corner frequency and

Table 6.1: Model parameters used to simulate impedance as a function of temperature .

Temperature T (^{o}C)	Electric Permittivity κ (F/m)	Diffusion Coefficient d (m^2/s)
0	2.26E-2	0.694 E-9
25	2.63E-2	2.133 E-9
40	2.82E-2	3.413 E-9

phase information of the impedance response. From the experimental results of Figure 6.2a we see that the corner frequency continually increases with rising termperature, as does the phase transition of the impedance. This shift in corner frequency is indicative of an increase in d. From the parametric study of Chapter 4, we see that the the permittivity has an opposing influence on the corner frequency, as related in the expression for the system's time constant λ,

$$\lambda = d\gamma^2 = d\frac{F^2C^-}{\kappa RT}$$

From this expression we see that the material's time constant is proportional to the material's diffusion coefficient and inversely proportional to the effective permittivity and temperature. Therefore, the diffusion coefficient must be the dominant mechanism in order for the corner frequency of the impedance to increase in the steady manner represented in Figure 6.2a.

If we apply this reasoning to the modeling approach, we can generate the predictive impedance curves of Figure 6.2b. In this set of simulations the impedance at room temperature $T = 298K$ is used as the baseline. From this impedance profile, the model from Chapter 4 is fit to the data by fixing the temperature to $T = 298K$ and tuning the diffusion coefficient d and permittivity κ to match the experimental response. From this initial fit, the temperature is defined by the experimental conditions and the diffusion coefficient is scaled following the relationship prescribed by Yeager *et al.* [99], and illustrated in Figure 4.19a. Therefore the free variable in this analysis was the effective permittivity κ. This parameter was initially fit to the response at $T = 298K$ and then used to match scaling of the low frequency impedance. The specific values used in this matching process are presented in Table 6.1. Applying these values to the predictive model, we obtain the simulation results of Figure 6.2b, which are compared to the experimental data of Figure 6.2a. Comparing the experimental and analytical responses, we see that there is good agreement as the polymer transitions to its high frequency resistive response. At low frequencies there is some discrepancy in the slope of the capacitive response, however this is attributed to the DC resistance of the transducer which is not accounted for in the transport equation. This also accounts for the phase behavior at low frequencies as the experimental data levels off near -60^o. Below 1Hz the phase actually increases back to 0^{o}in response to the DC resistance. In the region near the corner frequency we find good correlation between the model predictions and experimental results. Tuning the model to the room temperature response, we rely on measurements

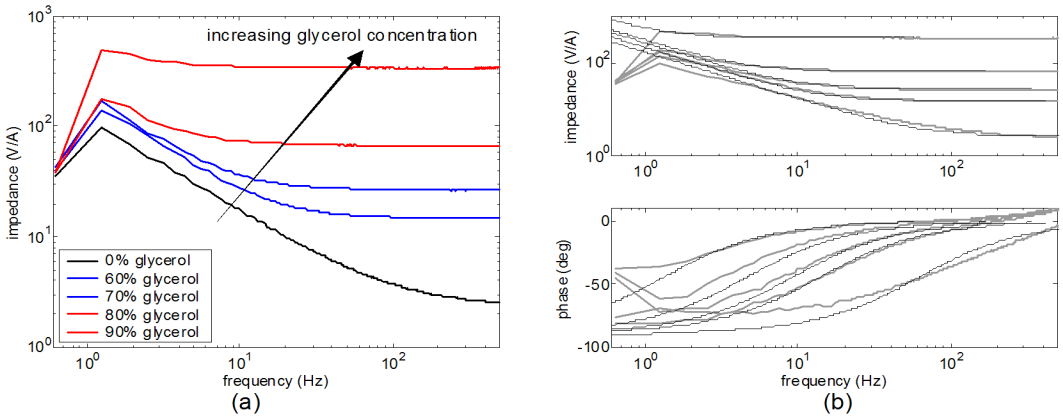

Figure 6.3: Impedance response of an IPT as a function of solvent viscosity, ranging from 1.01*cp* to 265.98*cp*. Plot (a) presents the results measured directly from the experimement while (b) presents a comparison with model predictions. In the comparison of (b) the gray curves correspond to experimental data and black curves correspond to model predictions.

of T and previously published scaling of d to predict the impedance response at $T = 273K$ and $T = 313K$. Slight variations in the electric permittivity κ were also used to scale the low frequency magnitude response to correspond with similar shifts in the electrical impedance of the material. From Table 6.1 we see that only minor shifts in the permittivity ($2.26x10^{-2}$ F/m to $2.82x10^{-2}$ F/m) were used to tune the response. If we neglect variations due to the DC resistive term, we see that the model is effective a predicting the impedance response, both in the tuned region and as a function of the ambient temperature.

6.1.2 Impedance response as a function of solvent viscosity

The second set of experiments revisit the viscosity study of Chapter 3. Using varying concentrations of a glycerol-water mixture we obtain viscosity levels that range from 1cp to 265cp. Samples were driven with a random excitation signal while the impedance response was measured using a Tektronix 2630 Fourier analyzer. The transconductance amplifier designed by Newbury [65] was again used to condition and measure the voltage and current signals being sent to the test sample. The impedance response for the five viscosity levels are shown in Figure 6.3a. This figure illustrates the highly resistive nature that results for solvents with increasing viscosity. Relative to the model, this type of behavior is expected to have the greatest influence on the diffusion coefficient based upon the trends established in the parametric studies of Chapter 4. The model predictions for the viscosity response are shown in Figure 6.3b and the corresponding model parameters used in each prediction are presented in Table 6.2. In addition to the standard model parameters T, d and κ, a gain factor g is introduced and associated with the electrode area of the IPT transducer. This gain factor is introduced to account for variations in the elctrode conductivity that result from the polymer being imbibed with different concentrations of glycerol. As in Chapter 3, it was visually

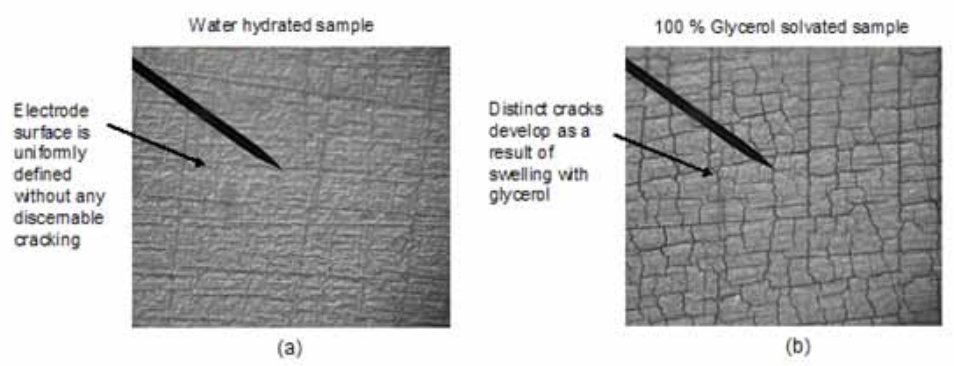

Figure 6.4: Magnified images of the surface electrode for samples solvated in 100% water (a) and 100% glycerol (b). The baseline water-based sample shows a uniform electrode surface whereas the glycerol sample illustrates distinct cracking in the surface electrode as a result of membrane swelling.

apparent during testing that higher glycerol contents produce thin films of glycerol which coated the IPT's electrodes. Additionally, the higher glycerol concentrations were seen to induce more swelling in the membrane, producing more stress on the outer electrodes of the test sample. Upon closer examination of the electrode surface, a noticable degree of cracking was seen in the electrode, as shown in Figure 6.4. From visual inspection it can seen that electrode cracking becomes more severe at higher glycerol concentrations, a feature that is expected to greatly affect the electrode conductivity. The model developed in Chapter 4 is a one-dimensional model of the internal potential and ITIC through the thickness dimension of the transducer. The result of the model is an expression for the ITIC, or current density $\left(A/m^2\right)$, of the polymer. To obtain predictions of the measureable surface current, an effective area must be applied to estimate the total current in amperes. For a surface electrode with 0 Ohm resistance, the area would correspond to the physical dimensions of the transducer. However, since the surface electrodes considered in this experiment became less conductive with higher concentrations of glycerol, the gain factor g was introduced to account for unmodeled effects in the surface conductivity associated with using the 1D model to predict the current response of a physical 3D tranducer.

Since the experiments were all conducted at room temperature, T was set to be $293K$ in each of the

Table 6.2: Model parameters used to simulate impedance as a function of viscosity .

Glycerol Content (%)	Viscosity (cp)	Temperature T (K)	Electric Permittivity κ (F/m)	Diffusion Coefficient d (m^2/s)	Gain g
0	1.01	293	0.30 E-2	13.00 E-11	0.475
60	10.68	293	1.00 E-2	9.75 E-11	0.114
70	23.04	293	1.20 E-2	7.80 E-11	0.076
80	59.90	293	1.20 E-2	3.90 E-11	0.067
90	265.98	293	1.40 E-2	1.30 E-11	0.038

simulations, leaving us with the tuning parameters κ, d and g. Looking initially at the experimental response of Figure 6.3a, we see that there is a significant change in the resistive nature of the transducer with increasing solvent viscosity. Because of this we expect a significant variation in the polymer's diffusion coefficient at higher viscosity levels. We also see a shift in the magnitude of the low frequency response (near 1.2Hz) which is a characteristic feature of the material's capacitive response, indicating an expected variation in the polymer's effective permittivity as well. Relating the trends in the response of Figure 6.3a with the parametric study of Chapter 4, we expect a general decrease in d and an increase in κ to correspond with the changes in increased solvent viscosity. Looking at the tuning parameters of Table 6.2 we see that this is indeed the scaling trend exhibited by the material parameters d and κ. We also note that there is a steady decline in the gain factor g as the solvent viscosity increases. This trend is attributed to higher glycerol concentrations within the polymer and their effect of diminishing performance of the transducer's electrode. As discussed previously, the increased glycerol content produces stress fractures in the electrode due to increased swelling in the transducer. When these degredations in the electrode are taken into consideration it is reasonable to expect the overall conductivity of the electrode to decrease, and for the measured current to decline as well. This is precisely the effect seen in the results of Figure 6.3b as the polymer becomes much more resistive at higher glycerol concentrations. This trend is also evident in the gain factor g of Table 6.2. As solvent viscosity increases, the resultant current must decline to account for the deterioration of the polymer's electrodes. Once all of these factors are applied to the modeling approach, we see that the impedance model can effectively predict the IPT's performance for different glycerol concentrations and viscosities. Additionally, the overall gain factor provides some accountablity for changes in the properties of the external electrode.

6.1.3 Impedance response as a function of pretension

The third set of experiments considered in this chapter focus on the IPT's impedance response under pretension. For this set of experiments the fixture of Figure 6.5a was built to apply a longitudinal preload to the IPT during impedance measurements. The fixture relies on four parallel springs (individual spring constants: 2325 N/m) to apply tension to the test sample. Three levels of tension were applied to the test sample, corresonding to loads of 27.93N, 102.32N and 152.12N. The Tektronix 2630 Fourier analyzer was used for data acquisition and the transconductance amplifier of Newbury [65] was used to condition both voltage and current signals being supplied to the test sample.

The impedance response for these three pretension levels are presented in Figure 6.5b. The trend in this data indicates that the polymer becomes more resistive as a function of the applied tension. At low frequencies the response shows very little variation between different test conditions, indicating that the capacitive nature of the IPT is relatively invariant to change over the range of preloads considered in this study. From these trends we conclude that pretension has a predominant effect on the diffusion properties of the IPT. Since the capacitve nature does not exhibit much variation, the effective permittivity is not expected to vary greatly with longitudinal loading. Using

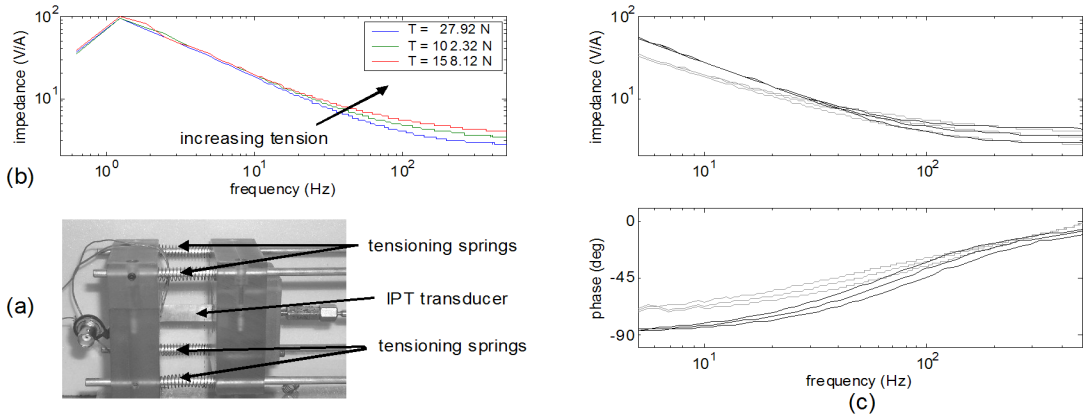

Figure 6.5: Impedance response of an IPT as a function of pretension, ranging from 27.92N to 152.12N of applied tension. Plot (a) presents the results measured directly from the experimement while (b) presents a comparison with model predictions. In the comparison of (b) the gray curves correspond to experimental data and black curves correspond to model predictions.

these trends as guidelines, we can simulate the polymer's predicted response using the values tabulated in Table 6.3. These predictions are compared to the experimental results in Figure 6.5c. From this figure we see that there is good agreement with the high frequency response, however some variation is evident in the low frequency slope, again attributed to the DC resistance in the test sample which not addressed in the transport model. If we now look to the model parameters used in this simulation, we see that T, κ and the gain factor g remain very consistant throughout the analysis, making the diffusion coefficient d the dominant tuning parameter. In this set of experiments an overall gain factor g is again introduced to account for mechanical cracking in the electrode that results from the initial pretensioning of the sample. This parameter is tuned according to the lowest level of applied tension and held fixed for the subsequent tests at 102.32N and 152.12N.

From the parametric study of Chapter 4 we note that the permittivity term is only effective in scaling the capacitive component of the IPT response, whereas the variable gain factor g would simply produce shifts in the magnitude of the entire impedance response. Since the low frequency component of the measured data in Figure 6.5 shows only minimal variation, neither of these parameters are suitable for describing the observed behavior. Based upon this analysis we conclude that the ionic polymer's impedance response is dominated by the diffusion coefficient

Table 6.3: Model parameters used to simulate impedance as a function of pretension.

Pretension (N)	Temperature T (K)	Electric Permittivity κ (F/m)	Diffusion Coefficient d (m^2/s)	Gain
27.92	293	2.64 E-3	1.82 E-10	0.132
102.32	293	2.60 E-3	1.43 E-10	0.132
152.12	293	2.58 E-3	1.17 E-10	0.132

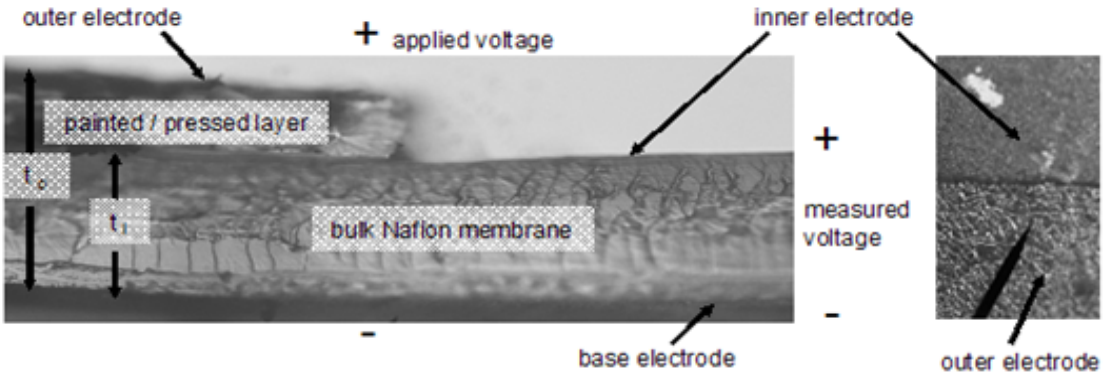

Figure 6.6: Schematic for the layered transducer.

in the case where the polymer is subject to a preload. Physically this implies that stress applied orthogonal to the thickness has an effect on the internal structure of the polymer which impedes the motion of ions through the polymer thickness. One possible explanation for this effect could come from the slight thinning effect that would be expected in the width and thickness directions due to the applied longitudinal load. Intuitively this thinning would deform the internal structure of the polymer, potentially distorting ion clusters as well as ion transport channels. Currently this is a heuristic explanation for the observed phenomena, however future work may provide morphological insight into the polymer's structure that could be used in fundamental design of new ionomer membranes.

6.2 Internal potential

The final series of experiments considered in this chapter shift our focus away from the frequency domain as we consider the polymer's internal voltage response in the time domain. In the previous section we considered experimental results which were used to validate the modeling approach developed in Chapter 4, describing the IPT's electrical impedance. In this section we turn our attention to the boundary layer analysis of Chapter 5. The focal point of Chapter 5 is modeling the steady-state potential profile expected to develop under different simplifications of the transport equation. To analyze this approach experimentally, we use a series of layered transducers to try and gain insight into the internal potential, trying to measure internal potential at specific points within the polymers thickness. The goal is to then take these measured data points and compare them with the potential profiles predicted in Chapter 5. To obtain these layered transducers, we use the melt-press fabrication technique developed by Akle *et al.* [2]. The cross-section of a representative sample is shown in Figure 6.6 along with the relevant nomenclature which will be used throughout this discussion. The fabrication technique used to plate these test samples begins with the base, or bulk, Nafion membrane. A full gold electrode is pressed on the bottom of the membrane (base electrode)

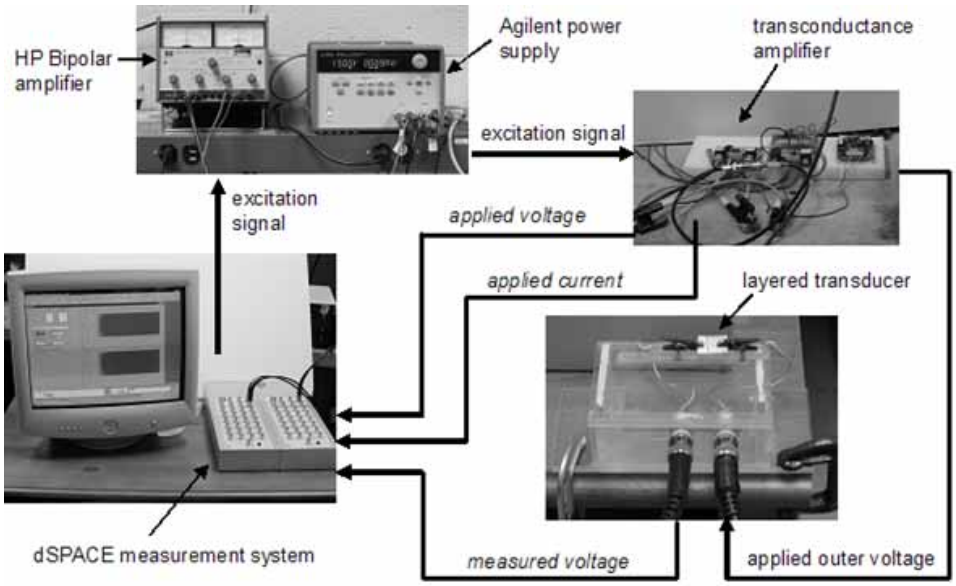

Figure 6.7: Test fixture used to characterized the layered transducers.

and a partial electrode is pressed on the top of the bulk Nafion membrane (inner electrode). Once these electrodes are in place, a second layer of Nafion is either hot-pressed or painted on top of the bulk Nafion membrane and the inner electrode. The painting method offers very fine adjustments of this top layer and was therefore adopted as the method for this experimental study. Once the desired number of layers of Nafion have been added on top of the inner electrode, a third layer of gold is pressed onto the newly deposited polymer, establishing the outer electrode shown in Figure **??**. Two distinct sets of experiments were conducted for the layered transducer, the first focuses on a 180μm Nafion membrane swollen in the organic solvent formamide, and the second on a 120μm Nafion membrane swollen in the ionic liquid 1-ethyl-3-methylimidazolium trifluoromethanesulfonate (EMI-Tf).

A schematic for the experimental set-up is shown in Figure 6.7. A dSPACE 1005 controller with DS2103 DAC / DS2002/2003 MUX AD Boards was again used for signal generation and measurement of the voltage and current responses of the ionic polymer sample in both test cases. The transducers were driven by 1V, 0.2Hz harmonic and square wave excitations through an HP 6825A Bipolar Power Supply / Amplifier. A transductance amplifier [65], powered by an Agilent E3648A Dual Output DC Power Supply, was used to condition the voltage signal into the ionic polymer, and to measure the current drawn by the polymer as the tests were run. Voltage was applied across the outer and base electrodes to excite the test sample, while the internal voltage was measured across the inner and base electrodes. The same test procedure was used in each of the test cases, both of which are discussed in detail in the following sections.

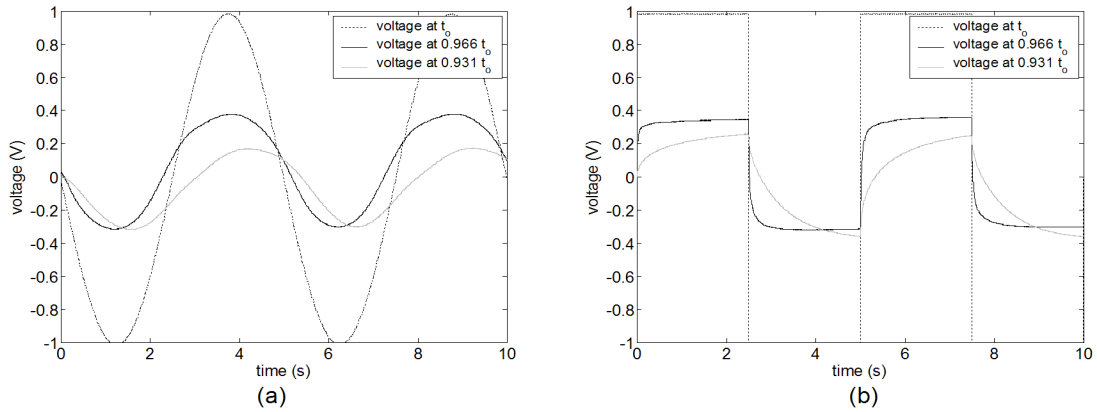

Figure 6.8: Voltage response for two layered ionic polymer transducers with formamide as a diluent. Plot (a) presents the harmonic voltage response for two layered transducers with electrodes at different locations within the polymer. Plot (b) presents the square wave response to a 0.2 Hz, 1V square wave.

6.2.1 Formamide based transducer

The first series of tests considered in this analysis focused on layered transducers fabricated from 180μm Nafion membranes swollen in the organic solvent formamide. Since we are most concerned with the internal potential near the boundary layers, two transducers were fabricated with innner electrodes positioned at t_i = 93.1% and 96.6% of the total thickness t_o. The transducers were subject to a 1V, 0.2Hz harmonic and square wave excitation while the internal potential was monitored at the inner electrode. The results of these tests are shown in Figure 6.8.

From these results we clearly see that the internal potential diminishes significantly with smaller ratios of $\frac{t_i}{t_o}$. This characteristic is evident in both the harmonic and square-wave excitatations. An interesting feature does develop in the response measured at an inner electrode location of $t_i = 0.931t_o$. For this sample, the applied voltage is symmetric between -1V and 1V, however the inner response exhibits a DC offset of -0.05V. The response at $t_i = 0.931t_0$ also contains a phase lag relative to the excitation signal applied across the outer electrodes. This feature was seen consistently in repeated tests, however since it is only a single sample it is difficult to draw conclusions. Therefore, we broaden our study to include the ionic liquid based transducers to see if similar trends are observed in their response.

6.2.2 EMI-Tf based transducer

The EMI-Tf based transducers were fabricated using the same basic approach as the formamide samples, except using a 120μm Nafion membrane rather than the 180μm membrane used in the formamide samples. Another minor distinction also exists between these two solvents as the ionic liquid samples were more amenable to the fabrication process. The formamide samples could not be fabricated at the same melt-press temperatures as the EMI-Tf samples,

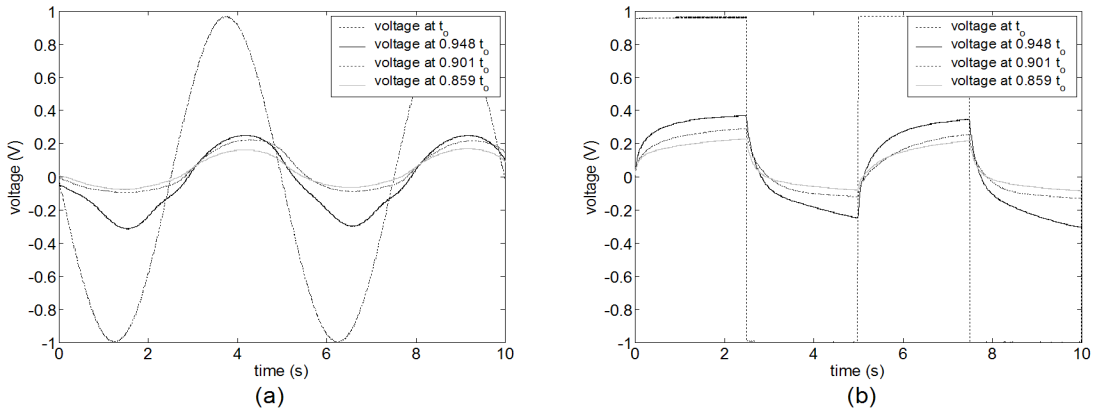

Figure 6.9: Voltage response for two layered ionic polymer transducers with an EMI-Tf serving as the diluent. Plot (a) presents the harmonic voltage response for three layered transducers. Plot (b) presents the square wave response to a 0.2 Hz, 1V square wave.

and therefore the gold electrodes were found to be more fragile in the case of the formamide samples.

For the ionic liquid based IPTs, we were able to fabricate three separate samples, with t_i/t_o ratios of 0.859, 0.901 and 0.948. Using the same test procedure, the results of Figure 6.9 were obtained. The square wave response of Figure 6.9b exhibits a rather symmetric response about $V = 0$, however some interesting features seem to develop in the harmonic response of Figure 6.9a. In this response the internal voltage near $t_i = 0.948t_o$ exhibits an noticably nonlinear response with what appears to be a cubic nonlinearity present in the measured signal. This result follows the observations of Kothera [39], who examined the nonlinear relationships found in the low frequency response of ionic polymers swollen various ionic liquids. Since we are operating at low frequencies it is not surprising to encounter nonlinearities, however it is interesting to see them develop in the voltage measurement since we are driving the polymer with an similar voltage signal. In the work by Kothera, the nonlinearities were observed between the voltage and current responses of the polymer. To our knowledge, this is the first result indictating a nonlinear relationship between the external voltage and a signal measured inside the polymer.

We also notice a slower initial response in the square-wave excitation from Figure 6.9b. When compared to the formamide samples of the previous section (Figure 6.8b), we see that the formamide samples exhibit a fast initial rise in the internal potential with the application of a step change in the excitation voltage across the outer electodes. In comparison the EMI-Tf sample has a much slower response, indicative of a solvent with either higher viscosity or lower dielectric properties as discussed in the studies of Chapter 3. Based upon the properties of the ionic liquid, we attribute this slow response to the more viscous nature (45cp) of the solvent when compared to formamide (3.3-3.7cp).

Formamide samples		Ionic Liquid samples	
Thickness	Voltage (V)	Thickness	Voltage (V)
1.00 t_o	0.984	1.00 t_o	0.962
0.966 t_o	0.344	0.948 t_o	0.368
0.930 t_o	0.257	0.901t_o	0.292
		0.859 t_o	0.229

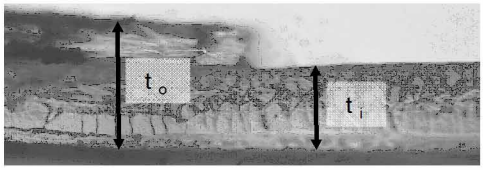

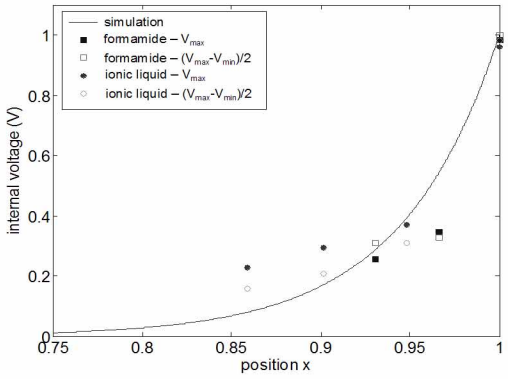

Figure 6.10: Comparison of the peak voltage responses for the formamide and EMI-Tf based transducers.

6.2.3 Comparison of results

Comparing the results of the formamide and EMI-Tf based transducers, we find that both systems predict a significant decrease in internal voltage as the inner thickness t_i becomes small relative to the outer thickness t_o. The EMI-Tf samples show this trend very clearly in the experimental results of Figure 6.9. The formamide sample also illustrates this trend, however there is the presence of a DC offset in the response at $t_i = 0.930t_o$. This behavior is also evident in the square-wave response of the ionic liquid sample, however the offset is in the positive direction for the EMI-Tf sample and it appears to be uniform for each of the test samples. Currently we do not have a conclusive explanation for this phenomena, however it is most likely attributed to the polymer's interaction with the transconductance amplifier. Previous work by Kothera has indicated that measureable variations do exist in the circuit for different polymers tested under similar conditions. The EMI-Tf sample is also seen to exhibit a slight nonlinearity in the response at $t_i = 0.948t_o$. This nonlinearity is cubic in nature and is similar to previous results obtained by Kothera [39] for the low frequency voltage to current relationship. While we observe this nonlinearity in internal to applied voltage relationship, it is reasonable to believe that the same fundamental mechanism is at work.

The overall response of the formamide and EMI-Tf samples support the steady-state voltage profiles predicted in the linearized models of Chapters 4 and 5, as well as the numerical predictions of Wallmersperger for the full nonlinear model of the transport equation. These experimental results predict a significant decline in the internal potential near the boundary region in each of the test samples. When peak voltage is plotted as a function of the thickness fraction $\frac{t_i}{t_o}$, we obtain the spatially distributed internal potential shown in Figure 6.10. This figure presents a comparison of the peak voltage (V_{max}) with the average peak-to-peak voltage $\left(\frac{V_{max}-V_{min}}{2}\right)$ measurements extracted form the results presented in Figures 6.8 and 6.9. The curve overlain on the data corresponds to the model prediction of the linearized model from Chapter 5. The value of ϵ used to generate this curve is defined as 200x greater than the estimated characteristic length for Li^+based sample in water hydrated form. The important result of

this comparison is that the exponential profile of the linearized model offers a much better fit of this experimental data than do the linear profiles of the LCE system with nonlinear boundary conditions or the approximate NLCE system developed in Chapter 5.

6.3 Chapter Summary

This chapter has presented a number of experimental studies which support and validate the models proposed in Chapters 4 and 5. Results were taken for both frequency and time domain analyses of the ionic polymer transducer, focusing on the impedance and internal potential response of various test samples. The frequency domain impedance study was designed to investigate three variations on the system: (1) ambient temperature, (2) solvent viscosity and (3) pretension of the transducer in the longitudinal direction. In each case, the model could successfully predict the resulting change in the transducer's response, offering insight into how changes in the effective permittivity and diffusion properties effect the ionic polymer membrane. For test conditions where the transducers experienced damage in the surface electrodes, a gain factor was introduced to account for decreased electrical conductivity due to excessive cracking. In the temperature study, parameters in the impedance model were tuned to the room temperature response. Then, temperature values were tuned in accordance with experimental conditions and the diffusion coefficient was scaled through previously published results of Yeager *et al.* [98, 99]. These terms were then applied to the model to predict the response at temperatures above and below the room temperature baseline. Results indicate very good correlations between the predicted response and measured data, supporting the validity of the modeling approach of Chapter 4.

A series of layered transducers were also fabricated and tested in an effort to measure the internal potential of an ionic polymer when subject to an external voltage. Numerous transducers were fabricated to investigate this internal potential response near the outer electrode of the polymer actuator. Experimental results indicate significant drops in the voltage near the electrode, supporting the presence of exponential profiles of the internal potential through the polymer thickness. These results support our linearized model of Chapters 4 and 5, and provide experimental support for numerical simulations performed by Wallmersperger on the full nonlinear model of the transport equations. The following chapter will present the overall conclusions of this work and their contribution to the current field of research in ionic polymer transducers.

Chapter 7

Summary and Conclusions

Throughout this research, the primary objective has been the development of a model which describes the internal potential and charge motion within ion transport membranes. This chapter provides a summary of the major research results, conclusions and contributions of this work. The most notable results and conclusions are presented first, followed by a discussion of the significant contributions that this research offers to the field of active materials. Finally, recommendations for future work are presented at the end of the chapter.

7.1 Research Conclusions

The research presented in this dissertation focuses on the modeling and characterization of ionic polymer transducers. Chapter 1 begins the discussion by providing an overview of the history and development of this class of active material, starting from the material's inception for fuel cell applications in the 1960s to the discovery of their actuation and sensing capabilities in the early 1990s. From this historical overview, this discussion shifts toward the experimental and analytical characterizations that have been performed on these transducers over the last decade. One of the key points made in this discussion is that most of the existing studies have focused solely on the actuation (voltage to displacement) response of the IPT. The point is also made that while there have been a number of models proposed for the ionic polymer, there still does not exist a concensus regarding the fundamental mechanism that gives rise to the electromechanical response. This prevailing trend in modeling the actuation characteristics of the IPT motivates our study of the sensing and impedance responses of the ionic polymer. Since these modes of operation are not as well understood as the actuation response, improved modeling techniques will provide additional insight into the underlying mechanisms that give rise to the transduction phenomena exhibited by the ionic polymer transducer.

The first modeling approach considered in dissertation begins with the sensing model of Chapter 2. A basic transport model is proposed based upon the Nernst-Planck expression and the initial charge density is assumed to

be linearly proportional to an imposed stress upon the material. Thus, under a mechanical deformation a charge imbalance is induced within the polymer, resulting in a current, or charge, response that is measurable at the polymer's outer electrodes. Experimental studies were conducted to validate this model for step changes in the tip deflection of an IPT, and the effect was shown to scale proportionally with the transducer's geometry as predicted in the model. From this the experimental study was expanded to consider other factors in the ionic polymer's sensing response, namely counterion species, solvent viscosity and solvent dielectric. The experimental study was also extended to consider the actuation and impedance response of the test samples, all considered in both the time and frequency domain. In these studies the water-based transducer in Li^+form was used as a baseline sample. In each iteration of the experimental study, noticeable changes were observed in each of the measured responses: actuation $\left[\frac{\mu\epsilon}{V}\right]$, sensing $\left[\frac{C}{\mu\epsilon}\right]$ and impedance $\left[\frac{V}{A}\right]$. Interestingly, variations in the actuation and sensing responses could be reduced significantly by normalizing each by the transducer's impedance response. Therefore, it is observed that test samples exhibit very similar actuation and sensing responses when expressed in terms of $\left[\frac{\mu\epsilon}{C/m^2}\right]$ and $\left[\frac{V}{\mu\epsilon}\right]$, respectively. This result supports findings of Akle [1] and provided motivation for the impedance model developed in Chapter 4.

Basic transport theory was again revisited in the development of this impedance model. Using a nondimensional form of the transport equation, a series of expressions were developed to describe the internal potential and charge density as functions of either step or harmonic excitation voltages. From this expression for the internal charge density two characteristics of the polymer could be studied: saturation of ρ at the anode due to high excitation voltages, and the formation of surface currents at the electrode which can be related to the excitation voltage to yield an overall impedance model for the polymer. The study of these saturation effects reflects a similar concept proposed by Nemat-Nasser [59] for step excitations. In his work Nemat-Nasser postulates that cations could fully deplete regions around the anode under sufficient voltage, causing a fixed charge density to develop in this region due to the fixed anion concentration C^-. The research presented in this dissertation extends this analysis to actually quantify the voltage associated with a step excitation signal, and to develop relationships for the harmonic excitation. In the case of a harmonic excitation, the saturation voltage is seen to be a function of the excitation frequency, requiring higher threshold voltages at higher frequencies. In addition to the saturation study, the charge density is also used to develop an expression for the surface current, offering a way to predict the internal impedance of the ionic polymer. For the case of a harmonic excitation, the voltage to current relationship was characterized as a function of the driving frequency, producing a set frequency response predictions that could be compared to experimental results. A parametric study of this model was conducted to consider the effect of diffusion coefficient, permittivity and temperature on the impedance predictions. These predictions were then compared to experimental studies in Chapter 6, finding good correlation between the analytical and experimental results.

In developing both the sensing and impedance models, a linearized expression for the transport equation was assumed. Chapter 5 relaxed this assumption and considered different simplifications of the nonlinear Nernst-Planck relationship to see if any additional insight could be gained through these alternate simplifications. Four cases

were considered in this study, focusing on the linear system with linear and nonlinear boundary conditions, and on two simplifications of the nonlinear system with nonlinear boundary conditions. The most interesting result of this analysis is that the linear system was actually found to provide the best approximation of the full nonlinear problem. This conclusion is based upon comparisons with numerical simulations by Wallmersperger [47, 89], and is attributed to the interaction between the flux boundary condition and the governing differential equation. It was found that a straightforward linearization of the problem maintained the same relationship seen in the full nonlinear expression, producing spatial profiles of the internal potential which were consistent with the simulations of Wallmersperger. These conclusions were also supported by experimental measurements of the internal potential in Chapter 6.

7.2 Research Contributions

The purpose of this research has been to better the general understanding of ionic polymer transducers, and to characterize their performance through analytical modeling. The major results of this research have been presented in the previous section, now we shift the focus to consider the contributions that this research has on the study of ionic polymers, and their role as active materials.

- *Development of an Analytical Sensing Model Based on Transport Theory.* The dominant trend in research on ionic polymers has focused on the actuation response of these plated ionomer membranes. Very little emphasis has been placed on the sensing response of these materials, motivating the investigation presented in Chapter 2 of this dissertation. Only two models of this sensing response had been proposed in the literature at the outset of this research, one focusing on the work of Nemat-Nasser and Li [61] which considers a pseudo-dipole model of the cation-anion pair, and the other proposed by Newbury and Leo [67] which relies on constitutive equations to produce a coupled sensing and actuation model. The approach presented in this dissertation considers the reciprocity concept suggested by Newbury and Leo in their coupled constitutive model. Thus, a sensing model has been derived and validated using the same transport equations used by Nemat-Nasser [61, 59] to describe the actuation response of the ionic polymer. The resulting sensing model successfully predicts the polymer's charge response to step changes in deformation of the cantilevered sample, and accounts for geometric scaling in the transducer. Most importantly, the model demonstrates that the same basic theory can be used to predict both sensing and actuation responses of the ionic polymer transducer.

- *Characterization of the Actuation, Sensing and Impedance Responses as Functions of Counterion, Solvent Viscosity and Solvent Dielectric Properties.* One interesting feature of the ionic polymer is that it's electromechanical response can be tailored with simple changes in the counterion specie or by changes in the solvent used to swell the membrane. Some initial work in this area has been conducted by Shahinpoor and Kim [79] and Nemat-Nasser *et al.* [59, 64, 100, 63]. Their findings indicate that appreciable changes can

be observed in the actuation response as counterion and solvent are varied within the polymer. The results presented in Chapter 3 extends this work to consider frequency domain analysis, and to incorporate the sensing and impedance responses of each sample into the analysis. As in the previous studies, significant changes were noticed in each of the measured responses. Upon further analysis, it was noticed that these changes were directly linked to the impedance response of the transducer. By normalizing the measured actuation and sensing responses by the transducer's measured electrical impedance, results were seen to coalesce. Thus, the changes in counter-ion and solvent type were seen to predominantly effect the electrical properties of the test sample, rather than the mechanical properties of the IPT. This result lends credibility to the impedance modeling of Chapter 4, illustrating the importance of ion transport in the overall electromechanical response of the ionic polymer.

- *Development of an Impedance Model.* The experimental results of Chapter 3 provide direct motivation for the development of an impedance model of the ionic polymer transducer. This model begins with the same transport theory considered in the sensing and actuation models, and is derived to yield a solution for the surface current that is expected to develop in response to an applied harmonic voltage. From this model a frequency domain representation of the electrical impedance can be extracted as a function of ambient temperature T, anion concentration C^-, polymer thickness L, diffusion coefficient d and effective permittivity κ. The first three of these parameters T, C^- and L can be measured directly or obtained from the membrane manufacturer. Thus, the benefit of this model is that it offers the ability to approximate diffusion coefficients and effective permittivity parameters directly from simple impedance measurements. Since these parameters are typically more difficult to measure, this ability eases the characterization of new membranes. Additionally, this model could provide insight into the design of new ionomer membranes. With the ability to predict the impedance, and consequently the electromechanical response of an ionomer, it would not be difficult to predict which properties would be desirable in new membrane materials. Thus, if used in conjunction with collaborations with Polymer Chemists it may be possible to significantly enhance the performance capabilities of new ionomers.

- *Use of Approximate Methods to Investigate Other Simplifications of the Nonlinear Transport Equation.* One of the major assumptions of any of the analytical models for the ionic polymers is that the transport equations can simply be linearized and studied accordingly. A simple comparison of coefficients is typically used to justify this linearization, however it was felt that some consideration should be given to other simplifications of the nonlinear set of transport equations. Therefore, a case study was undertaken to consider the effect that nonlinear boundary conditions have on the linearized transport equation, and to consider other approximate solutions to the nonlinear transport equation. Each variant of the system was analyzed, and a spatial profile of the internal potential was determined. These results were then compared to numerical simulations of the

full nonlinear system provided by Wallmersperger of the Universität Stuttgart. Comparison of these results indicate that the linear system with linear boundary conditions actually provides the best approximation of the full nonlinear system. This result is attributed to the unique interaction that exists between the transport equation and the flux boundary conditions, providing additional support for analysis of the linearized transport problem

7.3 Recommendations for Future Work

While the research presented in this dissertation has addressed each of the issues which motivated the study, there are several additional areas which could be investigated in future work. Recommendations for these future studies are as follows,

- The model developed here characterizes the impedance characteristics of the polymer as a function of numerous geometric, environmental and intrinsic properties of the membrane. It offers insight into the performance capability of a polymer membrane, however it does not offer direct predictions of the actuation response. Using the charge density predictions of this model, the system could be coupled with an electromechanical model, such as that proposed by Weiland and Leo [94], to produce time and frequency domain predictions of the actuation response.
- New electroding techniques could be used to produce experimental samples with a much broader range of solvents than those considered in Chapter 3. A greater number of samples would provide additional information which could be used to further distinguish the effects that solvent viscosity and dielectric coefficient have on the ionic polymer's electromechanical and impedance responses.

Bibliography

[1] B. Akle. *Characterization and Modeling of the Ionomer-Conductor Interface in Ionic Polymer Transducers*. Virginia Polytechnic Institute and State University, Blacksburg, Virginia, 2005.

[2] B.J. Akle, M.D. Bennett, and D.J. Leo. Ionic electroactive hybrid transducers. *Proceedings of the SPIE*, 5759:153–164, 2005.

[3] B.J. Akle, M. Hickner, D.J. Leo, and J.E. McGrath. Correlation of capacitance and actuation in ionomeric polymer transducers. *Journal of Materials Science*, 40(14):3715–3724, 2004.

[4] K. Asaka, N. Fujiwara, K. Oguro, K. Onishi, and S. Sewa. State of water and ionic conductivity of solid polymer electrolyte membranes in relation to polymer actuators. *Journal of Electroanalytical Chemistry*, 505:24–32, 2001.

[5] K. Asaka and K Oguro. Bending of polyelectrolyte membrane platinum composites by electric stimuli, part ii. response kiinetics. *Journal of Electroanalytical Chemistry*, 480:186–198, 2000.

[6] V. Barbi, S. Funari, R. Gehrke, N. Scharnagl, and N. Stribeck. Nanostructure of nafion membrane as a function of mechanical load studied by saxs. *Polymer*, 44:4853–4861, 2003.

[7] M. Bennett. *Manufacture and characterization of ionic polymer transducers employing non-precious metal electrodes*. Virginia Polytechnic Institute and State University, Blacksburg, Virginia, 2002.

[8] D. Bernardi and M. Verbrugge. *Modeling of batteries and fuel cells*, chapter Mathematical model of a solid-polymer-electrolyte fuel cell, pages 240–280. American Chemical Society, 1991.

[9] M. Buechler. *Variational modeling of ionic polymer-based structures*. Virginia Polytechnic Institute and State University, Blacksburg, Virginia, 2005.

[10] P. de Gennes, K. Okumura, M. Shahinpoor, and K.J. Kim. Mechanoelectric effects in ionic gels. *Europhysics Letters*, 50:513–518, 2000.

[11] A. Eisenberg and J.S. Kim. *Introduction to ionomers*. John Wiley & Sons, INC., New York, NY, 1998.

[12] A. Eisenberg and M. Rinaudo. Polyelectrolytes and ionomers. *Polymer Bulletin*, 24:671, 1990.

[13] K. Farinholt and D. Leo. Electromechanical modeling of charge sensing in ionic polymers. *Proceedings of the SPIE*, 5053-2, 2003.

[14] K. Farinholt and D. Leo. Effects of counterion, solvent type and loading condition on the material response of ionic polymer transducers. *Proceedings of the SPIE*, 5387-2, 2004.

[15] K. Farinholt and D. Leo. Modeling of electromechanical charge sensing in ionic polymer transducers. *Mechanics of Materials*, 36:421–433, 2004.

[16] K. Farinholt, K. Newbury, M. Bennett, and D. Leo. An investigation into the relationship between charge and strain in ionic polymer sensors. *Proceedings of the First World Conference on Biomimetics and Artificial Muscles*, 2002.

[17] P. Fedkiw and W. Her. An impregnation-reduction method to prepare electrodes on nafion spe. *Journal of the Electrochemical Society*, 136:899–900, 1989.

[18] L. Ferrara, M. Shahinpoor, K. Kim, B. Schreyer, A. Keshavarzi, E. Benzel, and J. Lantz. Use of ionic polymer-metal composites (ipmcs) as a pressure transducer in the human spine. *Proceedings of the SPIE*, 3669:394–401, 1999.

[19] M. Fugimura, T. Hashimoto, and H. Kawai. Small-angle x-ray scattering study of perfluorinated ionomer membranes 1. origin of two scattering maxima. *Macromolecules*, 14:1309–1315, 1981.

[20] M. Fugimura, T. Hashimoto, and H. Kawai. Small-angle x-ray scattering study of perfluorinated ionomer membranes 1. models for ionic scattering maximum. *Macromolecules*, 15:136–144, 1982.

[21] G.Frenning, A. Johsson, A. Larsson, and M. Strϕmme. Theoretical investigation of ion conduction in three-layered ion-conductor systems: derivation of the isothermal transient ionic current and frequency dependent impedance. *Journal of Applied Physics*, 94:1629–1638, 2003.

[22] G.Frenning and M. Strϕmme. Theoretical derivation of the isothermal transient ionic current in an ion conductor: Migration diffusion and space-charge effects. *Journal of Applied Physics*, 90:5570–5575, 2001.

[23] T.D. Gierke. Ion clustering in nafion perfluorosulfonic acid membranes and its relationship to hydroxyl rejection and chlor-alkali current efficiency. Presented at the 152nd National Meeting - The Electrochemical society, Abstract No. 438, 1977.

[24] T.D. Gierke and W. Hsu. *Perfluorinated Ionomer Membrane*, chapter 13 - The cluster-network model of ion clustering in perfluorosulfonated membranes, pages 283–307. American Chemical Society, 1982.

[25] T.D. Gierke, G.E. Munn, and F.C. Wilson. Morphology of perfluorosulfonated membrane products wide-angle and small-angle x-ray studies. *Journal of Polymer Science: Polymer Physics Edition*, 19:1687–1704, 1981.

[26] T.D. Gierke, G.E. Munn, and F.C. Wilson. *perfluorinated Ionomer Membrane*, chapter 10 - The Morphology in Nafion perfluorinated membrane products, as determined by wide- and small-angle X-ray studies. American Chemical Society, 1982.

[27] A. Goswami, A. Acharya, and A.K. Pandey. Study of self-diffusion of monovalent and divalent cations in nafion-117 ion-exchange membrane. *Journal of Physical Chemistry B*, 105:9196–9201, 2001.

[28] G. Greeuw and B.J. Hoenders. Theoretical solution of the transient current equation for mobile ions in a dielectric film under the influence of a constant electric field. *Journal of Applied Physics*, 55:3371–3375, 1984.

[29] P.E. Grimshaw, J.H. Nussbaum, and A.J. Grodzinsky. Kinetics of electrically and chemically induced swelling in polyelectrolyte gels. *Journal of Chemical Physics*, 93:4462–4472, 1990.

[30] R. Hamlen, C. Kent, and S. Shafer. Electrochemically activated contractile polymer. *Nature*, 206:1149–1150, 1965.

[31] T. Hashimoto, M. Fugimura, and H. Kawai. *Perfluorinated Ionomer Membrane*, chapter 11 - Structure of sulfonated and carboxylated perfluorinated ionomer membranes - small-angle and wide-angle x-ray scattering and light scattering. American Chemical Society, 1982.

[32] W. Hsu and T. Gierke. Elastic theory for ionic clustering in perfluorinated ionomers. *Macromolecules*, 15:101–105, 1982.

[33] R. Kanno, A. Kurata, S. Tadokoro, T. Takamori, and K. Oguro. Characteristics and modeling of icpf actuator. *Proceedings of the Japan-USA Symposium on Flexible Automation*, pages 219–225, 1994.

[34] R. Kanno, S. Tadokoro, T. Takamori, and M. Hattori. Linear approximate dynamic model of icpf (ionic conducting polymer gel film) actuator. *Proceedings of the IEEE International Conference on Robotics and Automation*, pages 219–225, 1996.

[35] A. Katchalsky. Rapid swelling and deswelling of reversible gels of polymeric acids by ionization. *Experientia*, 5:319–320, 1949.

[36] A. Keshavarzi, M. Shahinpoor, K. Kim, and J. Lantz. Blood pressure, pulse rate, and rhythm measurement using ionic polymer-metal composite sensors. *Proceedings of the SPIE*, 3669:369–376, 1999.

[37] K.J. Kim and M. Shahinpoor. Ionic polymer-metal composites - ii. manufacturing techniques. *Smart Materials and Structures*, 12:65–79, 2003.

[38] C. Kothera. *Micro-manipulation and bandwidth characterization of ionic polymer actuators*. Virginia Polytechnic Institute and State University, Blacksburg, Virginia, 2002.

[39] C. Kothera. *Characterization, modeling and control of the nonlinear actuation response of ionic polymer transducers*. Virginia Polytechnic Institute and State University, Blacksburg, Virginia, 2005.

[40] C.S. Kothera and D.J. Leo. Bandwidth characterization in the micropositioning of ionic polymer actuators. *Journal of Intelligent Material Systems and Structures*, 16(1):3–13, 2005.

[41] C.S. Kothera and D.J. Leo. Identification of the nonlinear response of ionic polymer actuators using the volterra series. *Journal of Vibration and Control*, 11(4):519–541, 2005.

[42] W. Kuhn. Reversible dehung und kontraktion bei anderung der ioisation eines netzwerks polyvalenter fadenmolekulionen. *Experientia*, 5:318–319, 1949.

[43] W. Kuhn, B. Hargitay, A. Katchalsky, and H. Eisenberg. Reversible dialation and contraction by changing the state of high-polymer acid networks. *Nature*, 165:514–516, 1950.

[44] N. Lakshminarayanaiah. *Transport phenomena in membranes*. Academic Press, New York, NY, 1969.

[45] N. Lakshminarayanaiah. *Equations of membrane biophysics*. Academic Press, New York, NY, 1984.

[46] J. Lee, J. Nam, H. Choi, H.M Kim, J. Jeon, and H.K. Kim. Water uptake and migration effect on ipmc (ion-exchange polymer metal composite) actuator. *Proceedings of the SPIE*, 4329:84–92, 2001.

[47] D.J. Leo, K. Farinholt, and T. Wallmersperger. Computational models of ionic transport and electromechanical transduction in ionomeric polymer transducers. *Proceedings of the SPIE*, 5759:170–181, 2005.

[48] R. Liu, W. Her, and P. Fedkiw. In situ electrode formation on a nafion membrane by chemical platinization. *Journal of the Electrochemical Society*, 139:15–23, 1992.

[49] M. Lopez, B. Kipling, and H. Yeager. Ionic diffusion and selectivity of a cation exchange membrane in nonaqueous solvents. *Analytical Chemistry*, 77:629–632, 1979.

[50] K. Mallavarapu and D. Leo. Feedback control of the bending response of ionic polymer actuators. *Journal of Intelligent Material Systems and Structures*, 12:143–155, 2001.

[51] P. Millet. Determination of self-diffusion coefficients from conductivity measurements in ionomer membranes. *Journal of Membrane Science*, 50:325–328, 1990.

[52] P. Millet, F. Andolfatto, and R. Durand. Preparation of solid polymer electrolyte composites: investigation of the ion-exchange process. *Journal of Applied Electrochemistry*, 25:227–232, 1995.

[53] P. Millet, F. Andolfatto, and R. Durand. Preparation of solid polymer electrolyte composites: investigation of the precipitation process. *Journal of Applied Electrochemistry*, 25:233–239, 1995.

[54] P. Millet, R. Durand, and M. Pineri. New solid polymer electrolyte composites for water electrolysis. *Journal of Applied Electrochemistry*, 19:162–166, 1989.

[55] C.S. Miner and N.N. Dalton. *Glycerol*. Reinhold Publishing Corporation, New York, NY, 1953.

[56] M. Mojarrad and M. Shahinpoor. Ion-exchange-metal composite sensor films. *Proceedings of the SPIE*, 3042:52–60, 1997.

[57] A. Nayfeh. *Introduction to Perturbation Techniques*. John Wiley & Sons, Inc., New York, 1993.

[58] A. Nayfeh. *Problems in Perturbations*. John Wiley & Sons, Inc., New York, 1993.

[59] S. Nemat-Nasser. Micro-mechanics of actuation of ionic polymer-metal composites. *Journal of Applied Physics*, 92:2899–2915, 2002.

[60] S. Nemat-Nasser. Nano-mechanics of actuation of ionic polymer-metal composites as soft actuators and sensors. Presentation at the First World Congress on Biomimetics and Artificial Muscles, December 2002.

[61] S. Nemat-Nasser and J. Li. Electromechanical response of ionic polymer metal composites. *Journal of Applied Physics*, 87:3321–3331, 2000.

[62] S. Nemat-Nasser and C.W. Thomas. *Electroactive Polymer (EAP) Actuators as Artificial Muscles*, chapter 11 Ionomeric Polymer-Metal Composites, pages 139–191. SPIE Press, 2000.

[63] S. Nemat-Nasser and Y. Wu. Tailoring actuation of ionic polymer-metal composites through cation combination. *Proceedings of the SPIE*, 5051:245, 2004.

[64] S. Nemat-Nasser and S. Zamani. Experimental study of nafion- and flemion-based ionic polymer-metal composites with ethylene glycol as solvent. *Proceedings of the SPIE*, 5051:233, 2003.

[65] K.M. Newbury. *Modeling, characterization, and control of ionic polymer transducers*. Virginia Polytechnic Institute and State University, Blacksburg, Virginia, 2002.

[66] K.M. Newbury and D.J. Leo. Electromechanical modeling and characterization of ionic polymer benders. *Journal of Intelligent Material Systems and Structures*, 2002.

[67] K.M. Newbury and D.J. Leo. Linear electromechanical model of ionic polymer transducers - part i: model development. *Journal of Intelligent Material Systems and Structures*, 14:333–342, 2003.

[68] K.M. Newbury and D.J. Leo. Linear electromechanical model of ionic polymer transducers - part ii: experimental validation. *Journal of Intelligent Material Systems and Structures*, 14:343–357, 2003.

[69] K. Oguro, Y. Kawami, and H. Takenaka. Bending of an ion-conducting polymer film-electrode composite by an electric stimulus at low voltage. *Journal of Micromachine Society*, 5:27–30, 1992.

[70] J. W. Paquette and K. J. Kim. Ionic polymer-metal composites as smart materials under subzero temperature conditions. *Proceedings of MRS Symposium*, 785:D8.1, 2003.

[71] J. W. Paquette, K. J. Kim, and D. Kim. Behavior of ionic polymer-metal composites under subzero temperature conditions. *Proceedings of IMECE*, page 42929, 2003.

[72] J. W. Paquette, K. J. Kim, and D. Kim. Low temperature characteristics of ionic polymer-metal composite actuators. *Sensors and Actuators A: Physical*, 118:135–143, 2005.

[73] Jason W. Paquette, Kwang J. Kim, Jae-Do Nam, and Yong S. Tak. An equivalent circuit model for ionic polymermetal composites and their performance improvement by a clay-based polymer nano-composite technique. *Journal of Intelligent Material Systems and Structures*, 14:633–642, 2003.

[74] O. Parrott, A. Nicolaisen, and D. Leo. Extensional transduction properties of ionic polymer materials. *Proceedings of the SPIE*, 4695, 2001.

[75] R. Rees and D. Vaughan. *Polymer Preprints. American Chemical Society. Division of Polymer Chemistry*, 6:287–295, 1965.

[76] K. Sadeghipour, R. Salomon, and S. Neogi. Development of a novel electrochemically active membrane and 'smart' material based vibration sensor/damper. *Smart Materials and Structures*, 1:172–179, 1992.

[77] D. Segalman, W. Witkowski, D. Adolf, and M. Shahinpoor. Theory and application of electrically controlled polymeric gels. *Smart Materials and Structures*, 1:95–100, 1992.

[78] M. Shahinpoor, Y. Bar-Cohen, J. Simpson, and J. Smith. Ionic polymer-metal composites (ipmc's) as biomimetic sensors, actuators and artificial muscles - a review. *Smart Materials and Structures*, pages R15–R30, 1998.

[79] M. Shahinpoor and K.J. Kim. The effect of surface-electrode resistance on the performance of ionic polymer-metal composite (ipmc) artifical muscles. *Smart Materials and Structures*, 9:543–551, 2000.

[80] M. Shahinpoor and K.J. Kim. Effects of counter-ions on the performance of ipmcs. *Smart Materials and Structures: Electroactive Polymer Actuators and Devices*, 3987:110–120, 2000.

[81] M. Shahinpoor and K.J. Kim. Ionic polymer-metal composites: I. fundamental. *Smart Materials and Structures*, 10:819–833, 2001.

[82] M. Shahinpoor and K.J. Kim. Novel ionic polymer-metal composites equipped with physically loaded particulate electrodes as biomimetic sensors, actuators and artifical muscles. *Sensors and Actuators, A*, 96:125–132, 2002.

[83] M. Shahinpoor, M. Mojarrad, and K. Salehpoor. Electrically induced large amplitude vibration and resonance characteristics of ionic polymeric membrane-metal composites artifical muscles. *Proceedings of the SPIE*, 3041:829–838, 1997.

[84] B. Steck and H. Yeager. Water sorption and cation-exchange selectivity of a perfluorosulfonate ion-exchange polymer. *Journal of the Electrochemical Society*, 83:1880–1884, 1981.

[85] S. Tadokoro, S. Yamagami, T. Takamori, and K. Oguro. Modeling of nafion-pt composite actuators (icpf) by ionic motion. *Proceedings of the SPIE*, 3987, 2000.

[86] M. Verbrugge and R. Hill. Ion and solvent transport in ion-exchange membranes - i. a macrohomogeneous mathematical model. *Journal of the Electromechanical Society*, 137:886–893, 1990.

[87] M. Verbrugge and R. Hill. Ion and solvent transport in ion-exchange membranes - ii. a radiotracer study of the sulfuric-acid, nafion-117 system. *Journal of the Electromechanical Society*, 137:893–899, 1990.

[88] M. Verbrugge and R. Hill. Transport phenomena in perfluorosulfonic acid membranes during the passage of current. *Journal of the Electromechanical Society*, 137:893–899, 1990.

[89] T. Wallmersperger, B. Kroplin, and R. Gulch. *Electroactive Polymer (EAP) Actuators as Artificial Muscles*, chapter 11 Modeling and analysis of chemistry and electromechanics, pages 285–308. SPIE Press, 2001.

[90] T. Wallmersperger, B. Kroplin, and R. Gulch. Numericial simulation of a coupled chemo-electric-formulation for ionic polymer gels in electric fields. *Proceedings of the SPIE*, 4695:303–314, 2002.

[91] T. Wallmersperger, B. Kroplin, and R.W. Gulch. Coupled chemo-electro-mechanical formulation for ionic polymer gels - numerical and experimental investigations. *Mechanics of Materials*, 36(5-6):411–420, 2004.

[92] L.M. Weiland and D.J. Leo. Electrostatic analysis of cluster response to electrical and mechanical loadingin ionic polymers with cluster morphology. *Smart Materials and Structures*, 13(2):323–336, 2004.

[93] L.M. Weiland and D.J. Leo. Computational analysis of ionic polymer cluster energetics. *Journal of Applied Physics*, 97(013541), 2005.

[94] L.M. Weiland and D.J. Leo. Ionic polymer cluster energetics: Computational analysis of pendant chain stiffness and charge imbalance. *Journal of Applied Physics*, 97(123530), 2005.

[95] Y. Xiao and Bhattacharya. Modeling electromechanical properties of ionic polymers. *Proceedings of the SPIE*, 4329:292–300, 2001.

[96] I. Yannas and A. Grodzinsky. Electromechanical energy conversion with collagen fibers in an aqueous medium. *J. Mechanochem. Cell Motility*, 2:113–125, 1973.

[97] H. Yeager. *Perfluorinated ionomer membrane*, chapter 4 - Transport properties of perfluorosulfonate polymer membranes. American Chemical Society, 1982.

[98] H. Yeager and B. Kipling. Ionic diffusion and ion clustering in a perfluorosulfonate ion-exchange membrane. *Journal of Physical Chemistry*, 83:1836–1839, 1979.

[99] H. Yeager and B. Steck. Cation and water diffusion in nafion ion exchange membranes: influence of polymer structure. *Analytical Chemistry*, 52:1215–1218, 1980.

[100] S. Zamani and S. Nemat-Nasser. Controlled actuation of nafion-based ionic polymer-metal composites (ipmcs) with ethylene glycol as solvent. *Proceedings of the SPIE*, 5385:159, 2004.

Vita

Kevin M. Farinholt was born on March 16, 1976 to Joseph and Linda Farinholt in Charlottesville, Virginia. He graduated from Albemarle High School in May 1994 and began his college education at Piedmont Virginia Community College in August of that year. Completing an Associates in Science in May 1997, Kevin transfered to Virginia Tech to begin courses in Mechanical Engineering that same month, and graduated Summa Cum Laude three years later in May of 2000. During his time as an undergraduate Kevin participated in the co-op program at Virginia Tech, from which he gained a year of work experience with AlliedSignal in Chester, Virginia. He was also admitted into the 5 year MS/BS program at Virginia Tech in the fall of 1999, allowing him to complete several graduate level courses during his senior year. Following graduation, Kevin was selected as a participant in the Space Scholars program at the Air Force Research Laboratory in Albuquerque, New Mexico. Following this summer at AFRL, Kevin returned to Blacksburg to begin his Master's research in the area of acoustic controls with Dr. Donald J. Leo in the Center for Intelligent Material Systems and Structures (CIMSS). He successfully completed his Master of Science in October 2001, and began research in modeling of ionic polymer transducers with Dr. Leo soon afterward. Kevin continued to work with Dr. Leo over the next four years and completed his Doctor of Philosophy degree in November 2005. During this time Kevin was the recipient of the Virginia Space Grant Consortium fellowship, as well as the National Defense Science and Engineering Graduate fellowship for his research in the area of ionic polymer transducers.

Address: Center for Intelligent Material Systems and Structures
310 Durham Hall
Blacksburg, VA 24061

This dissertation was typeset with LaTeX 2$_\varepsilon$[1] by the author.

[1] LaTeX 2$_\varepsilon$ is an extension of LaTeX. LaTeX is a collection of macros for TeX. TeX is a trademark of the American Mathematical Society. The macros used in formatting this dissertation were written by Greg Walker, Department of Mechanical Engineering, Virginia Tech.